Spin Dynamics, Charge Transport and Electron–Phonon Coupling Effects in Strongly Correlated Electron Systems

Habilitationsschrift

zur Erlangung der Lehrbefugnis für das Fachgebiet
Theoretische Physik

der Fakultät für Mathematik und Physik
der Universität Bayreuth

vorgelegt von

Holger Fehske

Bayreuth, Oktober 1995

To my family,
for a multitude of reasons

Abstract

In this report we discuss the properties of strongly correlated electron–phonon systems with special emphasis on the field of high-T_c superconductivity. The physics behind the cuprate superconductors is highly nontrivial and to explain especially their unusual normal–state behaviour might require breaking away from conventional theoretical frameworks. Here, we focus on the investigation of the most fundamental microscopic models of the Hubbard/t–J (Holstein) variety, which are ultimately hoped to contain the essential low–energy physics relevant to experiments. Because these Hamiltonians have proven to be so complicated to become a challenge by themselves, the purpose of the present report is twofold. Firstly, we analyze the (extended) Hubbard, t–(t')–J, Holstein Hubbard and Holstein t–J models in a wide range of parameter space in a systematic way by the use of both purely numerical exact diagonalization methods for finite clusters and mainly analytical slave–boson techniques for the infinite system. This comparative study should bring out valuable information on various aspects of (low–dimensional) electron/phonon systems – quite independently of the high–T_c problem – ranging from itinerant magnetism, to phase separation, to lattice instabilities and polaron formation. Secondly, an attempt is made to relate our model calculations to the experimental data in the physically relevant limits.

The report is divided into two parts. The first six chapters are concerned with the purely electronic models and mechanisms, whereas the remaining four chapters are intended to discuss electron–phonon interaction effects. Each chapter is preceded by introductory notes on the subject and a brief review of other approaches and the related literature. In view of the variety of the material covered in this work, we prefer to give several short summaries at the end of the sections separately.

In chapter 1, the crystallographic and electronic structures, the generic phase diagrams, and some of the most noteworthy physical properties of both hole– and electron–doped families of cuprate superconductors are surveyed, where particular emphasis is given on experiments probing the Fermi surface, the spin dynamics, and the carrier response in the normal state. Moreover, we address the possible appearance of chemical and electronic phase separation in these materials.

The simplest microscopic models that have been proposed to describe the behaviour of charge carriers doped into an antiferromagnetically correlated environment are presented in chapter 2. We start from the three–band extended Hubbard model accounting for the band structure of the active CuO_2 planes and discuss the cluster mapping procedure onto effective one–band Hubbard and t–(t')–J models which seem to be – at least so far – the minimal fermionic lattice models for the cuprates. A great variety of numerical and novel analytical techniques have been developed to tackle the strong–correlation problem in terms of these models. We will end this chapter with a detailed discussion of a particular auxiliary field approach to the Hubbard model – the so–called slave–boson method.

In chapter 3 we review the results of our exact diagonalization studies of the t–J and strong–coupling (extended) Hubbard or t–t$_3$–J (–V) model on finite square lattices with up to 36 sites and various numbers of holes. A modified Lanczos algorithm allows for the classification of the ground state according to wave–vector, total spin, and point–group symmetry. In the one–hole sector, we calculate the effective band dispersion and find evidence for a Fermi surface which takes the form of small hole pockets located near [at] the momenta $(\pm\pi/2, \pm\pi/2)$ $[(\pm\pi, 0)$, $(0, \pm\pi)]$ for the t–[t$_3$]–J model with $J \gtrsim 0.2t$. At larger hole dopings, we study the question of hole binding and phase separation. For the t–J model, an extrapolation of our finite–size results to the thermodynamic limit yields a completely phase separated ground state for J larger than $J_{PS}/t = 4.1$ (± 0.1). On the other hand we focus on the the limit $J = 0$ $(U = \infty)$, which is especially interesting with respect to the existence of ferromagnetism in the Hubbard model (Nagaoka problem). Furthermore, we present results for the thermodynamics of the 2D t–J model on finite lattices in the grand canonical ensemble. This allows us to vary the particle density continuously. The specific heat and the spin susceptibility show signatures of strong antiferromagnetic correlations in the low–doping regime apart from J larger than the Nagaoka value. We give evidence that the phase separation observed in the ground state of the t–J model at large J may be suppressed with increasing temperature.

Chapter 4 presents a detailed study of the 2D t–(t')–J model using a spin–rotation–invariant slave-boson technique. The magnetic phase diagram of the t–t'–J model is derived within the saddle–point approximation, by taking into account also incommensurate spiral order. Compared to the pure t–J model, the t'–term stabilizes antiferromagnetic long–range order in the low–doping region. Analyzing both local and global criteria for thermodynamic instability, the domain of phase separation is determined. In a next step, we include the (Gaussian) fluctuation corrections beyond the paramagnetic saddle–point and derive a concise expression for the dynamic spin and charge susceptibilities of the t–t'–J model going beyond random phase approximation (RPA). We note that the instability line of the paramagnetic phase obtained from the divergence of the static spin susceptibility is in agreement with the saddle–point phase diagram. Treating the spin dynamics near the magnetic instability, we find a collective spin–fluctuation mode. To compare our theoretical results with normal–state experiments on high–T_c cuprates, a second–neighbour hopping t' of different sign is included to account for band structure and Fermi surface effects of both hole– and electron–doped systems. Calculating the renormalized slave–boson quasiparticle band, the doping and temperature dependences of the Hall resistivity are explored within the relaxation–time approximation, the results being in accord with experiments on $\mathrm{La_{2-x}Sr_xCuO_4}$, $\mathrm{YBa_2Cu_3O_{6+x}}$, and $\mathrm{Nd_{2-x}Ce_xCuO_4}$. Using a generalized RPA expression for the spin susceptibility, we investigate the spin dynamical properties of the metallic cuprates. We attribute the contrasting $\vec{q}$–dependence of the magnetic structure factor $S(\vec{q}, \omega)$ seen in neutron scattering experiments for LSCO– and YBCO–type systems to differences in their fermiology. Assuming that the antiferromagnetic correlations are spatially filtered by the hyperfine form factors we calculate the temperature dependences of spin–lattice and spin–spin relaxation rates for planar copper and oxygen sites; the results agree qualitatively well with various experiments on $\mathrm{YBa_2Cu_3O_{6+x}}$.

In chapter 5, we propose a theory of magnetic short–range order in the paramagnetic phase of the one–band Hubbard model on the basis of the Kotliar–Ruckenstein slave–boson approach. In the functional–integral scheme the bosonized action, expressed in terms of fluctuating local magnetizations and internal magnetic fields, is transformed to an effective Ising model treated in the Bethe cluster approximation. The theory is evaluated in the saddle–point approximation including short–range order effects in a fully self–consistent way. Comparing our results with previous approaches, we observe the suppression of antiferromagnetic and incommensurate spiral long–range ordered phases in favour of a paramagnetic phase with short–range order in a wide doping region. Using realistic values of the on–site Coulomb repulsion for $\mathrm{La_{2-x}Sr_xCuO_4}$, $U/t \simeq 8$, the critical doping concentration (δ_{c1}) for the destruction of antiferromagnetism is obtained as 3–4 %, in agreement with experiments. In the paramagnetic phase with antiferromagnetic short–range order, the uniform static spin susceptibility, as calculated in our theory, consists of interrelated 'itinerant' and 'local' parts and increases upon doping. The zero–temperature susceptibility exhibits a cusp at the transition ($\delta_{c2} > \delta_{c1}$) to the paramagnetic phase without short–range order and reduces to the usual slave–boson result for larger doping. The peak position ($\delta_{c_2} = 0.26$) as well as the doping dependence agree very well with low–temperature susceptibility experiments on $\mathrm{La_{2-x}Sr_xCuO_4}$ showing a maximum at a hole doping of about 25%.

Chapter 6 addresses the effects of an interatomic (nearest–neighbour) Coulomb interaction (V) in terms of the half–filled extended Hubbard model. Applying a two–sublattice saddle–point approach, the slave–boson ground–state phase diagram compares favourably with previous Monte Carlo and Lanczos results. In particular, the first–order transition from a spin–density–wave to a charge–density–wave state is displaced from the mean–field line $U = 4V$ towards larger V. For large negative U and V, the electrons undergo a condensation transition to a charge separated state.

Chapter 7 is devoted to a (rather incomplete) introductory discussion of polaronic effects in the copper and nickel oxides. In addition, we introduce the Holstein (Hubbard) Hamiltonian which has most often served as a paradigmatic model to treat polaron formation in strongly coupled electron–phonon systems and provide a brief overview of recent theoretical work on this subject.

In chapter 8 we investigate the ground–state properties of the 2D Hubbard model with an additional Holstein–type electron–phonon coupling by means of a modified variational Lang–Firsov approach appropriate for describing static phonon–staggered ordering, polaronic and squeezing effects. Adapting the scalar four–field slave–boson technique to the effective electronic Hamiltonian, which is obtained in the vacuum state of the transformed phonon subsystem, our theory is evaluated at the saddle–point level of approximation for arbitrary band filling over a wide range of electron–electron and electron–phonon interaction strengths. We determine the order parameters for long–range charge and/or spin ordered states from the self–consistency conditions for the auxiliary boson fields, including an optimization procedure with respect to the variational displacement, polaron and squeezing parameters. In order to characterize the crossover from the adiabatic to the non–adiabatic regime, the frequency dependences of these quantities are studied in detail. As a central result we present the slave–boson ground–state phase diagram of the 2D Holstein Hubbard model at finite phonon frequencies in the case of a moderate electron–phonon coupling, i.e., in the light–polaron regime. Depending on doping level and Coulomb interaction strength, we observe Peierls distorted states with predominant charge or magnetic long–range order as well as antiferro–, ferro– and paramagnetic phases. In the non–dimerized paramagnetic phase, for low enough phonon frequencies, an abrupt 'self–trapping' transition from light to heavy polarons is found. Concerning the nature of this self–trapping transition, we comment on limitations and shortcomings of the present approach. In the heavy–polaron regime, the frequency–dependent polaron hopping conductivity is calculated. There occur qualitative finite–density and correlation effects on the zero–temperature absorption spectrum which are discussed with respect to their possible relevance to the mid-infrared absorption in high–T_c superconductors. Finally, in a rather technical part of this chapter, we start from the modified Lang–Firsov–transformed Holstein Hubbard model and derive effective polaron and bipolaron models within the unified framework of Schrieffer–Wolff–type transformations in the strong correlation limit. The resulting polaronic t–J and bipolaronic local pairing models obtained for large positive and negative on–site interactions, respectively, exhibit different renormalizations of the hopping and interaction terms in the heavy and light polaron and bipolaron cases.

Chapter 9 summarizes our direct Lanczos diagonalization results obtained for the Holstein Hubbard model on finite lattices with up to ten sites. Previously the necessary truncation of the phononic Hilbert space caused serious limitations to either very small systems (four or even two sites) or to weak electron–phonon coupling, in particular in the adiabatic regime. Using parallel computers we were able to investigate a wide range of phonon frequencies, electron–electron and electron–phonon interaction strengths to study the transition from 'large' to 'small' polarons in detail. By resolving the low–lying eigenstates of the Hamiltonian and by calculating the spectral function we can identify a polaron band in the strong–coupling case, whose dispersion deviates from the free–particle dispersion at low and intermediate phonon frequencies. For two electrons (holes) we establish the existence of bipolaronic states and discuss the formation of a bipolaron band. In addition, we demonstrate that the inhomogeneous modified variational Lang–Firsov (IMVLF) approach combined with Lanczos diagonalization of the resulting effective Hamiltonian is in excellent agreement with the exact solution in the adiabatic and non–adiabatic weak– and strong–coupling regimes, and provides a reliable interpolation scheme at intermediate couplings and frequencies.

To study the formation of hole–(bi)polarons in materials exhibiting strong Coulomb correlations, such as $\mathrm{La_{2-x}Sr_xCuO_{4+y}}$ or $\mathrm{La_{2-x}Ni_xCuO_{4+y}}$, the 2D Holstein t–J model is examined in chapter 10 by means of the IMVLF–Lanczos method. In the adiabatic limit, we explore the ground–state phase diagram near half–filling using the frozen–phonon approximation. The nature of the ground state is analyzed, calculating self–consistently the local lattice distortions, one–site spin and charge densities, as well as charge and magnetic structure form factors. Including inhomogeneous static displacement field, polaron and squeezing effects at finite phonon frequencies, our approach allows for the description of nearly free polarons in the weak–coupling limit as well as for adiabatic Holstein polarons and non–adiabatic Lang–Firsov polarons in the case of strong electron–phonon interaction. At low doping levels and low phonon frequencies we demonstrate that antiferromagnetic spin correlations and electron–phonon interactions reinforce each other to the effect of lowering the threshold for polaronic self–localization in a strongly distorted lattice. This is contrasted with the non–adiabatic regime, where we observe the formation of Lang–Firsov–type polarons with moderate polaronic mass enhancement in a nearly undistorted lattice. Analyzing the hole binding energy and the hole–hole correlation function in the two–hole case, we find that hole binding is enhanced as a dynamical (static) effect of a rather weak (extremely strong) electron–phonon interaction for delocalized (self–trapped) polarons. At quarter filling we notice, in the adiabatic regime, a sequence of transitions as the electron–phonon coupling increases from nearly free mobile polarons to a polaronic superlattice resembling the recently observed ordering of polarons in $\mathrm{La_{1.5}Ni_{0.5}CuO_4}$, and finally to a charge separated state. The ordering of polarons disappears at higher phonon frequencies.

Contents

List of Figures

List of Tables

List of Abbreviations

AFM	antiferromagnet(ic)
AHBP	adiabatic Holstein bipolaron
AHP	adiabatic Holstein polaron
ARPES	angular resolved photoemission spectroscopy
CDFT	constrained density–functional theory
CDW	charge–density–wave
CPA	coherent potential approximation
CT	charge transfer
CTI	charge transfer insulator
D	dimension(al)
ED	exact diagonalization
EP	electron–phonon
FIM	ferrimagnet(ic)
FM	ferromagnet(ic)
FP	nearly free polaron
FS	Fermi surface
HF	Hartree–Fock
HTSC	high–temperature superconductivity
IMVLF	inhomogeneous modified variational Lang–Firsov transformation
INS	inelastic neutron scattering
IR	infrared reflectivity
KR	Kotliar–Ruckenstein
LDA	local density approximation
LF	Lang–Firsov transformation
LP	large polaron
LRO	long–range order
LSCO	$\mathrm{La_{2-x}Sr_xCuO_4}$
NCCO	$\mathrm{Nd_{2-x}Ce_xCuO_4}$
NLFP	non–adiabatic Lang–Firsov polaron
NMR	nuclear magnetic resonance
NN	nearest–neighbour
NNN	next–nearest–neighbour
NQR	nuclear quadrupole resonance
NZA	News–Zou–Anderson
PM	paramagnet(ic)
QMC	quantum Monte Carlo
RPA	random phase approximation
RVB	resonating valence bond

SB	slave boson
SDW	spin–density–wave
SMVLF	staggered modified variational Lang–Firsov transformation
SRI	spin–rotation invariance
SRO	short–range order
UMVLF	uniform modified variational Lang–Firsov transformation
VLF	variational Lang–Firsov transformation
YBCO	$YBa_2Cu_3O_{6+x}$
ZRS	Zhang–Rice singlet

Part I

On Electron Correlations in the Normal State of High–T_c Cuprates

Chapter 1

Materials and experimental results

Following the discovery of high–T_c superconductivity (HTSC) in the ceramic copper oxide material $La_{2-x}Ba_xCuO_4$ by Bednorz and Müller in 1986 [1], an intensive but mainly empirical search for the preparation of materials with even higher critical temperatures was pursued by physicists and material scientists. To date a large number of superconducting compounds (approximately 40) with the characteristic CuO_2 planes have been synthesized. As a result T_c has raised from 30 K for $La_{2-x}Ba_xCuO_4$ to 156 K [2] in mercury–based $HgBa_2CuO_{4+y}$. Most noticeably during this period a more consistent experimental description of many properties of the principal cuprate families such as BiSrCaCuO, LaSrCuO, NdCeCuO, TlBaCaCuO, YBaCuO, and HgBaCaCuO has emerged. At the same time, the problem of understanding the mechanism of HTSC has attracted an enormous amount of theoretical work not only because T_c is high but because the copper oxides are strongly correlated electron systems exhibiting many unconventional normal–state properties.

This introductory chapter provides a short overview of the crystallographic and electronic structures, comments on the phase diagrams, and collects some characteristic experimental results of the most widely studied high–T_c oxides, where special emphasis is given on experiments probing magnetic correlations and transport phenomena in the normal state.

1.1 Crystal structure and phase diagram of the cuprates

The crystallographic structure of the perovskite–type HTSC cuprates may be visualized as a specific stacking sequence of conducting CuO_2 planes and insulating ionic layers. It is generally believed that the electron transport and the physical processes leading to superconductivity take place in the CuO_2 planes, with the other layers simply serving as a charge reservoir. Using this concept of block layers [3], Fig. 1.1 shows the lattice structure of three representative HTSC compounds, body–centered–tetragonal (bct) $Nd_{2-x}Ce_xCuO_4$ (NCCO, so–called T–phase), bct $La_{2-x}Sr_xCuO_4$ (LSCO, T'–phase), and orthorhombic $YBa_2Cu_3O_{6+x}$ (YBCO). In the CuO_2 planes, which are the most important structural elements, each Cu atom is strongly bound to four oxygen ions with a Cu-O distance of $\sim$ 1.9 Å, where, depending on the number (=0,1,2) of the apical oxygen(s), the two–dimensional (2D) networks are formed of squares, octahedra or pyramids. The out–of–plane Cu-O distance is about 2.4 Å.

Metallic behaviour is observed to arise when the insulating $[CuO_2]^{2-}$ planes of the antiferromagnetic ordered parent compounds Nd_2CuO_4, La_2CuO_4 and $YBa_2Cu_3O_6$ are doped with electrons or holes. The number of chemically doped charge carriers is related to an effective $[CuO]^{+p}$ charge. HTSC only emerges in a narrow window of doping level x (see Fig. 1.2 below) and it is experimentally well established that the nominal copper valence [2+p] is strongly correlated to the magnitude of T_c [4, 5]. In this context, the notations of underdoped and overdoped cuprates are frequently used with respect to the ‘optimal’ composition at which T_c becomes largest. It is interesting to note that the structure–sensitivity of the carrier–doping characteristics depends mainly on the pattern of Cu-O networks: the $\mathrm{CuO_2}$ sheets with squares sustain electron–like (n–type) carriers (NCCO), while those are built from octahedral (LSCO) and pyramidal (YBCO) networks can only be easily hole–doped (p–type carriers). In the simple single–layered compounds NCCO and LSCO the $\mathrm{CuO_2}$ plane is sandwiched between two equally charged block layers G$(-)$ and L$(+)$ of n– and p–type, respectively, whereas in YBCO the two $\mathrm{CuO_2}$ sheets per unit cell are embedded in a $(+,-)$ block–layer combination.

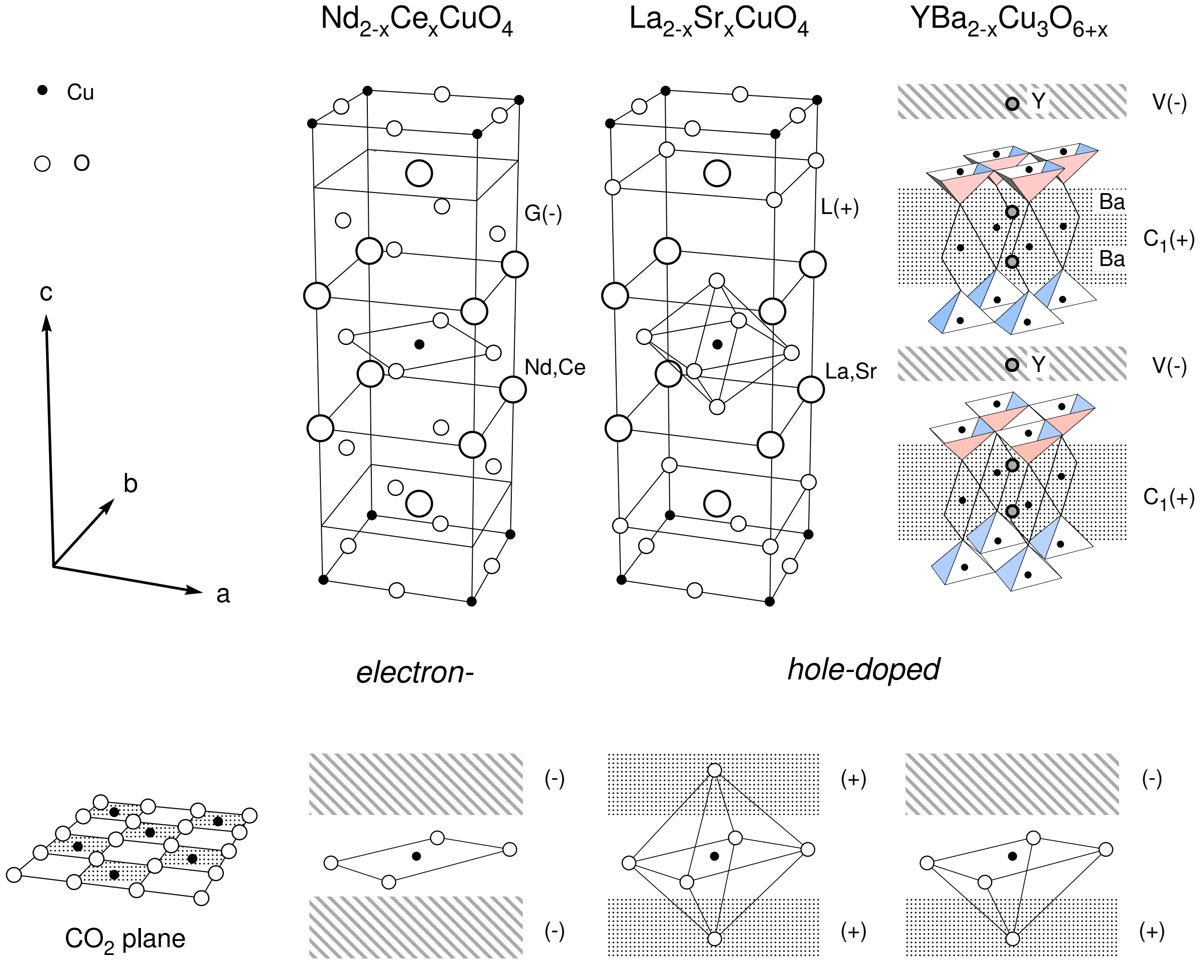

Figure 1.1: Crystal structures of $\mathrm{Nd_{2-x}Ce_xCuO_4}$, $\mathrm{La_{2-x}Sr_xCuO_4}$, and $\mathrm{YBa_2Cu_3O_{6+x}}$ (upper panel); basic structural elements forming the $\mathrm{CuO_2}$ layers (lower panel, after [3]).

In 214 $\mathrm{Nd_{2-x}Ce_xCuO_4}$ ($\mathrm{La_{2-x}Sr_xCuO_4}$), the charge of the $[\mathrm{G}]^{2+\mathrm{x}}$– ($[\mathrm{L}]^{2-\mathrm{x}}$–) layer is reduced (enhanced) with $\mathrm{Ce^{4+}}$– ($\mathrm{Sr^{2+}}$) substitution of trivalent La (Nd). Thus the effective $[\mathrm{CuO}]^{\mathrm{p}}$ charge is $-x$ or x for electron or hole doping. Here, it should be mentioned that electron– and hole–doping processes are different microscopically. In the former case, charge neutrality requires that excess electrons are transferred into the $\mathrm{CuO_2}$ plane, where each added electron creates locally a hole on Cu, producing a $S = 0$ closed d–shell ($[\mathrm{Cu}]^{+}$) configuration. On the other hand, to achieve charge neutrality for the Sr^{2+} dopants, an equivalent amount of in–plane oxygen atoms change their configuration from O^{2-} to O^{-} creating one hole in their p–shell and thereby leaving mobile hole–like charge carriers in the CuO_2 planes. This has been confirmed by the experimentally observed sign of the Hall coefficient (cf. Sec. 1.3.3 below).

In 123 $YBa_2Cu_3O_{6+x}$, hole doping amounts to the oxygenation of another Cu-O network, CuO_x, within the so–called C_1– layer [3]. The formation of these Cu-O chains becomes complete in fully oxygenated $YBa_2Cu_3O_7$, where the nominal valence of Cu in the C_1 block layer is (+1) for the parent compound $YBa_2Cu_3O_6$. It is believed that the added oxygens remove electronic charge from other parts of the materials, i.e., in particular from the CuO_2 planes, in order to form O^{2-} ions in the Cu-O chains. However, due to subtle details in the chain formation, the hole concentration in the CuO_2 layer depends on the oxygen content x in a complicated manner.

All cuprate superconductors have a similar generic phase diagram (cf. Fig. 1.2) and a successful theory of HTSC must be able to describe its main features. At very low carrier density the cuprates are usually AFM insulators below a Néel temperature of the order of 300 K. Upon doping the AFM vanishes rather rapidly and the system continuously varies between an anomalous semiconductor, a so–called 'strange metal' phase with strong Coulomb correlations and a more 'normal' paramagnetic metal. Upon lowering the temperature the materials become superconducting in a certain doping regime. Obviously, this rich phase diagram originates from the complicated interplay between strong AFM correlations and superconductivity in the vicinity of a Mott insulating state. To be more specific, Fig. 1.2 displays the actual phase diagrams of $Nd_{2-x}Ce_xCuO_4$, $La_{2-x}Sr_xCuO_4$ (left panel), and $YBa_2Cu_3O_{6+x}$ (right panel) in the T–x plane. Despite the remarkable similarities between electron– and hole–doped 214 systems, the combined diagram for these materials illustrates an apparent (quantitative) asymmetry regarding the stability of AFM long–range order. In LSCO, the AFM state is already destroyed for very small doping concentration, where above $x > 0.02$, the delocalized holes causing the AFM to give way to a 'frozen' spin glass phase (SG) which persists up to $x \sim 0.1$. The op-

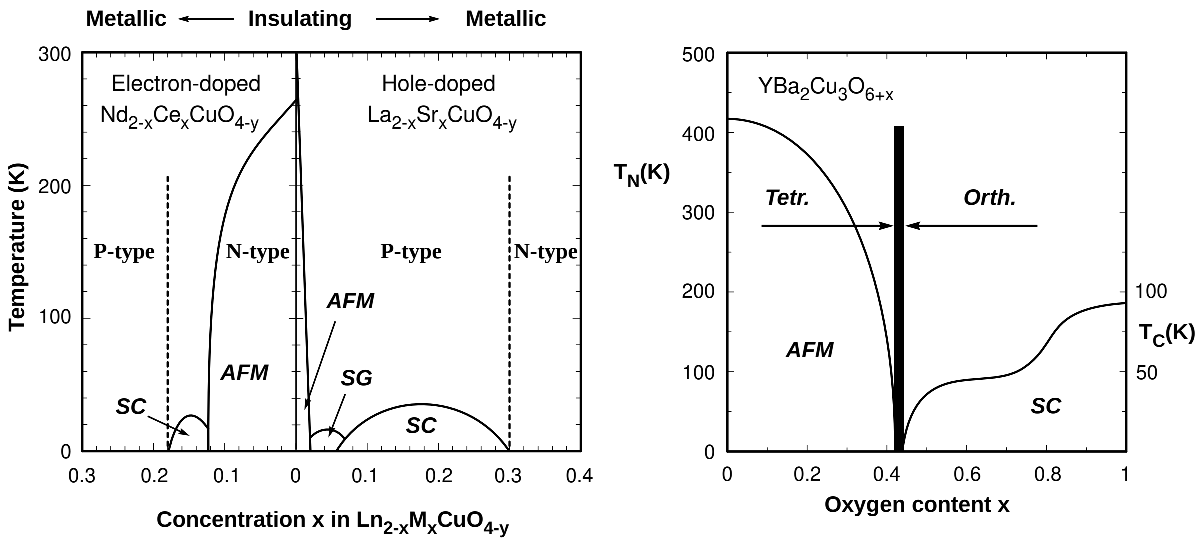

Figure 1.2: Phase diagram of $Nd_{2-x}Ce_xCuO_4$, $La_{2-x}Sr_xCuO_4$ (left panel, taken from [6, 7]), and $YBa_2Cu_3O_{6+x}$ (right panel, after [8]).

timal composition for HTSC is close to $x = 0.15$ in both compounds and superconductivity disappears again at higher dopings. In $YBa_2Cu_3O_{6+x}$, a structural phase transition occurs from a tetragonal insulating to a metallic orthorhombic state near $x_c \sim 0.4$. Details of the above–mentioned chain formation gives rise to the so–called 60 K plateau in the x–dependence of T_c . Note that the highest T_c is reached slightly below the fully oxygenated $123O_7$ compound.

1.2 Band structure and Fermi surface

The quasi two–dimensionality of the cuprate superconductors is reflected in their electronic structure which is determined by the strong Cu-O covalence in the conducting CuO_2 planes. Despite some structural peculiarities, it can be shown that in all cuprates the copper and oxygen orbitals are separate, as schematically displayed in Fig. 1.3. This basic framework of the electronic structure was corroborated by first–principles band theory calculations [11]. Besides a large number of less dispersive ‘spaghetti’ bands, the archetypal one–electron band structure of the undoped parent compounds shows only two bands of primary interest: the lowest bonding band that is full and the highest antibonding band which is exactly half–full – both bands are highly dispersive along k_x and k_y in the Brillouin zone of the basal CuO_2 plane [12, 13]. These general features of the band structure are well reproduced by a simple tight–binding analysis of a half–filled CuO_2 plane (see Fig. 1.4). Most notably this model, as

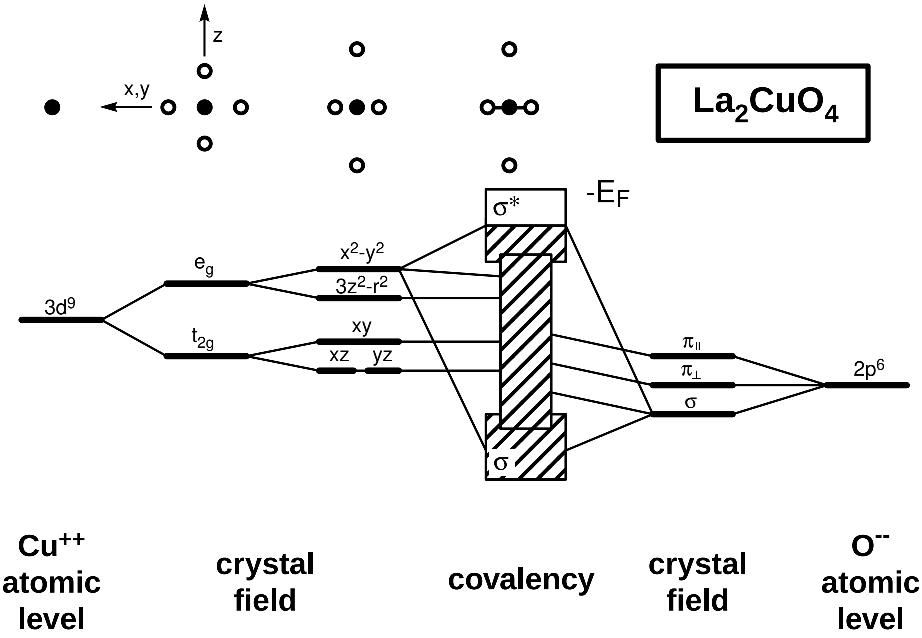

Figure 1.3: Bonding between a Cu^{2+} and two O^{2-} ions in La_2CuO_4. Only the $3d^9$ Cu and the $2p_x$ and $2p_y$ O orbitals are considered (after [9, 10]). Due to crystal field interactions, the Cu 3d orbitals are split into e_g and t_{2g} levels. Their degenerancy is further lifted by a Jahn–Teller distortion. The highest (antibonding) σ^* orbital has mainly $d_{x^2-y^2}$ character, and therefore the predominant coupling is the nearest–neighbour (NN) sigma–bonded coupling between Cu d–states and in–plane O p–states. This state carries the missing electron, i.e., with one hole per CuO_4 unit, La_2CuO_4 is expected to be metallic.

well as the more elaborated LDA (local density approximation) and quantum chemistry cluster calculations, predicts a metallic ground state for the undoped parent compounds being in reality antiferromagnetic insulators (cf. Sec. 1.1). The failure of the LDA calculations has been taken as direct evidence for the importance of strong correlation effects. However, the LDA reproduces well other properties of the systems, such as the electronic charge distributions [10]. Moreover, the LDA calculated Fermi surfaces (FS) agree surprisingly well with the experimental FS for the optimally doped materials. In particular, the large volume of the FS, determined by angle–resolved photoemission (ARPES) in the high–doping regime, appears to be consistent with the results of LDA calculations to first order.

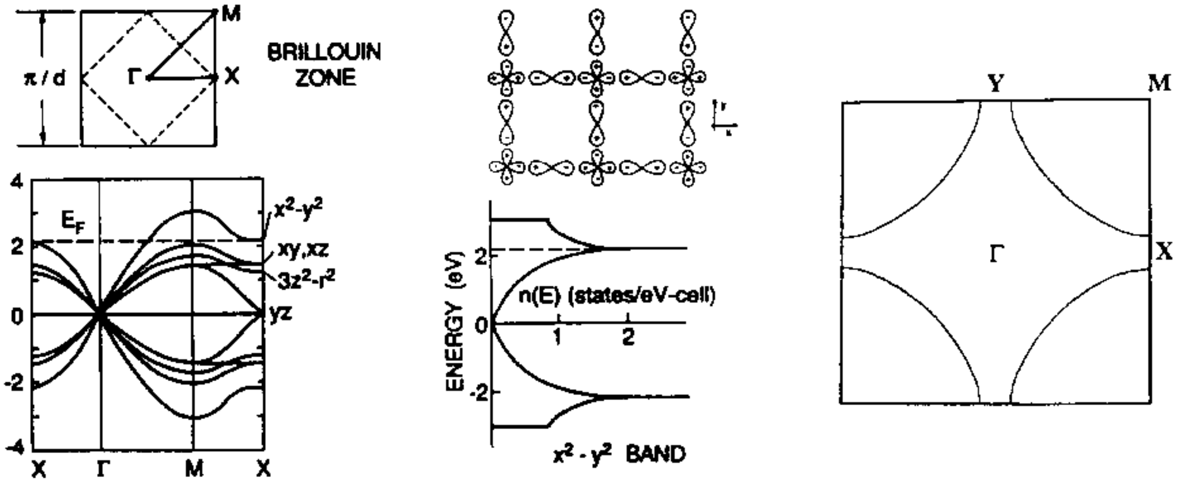

Figure 1.4: Tight–binding calculation of the electronic structure of a half–filled CuO_2 plane, where only NN interactions (Cu-O) are included ((left,center), after [14]). The highest band reaches its maximum at M and has a saddle point at X giving rise to a van–Hove singularity in the density of states. At zero doping the $x^2 - y^2$ band is half filled and a perfect nested square Fermi surface forms, where the Fermi energy lies at the van–Hove singularity. The inclusion of next–NN O-O coupling terms buckles the Fermi surface, with the main effect, that it moves the van–Hove singularity below the Fermi surface at half–filling (right panel, after [15]). Then, in a simple picture, electron (hole) doping will cause the Fermi surface to expand (contract) so that it is centered around the M (Γ) point, i.e., n–doping will move E_F farther away from the van–Hove singularity, while moderate p–type doping will bring it back [16].

As the near–E_F electronic structure and FS topology are important aspects in understanding the physical properties of high–T_c superconductors, many ARPES experiments have been carried out to address these issues where special attention has been paid to the doping behaviour of the cuprates (for an excellent survey on latest photoemission studies we refer to Ref. [16]). To perform a FS mapping using ARPES, it is necessary to determine the topological surface in $\vec{k}$–space where the quasiparticle peak disappears from the photoemission spectrum after it passes E_F. Despite some uncertainties regarding the photoemission lineshape and background and the related difficulties in determining the crossing position, ARPES unambiguously demonstrated the existence of a well–defined FS in the metallic cuprates (probably obeying Luttinger's theorem [17]). Typical examples of measured Fermi surfaces[1] are shown

---

[1] Due to differences in the crystal structure, the Brillouin zone notation differs for each cuprate family. Using

in Fig. 1.5. Obviously, the theoretical (LDA) FS for $YBa_2Cu_3O_7$ [18] has some of the essence of the experimental FS.

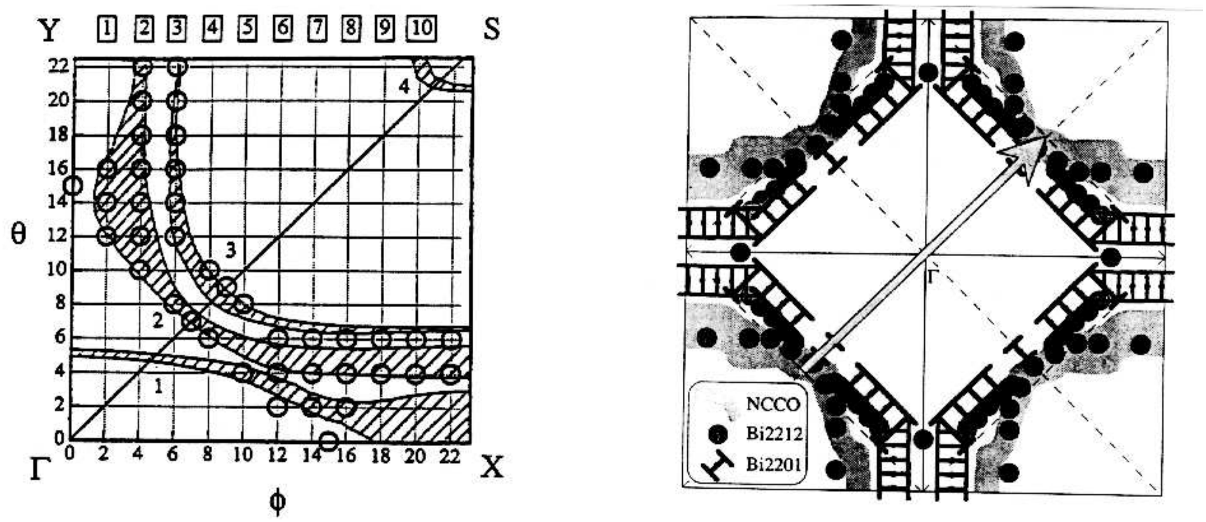

Figure 1.5: Experimental Fermi surface of $YBa_2Cu_3O_{6.9}$ [19] compared to a band theory FS of $YBa_2Cu_3O_7$ [18] where the smearing that incurred from the k_z–dispersion is indicated by shading of the crossings (left panel). Comparison of the experimental Fermi surfaces of $Bi_2Sr_2CaCu_2O_{8+\delta}$ (Bi2212), $Bi_2Sr_2CuO_{6+\delta}$ (Bi2201), and NCCO (right panel, taken from [16]). The FS of both Bi2201 and NCCO are closed around the X(Y) points. Note that the FS of Bi2212 is almost perfect nested where the nesting vector is nearly commensurate with the AFM wave vector $\vec{q}_{AFM} = (\pi, \pi)$. In contrast, only a small fraction of the FS of Bi2201 and YBCO appears to be nested along the (π, π) direction.

One of the most striking aspects of the experimental data is the presence of 'flat bands' in a variety of samples (see Fig. 1.6), i.e., the quasiparticle dispersion $E(\vec{k})$ observed in ARPES is nearly momentum independent over a significant $\vec{k}$–region. The results depicted in Fig. 1.6 show that the E *vs* $\vec{k}$ relationship is highly dispersive along the Γ–M direction, in particular around $(\pi/2, \pi/2)$, while an abnormal flat region appears near the X point $[(\pi, 0)$ in the 2D square lattice notation]. It is important to note that in the p–doped compounds the Fermi energy is only slightly above these flat regions. In addition, the saddle point of the dispersion was found close to the X–point (cf. the tight–binding analysis according to Fig. 1.4), and this 'extended' saddle point is expected to qualitatively change the nature of the divergence in the density of states [20]. By contrast, in the n–type cuprate NCCO, the flat bands are located well below E_F and so they are of minor importance (see Fig. 1.6). The possibility that the more 'anomalous' behaviour of the hole–type cuprates may be related to this striking difference in the quasiparticle band structures of p– and n–type superconductors has been intensively discussed in the literature [16, 21]. Recently, it was suggested that the flat bands may have a many–body origin [7, 22, 23].

---

the notation of the 2D square lattice ($\Gamma \leftrightarrow (0,0)$, X [Y] $\leftrightarrow (\pi/a, 0)$ $[(0, \pi/a)]$, and M $\leftrightarrow (\pi/a, \pi/a)$), the Γ–X[Y] direction is along the Cu-O bonds, i.e., they are orientated along the edges of the Brillouin zone. Then, following [16], the one–to–one mapping for LSCO and NCCO is: $\Gamma \to \Gamma$, $M \to X[Y]$, and $X[Y] \to G_1$; for Bi2212 it is $\Gamma \to \Gamma$, $M \to X[Y]$, and $X[Y] \to \bar{M}$; and for YBCO it is $\Gamma \to \Gamma$, $M \to S$, and $X[Y] \to Y[X]$. Again, the orientation of the Cu-O bonds is parallel to the edges of the Brillouin zone.

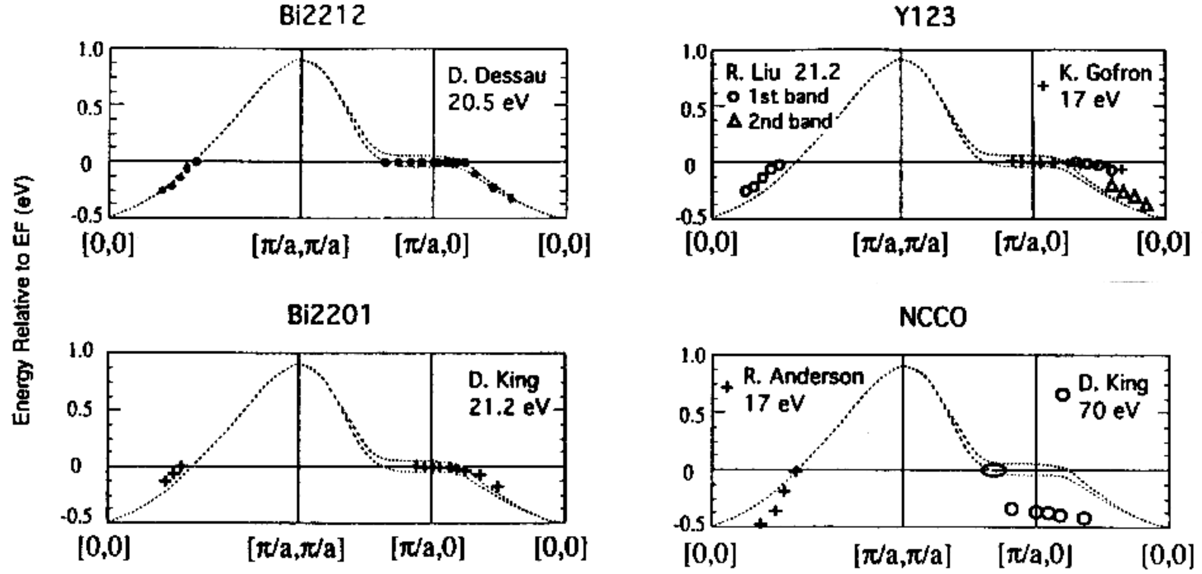

Figure 1.6: Quasiparticle dispersion for Bi2212, Bi2201, YBCO (Y123), and NCCO obtained using ARPES techniques (after [16]; see also [24, 25]). The dotted lines are a fit to a simple E *vs* $\vec{k}$ relationship [26] compatible with the Bi2212 data.

1.3 Normal–state properties

The interplay of charge and spin dynamics in the normal state holds the key to the understanding of the physical mechanism behind HTSC in the cuprates. Both macroscopic measurements of transport (resistivity, Hall effect, thermoelectric power) and magnetic (susceptibility, magnetization) properties as well as microscopic measurements probing the charge (optical conductivity) and spin (dynamical structure factor, nuclear relaxation rates) excitation spectra were fundamental in establishing the anomalous normal–state properties of these materials. Here the phrasing ‘unusual’ or ‘anomalous’ is commonly used to emphasize the differences with what is ‘usually’ found in most metallic systems and thought to be well understood in terms of a Fermi liquid picture.[2] Among the most striking features of the high–T_c oxides are the unusual frequency (ω) and temperature (T) dependences of magnetic and transport quantities,[3] e.g., the familiar nearly T–linear resistivity, the associated frequency–dependent free–carrier conductivity ($\propto 1/\omega$), and the pronounced T–dependent Hall effect [29]. Furthermore the charge response and spin excitations are highly anisotropic due to the ‘confinement’ of the carriers in the CuO_2 planes. Other peculiarities are related to the unusual range of parameters in the superconducting state, i.e., the short coherence lengths, the large penetration depths, and the high operating temperatures allowed by the high T_c [30].

---

[2] To set the stage, the two main characteristics of a Fermi liquid are [27]: (i) The existence of well–defined fermionic quasiparticles (with excitation energy ($\varepsilon \ll E_F$)) living in momentum space in a narrow strip around the Fermi surface. (ii) At low frequencies and long wavelengths the physical properties of these elementary excitations can be described by a Boltzmann transport equation.

[3] In a canonical Fermi liquid the spin susceptibility ($\chi \propto$ constant), resistivity ($\rho \propto T^2$), Hall coefficient ($R_H \propto$ constant), electronic specific heat ($C_v \propto T^3 + T \ln T$ in 3D), and NMR relaxation rate ($T_1^{-1} \propto T$) scale as powers of (T/E_F). Although such relations are very restrictive, their validity is a frequently used criterion to define Fermi liquid behaviour [28].

In the remainder of this section we mainly focus on those experiments which will be addressed in our subsequent theoretical analyses. For a more complete recent overview of various experimental subfields on high–T_c research see Ref. [31].

1.3.1 Spin dynamics

The spin dynamics in the cuprates were first studied in the undoped compounds. Here bulk susceptibility measurements [32] and the occurrence of a magnetic Bragg peak in (inelastic) neutron scattering (INS) experiments on $\mathrm{La_2CuO_4}$ [33] and $\mathrm{YBa_2Cu_3O_6}$ [32] have proven the 3D AFM ordering at low temperatures. The magnetic moments on Cu ($\approx 0.6\ \mu_B$) are oriented perpendicular to the crystallographic c–axis with a magnetic order vector in (1,1)–direction and an AFM coupling of adjacent $\mathrm{CuO_2}$ planes, where a very small additional spin canting in c–direction has been found in $\mathrm{La_2CuO_4}$ [34]. Using the linear spin–wave theory for the 2D $S = 1/2$ AFM Heisenberg model, the effective in–plane Cu-Cu exchange energy J_{Cu-Cu} has been estimated to be 0.1 ± 0.02 eV in $\mathrm{YBa_2Cu_3O_{6.15}}$ and 0.136 ± 0.005 eV in $\mathrm{La_2CuO_4}$ from INS data (for a more detailed discussion, see Ref. [35]). The observed c–axis anisotropy is extremely large $J_\perp/J_\| \sim 10^{-5}$ [32], i.e., above the Néel temperature the magnetic correlations are essentially two–dimensional.

As the compounds are doped away from half-filling, the spin–wave velocity softens considerably, the magnetic ordering quickly vanishes, and metallic behaviour sets in. However, the antiferromagnetic spin correlations are still strong in the weakly doped metallic state. The spin–spin correlation length ξ is found to be in the order of several lattice spacings and, with increasing x, becomes considerably larger than the average separation distance $3.8/\sqrt{x}$ Å between holes (assuming them to be static) [35, 7]. Thus, one expects that pronounced antiferromagnetic short–range order (SRO) fluctuations are retained, at least when the doping is not too large. In particular it has been argued [36, 37, 38] that the observed strong temperature and doping dependence of the spin susceptibility, which is difficult to reconcile with the Fermi liquid picture, might be due to SRO effects attributed to the local moment character of these AFM spin fluctuations.

The magnetic susceptibility $\chi(T)$ is plotted in Fig. 1.7 for the LSCO and YBCO families at various hole concentrations. Common to both compounds is the pronounced S-shaped form for the samples close to half filling and an almost T–independent Pauli–like susceptibility for large hole concentrations. At low doping $\chi(T)$ appears to decrease with decreasing T. The results for $\mathrm{La_{2-x}Sr_xCuO_4}$ show a broad maximum (filled triangles) of $\chi(T)$ at T_{max} moving with growing x towards lower temperatures. This can be qualitatively understood if one assumes that the Cu-Cu superexchange interaction is reduced by the presence of doped holes and $T_{max} \propto J_{Cu-Cu}(x)$ (see also Refs. [35, 7]). Note that in the intermediate doping range ($x \approx 0.25$), where the magnetic exchange interaction is small and local magnetic moments are uncorrelated but do still exist [38, 39] (cf. Chap. 5), the bulk susceptibility grows monotonically with decreasing temperature. Obviously, the x– and T–dependence of $\chi(T, x)$ results from the complicated interplay of local moments and itinerant behaviour. For the $\mathrm{YBa_2Cu_3O_{6+x}}$ systems near optimal stoichiometry, the susceptibility is almost flat. It has been argued that this flattening may be due to contributions from the Cu-O chains [40]. Here it should be stressed that there is considerable uncertainty in interpreting the direct susceptibility measurements. In the experimental analysis the Pauli terms have to be deduced from the raw data as one of several contributions to χ. Among the others are the core and Landau diamagnetic and Van Vleck paramagnetic terms [28].

One of the remarkable differences between $\mathrm{La_{2-x}Sr_xCuO_4}$ and $\mathrm{YBa_2Cu_3O_{6+x}}$ types of high–T_c cuprates is the nature of spin excitations in the metallic phase probed by INS (see Fig. 1.8).

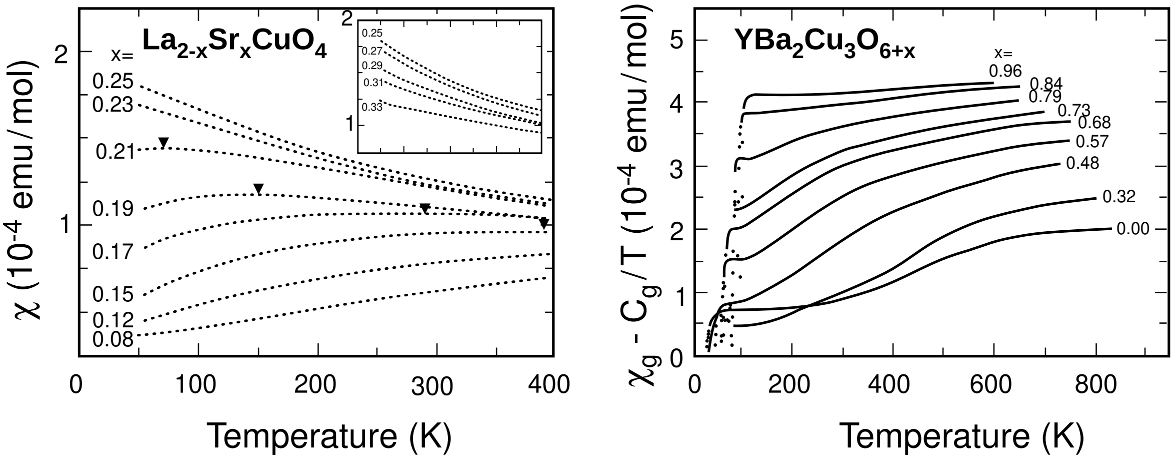

Figure 1.7: Temperature dependence of the uniform magnetic susceptibility in sample series of $La_{2-x}Sr_xCuO_4$ (left panel, after [41]) and $YBa_2Cu_3O_{6+x}$ (right panel, after [42] and [40]).

In hole–doped LSCO with $x = 0.075$ and $x = 0.14$, incommensurate Bragg peaks around $\vec{q}_{IC} = (\pi/a)(1 \pm q_o, 1)$, $(\pi/a)(1, 1 \pm q_o)$ have been reported in the dynamic structure factor $S(\vec{q}, \omega)$ at low temperatures [43], whereas, upon doping, $S(\vec{q}, \omega)$ keeps its commensurate maximum at $\vec{q}_{AFM} = (\pi, \pi)$ for the YBCO system. The deviation of $\vec{q}_{IC}$ from $\vec{q}_{AFM}$ roughly scales as $q_o \simeq 2x$ [44] in the hole–doped 214 compounds. Whether the broad maximum of the YBCO data can be interpreted as four unresolved incommensurate peaks, i.e., whether the incommensurate correlations are an intrinsic feature of all cuprates, is still under discussion [7, 47]. On the other hand, the magnetic correlations in the electron–doped 214 materials (NCCO) showed no indications of incommensurability at least up to 10 % doping [48]. So it is possible that the contrasting wave–vector dependences of $S(\vec{q}, \omega)$ are merely attributable to band structure effects and differences in the fermiology [49, 50, 51].

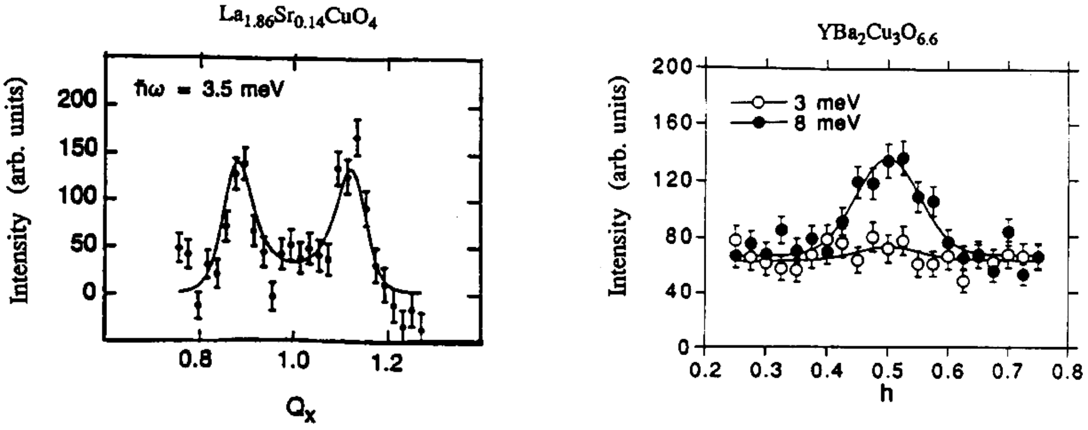

Figure 1.8: Neutron scattering cross section in LSCO (left panel, from Ref. [43, 45]) at $T =$ 35 K for a scan $\vec{q} = (\pi/a)(Q_x + q_o/2, Q_x - q_o/2)$, i.e., along two of the four maxima at $\vec{q}_{IC} = (\pi/a)(1 \pm q_o, 1)$, $(\pi/a)(1, 1 \pm q_o)$ where $q_o = 0.245$ [43], and in YBCO (right panel, from Ref. [46]) at $T = 10$ K for a diagonal scan $\vec{q} = (2\pi h/a)(1, 1)$.

In addition to the $\vec{q}$–structure, the temperature and frequency dependences of the spin susceptibility have also been extensively studied. One remarkable result is the ω/T–scaling of the local, i.e., momentum integrated, dynamical spin susceptibility in lightly–doped non-superconducting LSCO [52] and YBCO [46], which reveals the temperature as the relevant energy scale for the spin dynamics. However, note that this scaling behaviour, being the basic assumption of the so–called 'marginal Fermi liquid' ansatz [53], holds only for intermediate energies (e.g., in the energy range 4 meV $\lesssim \omega \lesssim$ 15 meV between 10 K $\lesssim T \lesssim$ 500 K for $La_{1.96}Sr_{0.04}CuO_4$ [35]). Another interesting feature is the appearance of a pseudo–gap in the low–energy part of the spin excitation spectrum in underdoped YBCO [54]. In contrast, no pseudo–gap appears in the overdoped metallic regime ($YBa_2Cu_3O_7$). The energy scans obtained for $YBa_2Cu_3O_{6.69}$ as a function of temperature are reported in Fig. 1.9 in the form of $Im\ \chi(\vec{q},\omega)$ [54]. A gap value of $E_G = 16$ meV ($\sim 3k_BT_c$), defined by the inflection point, has been determined in $YBa_2Cu_3O_{6.69}$. The most striking point seems to be the persistence of a pseudo–gap well above T_c. Since the $\vec{q}$–width of the spectrum is temperature independent, the T–dependence of the slope of $Im\ \chi(\hbar\omega = 8\,\mathrm{meV})$ (cf., inset of Fig. 1.9) clearly demonstrates the development of the pseudo–gap at $T^* \sim 150\ K$. Moreover, it has been emphasized [54, 55] that the unusual T–dependence of the nuclear magnetic/quadrupole resonance (NMR/NQR) data for $1/T_1T$ and T_{2G}/T_1T can be put down to the pseudo–gap opening, i.e., to a redistribution of low–energy spectral weight to high energies in the excitation spectrum. At $\hbar\omega \to 0$, the temperature dependence of $Im\ \chi(\hbar\omega)/\hbar\omega$ probed by INS can be nicely compared with that of $1/(T_1T)$ measured by NMR [57]. The NMR data [56] for a single–crystal sample with the same T_c as the neutron sample are displayed in Fig. 1.10 (upper panel). Obviously, the temperature dependences of $1/(T_1T)$ and $Im\,\chi(\hbar\omega)$ are found to be very similar. In particular, $1/(T_1T)$ exhibits a maximum at the same characteristic temperature T^*, i.e., both NMR and INS experiments have established the signature of the opening of a pseudo–gap below

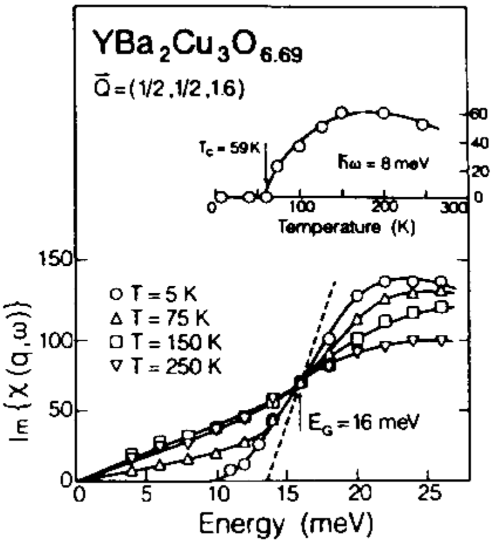

Figure 1.9: Low–energy part of the spin excitation spectrum $Im\ \chi(\vec{q},\omega)$ for $YBa_2Cu_3O_{6.6}$ below and above $T_c = 59$ K (from Ref. [54]).

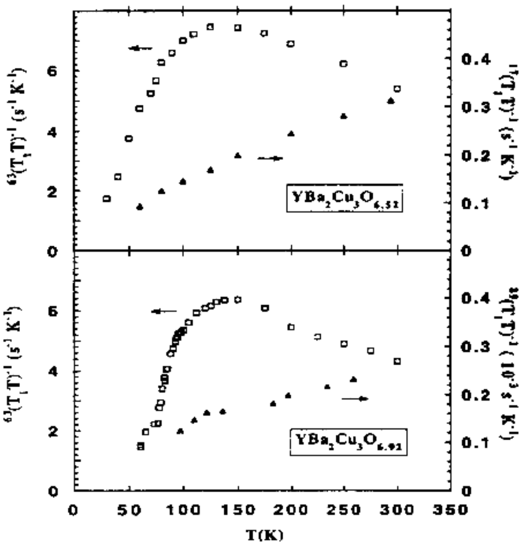

Figure 1.10: NMR relaxation rate of ^{63}Cu ($H_0 \parallel$ c–axis) and oxygen ^{17}O ($H_0 \perp$ c–axis) in the CuO_2 planes of $YBa_2Cu_3O_{6.52}$ (upper panel) and $YBa_2Cu_3O_{6.92}$ (lower panel) single crystals (after [56]).

$T^*(> T_c)$.

1.3.2 Charge dynamics

Assuming above T_c a 'normal' metallic phase for the conducting cuprates results in difficulties of explaining various extraordinary transport properties in the normal state. A prime example is the frequency dependence of the optical conductivity, which seems not to be consistent with the conventional electron–phonon scattering mechanism. Indeed, optical measurements provide strong evidence that the charge transport in the CuO_2 planes is dominated by spin scattering. In most experiments the optical conductivity is obtained from a Kramers–Kronig analysis of the reflectance. The optical spectra of the n– and p–type 214 compounds are displayed in Fig. 1.11 at several doping levels [58]. The undoped materials show a negligible conductivity in the lower mid–infrared region (< 1 eV) and a sharp excitonic peak at about 1.5 eV (in good agreement with a charge transfer gap of 1.5–2 eV observed in the insulating parent compounds). Upon doping the charge transfer peak gets weaker and spectral weight of the charge transfer excitation is transferred to the low–energy part of the spectrum. As a result, the low–energy excitations appear to be composed of a free–carrier ('Drude' like) absorption and a broad mid–infrared band [59]. Note that the low–frequency spectral weight increases faster than what is expected in a free–electron picture from the number of doped carriers. In $La_{2-x}Sr_xCuO_4$, the occurrence of the so–called mid–infrared band, centered about $\hbar\omega \sim 0.5eV$, has also been observed by electron–energy–loss–spectroscopy [60]. To date, the

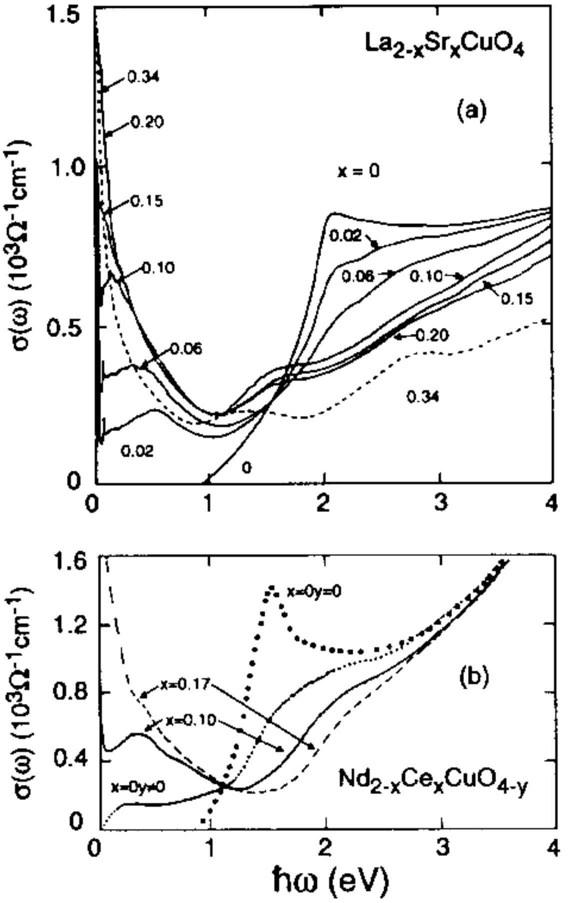

Figure 1.11: Real part $\sigma(\omega)$ of the in–plane optical conductivity *vs* energy for p–type $La_{2-x}Sr_xCuO_4$ (a) and n-type $Nd_{2-x}Ce_xCuO_4$ (b) at 300 K. Data are shown parametric with the Sr and Ce concentrations x (taken from Uchida *et al.* [58]). Doping does not cause any significant change in the optical spectra in the energy region higher than 5 eV.

origin of the mid–infrared band is highly controversial; a more detailed discussion of this phenomenon is given in Refs. [61, 7, 62].

Further information on the charge transport is gained from the resistivity and Hall effect data. As a result of the layered structure both quantities are highly anisotropic with different characteristic temperature dependences parallel and perpendicular to the CuO_2 planes. Here we will focus on the in–plane transport (for a short review on the inter–plane charge dynamics, see Ref. [63]).

In Fig. 1.12, results for the in–plane resistivity are shown for a series of LSCO samples with the composition ranging from the underdoped to the overdoped region. Since the conductivity in the basal plane is normally proportional to the number of charge carriers, a plot of $x \cdot \rho_{ab}(T)$ should bring $\rho_{ab}(T, x)$ on a similar scale and allows for an easier comparison of the T–dependent scattering rates [29]. First of all, it is important to note that the much highlighted linear behaviour, $\rho \sim T$, is observed only in a narrow concentration window near optimal doping. In the under– and overdoped samples, $\rho_{ab}(T)$ follows a different power–law, $\rho_{ab}(T) = \rho_{ab}^0 + aT^{n(T)}$, over a wide doping range. As can be seen from the inset of Fig. 1.12, at optimal doping, $n(T)$ is close to 1 up to 500 K, and it gradually changes from 1 towards 2 (near $x \sim 0.4$ [64]) upon increasing x at low T. For the overdoped region $\rho(T)$ shows an upturn at all temperatures. In the underdoped regime, the details of the T–dependence of $\rho_{ab}(T)$, in particular, the appearance of a knee at a characteristic temperature T^* and the near–linear increase above T^*, are very similar in the LSCO and YBCO families (cf. Fig. 1.12, right panel). Here T^* can be determined by the cusp of $\partial\rho/\partial T$ upon cooling [65, 64]. For the electron–doped materials $\rho(T, x)$ shows rather a quadratic dependence, $\rho(T) \sim T^2$, which is interpreted as the sign of usual Fermi liquid behaviour [66].

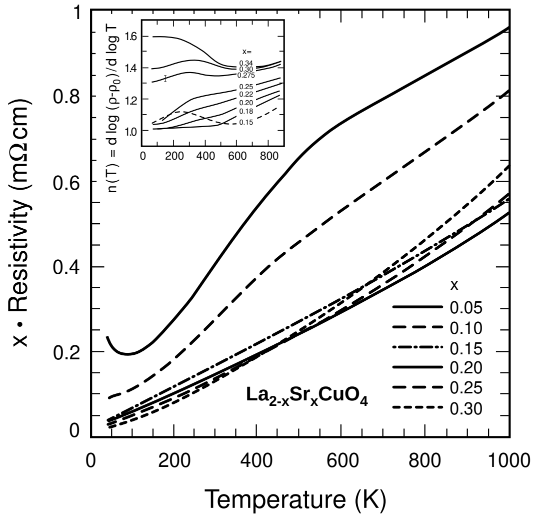

Figure 1.12: In–plane resistivity, $\rho_{ab}(T)$, of $La_{2-x}Sr_xCuO_4$ polycrystalline samples multiplied by the Sr concentration x. The inset shows the logarithmic derivative of $\rho(T)$, for $La_{2-x}Sr_xCuO_4$ in the optimal and overdoped region (re–drawn after [29, 64]).

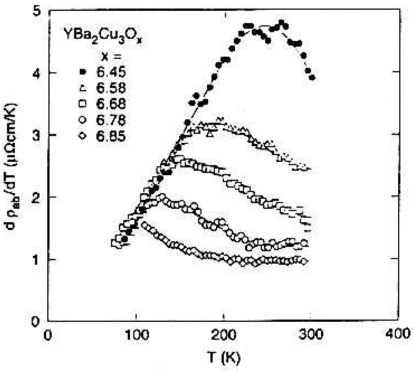

Figure 1.13: Temperature derivate of $\rho_{ab}(T)$ for a series of underdoped $YBa_2Cu_3O_{6+x}$ crystals (taken from [65, 64]).

Note that an analysis of the high–temperature resistivity at low doping in terms of Boltzmann transport theory [67] implies a small 'pocket–like' Fermi surface containing x holes or electrons (in striking contrast to the large ARPES Fermi surfaces, cf. Sec. 1.2). A small FS seems to be consistent with the large absolute value of the Hall coefficient ($\propto 1/x$) plotted for $Nd_{2-x}Ce_xCuO_4$ and $La_{2-x}Sr_xCuO_4$ against the composition of substitutes Ce and Sr in Fig. 1.14 [68]. The $1/x$–behaviour holds at a fixed temperature in the low–doping regime is often cited as the most serious problem for a Fermi liquid based description [28, 69]. Fig. 1.14 indicates clearly how the sign of R_H changes with increasing doping near the critical concentration where superconductivity disappears and the 'normal' metal behaviour recovers (cf. the corresponding phase diagram (Fig. 1.2)). The evolution of the temperature dependence of the Hall coefficient upon Sr substitution is given for the LSCO family in Fig. 1.15. Near optimal doping, R_H is strongly temperature dependent up to 500 K (i.e., far above any phonon related temperature ($\Theta_D \approx 400$ K)). However, a rescaling $R_H(T) = (R_H(T/T^*) - R(T = \infty))/R_H^*$ [70] of the Hall data shows that for all compositions $x \gtrsim 0.15$, i.e, in the optimal and higher than optimal doping region, the familiar strong T–dependence of R_H is observed only below a characteristic temperature $T^*(x)$, whereas R_H tends to be constant above T^*. The temperature scale $T^*(x)$ is very high at optimal doping ($\sim$ 500 K), but decreases rapidly with doping. Again, this unusual scaling behaviour seems to be inconsistent with a conventional (isotropic) electron–phonon scattering mechanism.

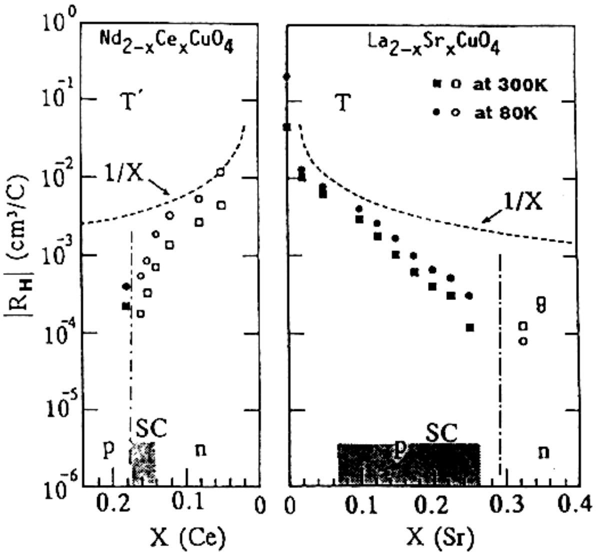

Figure 1.14: The absolute value of the Hall coefficient for reduced $Nd_{2-x}Ce_xCuO_{4-y}$ and $La_{2-x}Sr_xCuO_4$ as a function of Ce and Sr composition, respectively (from [68]).

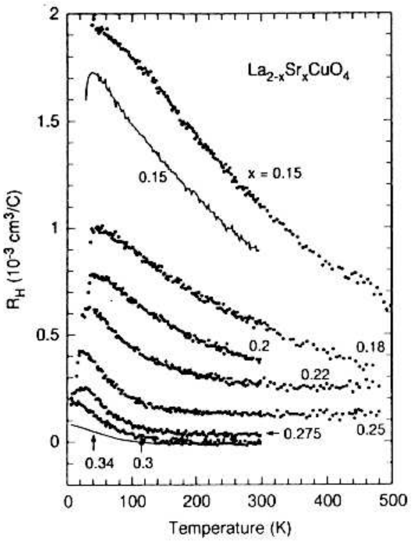

Figure 1.15: Hall effect in single–crystal thin films (solid lines) and polycrystalline samples (dots) of $La_{2-x}Sr_xCuO_4$ with $0 < x < 0.35$ (from [70]).

1.3.3 T*–x phase diagram

Recently, significant progress in elucidating the normal–state properties of high–T_c's has been achieved by comparing the characteristic temperatures obtained from charge and magnetic measurements respectively [64]. The discovery of a simple scaling of the Hall effect with T/T^* [70] discussed above was the first experiment to point out the existence of a characteristic temperature T^*. There $T^*(x)$ marks the crossover from a T–dependent low–temperature behaviour to a T–independent high–temperature limiting value of $R_H(T,x)$ (cf. Fig. 1.15). Analyzing the in–plane resistivity data of underdoped LSCO and YBCO, T^* can be determined by the knee of $\rho(T)$ at high T (Fig. 1.12) or by the increase of $d\rho(T)/T$ upon cooling (Fig. 1.13), respectively. In $\mathrm{La_{2-x}Sr_xCuO_4}$, e.g., $T^*(x \approx 0.05)$ is found to be $\sim$ 700 K [64] (decreasing with x); in YBCO, T^* ranges from 500 K ($x = 0.45$) to 200 K ($x = 0.85$) [65]. On the other hand, a similar temperature scale T^* may be identified as a broad maximum in the static magnetic susceptibility $\chi(T)$ (cf. Fig. 1.7). In Fig. 1.16, reproduced from Ref. [64], the qualitative

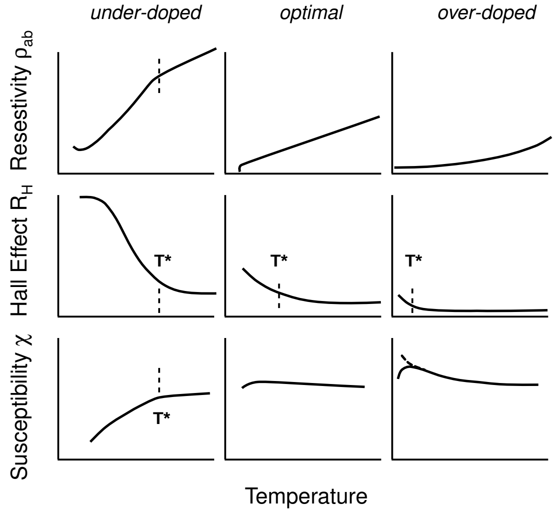

Figure 1.16: Signatures of characteristic temperatures T^* in the temperature dependence of $\rho(T)$, $R_H(T)$, and $\chi(T)$ (after [64]).

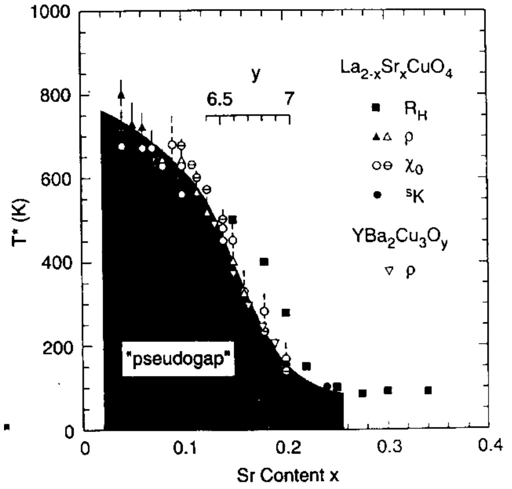

Figure 1.17: Normal–state phase diagram T^*–x for $\mathrm{La_{2-x}Sr_xCuO_4}$; T^* marks the development of a pseudo–gap (taken from Ref. [64]).

behaviour of $\rho(T)$, $R_H(T)$ and $\chi(T)$ obtained by probing different parts of the spin and charge response is illustrated for the three characteristic doping regimes. Obviously, T^* provides a link between transport and magnetic measurements and delineates two different regions in a $T^* - x$ phase diagram given for $\mathrm{La_{2-x}Sr_xCuO_4}$ in Fig. 1.17. In the underdoped region, the anomalous decrease of $\chi(T)$ and the NMR relaxation rates with decreasing T, the S-shaped T–dependence of $\rho(T)$ as well as the suppression of the excitation spectrum observed in specific heat measurements at low temperatures can be ascribed to the opening of a pseudo–gap below T^* in the *entire* electronic excitation spectrum involving *both* spin and charge degrees of freedom [64]. Starting from about 700–800 K, $T^*(x)$ decreases rapidly with increasing doping to $\sim$ 100 K at $x \simeq 0.25$, where the superconductivity disappears. Note that the T^*'s obtained from $\rho(T)$ of $\mathrm{YBa_2Cu_3O_{6+x}}$ (superimposed with respect to the optimal hole concentrations of LSCO and YBCO systems) roughly follow the 'border' $T^*(x)$ of LSCO compounds. Therefore it is has been suggested that the $T^* - x$ phase diagram is generic to all hole–doped cuprates [64].

1.3.4 Phase separation

The presence of large amplitude charge–density inhomogeneities (at short distances and time scales) and phase separation in the high–T_c's has recently attracted considerable attention [71, 72]. There is now uncontroversial experimental evidence that phase separation occurs in two special cases: in photo–doped cuprates perovskites (e.g., in $\mathrm{YBa_2Cu_3O_{6+x}}$ with $x \leq 0.4$ [73])

and in oxygen–doped LSCO systems [74, 75, 76]. First indications of a macroscopic charge segregation were obtained from neutron scattering experiments [74] on the O–doped 38 K superconductor $La_2CuO_{4+\delta}$, (see Fig. 1.18). Here, phase separation occurs between nearly stochiometric $La_2CuO_{4+\delta'}$ ($\delta' \approx 0 - 0.01$) with $T_N \approx 250$ K and oxygen–rich $La_2CuO_{4+\delta''}$ ($\delta'' \approx 0.05 - 0.08$) which becomes superconducting below about 35 K. Using La NMR [75], the temperature T_{PS}, below which hole–poor and hole–rich phases coexist, is found to be in the range 247 K to 265 K. It was soon realized that the phase separation below T_{PS} is electronically driven by the physics of the CuO_2 planes, not by the superfluous oxygen 'chemistry' [78]. Then, in discussing the underlying physics, one possible scenario is that the cost of kinetic energy due to the confinement of the doped charge carriers (holes) is outweighted by the gain of AFM exchange energy in the hole–poor regions. This seems to be corroborated by the special significance of the two coexisting phases: The hole–rich phase is an optimal doped superconductor and the hole–poor phase lies on the boundary where antiferromagnetism develops [72]. In addition, in $La_2CuO_{4+\delta}$ the oxygen mobility is claimed to be exceptionally large at T_{PS} ($\lesssim T_N$) [75], i.e., the excess oxygens are able to follow the in–plane holes ensuring the charge neutrality of the system. However, the situation becomes much more complex in other lightly–doped cuprates, e.g., in the more widely analyzed $La_{2-x}Sr_xCuO_4$, where the Sr^{2+} substituents are evidently immobile and cannot migrate along with the doped holes [79]. Although in these cases long–range Coulomb forces absolutely prevent a macroscopic segregation of doped holes ('frustrated' phase separation [72]), a *local* tendency towards phase separation has been claimed to lead to a nanoscopic and possibly dynamic inhomogeneous charge (hole) distribution [72, 79]. Unfortunately, most of the available experimental data are not accurate enough to convincingly verify an inhomogeneous doped–hole distribution in $La_{2-x}Sr_xCuO_4$, i.e., to confirm or rule out the postulated frustrated phase separation.

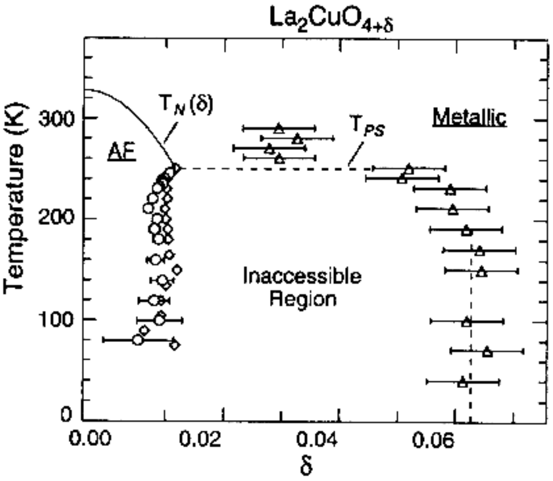

Figure 1.18: Phase diagram of $La_2CuO_{4+\delta}$. The oxygen–poor phase described by the left set of data exhibits long–range AFM order below T_N. The second phase (right set of data) having higher doping is metallic. The regime of doping fractions between $\delta \sim 0.01$ and ~ 0.06 is thermodynamically unstable below T_{PS} (from [77]; see also [7]).

Phase separation is also appealing from a theoretical point of view. In fact, phase separation was found to be the rule rather that the exception in a wide class of microscopic models of dilute holes in an antiferromagnet [80], including for example the familiar t–J model. The central feature of these models is that they describe mobile charge carriers doped into a highly correlated insulating state (AFM) for which the associated long–range order is *commensurate* with the lattice. Consequently, there is a strong tendency for the system to expel these excess holes which tend to destroy the commensurate ordering. Thus, in particular in the low–doping region, where the strong AFM correlations most effectively depress the stabilizing effect of the quasiparticle kinetic energy, phase separation may result as a 'localization' effect of the short–

range interactions. Finally, let us emphasize that in the vicinity of phase separation strong superconducting correlations have been detected in the (approximative) ground states of the 2D t–J and Kondo lattice models [81, 82]. The possible connection between phase separation and superconductivity has been explored in recent work [7, 71, 72, 83].

Chapter 2

Microscopic models and theoretical concepts

The problem of understanding HTSC has been a challenge to theoreticans from a wide variety of fields. Many theoretical investigations have been carried out in order to identify the mechanism of this fascinating phenomenon as well as to establish the canonical model itself. Although excellent progress is being made in deducing a consistent description of the high–T_c systems from a first–principles theory, at present no microscopic theory can account for their 'unconventional' normal–phase data as a whole.

Among the different theoretical scenarios, the more 'conventional' theories start from a Fermi liquid picture in the normal state. However, it is clear from experiments that the strict interpretation of a Landau Fermi liquid is not correct for the cuprates [84]. Thus, corrections beyond the leading order terms of Fermi liquid theory have to be taken into account, for example, the T–dependent corrections to Landau parameters etc. obtained in the framework of quasiclassical Boltzmann–Landau transport theory [85, 86]. Moreover, 'non–Fermi–liquid' corrections, arising, e.g., from a coupling of quasiparticles to collective modes and not describable by quasiclassical Boltzmann transport equation, seem to be of great significance in 2D [27]. Other 'extensions' of the standard Fermi liquid theory are the 'almost localized' and 'almost magnetic' Fermi liquid descriptions [28]. The former emphasize strong Coulomb correlations [87, 88, 89] and build on analogies with the heavy fermion metals [90]. The latter, including spin–bag theories [91, 92], nearly antiferromagnetic Fermi liquid approaches [93], and $d_{x^2-y^2}$ theories [94], combine pairing ideas with the presence of AFM spin correlations and might be viewed as more appropriate to the weak– and intermediate–coupling regime, or the RPA limit. In addition, nested Fermi liquid [95] and (antiferromagnetic) van–Hove scenarios ([96]) [97] should be placed in this category. Although these theories are close to having genuine electron–like quasiparticles, the elementary excitations may be very different from 'usual' Landau quasiparticles, e.g., the overlap between bare and dressed hole states is extremely small in the spin–bag approach [84, 98].

On the other hand, the unusual normal–state properties have been ascribed by some researchers to a 'non–Fermi–liquid' metallic state, the microscopic origin of which remains to be established. Along this line, the marginal Fermi liquid approach [53], gauge theories [99], anyon superconductivity [100, 101], or the concept of a 'tomographic Luttinger liquid' [102] in which the elementary excitations are deconfined spinons ($e = 0$, $s = 1/2$) and holons (e, $s = 0$) have attracted considerable attention.

Despite the intense theoretical studies of the cuprates our current understanding of these highly correlated systems remains incomplete. The main problem is that the superconducting state is obtained in the vicinity of the AFM Mott insulating state, and the quantum fluid that goes superconducting is built of the same electrons that are participating in making the antiferromagnetically spin structure [103, 84]. This means, in practice one cannot avoid the strong correlation condition, and as Anderson stated from the beginning: "We must solve the old problem of doping a single Mott–Hubbard band before we can *begin* the problem of high–T_c" [104]. Thus it was that there has been a renewed interest in simplified model Hamiltonians describing strongly correlated charge carriers moving in a single band, where special attention has been paid on the two–dimensional case.

Starting out from the three–band extended Hubbard model accounting for the band structure of the CuO_2 planes, we will focus in this work on the more simple effective one–band Hubbard and t–J models. In order to deal with the strong electronic correlations, we proceed along two different lines. One is by exact numerical diagonalization of small lattices. The other is by the use of slave–boson techniques. We stress that both numerical and analytical approaches are very important to clarify the properties of these model in the intermediate– and strong–coupling regions.

2.1 Three–band Hubbard model

Analyzing in some detail the band structure of the cuprates (cf. Sec. 1.2), the three–band extended Hubbard or Emery model [105] has been proposed as a minimal model for describing the physical properties of these systems. Using the hole notation (relative to a filled–shell [$3d^{10}$, $2p^6$] configuration (see Fig. 1.3)), the three–band Hubbard Hamiltonian is given as

$$\mathcal{H} = \mathcal{H}_0 + U_d \sum_i n^d_{i\uparrow} n^d_{i\downarrow} + U_p \sum_j n^p_{j\uparrow} n^p_{j\downarrow} + U_{pd} \sum_{\langle ij\rangle\sigma\sigma'} n^d_{i\sigma} n^p_{j\sigma'} \tag{2.1}$$

with the (2D) tight–binding part

$$\mathcal{H}_0 = \varepsilon_d \sum_{i\sigma} d^\dagger_{i\sigma} d_{i\sigma} + \varepsilon_p \sum_{j\sigma} p^\dagger_{j\sigma} p_{j\sigma} + \sum_{\langle ij\rangle\sigma} t^{(ij)}_{pd} (d^\dagger_{i\sigma} p_{j\sigma} + \text{H.c.}) + \sum_{\langle jj'\rangle\sigma} t^{(jj')}_{pp} (p^\dagger_{j\sigma} p_{j'\sigma} + \text{H.c.})\,, \tag{2.2}$$

where $d^\dagger_{i\sigma}$ ($p^\dagger_{j\sigma}$) denote the fermionic creation operators for a hole in the $3d_{x^2-y^2}$ ($2p_{x(y)}$) state on Cu (O) sites i (j), $n^d_{i\sigma} = d^\dagger_{i\sigma} d_{i\sigma}$, $n^p_{j\sigma} = p^\dagger_{j\sigma} p_{j\sigma}$, σ is the spin index, and $\langle ij\rangle$ ($\langle jj'\rangle$) refers NN Cu-O (O-O) pairs. As can be seen from Fig. 2.1, the difference in symmetries between the Cu and O orbitals imply additional phase factors for the hopping matrix elements, i.e., $t^{(ij)}_{pd}$ [$t^{(jj')}_{pd}$] takes the values $\pm t_{pd}$ [$\pm t_{pp}$] alternately within the layer. The largest transfer term $|t_{pd}|$ is roughly proportional to the σ^*–overlap of the Cu and O orbitals. The significance of direct O-O hopping terms t_{pp}, e.g., for charge instabilities and phase separation, has been emphasized recently [106]. Both hopping terms allow the movement of holes on the lattice. The dominant interaction included in (2.1) is the on–site Coulomb repulsion U_d between two holes on a copper site i. For completeness, also included are the Coulomb repulsion U_p within oxygen orbitals and the repulsion U_{pd} between NN holes on the Cu and O sites – both are believed to be of minor importance.

In the absence of the interaction terms, $\mathcal{H}_0$ will give, for the hybridization scheme of Fig. 2.1 and one hole (five electrons) per CuO_2 unit cell, the schematic band structure shown in Fig. 2.2 (a) (energy axis in electron notation). For the undoped case, depending on the relative strengths of the Hubbard repulsion U_d and the charge transfer (CT) energy $\Delta = \varepsilon_p - \varepsilon_d$ (> 0), which are the two key parameters of the three–band Hubbard model (2.1), the final band structure may correspond to a Mott–Hubbard insulator for t_{pp}, $t_{pd} \ll U_d \ll \Delta$ or, alternatively, to a so–called charge transfer insulator (CTI) for t_{pp}, $t_{pd} \ll \Delta \ll U_d$ (see Fig. 2.2 (b)) [107].

For the parent cuprate compounds, electron spectroscopy experiments favour the CTI situation [62]. A typical parameter set obtained from constrained density–functional calculations [108] is

$$t_{pd} = 1.3 \text{ eV}, \;\; t_{pp} = 0.65 \text{ eV}, \;\; U_d = 10.5 \text{ eV}, \;\; U_p = 4 \text{ eV}, \;\; U_{pd} = 1.2 \text{ eV} \Rightarrow \Delta = 3.6 \text{ eV} \quad (2.3)$$

(a detailed discussion of the three–band model parameters is given in Ref. [62], cf. also Sec. 2.3).

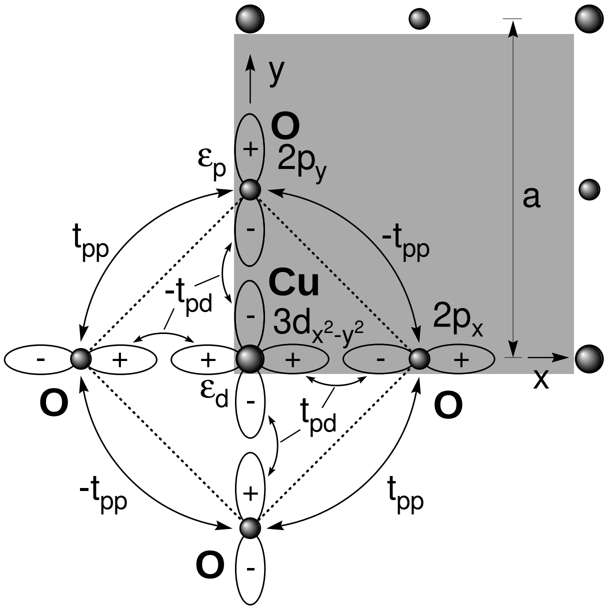

Figure 2.1: Schematic diagram of a CuO$_4$ plaquette in the Cu–oxide layer showing the orbitals (Cu 3d$_{x^2-y^2}$, O 2p$_x$ and 2p$_y$), their symmetries, and hybridizations. Here t_{pd} denotes the copper–oxygen transfer integral, t_{pp} labels the direct oxygen hopping, and ε_d (ε_p) is the Cu (O) on–site energy. The shaded area denotes the CuO$_2$ unit cell.

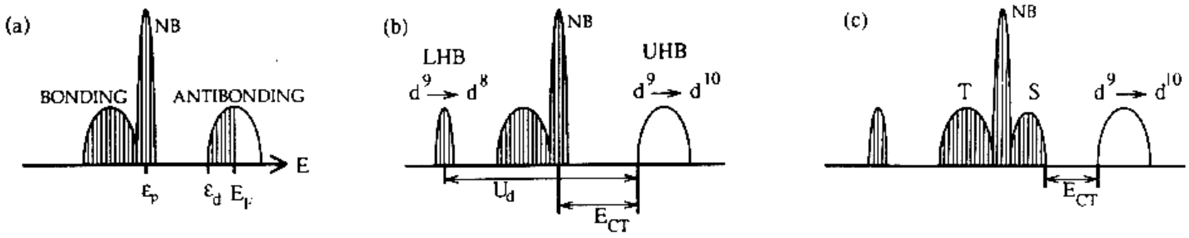

Figure 2.2: Schematic density of one–electron states for the three–band Hubbard model: (a) metal, (b) charge transfer insulator without and (c) with Zhang–Rice singlet(S)–triplet(T) splitting (reproduced from Ref. [35]). Shaded regions indicate occupied states (electron notation). NB, LHB, and UHB denote the non–bonding, lower, and upper Hubbard band, respectively. The non–bonding band is dispersionless for $t_{pp} = 0$. E_{CT} is the effective charge transfer gap separating the Zhang–Rice singlet band (ZRS) from the upper Hubbard band ($E_{CT} \approx 1.7$ eV for La$_2$CuO$_4$ [109]).

In the undoped case, the virtual hopping process involving doubly occupied Cu hole states produces an antiferromagnetic superexchange between NN Cu moments, and as a result the

Hamiltonian (2.1) can be pertubatively mapped onto a $S = 1/2$ Heisenberg model [110, 111]

$$\mathcal{H}_S = J_{Cu-Cu} \sum_{\langle ij \rangle} \vec{S}_i \vec{S}_j \,, \quad J_{Cu-Cu} = \frac{4t_{pd}^4}{(\Delta + U_{pd})^2} \left(\frac{1}{U_d} + \frac{1}{\Delta + U_p/2} \right) . \tag{2.4}$$

In good agreement with values obtained from two–magnon Raman scattering [62], an AFM superexchange interaction J_{Cu-Cu} ≈0.13 eV has been extracted from exact cluster diagonalizations [112].

In the p–doped materials, additional holes are introduced in the CuO_2 layers. For $U_d > \Delta$ (cf. Fig. 2.2 (b)), the extra holes preferentially go onto the oxygen 2p orbitals. This effect is in accord with electron–energy–loss–spectroscopy experiments [113]. In the limit where the pd–σ hybridization dominates, the Cu $3d_{x^2-y^2}$ hole orbit can be combined with a symmetric or antisymmetric combination of the four surrounding O $2p_{x,y}$ hole orbits (with respect to the central Cu ion) to form bonding singlet and antibonding triplet states or non–bonding states, respectively. Then, to second order in perturbation with respect to t_{pd}/Δ (neglecting the effects of U_p and U_{pd}), the 'symmetrized' oxygen hole and the copper hole interact by a strong Kondo exchange coupling [35]

$$J_{Cu-O} = t_{pd}^2 \left(\frac{1}{\Delta} + \frac{1}{U_d - \Delta} \right) . \tag{2.5}$$

The main effect of J_{Cu-O} is to split up the bonding band, where the so–called Zhang–Rice singlet (ZRS) [triplet] states are pushed above [below] the non–bonding states [114]. As a consequence of this picture the (spin–σ) hole originally located on O has been replaced by a (spinless) ZRS state centered at Cu. The resulting band structure is displayed in Fig. 2.2 (c). Obviously, the lowest particle–hole excitations appear as result of correlations across the effective charge transfer gap E_{CT}.

2.2 Effective one–band Hubbard and t–J models

The three–band Hubbard model which includes both Cu and O degrees of freedom is expected to represent the main features of the electronic structure of the active CuO_2 planes. However, it contains several parameters, and therefore it is still a somewhat complicated starting point. The charge transfer picture illustrated in Fig. 2.2 suggests that the dynamics of charge carriers near the CT gap region may be described accurately by a simpler, effective one–band Hamiltonian.

Anderson [104] argued that the essential low–energy physics of the CuO_2 planes is contained in the two–dimensional one–band Hubbard model[1]

$$\mathcal{H} = \sum_{i,j,\sigma} t_{ij} c_{i\sigma}^{\dagger} c_{j\sigma} + U \sum_i n_{i\uparrow} n_{i\downarrow} \,. \tag{2.6}$$

---

[1] Note that the Hubbard model (independently proposed in 1963 by Gutzwiller [115], Hubbard [116] and Kanamori [117]) was originally designed to describe the ferromagnetism of transition metals. The physics of the model is governed by the competition between itinerancy (t; delocalization) and short–range Coulomb repulsion (U; localization, magnetic order), where the fermionic nature of the charge carriers is of great importance (Pauli exclusion principle, i.e., the existence of an 'effective' long–range interaction). Besides the ratio U/t, the particle density n, the temperature T, and the spatial dimension D (geometry of the lattice) are crucial parameters involved in the model. Successively, the Hubbard model was studied in the context of magnetism, metal–insulator (Mott) transition, heavy fermions and HTSC as the probably most simple model to account for strong correlation effects. However, although a tremendous amount of work has been devoted to its solution, exact results are very rare and only a few special cases and limits have so far been understood. For an overview on the major contributions to this subject, see Refs. [118, 119].

Here, as usual, $c_{i\sigma}^\dagger$ ($c_{i\sigma}$) is a fermionic creation (annihilation) operator of a spin σ ($=\uparrow,\downarrow$) electron, and $n_{i\sigma} = c_{i\sigma}^\dagger c_{i\sigma}$ (electron notation). U denotes the on–site Coulomb repulsion, and t_{ij} are the hopping matrix elements, where, in the context of copper oxides, the ij indices label a square lattice of planar copper sites. In the strong–coupling limit, the one–band Hubbard model tries to mimic the presence of the CT gap in terms of a Mott–Hubbard picture, i.e., the value of the *effective* Hubbard interaction has to be comparable to the CT gap ($U \approx E_{CT}$). Then the lower and upper Hubbard bands of this model correspond to the NB oxygen band (ZRS band) of Fig. 2.2 (b) (Fig. 2.2 (c)) and to the $\mathrm{d}^9 \to \mathrm{d}^{10}$–structure in the spectra of the three–band Hubbard (Emery) model, respectively. For one hole per copper site (half–filled band case), the Hubbard model in the large–U/t limit reduces to a effective Heisenberg model, with an exchange coupling $J = 4t^2/U$ and a charge excitation gap of $U - 8t$, and one knows that the Heisenberg model describes well the spin dynamics of the insulating cuprates (cf. Sec. 1.3.1).

Another effective single–band model which connects to a Heisenberg model in the absence of doping is the t–J model[2] defined as

$$\mathcal{H}_{t-J} = \sum_{i,j,\sigma} t_{ij}\, \tilde{c}_{i\sigma}^\dagger \tilde{c}_{j\sigma} + J \sum_{\langle ij \rangle} \left(\vec{S}_i\, \vec{S}_j - \frac{\tilde{n}_i \tilde{n}_j}{4} \right) . \tag{2.7}$$

$\mathcal{H}_{t-J}$ acts in a projected Hilbert space without double occupancy, where $\tilde{c}_{i\sigma}^{(\dagger)} = c_{i\sigma}^{(\dagger)}(1 - \tilde{n}_{i-\sigma})$, $\vec{S}_i = \frac{1}{2}\sum_{\sigma\sigma'} \tilde{c}_{i\sigma}^\dagger \vec{\tau}_{\sigma\sigma'} \tilde{c}_{i\sigma'}$, and $\tilde{n}_i = \sum_\sigma \tilde{c}_{i\sigma}^\dagger \tilde{c}_{i\sigma}$. Due to the projectors $(1 - \tilde{n}_{i-\sigma})$, this model has only three possible states per site, i.e., an electron with spin up or down, or a hole. Thus the t–J model is inherently a strong–coupling model that spans the Hilbert subspace consisting of spin $s = 1/2$ or spin singlet states on each site of the lattice. In the absence of doping, each spin-$\frac{1}{2}$ is coupled to its NN spins with a AFM Heisenberg term ($\propto J$) and this model applies to the low–energy spectrum of the Cu^{2+} Mott insulators. Then, introducing a single hole is equivalent to removing one Cu spin-$\frac{1}{2}$ from the square lattice of copper spins and, as proposed by Zhang and Rice [114], one can identify this empty site directly with the charge carrying singlet of the three–band model. It is generally believed that there are sizeable matrix elements to move these tightly bound singlets from square to square, which correspond in the effective t–J model to the hopping process of electrons (or holes) ($\propto t$) without changing their spins.

In (2.6) and (2.7) the hopping matrix elements t_{ij} are usually restricted to NN transfer processes (t) on a square lattice. However, starting from a three–band model, quantum cluster calculations [108], have revealed that the relative large direct transfer between NN oxygen sites ($t_{pp} \lesssim t_{pd}/2$) leads to a sizeable next–nearest–neighbour (NNN) hopping (t') in the context of an effective one–band description (cf. Sec. 2.3), i.e., we get

$$\sum_{i,j} t_{ij}\, \tilde{c}_{i\sigma}^\dagger \tilde{c}_{j\sigma} = -t \sum_{\langle ij \rangle} \left(\tilde{c}_{i\sigma}^\dagger \tilde{c}_{j\sigma} + \text{H.c.} \right) - t' \sum_{\langle\langle ij \rangle\rangle} \left(\tilde{c}_{i\sigma}^\dagger \tilde{c}_{j\sigma} + \text{H.c.} \right) . \tag{2.8}$$

More recently, the t'–term has been introduced to reproduce the different FS geometries of YBCO and LSCO (in the noninteracting limit) [50, 123, 124, 125, 126]. In addition, the inclusion of t'–coupling the same sublattice becomes crucial for the low–lying magnetic excitations [127, 51] (cf. Chap. 4).

Of course, the Hubbard and t–J models are closely related in the strong–coupling limit where $U/t \gg 1$ and $J/t \ll 1$. In fact, the t–J model can be derived from the Hubbard model

---

[2] Our knowledge of the ground–state properties (phase diagram) of the t–J model is even less advanced than for the Hubbard model, e.g., the t–J model in 1D is not soluble for general values of J/t but at the supersymmetric point $J/t = 2$ [120], whereas the 1D Hubbard model was solved by Lieb and Wu [121] $\forall U/t$, n using Bethe-Ansatz methods. Some recent results on the t–J model are summarized in Ref. [122].

in the limit $t/U \ll 1$ by a canonical transformation and a subsequent projection onto the subspace without doubly occupied sites [128]. Then, up to order t^2/U, the following strong–coupling Hamiltonian is obtained (cf. Sec. 8.5)

$$\mathcal{H}_{SC} = \mathcal{H}_{t-J} + \mathcal{H}_3 \,, \tag{2.9}$$

where now $J = 4t^2/U$, and the term

$$\mathcal{H}_3 = -\frac{t^2}{U} \sum_{\langle ijk\rangle\sigma} \left(\tilde{c}^\dagger_{i\sigma}\tilde{c}^\dagger_{j-\sigma}\tilde{c}_{j-\sigma}\tilde{c}_{k\sigma} + \tilde{c}^\dagger_{i-\sigma}\tilde{c}_{j-\sigma}\tilde{c}^\dagger_{j\sigma}\tilde{c}_{k\sigma} + \text{H.c.} \right) \tag{2.10}$$

includes virtual three–site hopping processes between NN pairs $\langle ij\rangle$ and $\langle ij\rangle$. This contribution is of the order t/U smaller than the leading hopping term, but it should be emphasized that the first term of $\mathcal{H}_3$ just describes sublattice hopping of a hole and therefore leaves, e.g., the Néel spin background unchanged [129]. Contrary, the second contribution of $\mathcal{H}_3$ corresponds to an NNN hop with an associated spin flip process. The term $-(n_i n_j)/4$ included in (2.7) appears spontaneously in the strong–coupling expansion of the Hubbard model.

Finally, it is important to remark that the mapping procedure of the original three–band Hubbard or Emery model onto the strong–coupling one–band Hubbard or t–J model is still controversial and, in particular, the equivalence of the low–energy physics of three– and effective one–band models has been questioned [130, 131, 132]. Today the most convincing justification for the reduction to a low–energy effective Hamiltonian results from the spectral mapping of small clusters [133, 134].

2.3 Finite–lattice diagonalizations

Computational techniques provide an useful tool to analyze the properties of microscopic models (Hamiltonians), at least, in the difficult regime where the many–body correlations are strong, and well–controlled analytical methods are not available. At present, the numerical algorithms mainly used for studying strongly correlated electron systems are based on exact diagonalization (Lanczos) and quantum Monte Carlo (QMC) methods (for recent comprehensive reviews on Lanczos and QMC results see Ref. [7] and Refs. [135, 136], respectively). The most appealing advantage of the Lanczos approach is that it allows the calculation of both *static* and *dynamical* properties [137, 138] of a given Hamiltonian (at zero temperature). In practice, the main limitation of this technique is the constraint of working on small clusters (memory requirements and cpu time scale as the size of the Hilbert space for sparse Hamiltonian matrices).

For example, using the Lanczos method, interesting information has been obtained by comparing the low–energy spectra of three– and one–band models on finite lattices. Along this line, Hybertsen *et al.* [112, 133] have demonstrated, in two successive stages of renormalization, that the low–energy Hamiltonian for a CuO_2 plane could be parameterized either as a one–band t–t'–U or as a t–t'–J model.

In a first step, they started from a three–band Hubbard model using constrained functional–density calculations (CDFT) to estimate the various parameters (e.g. hopping amplitudes, on–site and inter–site Coulomb interactions) that self–consistently match the CDFT energy surface and the LDA Cu-O pd–σ bands. The parameter set describing La_2CuO_4 was given in (2.3) [108]. Then, exact diagonalization studies of the resulting three–band Hubbard model have been performed on small clusters up to a Cu_5O_{16} ($N = 5$), where three cases were considered: $N-1$, N, and $N+1$ holes corresponding to the electron–doped, half–filled, and hole–doped case, respectively. Here, for example, the extrapolated CT gap $\Delta = E_{N+1} + E_{N-1} - 2E_N$ as well as the hole spectral functions (directly related to the spectra observed in photoemission) are in quantitative agreement with experiments.

In a second step, the low–energy spectrum of the three–band Hubbard model was mapped onto effective one–band Hamiltonians (see Fig. 2.3), e.g., the Heisenberg (a), t–t'–J, or one–band (t–t') Hubbard model (Figs. 2.3 (b)-(c)). At half–filling, the result of the mapping onto the spin–1/2 Heisenberg model gives

$$J = 128 \pm 5 \text{ meV } [139] \tag{2.11}$$

(neglecting a small NNN exchange interaction $J' = 3 \pm 1$ meV).

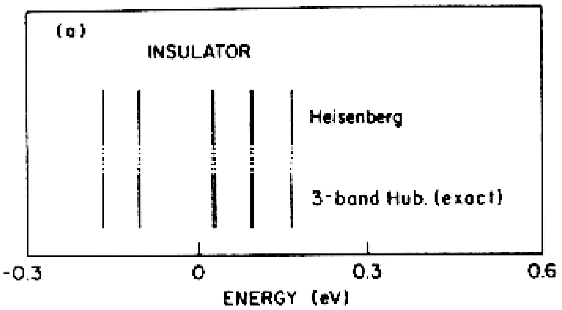

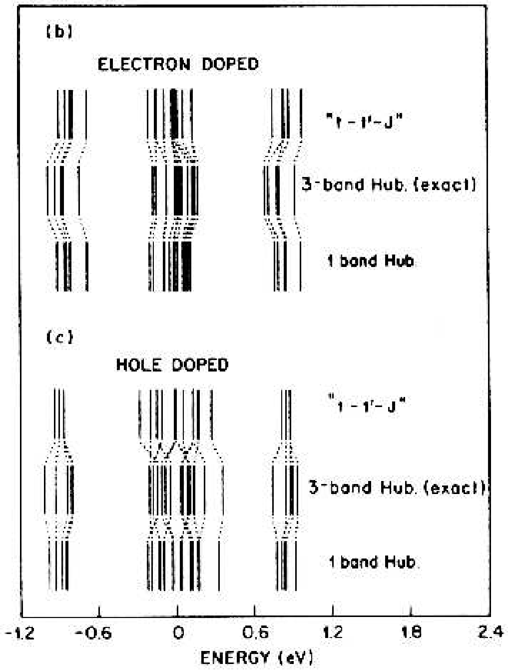

Figure 2.3: Low–energy spectra of the three–band Hubbard model on a Cu_5O_{16} cluster with (a) five holes (half–filled) compared to the Heisenberg model, (b) four holes (electron–doped) and (c) six holes (hole–doped case) compared to the one–band t–t'–J and t–t'–U (Hubbard) models (taken from [112]).

For the t–t'–J model (2.7)–(2.8), the local ZRS construction is found to be an excellent basis for the two–hole wave function, where the low–energy wave functions show a $\gtrsim 93\%$ projection onto the Hilbert space of the three–band Hamiltonian (2.1)–(2.3). The resulting hopping matrix elements are [112]

$$t = -410 \pm 5 \text{ meV}\,, \quad t' = +70 \pm 10 \text{ meV} \quad \text{electron doping}\,, \tag{2.12}$$

$$t = +440 \pm 5 \text{ meV}\,, \quad t' = -60 \pm 20 \text{ meV} \quad \text{hole doping} \tag{2.13}$$

(electron notation).

For the Hubbard model, from unconstrained mappings the parameter sets

$$t = -0.43 \text{ eV}\,, \quad t' = -0.07 \text{ eV} \quad U = 5.4\,\text{eV, i.e., } U/t \sim 12 \;\; [112]\,, \tag{2.14}$$

$$t = -0.43 \text{ eV}\,, \quad t' = -0.06 \text{ eV} \quad U = 4.1\,\text{eV, i.e., } U/t \sim 9.5 \; [133]\,, \tag{2.15}$$

have been found to reproduce accurately the three–band spectra for both hole and electron doping (note that a comparative Lanczos study by Bacci *et al.* [140] proposes a weaker Coulomb interaction $U/t \approx 8$ as more correct). As can be seen from Fig. 2.3, the one–band Hubbard model gives a somewhat better mapping in the hole–doped case (for the lowest manifold) due to the fact that the $\mathcal{H}_3$ contribution (2.10) was dropped in the reduction to the t–t'–J model.

In conclusion, the cluster mappings onto the t–t'–J and t–t'–U models show the importance of both strong–coupling parameterization (U, J) and inclusion of second–neighbour hopping (t'), and provide a strong test for the validity of an effective one–band description for the cuprates. Therefore, in the rest of this work, we restrict ourselves to the study of one–band models.

2.4 Slave–field methods

In recent years new and unconventional methods for treating strong electron–electron interactions have been developed, initiated in part by the discovery of mixed–valence heavy fermion metals [141, 142] and, in particular, high–T_c superconductors. To deal with the effects of a large or even infinite on–site Coulomb repulsion, for example, various auxiliary boson [143, 144] and slave–field [145, 146] techniques have been introduced and applied to a variety of theoretical models (including the single–impurity Kondo [147, 148] and Anderson lattice models [149, 150], the t–(t')–J model(s) [151, 152, 153, 154, 155], or the one– and multi–band Hubbard models [156, 88, 157]). Generally speaking, all these methods are designed to linearize the two–body interaction term at the expense of a coherent superposition of more complicated one–body (hopping or hybridization) terms containing auxiliary classical fields (Hubbard–Stratonovich formalism) or bosonic and fermionic slave–fields subjected to local constraints (slave–particle representation).

Among the various slave–field methods that have been proposed (for a critical overview, see Refs. [158, 146]), the four–field slave–boson (SB) scheme of Kotliar and Ruckenstein (KR) [156] is particularly appealing because of its conceptual simplicity and lucidity (complete mapping of all four atomic states to bosons) and because it reproduces the results of Gutzwiller's quasi–classical approximation [115, 159] at the static paramagnetic saddle–point and yields reasonable results in some important limiting cases (e.g., in infinite dimensions at $T = 0$). To illustrate briefly the main ideas, advantages and shortcomings of the KR SB approach compared with alternative slave–field representations, we will concentrate in this section on the finite–U one–band Hubbard model (2.6).

The scalar KR SB representation [156] of the Hubbard model is constructed by replacing the Hilbert space of fermion states by an enlarged one of pseudofermionic and bosonic states whose correspondence is given by:

$$\begin{array}{lcl}
\text{Initial representation} & \longrightarrow & \text{New representation} \\
|vac\rangle = \prod_i |\,0_i\rangle & \longrightarrow & |\,O\rangle = \prod_i |\,O_i\rangle = \prod_i e_i^\dagger\,|vac\rangle \\
|\,0_i\rangle & \longrightarrow & |\,O_i\rangle \\
|\uparrow_i\rangle = c_{i\uparrow}^\dagger\,|vac\rangle & \longrightarrow & p_{i\uparrow}^\dagger e_i f_{i\uparrow}^\dagger\,|O\rangle \\
|\downarrow_i\rangle = c_{i\downarrow}^\dagger\,|vac\rangle & \longrightarrow & p_{i\downarrow}^\dagger e_i f_{i\downarrow}^\dagger\,|O\,\rangle \\
|\uparrow\downarrow_i\rangle = c_{i\uparrow}^\dagger c_{i\downarrow}^\dagger\,|vac\rangle & \longrightarrow & d_i^\dagger e_i f_{i\uparrow}^\dagger f_{i\downarrow}^\dagger\,|O\rangle\,,
\end{array} \tag{2.16}$$

where the bosonic number operators $e_i^\dagger e_i$, $p_{i\sigma}^\dagger p_{i\sigma}$ and $d_i^\dagger d_i$ act as projectors on an empty, a singly occupied (spin σ) and a doubly occupied state on site i, respectively. The unphysical states in the extended Fock space are eliminated by imposing two sets of *local* constraints:

$$C_i^{(1)} = e_i^\dagger e_i + p_{i\uparrow}^\dagger p_{i\uparrow} + p_{i\downarrow}^\dagger p_{i\downarrow} + d_i^\dagger d_i - 1 = 0 \; , \tag{2.17}$$

expressing the completeness of the bosonic projectors (i.e., each lattice site i can only be occupied by exactly one boson), and

$$C_{i\sigma}^{(2)} = f_{i\sigma}^\dagger f_{i\sigma} - p_{i\sigma}^\dagger p_{i\sigma} - d_i^\dagger d_i = 0 \; , \tag{2.18}$$

relating the pseudofermion number $f_{i\sigma}^\dagger f_{i\sigma}$ to the number of p and d slave bosons. Correspondingly, the KR mapping of the physical electron (destruction) operators into products of new (pseudo) fermions (f) and (slave) bosons ($e^{(\dagger)}, p^{(\dagger)}, d^{(\dagger)}$) is given as

$$c_{i\sigma} \;\to\; z_{i\sigma}\, f_{i\sigma} \; , \tag{2.19}$$

where the *simplest* form for the bosonic hopping operator is $z_{i\sigma} = e_i^\dagger p_{i\sigma} + p_{i-\sigma}^\dagger d_i$. In (2.6) the interaction term is bosonized via $n_{i\uparrow} n_{i\downarrow} \to d_i^\dagger d_i$, i.e., the KR transformation to SB fields as described by Eqs. (2.17)–(2.19) results in a linearization of the Hubbard interaction being simply proportional to the d–boson number operator. Then the SB Hubbard Hamiltonian

$$\mathcal{H}^{SB} = \sum_{i,j,\sigma} t_{ij} z_{i\sigma}^\dagger z_{j\sigma} f_{i\sigma}^\dagger f_{j\sigma} + U \sum_i d_i^\dagger d_i \tag{2.20}$$

provides an exact representation of the original Hubbard model (2.6) as long as the constraints (2.17) and (2.18) are satisfied.

Let us add some remarks:

(i) A slave–field representation of the Hubbard Hamiltonian may be formulated in substantially different ways, by introducing auxiliary fermions and bosons. As two possible alternatives, one can represent the electronic annihilation operator $c_{i\sigma}$ as a composite particle of fermionic and bosonic components according to:

$$\begin{aligned} c_\sigma &= e^\dagger s_\sigma + \sigma s_{-\sigma}^\dagger d && \text{(mapping)} \\ e^\dagger e + \sum_\sigma s_\sigma^\dagger s_\sigma + d^\dagger d &= 1 && \text{(constraint)}\,, \end{aligned} \tag{2.21}$$

where

representation	fermions	bosons	
NZA slave–boson scheme [87, 151]	s_σ	$e,\, d$	(2.22)
slave–fermion scheme [154]	$e\,, d$	$s_\sigma\,.$	

Note that in both cases there is only one constraint to be imposed. The NZA SB and slave–fermion representations are frequently used to treat the infinite Coulomb repulsion ($U = \infty$) models with minimal double occupancy, where either the d or the e operators drop out. The disadvantage of the 'non–magnetic' NZA SB method shows up in the $1/N$–expansion of the corresponding generalized N–orbital Hubbard model: While charge fluctuations appear at $\mathcal{O}(1/N)$, the study of spin excitations require expanding to order $1/N^2$ [158]. Therefore, the 'magnetic' slave–fermion (or Schwinger–boson) approach has been mainly adopted to investigate spin fluctuations in the quantum Heisenberg model [153, 160, 161] as well as spin and charge correlations in the framework of the spinon–holon picture for the t–J model [154, 155, 162, 163]. The difficulty here is to get Fermi liquid behaviour, i.e., two fermionic excitations ($\sigma = \uparrow, \downarrow$) out of spinless fermions [158]. Obviously, the drawbacks of both representations result in part from the fermion–boson mixing in conjunction with an asymmetric treatment of spin and charge degrees of freedom when one makes approximations.

(ii) In contrast, the KR mapping of all four atomic states to slave–bosons provides a symmetric representation of spin and charge dynamics [158]. In particular, the introduction of two 'magnetic' bosons $p_{i\sigma}$ allows a consistent description of magnetic ground states and magnetic fluctuations already at $\mathcal{O}(1)$ and $\mathcal{O}(1/N)$ [164], respectively.

(iii) In the KR scheme the anticommutation relations of the original fermionic operators $c_{i\sigma}$ are automatically preserved because the transformed field operators $f_{i\sigma}$ (e_i, $p_{i\sigma}$, d_i) obey Fermi (Bose) statistics. Moreover, the (physical) electron number $n_i = \sum_\sigma c_{i\sigma}^\dagger c_{i\sigma}$ is the same as the pseudofermion number $n_i^f = \sum_\sigma f_{i\sigma}^\dagger f_{i\sigma}$, i.e., there is a one–to–one correspondence between physical electrons and quasiparticles arising from the renormalization of the electron interaction. Therefore, the KR approach is compatible with the Fermi liquid quasiparticle picture (but the NZA SB scheme is not, cf. the discussion in Ref. [165]).

(iv) The choice of the KR hopping factors $z_{i\sigma}$ is not unique. In principle, one could incorporate in $z_{i\sigma}$, within each pair of operators, any diagonal subsidiary operator $R_{i\sigma}$ which acts as the unit operator in the physical subspace ($[e_i^\dagger p_{i\sigma} + p_{i-\sigma}^\dagger d_i] \neq 0$), but may have arbitrary values for states for which the condition $[e_i^\dagger p_{i\sigma} + p_{i-\sigma}^\dagger d_i] = 0$ holds. Although all the

$$z_{i\sigma} = e_i^\dagger R_{i\sigma} p_{i\sigma} + p_{i-\sigma}^\dagger R_{i\sigma} d_i \tag{2.23}$$

are equivalent on the operator level so far as the constraints are guaranteed exactly, an approximative treatment of the constraints leads to different results depending on the special choice of $z_{i\sigma}$. KR proposed to exploit the arbitrariness in choosing $R_{i\sigma}$ to reproduce at the *mean–field level* (where the constraints are satisfied only on average) and for *any band filling* the correct free–fermion result at $U = 0$ and the Gutzwiller approximation for any finite U. This can be achieved by defining [156]

$$R_{i\sigma} = \left(1 - p_{i\sigma}^\dagger p_{i\sigma} - d_i^\dagger d_i\right)^{-1/2} \left(1 - p_{i-\sigma}^\dagger p_{i-\sigma} - e_i^\dagger e_i\right)^{-1/2} . \tag{2.24}$$

(v) Unfortunately, the original KR SB representation $|\sigma_i\rangle = f_{i\sigma}^\dagger p_{i\sigma}^\dagger |vac\rangle$ breaks the spin–rotation invariance (SRI) in the bosonic space by the assumption of a spin quantization axis. To avoid the difficulties which may arise from the scalar nature of the p_σ–bosons in approximative treatments, Li, Wölfle and Hirschfeld [166] proposed a manifest SRI SB formulation which automatically preserves the $SU(2)$ invariance, by introducing a two–component (singlet $S = 0$ and triplet $S = 1$) matrix operator $\underline{p}_i^{(\dagger)}$ representing the single occupied lattice site (hereafter underbars denote a 2×2 matrix in the spin variables). Combining the pseudofermionic spinor field $f_{i\rho}^{(\dagger)}$ and the $\underline{p}_i^{(\dagger)}$–boson, the states

$$|\sigma_i\rangle = \sum_\rho f_{i\rho}^\dagger p_{i\rho\sigma}^\dagger |vac\rangle \tag{2.25}$$

transform as spinor states under spin rotation, i.e., the spin–1/2 character of $|\sigma_i\rangle$ is preserved. Then, following Frésard and Wölfle [158], the SRI KR constraints, electron operator mapping prescription, and bosonic hopping matrix elements are obtained as

$$\begin{aligned} C_i^{(1)} &= e_i^\dagger e_i + 2\sum_{\rho\rho'} p^\dagger_{i\rho\rho'} p_{i\rho'\rho} + d_i^\dagger d_i - 1 = 0 \\ C_{i\bar{\rho}\rho}^{(2)} &= f^\dagger_{i\rho} f_{i\bar{\rho}} - 2\sum_{\rho'} p^\dagger_{i\bar{\rho}\rho'} p_{i\rho'\rho} - d_i^\dagger d_i \, \delta_{\bar{\rho}\rho} = 0 \ , \end{aligned} \tag{2.26}$$

$$c_{i\sigma} \longrightarrow \sum_\rho z_{i\sigma\rho}\, f_{i\rho} \ , \tag{2.27}$$

and

$$\underline{z}_i = \underline{L}_i e_i^\dagger M_i \underline{p}_i \underline{N}_i + \underline{L}_i \underline{\tilde{p}}_i^\dagger M_i d_i \underline{N}_i \tag{2.28}$$

with

$$\begin{aligned} \underline{L}_i &= [(1 - d_i^\dagger d_i)\underline{1} - 2\underline{p}_i^\dagger \underline{p}_i]^{-1/2} \ , \\ \underline{N}_i &= [(1 - e_i^\dagger e_i)\underline{1} - 2\underline{\tilde{p}}_i^\dagger \underline{\tilde{p}}_i]^{-1/2} \ , \\ M_i &= [1 + e_i^\dagger e_i + d_i^\dagger d_i + 2\,Tr\, \underline{p}_i^\dagger \underline{p}_i]^{1/2} \end{aligned} \tag{2.29}$$

($\tilde{p}^{(\dagger)}_{i\rho\rho'} := \rho\rho' p^{(\dagger)}_{i-\rho'-\rho}$), respectively. The (KR) SRI SB method was used, e.g., to investigate mean–field solutions with spiral magnetic order [167, 168] and to calculate the $T^3 \ln T$ spin fluctuation contribution to the specific heat in terms of the Hubbard model [169]. A detailed study of the t–t'–J model including Gaussian fluctuations within the framework of the SRI SB approach is presented in Chap. 4.

To proceed further, it is convenient to represent the grand canonical partition function for the SB Hamiltonian (2.20) in terms of a coherent–state functional integral over Grassmann fermionic ($\bar{f}_{i\sigma,m}$, $f_{i\sigma,m}$) and complex bosonic ($e^{(*)}_{i,m}$, $p^{(*)}_{i\sigma,m}$, $d^{(*)}_{i,m}$) fields as [170, 171]

$$\begin{aligned} \mathcal{Z} \ = \ & \lim_{M\to\infty} \int \prod_{m=0}^{M-1} \prod_i d\lambda_i^{(1)} \Big(\prod_\sigma d\lambda^{(2)}_{i\sigma} \Big) \mathcal{D}\,[e^*, e]_{i,m}\, \mathcal{D}\,[d^*, d]_{i,m} \Big(\prod_\sigma \mathcal{D}\,[p^*, p]_{i\sigma,m}\, \mathcal{D}\,[\bar{f}, f]_{i\sigma,m} \Big) \\ & \times \exp\left\{ -\varepsilon \sum_{m=0}^{M-1} \sum_i \Big(W^{(F)}_{i,m} + W^{(B)}_{i,m} + W^{(FB)}_{i,m} - \lambda_i^{(1)} \Big) \right\} \ , \end{aligned} \tag{2.30}$$

where the time–independent Lagrange multipliers $\lambda_i^{(1)}$, $\lambda_{i\sigma}^{(2)}$ are introduced to enforce the constraints (2.17)–(2.18) via a suitable integral representation of the δ–functions [172]

$$\delta(C^{(l)}) = \frac{\beta}{2\pi i} \int\limits_c^{c+2\pi i/\beta} d\lambda^{(l)}\ e^{-\beta\lambda^{(l)} C^{(l)}} \tag{2.31}$$

(the path of the λ–integration is extended parallel to the imaginary axis, and one finds $\lambda \in \mathbf{R}^+$ at the physical saddle point). In (2.30) the pure fermionic and bosonic parts of the action are given as

$$W^{(F)}_{i,m} \ = \ \sum_\sigma \Big(\bar{f}_{i\sigma,m} \partial_{\tau_m} f_{i\sigma,m} - \mu \bar{f}_{i\sigma,m} f_{i\sigma,m-1} + \lambda^{(2)}_{i\sigma} \bar{f}_{i\sigma,m} f_{i\sigma,m-1} \Big) \ , \tag{2.32}$$

and

$$
\begin{aligned}
W^{(B)}_{i,m} &= e^*_{i,m}\partial_{\tau_m} e_{i,m} + d^*_{i,m}\partial_{\tau_m} d_{i,m} + \sum_\sigma p^*_{i\sigma,m}\partial_{\tau_m} p_{i\sigma,m} \\
&\quad + \lambda^{(1)}_i \left(e^*_{i,m} e_{i,m-1} + \sum_\sigma p^*_{i\sigma,m} p_{i\sigma,m-1} + d^*_{i,m} d_{i,m-1}\right) \\
&\quad - \sum_\sigma \lambda^{(2)}_{i\sigma} \left(p^*_{i\sigma,m} p_{i\sigma,m-1} d^*_{i,m} d_{i,m-1}\right) + U d^*_{i,m} d_{i,m-1}\,, \qquad (2.33)
\end{aligned}
$$

respectively, where μ is the chemical potential. The mixed fermion–boson contribution

$$
W^{(FB)}_{i,m} = \sum_{j\sigma} t_{ij}\, \bar{f}_{i\sigma,m} z^*_{i\sigma,(m-1,m)} z_{j\sigma,(m,m-1)} f_{j\sigma,m-1} \qquad (2.34)
$$

includes the bosonic hopping operator $z_{i\sigma,(m,m')}$ (2.23), and therefore depends on the special choice of $R_{i\sigma,(m,m')}$. Here, we have used the short–hand notation $\partial_{\tau_m} = (\phi_{i,m} - \phi_{i,m-1})/\varepsilon$, where $m = 0, \dots, M-1)$ labels the discretized time mesh, $\tau_m = \varepsilon m$, breaking up the (imaginary time) interval $[0, \beta = 1/k_B T]$ (*i.e.*, $\varepsilon = \beta/M$).

As a next step, it has been common practice in the various slave–boson approaches to perform the continuum limit in time of the functional integral at the outset of the calculation (interchanging the limit $M \to \infty$ ($\varepsilon \to 0$) and functional integration) [166, 173, 174, 175, 176]. Then, exploiting the gauge symmetry of the action, one usually performs the following local time–dependent phase transformations [177]:

$$
\begin{aligned}
f_{j\sigma}(\tau) &\to f_{j\sigma}(\tau)\, \mathrm{e}^{-i\vartheta_{j\sigma}(\tau)} \qquad & e_j(\tau) &\to e_j(\tau)\, \mathrm{e}^{-i\chi_j(\tau)} \\
p_{j\sigma}(\tau) &\to p_{j\sigma}(\tau)\, \mathrm{e}^{-i\theta_{j\sigma}(\tau)} \qquad & d_j(\tau) &\to d_j(\tau)\, \mathrm{e}^{-i\phi_j(\tau)} \qquad (2.35)
\end{aligned}
$$

(where the original as well as the transformed Bose fields are complex). Under the transformation (2.35) the kinetic part exhibits extra terms violating a $U(1)^{\otimes 4}$ symmetry [176, 158, 178]. Transforming the Lagrange multipliers into Bose fields

$$
\begin{aligned}
\lambda^{(1)}_j &\to \lambda^{(1)}_j + i\dot{\chi}_j(\tau)\,, \\
\lambda^{(2)}_{j\sigma} &\to \lambda^{(2)}_{j\sigma} + i\dot{\chi}_j(\tau) - i\dot{\theta}_{j\sigma}(\tau)\,, \qquad (2.36)
\end{aligned}
$$

and, in addition, restricting the phase transformation to $U(1)^{\otimes 3}$ symmetry by

$$
\begin{aligned}
\vartheta_{j\sigma} &= \chi_j - \theta_{j\sigma}\,, \\
\phi_j &= \theta_{j\uparrow} + \theta_{j\downarrow} - \chi_j\,, \qquad (2.37)
\end{aligned}
$$

the gauge invariance of the action is satisfied. Obviously, one can now make use of the gauge freedom to remove three phases of the Bose fields in the so–called radial gauge, where the fields are given as modulus times a phase factor, e.g. $e_j(\tau) = \tilde{e}_j(\tau)\, \mathrm{e}^{-i\tilde{\chi}_j(\tau)}$ with $\tilde{e}_j \in \mathbf{R}^+$. Note that one of the Bose fields remains complex [176, 158, 179]:

$$
d_j(\tau) \to \tilde{d}_j(\tau)\, \mathrm{e}^{-i\phi_j(\tau)}\,, \text{ where } \phi_j = \tilde{\phi}_j - \tilde{\theta}_{j\uparrow} - \tilde{\theta}_{j\downarrow} + \tilde{\chi}_j \neq 0\,. \qquad (2.38)
$$

Accordingly, the partition function (2.30) can be expressed as a functional integral over the real–valued fields e, p_σ, $\lambda^{(1)}$, $\lambda^{(2)}_\sigma$, the complex fields $[d^*, d]$, and the Grassmann variables $[\bar{f}_\sigma, f_\sigma]$ (in the following we suppress the tilde that marks the radial parts of the boson fields). Performing the Gaussian integral over the fermion fields, one obtains

$$
\mathcal{Z} = \int \mathcal{D}[e]\mathcal{D}[p_\sigma]\mathcal{D}[\lambda^{(1)}]\mathcal{D}[\lambda^{(2)}_\sigma]\mathcal{D}[d^*, d]\; \mathrm{e}^{-S_{eff}}\,, \qquad (2.39)
$$

with the effective bosonized action

$$\begin{aligned}\mathcal{S}_{eff} &= \int_0^\beta d\tau \sum_i \Big[\lambda_i^{(1)}(e_i^2-1) + \sum_\sigma (\lambda_i^{(1)} - \lambda_{i\sigma}^{(2)})p_{i\sigma}^2 + d_i^*(\partial_\tau + \lambda_i^{(1)} - \lambda_{i\uparrow}^{(2)} - \lambda_{i\downarrow}^{(2)} + U)d_i\Big] \\ &\quad - \mathrm{Tr}\ln\Big[(\partial_\tau - \mu + \lambda_\sigma^{(2)})\delta_{ij} + t_{ij} z_{i\sigma}^* z_{j\sigma}\Big]\,, \qquad (2.40)\end{aligned}$$

where Tr means the trace over time, space and spin.

The natural strategy to deal with the remaining bosonic functional integral for the partition function seems to be performing a straightforward loop expansion. However, despite the great success of this technique at the saddle–point level [180], it turns out to be difficult to control the loop expansion (and even the correct $U = 0$ limit) beyond mean–field [176]. In particular, although the continuum imaginary–time assumption for $\mathcal{S}_{eff}^B$ does not pose any problem within the saddle–point approximation, this limiting procedure has to be taken with care when fluctuation corrections are included [170]. As demonstrated by Arrigoni *et al.* [170, 181, 182, 164] in a series of recent papers, a proper treatment of the continuum limit of the functional integral together with an appropriate normal–ordering prescription of the bosonic operator products, in particular of the nonlinear hopping operator (2.24)

$$R_{i\sigma} =: R_{i\sigma} : + \frac{1}{N} : R_{i\sigma}^{(1)} : + \mathcal{O}\left(\frac{1}{N^2}\right)\,, \qquad (2.41)$$

gives rise to additional contributions in the free energy even at the Gaussian level. Accordingly, using an one–level two–site ‘toy’ model, Arrigoni and Strinati [164] have shown that both types of $1/N$–corrections (those due to the discretized form of the action and those induced by the non–commutativity of the Bose fields) are essential to obtain a reasonable agreement with the exact solution and to recover the free–particle limit ($U = 0$) at any doping maintaining the KR form (2.23) of $z_{i\sigma}$. At present, however, it is not known how to carry out in practice a consistent $1/N$–expansion in more involved cases (including, for instance, magnetically ordered phases).

Chapter 3

Exact diagonalization analysis of strong–coupling models

The lack of exact results for the simplest prototype models of interacting fermion systems in more than one dimension, such as the Hubbard model and the t–J model, has stimulated the development of numerical methods, like exact diagonalization (ED) techniques, that allow investigating the properties of these models on *finite* lattices. Almost all of the numerical studies were carried out in the physically most important regimes representing weakly doped AFM insulators, where one can hope to gain some insight into the nature of the charge carriers responsible for HTSC. Although the ultimative goal of a correct and complete phase diagram in the thermodynamic limit is far beyond reach, numerous Lanczos diagonalizations of the t–J and Hubbard models on small clusters (up to 36 sites) have provided useful informations about their ground–state properties [7]. Thereby a particularly intriguing and highly nontrivial problem studied in most of the ED approaches is the behaviour of doped charge carriers (holes or electrons) in a quantum antiferromagnet. Here the spin configuration that minimizes the total energy of the system arises from the complicated interplay of strong AFM correlations in the spin background (which tend to localize the charge carriers) and a locally depleted AFM order (spin bag [92]) in the vicinity of the carriers (increasing their mobility inside such a spin bag [92][1]). Of course, in 2D, the fundamental question is whether well–defined quasiparticles emerge in this strongly correlated quantum liquid, i.e., a Fermi liquid description holds, or whether the charge and spin response share some similarity with the 1D (Tomonaga–Luttinger liquid) case [185, 186]. Other (related) issues addressed by ED in the framework of the (2D) Hubbard or t–J models are the behaviour of the electron–momentum distribution and the topology of the Fermi surface (‘large’ *vs.* ‘pocket–like’) [187, 188, 189], the question of hole pairing and clustering [190, 191], the analysis of the electronic spectral density [192] and the optical conductivity [193, 194, 7], the possibility of superconducting correlations (paring interactions) [82], and last but not least the long–standing puzzle regarding the (in)stability of ferromagnetism [195, 196, 197].

In this section we give a brief survey of our previous ED work [198, 199, 200, 201, 202], where we have confined ourselves mainly to the examination of the ground–state and thermodynamic properties of the Hubbard model in the strong–coupling limit. In particular, we present a complete classification of the ground state according to wave–vector, total spin, and point–group symmetry for finite lattices with up to 36 sites and different numbers of holes, both in the limit $J = 0$ (i.e., the $U = \infty$ Hubbard model) and for finite $J > 0$. Furthermore, we

---

[1] At very large Hubbard interactions there is even a tendency towards ferromagnetically aligned spins near the doped holes (Nagaoka spin polaron [183, 184]).

calculate the dispersion relation of a single hole in an AFM background and comment on the problem of hole binding and phase separation. For a comprehensive overview of the Lanczos literature, in particular with respect to results concerning the *dynamical* (spectral) properties and their comparison with experiments for the high–T_c cuprates, we refer to a recent review of Dagotto [7].

3.1 Ground–state properties [198, 199, 200, 202]

3.1.1 Cluster Hamiltonians and Lanczos method

Our starting point is the strong–coupling version of the 2D (extended) Hubbard model given by

$$\mathcal{H} = \mathcal{H}_1 + \mathcal{H}_2 + \mathcal{H}_3 + \mathcal{H}_4 \,, \tag{3.1}$$

where

$$\begin{aligned}
\mathcal{H}_1 &= -t \sum_{\langle ij \rangle \sigma} \left(\tilde{c}^{\dagger}_{i\sigma} \tilde{c}_{j\sigma} + \text{H.c.} \right), && (3.2)\\
\mathcal{H}_2 &= \frac{4t^2}{U} \sum_{\langle ij \rangle} \left(\vec{S}_i \, \vec{S}_j - \frac{\tilde{n}_i \tilde{n}_j}{4} \right), && (3.3)\\
\mathcal{H}_3 &= -\frac{t^2}{U} \sum_{\langle ijk \rangle \sigma} \left(\tilde{c}^{\dagger}_{i\sigma} \tilde{c}^{\dagger}_{j-\sigma} \tilde{c}_{j-\sigma} \tilde{c}_{k\sigma} + \tilde{c}^{\dagger}_{i-\sigma} \tilde{c}_{j-\sigma} \tilde{c}^{\dagger}_{j\sigma} \tilde{c}_{k\sigma} + \text{H.c.} \right), && (3.4)\\
\mathcal{H}_4 &= \sum_{i,j} V_{ij} \, \tilde{n}_i \tilde{n}_j \,. && (3.5)
\end{aligned}$$

As stated in Sec. 2.2, the electron annihilation (creation) operators $\tilde{c}^{(\dagger)}_{i\sigma}$ are chosen to constrain the configurations to those without double occupancy, thereby reducing the dimension of the Hilbert space from 4^N to 3^N where N is the number of sites on a finite square lattice. Note that the first term is now connected to the motion of $N_h = (1-n)N$ holes in the lower Hubbard band, hence its energy tends to zero if the number of electrons $N_e = N - N_h$ equals the number of sites ($n = N_e/N$ [$\delta = N_h/N$] is the mean electron [hole] number). $\mathcal{H}_1$ and $\mathcal{H}_2$ constitute the t–J model with the antiferromagnetic Heisenberg exchange interaction $J = t^2/U$, which is generated through a virtual double occupancy during a two–site hopping process [110]. The three–site (sublattice) hopping term $\mathcal{H}_3$ (with $t_3 = t^2/U$) should not be confused with the those t–t'–J model systems where t' denotes a *direct* intra–sublattice transfer (cf. Eq. (2.8)). In addition, we will include an interatomic Coulomb interaction V_{ij} in some of our calculations (with V_{NN} and V_{NNN} denoting NN and NNN interactions in $\mathcal{H}_4$). In a more realistic two–band model $\mathcal{H}_4$ reflects the Coulomb repulsion between charged singlets [103].

In the numerical work we consider bipartite clusters ($N=\sqrt{N} \times \sqrt{N}=8$, 10, 16, 18, 20, 26, 32 , 36, ...) with periodic boundary conditions[2] which cover the whole 2D square lattice. The general rule is $N = k^2 + l^2$, where the integers k and l are both even or odd [204]. Note that some of these square clusters have axis forming a nonzero angle with the lattice axis, i.e., they do not have all the symmetry properties of the square lattice (e.g., no reflections are allowed for N=10, 20, and 26). Besides using translational invariance to reduce the dimension of the Hilbert space we can exploit the point group symmetries contained in the little group of $\vec{K}$ [205].

---

[2] The case of antiperiodic and mixed boundary conditions was examined, e.g., by Riera [203] with respect to two–hole binding energies and the results are qualitatively insensitive to the boundary conditions used.

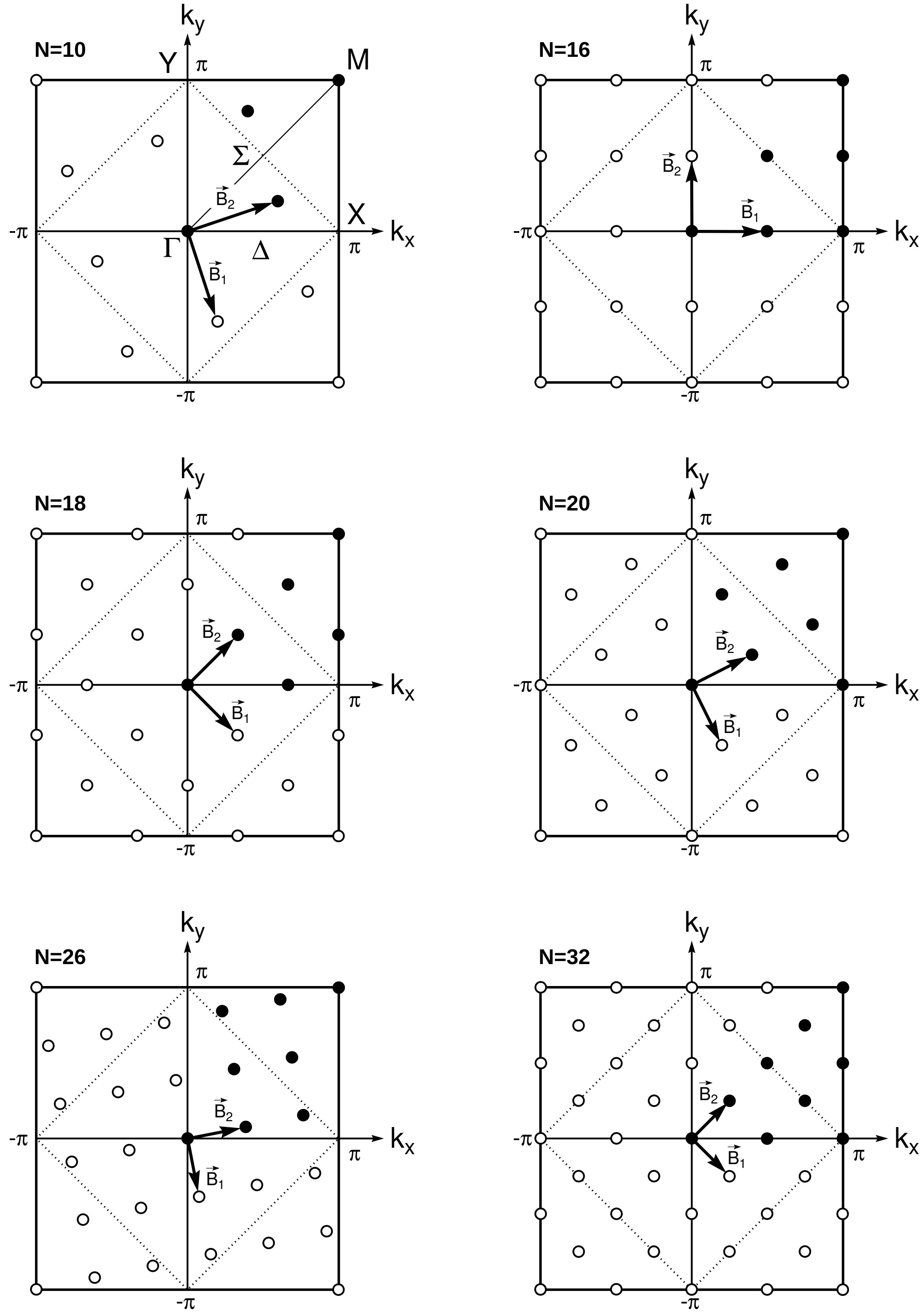

Figure 3.1: Brillouin zone for some popular (tilted) clusters with periodic boundary conditions. If $\vec{A}_1$ and $\vec{A}_2$ ($\vec{B}_1$ and $\vec{B}_2$) are the primitive vectors for the direct (reciprocal) lattice cell (i.e., $\vec{A}_i \cdot \vec{B}_j = 2\pi\delta_{ij}$), then the condition that $\vec{K}$ be a reciprocal lattice vector for the considered cluster shapes is satisfied by just those vectors that are linear combinations of the $\vec{B}_i$ with integral coefficients. Solid circles represent the $\vec{K}$–vectors unrelated by symmetry; the dotted square defines the pseudo Fermi surface at half–filling.

Moreover, the Hamiltonian (3.1) is spin rotational invariant and commutes with both the particle number operator $\hat{N}_e = \hat{N}_{e\uparrow} + \hat{N}_{e\downarrow} = \sum_{i=1}^{N}(\tilde{n}_{i\uparrow} + \tilde{n}_{i\downarrow})$ and the z–component of the total spin operator $\hat{S}^z = \hat{N}_{e\uparrow} - \hat{N}_{e\downarrow} = \sum_{i=1}^{N}(\tilde{n}_{i\uparrow} - \tilde{n}_{i\downarrow})$.

In order to calculate the eigenvalue spectrum of $\mathcal{H}$ we have constructed all basis states with fixed quantum numbers N_e, $S^z = S^z_{min}$, wave–vector $\vec{K}$, and irreducible representation (IR) of the point group $G(\vec{K})$ [205] and have diagonalized the strong–coupling Hamiltonian $\mathcal{H}$ in the projected Hilbert space without double occupancy using an improved Lanczos iteration method [205] which is different from the one proposed by Dagotto and Moreo [206]. In their method the Hamiltonian is projected onto Krylow subspaces of dimension m parameterized by a starting vector Ψ_0 much smaller than the dimension of the Hilbert space. One then diagonalizes the resulting tridiagonal matrix T^m – the Lanczos matrix – and uses the back–transformed eigenvector corresponding to the lowest eigenvalue of T^m as a starting vector Ψ_0' for the next subspace generation. Iterating this procedure the starting vector will converges to the ground–state eigenvector and the lowest eigenvalue of T^m converges to the ground–state energy. In our Lanczos method we follow more closely the algorithm described by Cullum and Willoughby [207]. Starting with any vector which is *not* an eigenvector we generate the Lanczos matrices T^m. Increasing m we check for the convergence of an eigenvalue of T^m in a specified range. This way we can avoid spurious eigenvalues for fixed Lanczos dimension m which disappear as one varies m [207]. Sturm sequencing is used to effectively calculate the desired eigenvalue of T^m and allows for using results of tridiagonalization for smaller values of m. Since this method directly iterates for the eigenvalue it is generally faster than a method that iterates for an eigenvector. Sturm sequencing also allows one to generate more eigenvalues than just the ground state which is necessary if one wants to classify eigenvalues according to $\hat{S}^2$ (total spin).[3] Our numerical procedure was checked by reproducing the lowest eigenvalue for the pure t–J model obtained in Refs. [208] and [209] ($N = 18$, $N_h = 1, 2$); whereas for the case $N = 18$, $N_h = 1$ we found lower eigenvalues than those stated by Elser *et al.* [210] at several $\vec{K}$ points.

3.1.2 Single–hole properties

First of all we report results for the one–hole sector. The momentum $\vec{K}$, total spin S and the symmetry classification of the ground state are given in Table 3.1 for both the t–J and the t–t$_3$–J model as a function of U, where $U > 4t$ ($\Leftrightarrow J < t$),[4] for the 10–, 16–, 18– and 20–site lattices (here and in the following all energies are measured in units of t). In the strong–coupling regime, the momentum of the ground state is shifted with increasing interaction strength U from a value near the perfect nested Fermi surface of the half–filled Hubbard model to $\vec{K} = (0,0)$ $[(\pi,\pi)]$ for $N/2$ odd [even] near the Nagaoka transition [183]. At this value of U the ground state becomes fully ferromagnetically polarized ($S = S_{max}$ for $U \geq U_N$). The non-monotonic behaviour of the momentum of the Nagaoka state is caused by the finiteness of the system in connection with periodic boundary conditions; the same change of momentum can be seen in the ($N_h = 0$) Heisenberg ground state (the ground–state energies for the 2D Heisenberg model are listed in Table 3.2.) As illustrated in Fig. 3.2 this behaviour is smeared out for larger lattice sizes. The difference of ground–state energies $[E(\vec{K} = (0,0)) - E(\vec{K} = (\pi,\pi))]$ tends – as it should – to zero in the limit $N \to \infty$ (alternating in sign).

---

[3] The total spin of the ground state could be determined by raising S^z until a higher energy value than $E(\vec{K}, S^z_{min})$ was found.

[4] Irrespective of the fact that the t–J or better the t–t$_3$–J model describes the behaviour of the one–band Hubbard model only for $t/U \ll 1$, it is interesting to study the t–J model as a model of its own right in the whole parameter regime of J/t and even in the limit $J/t \gg 1$ [211].

N	U (t–J)	U (t–t$_3$–J)	$\vec{K}$	IR/$G(\vec{K})$	S
10	$0 - 1.1$	–	$(0,0)$	A/C_4	$\frac{1}{2}$
	$1.2 - 15.2$	$4.0 - 26.6$	$(\frac{3\pi}{5},\frac{\pi}{5})$	A/C_1	$\frac{1}{2}$
	$15.3 - 21.7$	–	$(\frac{2\pi}{5},\frac{4\pi}{5})$	A/C_1	$\frac{1}{2}$
	$21.8 - 27.1$	$26.7 - 28.5$	(π,π)	A/C_4	$\frac{3}{2}$
	$27.2 - 28.9$	$28.6 - 30.8$	$(0,0)$	A/C_4	$\frac{5}{2}$
	$30.0 - \infty$	$30.9 - \infty$	$(0,0)$	A/C_4	$\frac{5}{2}$
16	$0 - 0.6$	–	$(0,0)$	A_1/C_{4v}	$\frac{1}{2}$
	$0.7 - 1.9$	–	$(\frac{\pi}{2},0)$	A'/C_s	$\frac{1}{2}$
	$2.0 - 51.3$	$4.0 - 57.0$	$(\pi,0)$	A_1/C_{2v}	$\frac{1}{2}$
	$2.0 - 51.3$	$4.0 - 57.0$	$(\frac{\pi}{2},\frac{\pi}{2})$	A'/C_s	$\frac{1}{2}$
	$51.4 - 52.2$	–	(π,π)	A_1/C_{4v}	$\frac{3}{2}$
	$52.3 - 63.3$	$57.1 - 67.4$	$(0,0)$	A_1/C_{4v}	$\frac{5}{2}$
	$63.4 - 63.5$	–	(π,π)	A_1/C_{4v}	$\frac{7}{2}$
	$63.6 - \infty$	$67.5 - \infty$	(π,π)	A_1/C_{4v}	$\frac{15}{2}$
18	$0 - 0.4$	–	$(0,0)$	A_1/C_{4v}	$\frac{1}{2}$
	$0.5 - 2.7$	–	$(\frac{\pi}{3},\frac{\pi}{3})$	A'/C_s	$\frac{1}{2}$
	$2.8 - 21.5$	$4.0 - 27.7$	$(\frac{2\pi}{3},0)$	A'/C_s	$\frac{1}{2}$
	$21.6 - 77.3$	$27.8 - 85.7$	$(\frac{\pi}{3},\frac{\pi}{3})$	A'/C_s	$\frac{1}{2}$
	$77.4 - 84.6$	$85.8 - 91.5$	$(0,0)$	A_1/C_{4v}	$\frac{1}{2}$
	$85.0 - \infty$	$91.8 - \infty$	$(0,0)$	A_1/C_{4v}	$\frac{17}{2}$
20	$0 - 0.4$	–	$(0,0)$	B/C_4	$\frac{1}{2}$
	$0.5 - 1.0$	–	$(\frac{2\pi}{5},\frac{\pi}{5})$	A/C_1	$\frac{1}{2}$
	$1.1 - 72.6$	$4.0 - 78.7$	$(\frac{\pi}{5},\frac{3\pi}{5})$	A/C_1	$\frac{1}{2}$
	$72.7 - 74.5$	$78.8 - 83.8$	$(\frac{2\pi}{5},\frac{\pi}{5})$	A/C_1	$\frac{1}{2}$
	$74.6 - 96.6$	$83.9 - 103.4$	$(0,0)$	B/C_4	$\frac{1}{2}$
	$96.7 - \infty$	$104.5 - \infty$	$(0,0)$	B/C_4	$\frac{19}{2}$

Table 3.1: The classification of the one–hole ground–state for the t–(t$_3$)–J model on a 10–, 16–, 18– and 20–site lattice due to momentum $\vec{K}$, total spin S, and irreducible representation (IR) of the point group $G(\vec{K})$ involved [200, 205], at various interaction strengths U.

To address the question of whether there are hole pockets in the Fermi surface of the infinite system (if such a Fermi surface exists) it is instructive to discuss the energy dispersion $E(\vec{K},S)$ of the vacancy band.[5] For $N = 18$ (20) we have six (seven) inequivalent wave–vectors $\vec{K}_i$ in

---

[5] As mentioned above our calculations were always done in a subspace of fixed total S^z which only imposes

Table 3.2: Ground–state energies E_H/N for the 2D antiferromagnetic ($S = 1/2$) Heisenberg model on finite square lattices with up to 36 sites (using periodic boundary conditions). The energies are measured in units of $J/4 = t^2/U$. The (extrapolated) value for the infinite system (error ±0.004) was taken from Tang and Hirsch [218]. The ground state is unique and has $S = 0$ (spin singlet) and momentum $\vec{K} = (0, 0)$ [(π, π)] for $N/2$ even [odd].

N	$4E_H/NJ$
10	-4.920 027
16	-4.807 121
18	-4.775 944
20	-4.763 232
26	-4.737 809
32	-4.720 717
36	-4.715 489
∞	≈-4.688 [218]

the Brillouin zone (see Fig. 3.1).[6] As has been standard in early Lanczos work [210], we can extend these six (seven) energies $E(\vec{K}_i, S; N_h = 1)$ throughout the whole Brillouin zone by the following energy dispersion:

$$E(\vec{K}_i, S) = \sum_{\substack{l,m=0 \\ (l+m)\leq 3}} a_{lm} \cos lK_x \cos mK_y \,. \tag{3.6}$$

We would like to stress that the band dispersion obtained by always taking the lowest eigenvalue [217] for each allowed $\vec{K}$–point results in a somewhat different dispersion relation.

Figures 3.3 (a)–(d) show as a comparison of the results for N=18 and 20 for both the t–J and t–t$_3$–J models at U/t=10. First we notice that, for not too small exchange interactions ($J/t > 0.2$), the minima of the lowest S=1/2 band are well separated from bands belonging to higher spin sectors, while around $\vec{K} = (0, 0)$, (π, π) higher spin sectors become lower in energy. So for this parameter range we conclude from our finite–size data that a usual spin–1/2 quasiparticle description may be adequate. Obviously, due to the inclusion of the $\mathcal{H}_3$–term the whole band structure is shifted to lower energies, but in addition there are small changes in the ground–state structure, in particular, the t–J and t–t$_3$–J models have different dispersions along the magnetic Brillouin zone boundary from $(0, \pi)$ to $(\pi, 0)$ [199] (cf. the discussion of Fig. 3.5 below).

Increasing the Coulomb interaction strength ($U/t > 40$) the states with larger spin become comparable in energy, a situation which suggests the formation of local ferromagnetic

---

a lower bound on the total spin S. Since, depending on $\vec{K}$, S–level crossings occur even at relative small values of U ($U/t = 10$), we have to determine those excited states of a lower S^z–sector which are not contained in the higher S^z–sectors to obtain a band dispersion with definite S.

[6] Note that previous numerical investigations on the 4×4 cluster gave rise to controversial interpretations due to the high symmetry of this particular system. In fact, using periodic boundary conditions, the 4×4 cluster exhibits an hidden symmetry (beyond C_{4v}), which makes it isomorphic to a 2^4 hypercubic lattice [212] and leads to an accidental degeneracy of the ground state (cf. Table 3.1; see also Refs. [208, 213, 214]). This is very unfortunate if one wants to obtain reliable information about the existence and location of hole pockets in the t–(t$_3$)–J model, because the only considered candidates [215, 216], $(\pm\pi/2, \pm\pi/2)$ and $(\pm\pi, 0)$, $(0, \pm\pi)$, being energetically degenerate on the 16–site lattice. Of course, the tilted $\sqrt{18} \times \sqrt{18}$ and $\sqrt{20} \times \sqrt{20}$ lattices do not possess this additional symmetry.

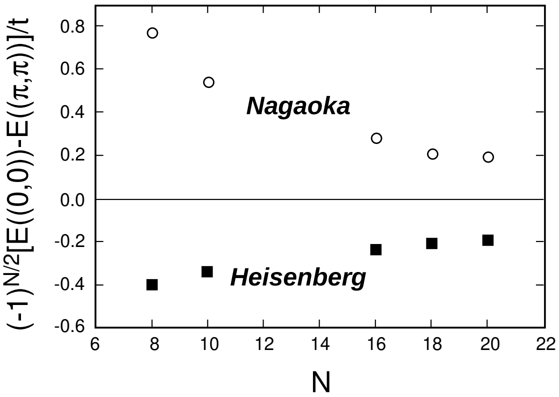

Figure 3.2: The energy difference $(-1)^{N/2}[E(0,0) - E(\pi,\pi)]$ is given for increasing lattice size N, where $E(\vec{K}) = \inf_S E(\vec{K},S)$. The open circles show the Nagaoka limit: $N_h = 1$, $U = \infty$; the solid squares the Heisenberg limit: $N_h = 0$ at $U = 10$.

polarons [219]. If one defines a 'coherent' bandwidth [210, 7]

$$\Delta E = \sup\,[E(\vec{K},S)] - \inf\,[E(\vec{K},S)]\,, \tag{3.7}$$

this quantity becomes very small at the transition to the Nagaoka state ($\Delta E = 0.035$ (0.027) for $N = 18$ (20) at $U/t = U_N/t = 91.5$ (103.5)) and tends to zero in the thermodynamic limit where $U_N \to \infty$. In this parameter range the usual quasiparticle picture fails. The situation is illustrated in Fig. 3.4 for two different values of U, namely the critical interaction U_N and $U \to \infty$.

In this section no attempt is made to calculate the hole spectral function

$$A_{\vec{K}\sigma}(\omega) = \sum_m |\langle \Psi_m^{N-1}| c_{\vec{K}\sigma} |\Psi_0^N\rangle|^2 \delta(\omega + E_m^{N-1} - E_0^N)\,, \tag{3.8}$$

which measures the overlap between the state where one hole is created in the Heisenberg ground state $|\psi_0^N\rangle$ and the exact eigenstates of the one–hole subspace (see, e.g., Refs. [220, 221, 7]). While for $J = 0$ the $\vec{K}$–integrated spectrum $A(\omega)$ is completely incoherent (see Fig. 8 of Ref. [221]), for finite J it shows a well–separated quasiparticle peak of width $\sim J$ below a broad incoherent spectrum (cf. Fig. 11 of Ref. [221]).[7] The important point, we would like to emphasize, is that the quasiparticle dispersion, which can be derived from this dominant peak [129, 221], can be related directly to our $S = 1/2$ band, thereby yielding additional evidence for the validity of the suggested quasiparticle description in this parameter regime.

Poilblanc and Dagotto [216] suggested that the hole momenta of minimal energy might depend on the inclusion of terms like $\mathcal{H}_3$ in (3.1). Indeed, our numerical results for the full Hamiltonian (3.1) lead to a minimum of $E(\vec{K},1/2)$, which is located on the *corners* of the pseudo FS, whereas the pure t–J model gives the minima at $(\pm\pi/2, \pm\pi/2)$. This is impressively demonstrated through the contour plots in Figs. 3.5 which show the energy dispersion (3.6) extended over the whole Brillouin zone in the $S = 1/2$ sector for both models and various U values. Notice that the 18– and 20–site clusters lead to qualitatively the same results [200]. In contrast to the noninteracting case (where doped holes distribute themselves uniformly along the FS indicated through the dotted square in Fig. 3.1), the holes in the interacting case will upon doping accumulate near the minima of the band dispersion (3.6) (indicated by large dots in Figs. 3.5), and form a pocket–like Fermi surface.[8] Such a topology was earlier conjectured by Lee [223] (see also Fulde [10]). The hole pockets are most pronounced for larger values

---

[7] This means, in the limit $J < t$, the characteristic energy for the hole motion is J and not t [103, 222, 216, 10].

[8] In a more recent work, Eder and Ohta [189] have examined the single–particle spectral and momentum distribution functions of the t–J model and found signatures of a FS which takes the form of small hole pockets as well.

of J (cf. also the contour plots given at $U/t = 4$ in Figs. 4–7 of Ref. [200]) and weaken with decreasing J (increasing U). At the same time the position of the minima moves away from the magnetic Brillouin–zone boundary, while the whole band structure flattens out. The difference in position of the pockets of the t–J and t–t$_3$–J model disappears for U greater than about 20 when the $\mathcal{H}_3$–term ($\propto 1/U$) is weakened [200]. Since the t–t$_3$–J model is a better approximation to the Hubbard model, it is interesting to speculate whether the Hubbard model

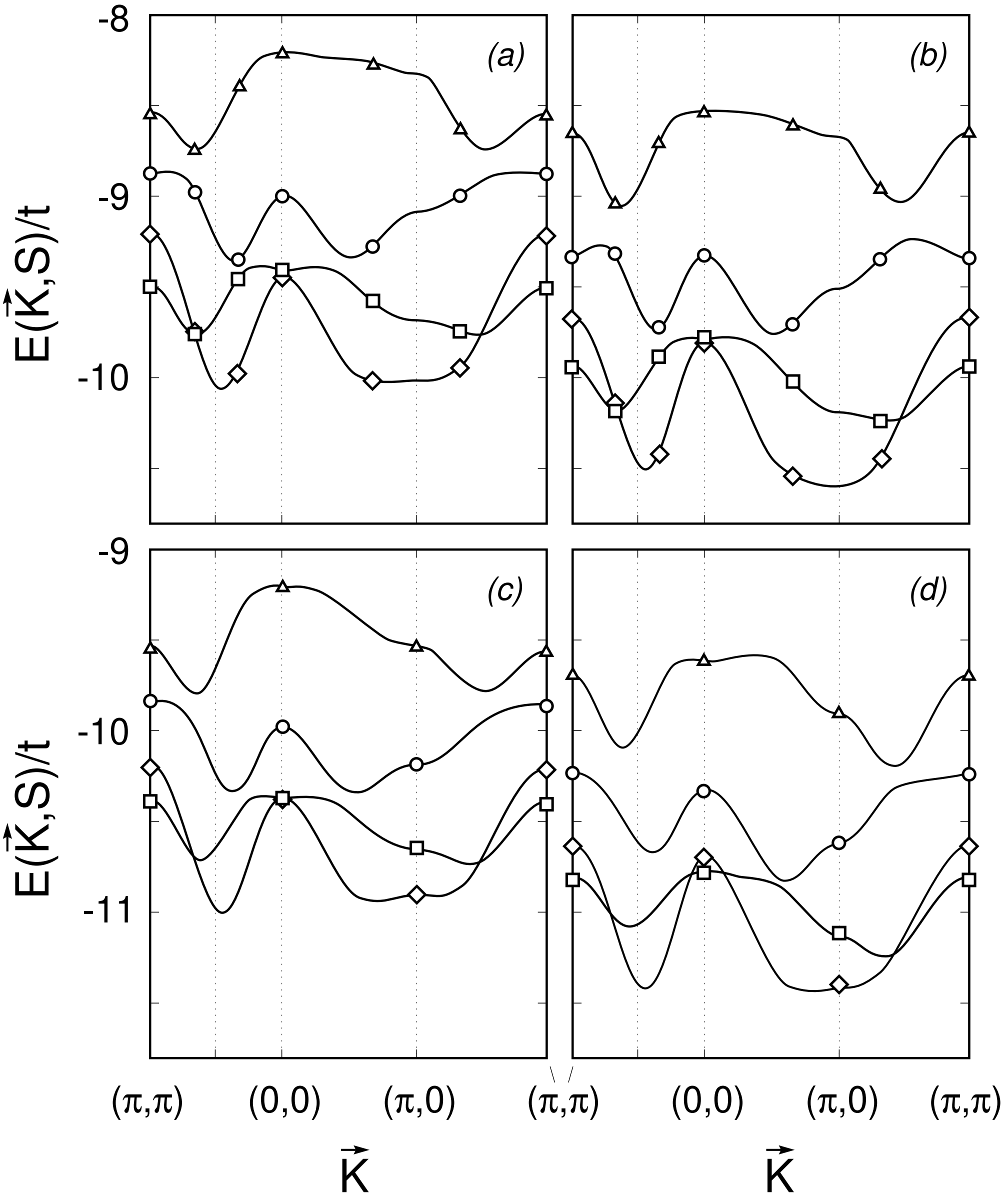

Figure 3.3: ‘Band structure’ for a single hole on the 18–site (upper panels) and 20–site (lower panels) lattices. The symbols denote different total spins [S: 1/2 (◇); 3/2 (□); 5/2 (◯); and 7/2 (△)] at the allowed $\vec{K}$–values. The interpolation is done with Eq. (3.6) for the t–J [(a),(c)] and t–t$_3$–J models [(b),(d)] at $U/t = 10$.

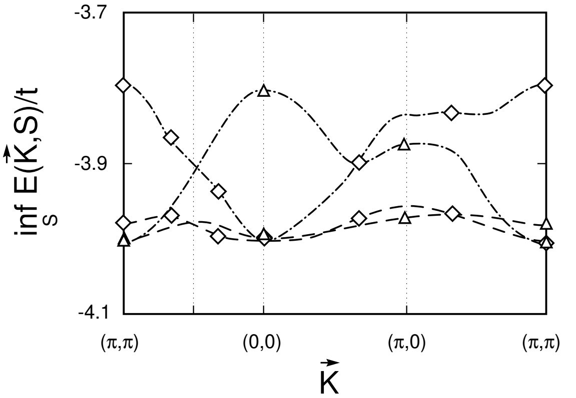

Figure 3.4: The lowest energy band for the t–t$_3$–J model given by the minimum of $E(\vec{K},S)$ at a given $\vec{K}$ for $U = U_N$ (dashed line and $U \to \infty$ (dashed dotted line) for the 18–site (◇) and 20–site (△) lattices.

also forms hole pockets around $(\pm\pi, 0)$, $(0, \pm\pi)$. However, in order to answer this question one would have to study the Hubbard model on at least a 18–site lattice because of the accidental degeneracy of the 16–site lattice mentioned above. Frequently in the past, quantum Monte Carlo calculations [224] did not find evidence for hole pockets in the Hubbard model, but these simulations can not be performed at those low temperatures that are necessary to resolve the small energy differences ($\sim 0.1t$ for $U/t = 10$, $N = 18$) along the pseudo FS. On the other hand, by combining a variational ansatz with QMC, Mattis *et al.* [225] have calculated the dispersion relation of a small fraction δ of extra holes (electrons) introduced into the Mott insulating phase of the 2D Hubbard model. They found that the charge carriers constitute a spin–1/2 Fermi liquid of δN (*not* $(1 \pm \delta)N$) quasiparticles, with an anisotropic dispersion, large effective masses, and pocket–like constant–energy contours near the Fermi energy. As pointed out by Schrieffer *et al.* [215] the formation of a pocket–like FS may give a nodeless pairing gap over the whole FS, although its formal symmetry can be of p– or d–wave type.

Another interesting difference between the t–J and the t–t$_3$–J model appears if one calculates the components of the effective mass tensor parallel and perpendicular to $\vec{K}_{min}$ at $\vec{K}_{min}$. Apart from the well–known increase in effective band mass with increasing U (cf. Ref. [226]) the effective mass tensor is rather isotropic for the t–t$_3$–J model and strongly anisotropic [225, 227] for the t–J model (see Table 3.3).

3.1.3 High–doping regime and low–density limit

In this section we extend the ED study of the t–(t$_3$)–J model to a larger number of holes. In the high–doping regime the AFM correlations become very short–range and the ground state behaves more as a dilute system of correlated fermions than, e.g., as a dilute system of massive spin polarons [228].

In Table 3.4 we present the values of the ground–state energy with respect to the Heisenberg energy $\bar{E}(N_h) = E(N_h) - E(0)$ and the complete symmetry classification of the ground state for up to six (two) holes for both the t–J and t–t$_3$–J model on the 18– (20–) site lattice at $U/t = 10$. It is known from a series of Lanczos studies [228, 213, 214, 208] for smaller lattices that the ground state for two and four holes is found to be a spin singlet ($S = 0$) independent of U.

For our larger systems, however, the $\vec{K}$ degeneracy of the ground state is lifted. The $\vec{K}$–dependence of the two–hole ground state is shown in Fig. 3.6 for the singlet ($S = 0$) and the triplet ($S = 1$) case. The $S = 0$ state exhibits at $\vec{K} = (0,0)$ a well–defined minimum and, as in the case of one hole, its total energy is reduced due to the inclusion of the $\mathcal{H}_3$–term.

Unlike the case of low *hole* doping, the regime of low *electron* density ($n = N_e/N \ll 1$) has

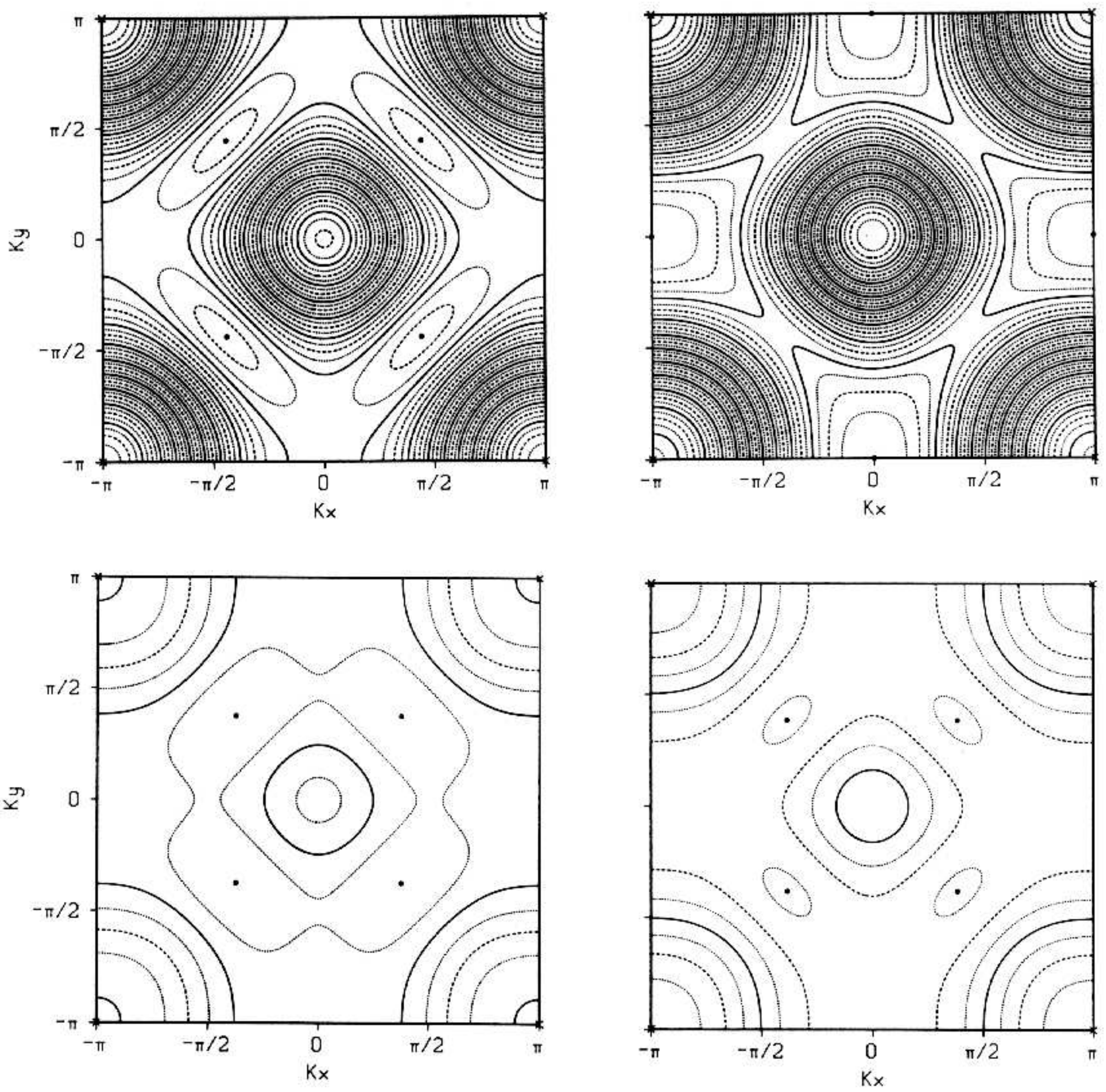

Figure 3.5: Contour plots of the 'quasihole' energy dispersion $E(\vec{K}, 1/2)$ in the Brillouin zone of the square lattice. The lines of constant energy are derived for the t–J (left panels) and for the t–t$_3$–J model (right panels) on the $\sqrt{18} \times \sqrt{18}$ lattice at $U/t = 10$ (upper panels) and $U/t = 40$ (lower panels). The crosses mark the maxima of $E(\vec{K}, 1/2)$ at the corners of the Brillouin zone, whereas the closed circles denote the minima (cf. Fig. 3.3). The energy difference between neighbouring solid lines is 0.1 t.

been studied only by few authors [229, 230, 231], as it seems less important for the description of the essential physics in the high–T_c copper oxides. Nevertheless, this limit is important for a more complete understanding of the t–J model as well. In fact, a systematic study of the low–density limit allows to address some interesting physical questions, e.g., the competition between weak–coupling (Fermi–liquid–like) and strong–coupling behaviour [230]. Furthermore, in Sec. 3.1.5 we will show that the problem of phase separation in the t–J model can be examined by a finite–size extrapolation of ED results obtained at low electron densities.

Table 3.3: Components of the effective–mass tensor at the minimum of the band dispersion $E(\vec{K}, S = 1/2)$ (for the $\sqrt{18} \times \sqrt{18}$) lattice located at $\vec{K}_{\min}$. $(m^*/m)_{||}$ and $(m^*/m)_{\perp}$ denote the values parallel and perpendicular to $\vec{K}_{\min}$, respectively.

	U	$\vec{K}_{\min}$	$\left(\left[\frac{m^*}{m}\right]_{\|\|};\left[\frac{m^*}{m}\right]_{\perp}\right)$
t–J	4	0.94 $(\frac{\pi}{2}, \frac{\pi}{2})$	(0.69; 3.54)
	10	0.89 $(\frac{\pi}{2}, \frac{\pi}{2})$	(1.30; 15.67)
	20	0.82 $(\frac{\pi}{2}, \frac{\pi}{2})$	(2.81; 31.55)
	40	0.75 $(\frac{\pi}{2}, \frac{\pi}{2})$	(7.01; 20.46)
t–t_3–J	4	$(\pi, 0)$	(2.72; 1.60)
	10	$(\pi, 0)$	(9.87; 5.55)
	20	$(\pi, 0)$	(22.82; 19.72)
	40	0.77 $(\frac{\pi}{2}, \frac{\pi}{2})$	(6.02; 22.29)

Table 3.4: Energy $\bar{E}$, spin, momentum, and symmetry group of the ground state for up to six (two) holes on a $\sqrt{18} \times \sqrt{18}$ ($\sqrt{20} \times \sqrt{20}$) lattice at $U/t = 10$.

N	N_h	$\vec{K}$	IR/$G(\vec{K})$	S	$\bar{E}(N_h)$	
					t–J	t–t_3–J
18	1	$(\frac{2\pi}{3}, 0)$	A'/C_s	$\frac{1}{2}$	-1.415 274	-1.938 938
	2	$(0, 0)$	B_1/C_{4v}	0	-3.266 077	-4.360 609
	3	$(\frac{2\pi}{3}, 0)$	A'/C_s	$\frac{1}{2}$	-4.713 952	-6.167 221
	4	$(0, 0)$	A_1/C_{4v}	0	-6.372 600	-8.094 627
	5	$(\frac{2\pi}{3}, 0)$	A'/C_s	$\frac{1}{2}$	-7.268 506	-8.952 948
	6	$(0, 0)$	B_1/C_{4v}	0	-8.077 757	-9.750 330
20	1	$(\frac{\pi}{5}, \frac{3\pi}{5})$	A/C_1	$\frac{1}{2}$	-1.440 691	-1.930 823
	2	$(0, 0)$	A/C_4	0	-3.273 336	-4.228 678

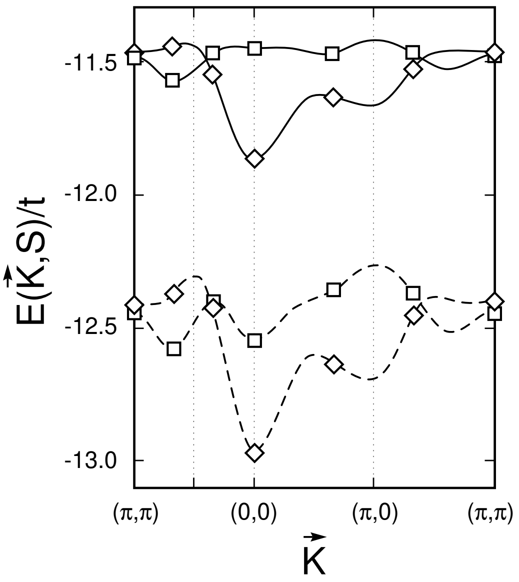

Figure 3.6: $\vec{K}$–dependence of the ground–state energy of two holes in the $S = 0$ (◇) and $S = 1$ (□) spin sector. The solid (dashed) lines are calculated for the t–J (t–t_3–J) model on a 18–site lattice at $U/t = 10$.

	$N_e = 2$				$N_e = 3$			
	J	$\vec{K}$	IR/G($\vec{K}$)	S	J	$\vec{K}$	IR/G($\vec{K}$)	S
$N = 20$	$0 - \infty$	$(0, 0)$	A/C_4	0	$0 - 10.35$	$(\frac{2\pi}{5}, \frac{\pi}{5})$	A/C_1	$\frac{1}{2}$
					$10.35 - \infty$	$(0, 0)$	B/C_4	$\frac{1}{2}$
$N = 26$	$0 - \infty$	$(0, 0)$	A/C_4	0	$0 - 11.64$	$(\frac{5\pi}{13}, \frac{\pi}{13})$	A/C_1	$\frac{1}{2}$
					$11.64 - \infty$	$(0, 0)$	B/C_4	$\frac{1}{2}$
$N = 32$	$0 - \infty$	$(0, 0)$	A_1/C_{4v}	0	$0 - 16.70$	$(\frac{\pi}{4}, \frac{\pi}{4})$	A'/C_s	$\frac{1}{2}$
					$16.70 - \infty$	$(0, 0)$	B_1/C_{4v}	$\frac{1}{2}$
$N = 36$	$0 - \infty$	$(0, 0)$	A_1/C_{4v}	0	$0 - 18.25$	$(\frac{\pi}{3}, 0)$	A'/C_s	$\frac{1}{2}$
					$18.25 - \infty$	$(0, 0)$	B_1/C_{4v}	$\frac{1}{2}$
	$N_e = 4$				$N_e = 5$			
$N = 20$	$0 - 1.570$	$(0, 0)$	B/C_4	0	$0 - 0.829$	$(\frac{2\pi}{5}, \frac{\pi}{5})$	A/C_1	$\frac{3}{2}$
	$1.570 - 4.692$	$(\frac{4\pi}{5}, \frac{2\pi}{5})$	A/C_1	0	$0.829 - 1.745$	$(\frac{2\pi}{5}, \frac{\pi}{5})$	A/C_1	$\frac{1}{2}$
	$4.692 - \infty$	$(0, 0)$	B/C_4	0	$1.745 - \infty$	$(\pi, 0)$	B/C_2	$\frac{1}{2}$
$N = 26$	$0 - 2.249$	$(0, 0)$	B/C_4	0	$0 - 0.993$	$(\frac{5\pi}{13}, \frac{\pi}{13})$	A/C_1	$\frac{3}{2}$
	$2.249 - 4.597$	$(\frac{10\pi}{13}, \frac{2\pi}{13})$	A/C_1	0	$0.993 - 2.715$	$(\frac{5\pi}{13}, \frac{\pi}{13})$	A/C_1	$\frac{1}{2}$
	$4.597 - \infty$	$(0, 0)$	B/C_4	0	$2.715 - 4.413$	$(\frac{9\pi}{13}, \frac{7\pi}{13})$	A/C_1	$\frac{1}{2}$
					$4.413 - 4.669$	$(\frac{5\pi}{13}, \frac{\pi}{13})$	A/C_1	$\frac{1}{2}$
					$4.669 - \infty$	$(\frac{9\pi}{13}, \frac{7\pi}{13})$	A/C_1	$\frac{1}{2}$
$N = 32$	$0 - 1.462$	$(0, 0)$	B_2/C_{4v}	0	$0 - 1.423$	$(\frac{\pi}{4}, \frac{\pi}{4})$	A''/C_s	$\frac{3}{2}$
	$1.462 - 2.665$	$(\frac{\pi}{2}, \frac{\pi}{2})$	A'/C_s	0	$1.423 - 1.687$	$(\frac{\pi}{4}, \frac{\pi}{4})$	A'/C_s	$\frac{1}{2}$
	$2.665 - 5.191$	$(\frac{\pi}{2}, 0)$	A'/C_s	0	$1.687 - 2.701$	$(\frac{3\pi}{4}, \frac{\pi}{4})$	A/C_1	$\frac{1}{2}$
	$5.191 - \infty$	$(0, 0)$	B_1/C_{4v}	0	$2.701 - 5.362$	$(\frac{\pi}{4}, \frac{\pi}{4})$	A''/C_s	$\frac{1}{2}$
					$5.362 - \infty$	$(\frac{3\pi}{4}, \frac{\pi}{4})$	A/C_1	$\frac{1}{2}$
$N = 36$	$0 - 2.086$	$(0, 0)$	B_1/C_{4v}	0	$0 - 1.239$	$(\frac{\pi}{3}, 0)$	A''/C_s	$\frac{3}{2}$
	$2.086 - 4.664$	$(\frac{2\pi}{3}, 0)$	A'/C_s	0	$1.239 - 2.387$	$(\frac{\pi}{3}, 0)$	A'/C_s	$\frac{1}{2}$
	$4.664 - \infty$	$(0, 0)$	B_1/C_{4v}	0	$2.387 - 3.834$	$(\frac{2\pi}{3}, \frac{\pi}{3})$	A_1/C_1	$\frac{1}{2}$
					$3.834 - 5.574$	$(\frac{\pi}{3}, 0)$	A'/C_s	$\frac{1}{2}$
					$5.574 - \infty$	(π, π)	$?\ /C_{4v}$	$\frac{1}{2}$

Table 3.5: The ground state of the of the 2D t–J model is classified in the whole parameter space $J > 0$. In the stated regions of J the ground state has the given momentum $\vec{K}$, spin S, and point–group symmetry IR/$G(\vec{K})$.

In Table 3.5 we present the classification of the ground state for the t–J model in the low–density limit. With the exception of the two–electron case, we obtained various transitions of the ground–state structure, similar to those discovered in the well–suited single–hole case [232, 200, 214]. For very large J we found a homogeneous state with $\vec{K} = (0,0)$ and S_{min} for $N_e = 3$ and 4, just as in the one–hole case (cf. Table 3.1) for $J \geq 3.40$, 6.55, 8.44 and 9.47 for $N = 10$, 16, 18 and 20 sites, respectively. Our results for $N_e = 3$ show a similar increase of this transition value to the homogeneous state ($\vec{K} = (0,0)$, $S = 1/2$) with the lattice size N. The total spin of the ground state always decreases to $S = S_{min}$, if only J is large enough (cf. Table 3.5 for $N_e = 5$). A similar transition from $S = 2$ to $S = 0$ can be found for $N_e = 6$; (e.g., for $N = 20$ this transition appears at $J = 0.820$, where the ground–state symmetry changes from B/C_4 to A/C_4 within the $\vec{K}$=(0,0) sector). Clearly, the different regimes in Table 3.5 are finite–size dependent, and might not be present in the thermodynamic limit, where one has an infinite number of allowed $\vec{K}$–values.

3.1.4 The limit $U = \infty$

Next, let us consider the limit $J = 0$ (i.e., $U = \infty$), which is especially interesting with respect to the existence of ferromagnetism in the Hubbard model. The probability for the appearance of ferromagnetic states is largest for $U = \infty$, since for any finite U there is always an effective antiferromagnetic exchange interaction. In the infinite–U limit the strong–coupling Hamiltonian (3.5) reduces to $\mathcal{H}_1$. At half–filling, due to the two possible spin orientations per site, there exists a large 2^N–fold ground–state degeneracy. For the case of a single hole, a rigorous proof could be given that the ground state on a bipartite lattice is ferromagnetic with maximum total spin $S = S_{max}$ [183]. For any finite number of holes in the infinite lattice – that means $\delta = 0$ – it is argued [233, 234] that the ground state is degenerate with the ferromagnetic ones ($S = S_{max}$) and the ground–state energy is given by $E(N_h, N = \infty, U = \infty) = -4N_h t$. The extension of Nagaoka's theorem [183] to finite hole densities in the thermodynamic limit remains unsettled until today (with the exception of some special lattices, such as the Kagome lattice [235, 236]). In the low–doping regime, the instability of the fully polarized ferromagnetic Nagaoka state with respect to spin flips has been under intensive investigation on various lattices in various dimensions (for a recent review on this problem area see Refs. [237, 238]).[9] In the opposite case of low electron densities, Kanamori [117] stated a paramagnetic ground state for $n < 0.23$.

Our ED results for $J = 0$ and lattice sizes between 18 and 36 sites are reported in Table 3.6. For the small cells with $N = 8$, 10 and 16 our procedure yields the same ground–state energy and spin values obtained earlier [195].[10] One observes a highly non-monotonic behaviour of total spin S as the number of holes increases which renders an extrapolation to the thermodynamic limit difficult. Near quarter–filling, however, there is a region with large S. The state with nine holes exhibits as the Nagaoka state *maximal* total spin; the nine electrons can therefore be described as spinless fermions which occupy the nine allowed $\vec{K}$ values within the magnetic Brillouin zone (cf. Fig 3.1). Spin multiplets are obviously connected to less symmetric irreducible representations of the point group $G(\vec{K})$. Let us stress that Barbieri *et al.* [242] have pointed out that the instability of the Nagaoka state for small numbers of

---

[9] For the 2D square lattice the early result $\delta_c = 0.49$, derived by Shastry *et al.* [239] for the critical hole density, above which the Nagaoka state is definitely not the ground state, was lowered to $\delta_c = 0.29$ [240]. Recently, from ED results an even smaller value $\delta_c = 0.195 \pm 0.01$ [197] was suggested.

[10] However, note that we found the true ground state for $N = 16$ sites and $N_h = 5$ holes to be $E = -12.180846$ with degenerate momenta $\vec{K} = (\pi, 0)$ and $\vec{K} = (\pi/2, \pi/2)$ and with spin $S = 1/2$, which is lower in energy than the $S = 5/2$ state stated by Riera and Young in Table III of Ref. [241].

holes N_h is an artifact of the small cluster size. They showed that the ferromagnetic state is in general locally stable with respect to single spin flips for $N_h \ll \ln N$. Our results obviously do not prove the existence of a ferromagnetic ground state at finite hole densities. We believe, however, that they show at low doping level a tendency of the system to form a ground state which is not a singlet. The same is argued by Zhou and Gong [243] from a different point of view. They showed that ferromagnetic correlations affect the motion of more than one hole through forming flux phases, where the total spins remains almost the same as that of the saturated ferromagnet.

Whereas all exact diagonalization studies at low hole doping give an erratic dependence of the ground–state spin S on N [200, 195], the results for electron densities well below quarter–filling show no irregularities. Instead, our results seem to be qualitatively independent of N. So we always found the ground–state momentum to be $\vec{K} = (0,0)$ for N_e even, or to be equal to the wave-vector next to the origin of the Brillouin zone, if N_e is odd. The ground state for $N_e = 6$ electrons has spin $S = 2 = S_{max} - 1$ for all unit cells considered. This can be understood in terms of a degenerate open shell in $\vec{K}$–space (cf. Tab. I in Ref. [230]).

Ground state for the $U=\infty$ model ($N=18$)				
N_h	$\vec{K}$	IR/G	S	$E(N_h)$
1	(0,0)	A_1/C_{4v}	$\frac{17}{2}$	-4.000 000
2	(0,0)	A_1/C_{4v}	0	-6.613 382
3	$(\frac{\pi}{3},\frac{\pi}{3})$	A'/C_s	$\frac{1}{2}$	-8.885 234
4	(0,0)	A_1/C_{4v}	0	-11.174 222
5	$(\frac{2\pi}{3},0)$	A''/C_s	$\frac{3}{2}$	-13.082 963
6	(π,π)	B_1/C_{4v}	1	-14.507 345
7	$(0,0)$	B_1/C_{4v}	$\frac{5}{2}$	-15.400 480
8	(0,0)	A_2/C_{4v}	4	-16.196 909
9	$(0,0)$	A_2/C_{4v}	$\frac{9}{2}$	-16.000 000
10	(0,0)	B_2/C_{4v}	0	-15.594 873
11	$(\frac{\pi}{3},\frac{\pi}{3})$	A''/C_s	$\frac{3}{2}$	-14.898 537
12	(0,0)	B_1/C_{4v}	2	-14.227 499
13	$(\frac{\pi}{3},\frac{\pi}{3})$	A''/C_s	$\frac{3}{2}$	-12.627 526
14	(0,0)	B_2/C_{4v}	0	-11.040 411
15	$(\frac{\pi}{3},\frac{\pi}{3})$	A'/C_s	$\frac{1}{2}$	-9.312 771
16	(0,0)	A_1/C_{4v}	0	-7.621 233
17	(0,0)	A_1/C_{4v}	$\frac{1}{2}$	-4.000 000

N	N_e	$\vec{K}$	IR/G	S	$E(N_e)$
20	2	$(0,0)$	A/C_4	0	-7.669 352
	3	$(\frac{2\pi}{5},\frac{\pi}{5})$	A/C_1	$\frac{1}{2}$	-9.620 288
	4	$(0,0)$	A/C_4	0	-11.596 329
	5	$(\frac{2\pi}{5},\frac{\pi}{5})$	A/C_1	$\frac{3}{2}$	-13.452 887
	6	$(0,0)$	B/C_4	2	-15.306 195
26	2	$(0,0)$	A/C_4	0	-7.762 484
	3	$(\frac{5\pi}{13},\frac{\pi}{13})$	A/C_1	$\frac{1}{2}$	-10.193 664
	4	$(0,0)$	B/C_4	0	-12.639 619
	5	$(\frac{5\pi}{13},\frac{\pi}{13})$	A/C_1	$\frac{3}{2}$	-14.996 089
	6	$(0,0)$	B/C_4	2	-17.342 315
32	2	$(0,0)$	A_1/C_{4v}	0	-7.814 563
	3	$(\frac{\pi}{4},\frac{\pi}{4})$	A'/C_s	$\frac{1}{2}$	-10.473 791
	4	$(0,0)$	B_2/C_{4v}	0	-13.152 254
	5	$(\frac{\pi}{4},\frac{\pi}{4})$	A''/C_s	$\frac{3}{2}$	-15.747 620
	6	$(0,0)$	$?\ /C_{4v}$	2	-18.347 940
36	2	$(0,0)$	A_1/C_{4v}	0	-7.840 549
	3	$(\frac{\pi}{3},0)$	A'/C_s	$\frac{1}{2}$	-10.687 410
	4	$(0,0)$	B_1/C_{4v}	0	-13.564 175
	5	$(\frac{\pi}{3},0)$	A''/C_s	$\frac{3}{2}$	-16.338 702
	6	$(0,0)$	$?\ /C_{4v}$	2	-19.127 690

Table 3.6: Energy $E(N_h)$ ($E(N_e)$) and symmetry classification ($\vec{K}$, IR/$G(\vec{K})$, and S) of the ground state, as a function of hole number, for the $U=\infty$ Hubbard model on the $\sqrt{18} \times \sqrt{18}$ lattice (left Table [200]) as well as, in the low–density limit, on the N=20–, 26–, 32–, and 36–site lattices (right Table [202]).

3.1.5 Pairing and phase separation [198, 200, 202]

Hole binding

Of special interest is the question whether there is hole binding or clustering. To comment on this problem we have computed the binding energies of various numbers of holes defined by

$$\begin{aligned} E_B^2 &= E(2)+E(0)-2E(1)\,, \\ E_B^3 &= E(3)+E(0)-E(2)-E(1)\,, \\ E_B^4 &= E(4)+E(0)-2E(2)\,, \\ E_B^6 &= E(6)+E(0)-E(4)-E(2)\,, \end{aligned} \tag{3.9}$$

where we chose those decompositions that maximize $E_B^{N_h}$ and therefore give the highest probability for the specific 'dissociation channel'. If N_h holes minimize their energy by forming a bound state, then $E_B^{N_h}$ becomes negative. Intuitively, it is clear that bound states of at last two holes will be formed in an otherwise undoped AFM at very large values of J/t, where binding originates from the 'minimization of the number of broken AFM links' [7]. Certainly, this crude argument is incorrect at small J/t and a careful analysis shows, for example, that two holes with antiparallel spins do not bind together at large U/t [222].

The various binding energies for the pure t–J model on the 18–site square lattice are depicted in Fig. 3.7 as a function of J/t. As mentioned previously [214, 241], there exists a parameter range ($10 \le U/t \le 40$) within which E_B^2 is negative but $E_B^{N_h}$, ($N_h > 2$), are positive.[11] This gives evidence for hole pairing but not for hole clustering. It should be stressed that the binding energy for two holes for the 18– and 20–site clusters in this parameter regime is more negative than the one for the smaller 16–site system [200]. The same is true for the t–t₃–J model [199, 205] (cf. Table 3.7). From an educated extrapolation of Green's–function

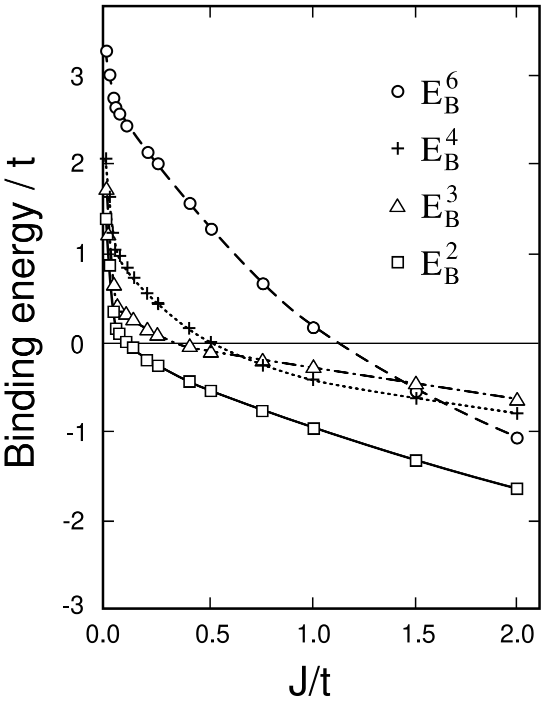

Figure 3.7: 'Binding energies' $E_B^{N_h}$ for N_h = 2 (□), 3 (△),4 (+), and 6(○) holes added to the half–filled band are depicted for the t–J model *vs* exchange interaction J for the 18–site lattice.

---

[11] Of course, $E_B^{N_h}$ should vanish in the thermodynamic limit ($N \to \infty$) if the holes do not form a bound state (independent holes). On a finite cluster, however, $E_B^{N_h}$ can be positive due to hole repulsion [7].

Monte Carlo results on 8×8 clusters [244] it was suggested that binding of two holes starts at $J/t \sim 0.3$, in good agreement with our ED data (cf. Fig. 3.7). Whether these results allow for the conclusion that there is pairing in the infinite system remains still controversial. As can be seen from Table 3.7, hole binding or clustering is weakened and finally lifted if we include long–range Coulomb forces like the $\mathcal{H}_4$ term into our Hamiltonian (3.1) [198, 205]. Figure 3.7 indicates that the parameter ranges ($J > t$) within which the finite–size results may be consistent with hole clustering are outside the regime of validity of the strong–coupling expansion. Therefore we did not use the $\mathcal{H}_3$–term for these studies.

t–t$_3$–J–V		E_B^2				E_B^3		E_B^4	
U	$(V_{NN};V_{NNN})$	N=10	N=16	N=18	N=20	N=16	N=18	N=16	N=18
10	(0;0)	-0.471	-0.273	-0.483	-0.427	0.126	0.132	0.493	0.627
	(1;0)	-0.108	-0.028	-0.302	-0.264	0.462	0.424	1.133	1.243
	$(1;1/\sqrt{2})$	0.247	0.180	-0.123	-0.102	0.837	0.739	1.860	1.920
20	(0;0)	-0.251	-0.132	-0.203	-0.181	0.305	0.260	0.757	0.832
	(1;0)	0.062	0.068	-0.053	-0.052	0.604	0.549	1.413	1.459
	$(1;1/\sqrt{2})$	0.418	0.266	0.103	0.083	0.969	0.873	2.133	2.167

Table 3.7: Binding energies $E_B^{N_h}$ of N_h=2, 3, and 4 holes in the t–t$_3$–J–V model.

Phase separation in the 2D t–J–(V) model

We now proceed to the problem of phase separation. If the exchange interaction J/t is large enough, it is widely believed that the ground state of the t–J model becomes phase separated into a hole–rich phase and an antiferromagnetically ordered region without holes [231, 78, 198, 245, 246]. Raising J above the critical value J_{PS}, the hole–rich state contains no more electrons, and the whole system becomes fully phase separated. Alternatively, in terms of electrons, phase separation could be pictured in such a way that starting from a dilute electron gas and increasing the electron density (at fixed t, J (U), V), an antiferromagnetic solid with fixed density (one electron per site) condenses out [247]. Let us recall some important previous results concerning this subject for the t–J model first.

The 1D t–J model has been examined extensively with QMC simulations [248] and Lanczos diagonalizations up to 16 sites [249] in the whole parameter range of J, yielding the result that the transition line for phase separation depends sensibly on the degree of doping δ. Thus, in the limit $\delta \to 0$, the critical value for the occurrence of (incomplete) phase separation is $J_c(\delta) = 3.5$, whereas the fully phase separated state is obtained for $J > J_{PS} \equiv J_c(\delta = 1) = 2.5$ [249]. Let us emphasize that now δ denotes the hole concentration of the *hole–rich* phase. Yokoyama and Ogata [250] found $J_{PS} = 3.3$ with a Gutzwiller–Jastrow variational wave function.

In the 2D t–J model the situation is less clear today. Within a semiclassical theory Marder *et al.* [245] found that the fully phase separated state appears for $J > J_{PS} = 4$. This value corresponds reasonably well with the result $J_{PS} = 3.8$, obtained by Puttika *et al* [246] by means of a high–temperature expansion. Emery *et al.* [78] found a slightly smaller value of $J_{PS} = 3.5$ from their Lanczos calculations on a 4×4 cluster. The main difference to the 1D case is the curvature of the critical line $J_c(\delta)$. Whereas $J_c(\delta)$ decreases with δ in 1D [246, 249], the critical value $J_c(\delta)$ increases with δ in 2D [245, 246].

Certainly, the regime of large J/t is not realized in the high–T_c compounds, and the most important question to be studied is whether phase separation exists also for *small* ratios J/t near half–filling [7]. As yet, this is a subtle and unresolved issue. Emery *et al.* [78] claimed that the t–J model shows an instability towards phase separation into hole–rich and AFM regions for *all* values of J/t and, in particular, the boundary of phase separation is suggested to converge to $J/t = 0$ as $\delta \to 0$.[12] In order to obtain the energy of such a two–phase state it is necessary to minimize the total energy of a system with N_s sites,

$$E = (N_s - N)\, e(0) + N\, e_h(\delta)\,, \tag{3.10}$$

with respect to the portions $(N_s - N)$ and N of the antiferromagnetic and the hole–rich phase. The energy per site of the hole–rich phase $e_h(\delta)$ depends only on the concentration $\delta = N_h/N$ of holes, and one has $e_h(0) = e_H$. Following [78] phase separation then exists for concentrations $\delta < \delta_m$ provided the function

$$e(\delta) = \frac{e_h(\delta) - e(0)}{\delta} \tag{3.11}$$

exhibits a minimum at $\delta = \delta_m$. Here the ground–state energy becomes a concave function of hole density δ. If one calculates the inverse isothermal compressibility per site [249],

$$\kappa^{-1} = n^2 \left[\frac{E(N_e+2) + E(N_e-2) - 2E(N_e)}{4N_e}\right], \tag{3.12}$$

we notice that κ^{-1} becomes negative for $\delta < \delta_m$ rendering the system unstabil (in finite–size systems it is favourable to compare quantities with even (odd) numbers of holes separately; see Fig. 3.8 below). An exact evaluation of Eq. (3.11) can be performed only for finite–size systems. For the t–J model $e(\delta)$ was computed by Emery *et al.* [78] using ED for the 4×4 cluster. The crucial step in such a calculation is that the energy of a finite cluster with a *finite number* of N_h holes is interpreted as the energy of the hole–rich phase with *hole concentration* $\delta = N_h/N$. The function $e(x)$ is shown in Fig. 3.8 (a) for the t–J model for various values of the exchange coupling. Obviously, we must distinguish between two regimes of the exchange coupling. In the strong–coupling regime, $J \ll t$, the minimum of $e(\delta)$ is shifted to lower concentrations raising the system size from 10, 16, 18 to 20 sites for $U = 10, 20$ (cf., Refs. [198, 199, 200]). This is due to the fact that the minimum is always connected to the two–hole ground state (provided $E_B^2 < 0$, i.e., $U/t \lesssim 50$). In this parameter range our finite–size results do *not* allow for the identification of δ_m by Emery, Kivelson, and Lin [78] as a critical concentration for the occurrence of phase separation. Moreover, the suggestion that phase separation occurs even at arbitrarily small values of J [231, 78] could not be verified from our finite–cluster study including a careful analysis of finite–size and even–odd effects [200, 198]. This result was confirmed later on by high–temperature expansions [246] as well as by quantum Monte Carlo and Lanczos studies [229]. For larger values of J, we find different behaviour. Here the minimum is more pronounced and is shifted towards $\delta = 1$ for $J \gg t$, which means towards the fully phase separated state. The possibility of hole clustering in this parameter regime is also visible in Fig. 3.7.

We would like to state that the minimum of $e(\delta)$, which is maintained in the t–t$_3$–J–V model [198], is destroyed quite rapidly by the inclusion of even a moderate interatomic Coulomb repulsion as shown in Fig. 3.8 (b) (cf. also Table 3.7), thereby restoring the homogeneity of

---

[12] Qualitative arguments for the occurrence of phase separation in the large–U Hubbard model were given earlier by Visscher [247] and by Ioffe and Larkin [251].

the system, for not too large J/t. Because E_B^3, $E_B^4 > 0$ the result of Emery *et al.* [78] that in the hole–rich phase the first instability is due to hole pairs seems reasonable in the case where phase separation is favourable.

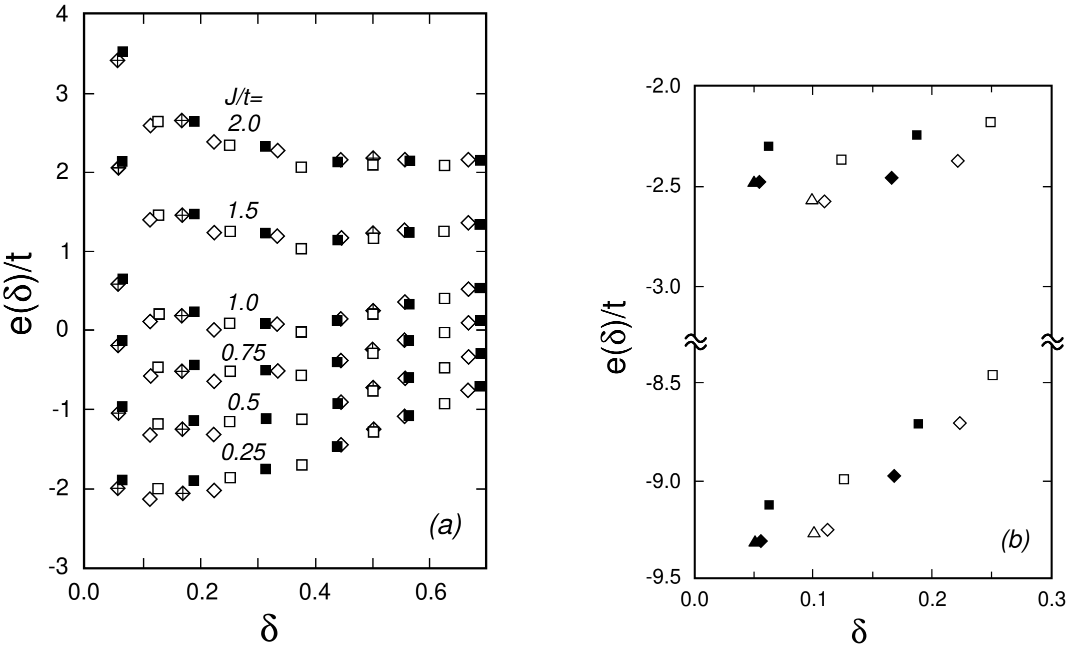

Figure 3.8: The function $e(\delta)$ (see text) is shown as a function of hole concentration δ for the t–J model (a) and the t–t$_3$–J–V model (b). The (tilted) squares and triangles denote the results for lattices with (18) 16 and 20 sites, where open (filled) symbols correspond to even (odd) numbers of holes N_h. In (b) the upper (lower) sets of data points belong to the cases $(V_{NN};V_{NNN}) = (0;0)$ and $(V_{NN};V_{NNN}) = (1;1/\sqrt{2})$, respectively.

In order to determine the transition value J_{PS}, where the system becomes fully phase separated, we used an approach which has been outlined in Refs. [201, 202]. At $J = J_{PS}$ the free energy $F(\bar{N}_e)$, given by

$$F(\bar{N}_e) = \inf_{l^-,l^+} \left[E(l^-) + \frac{E(l^+) - E(l^-)}{l^+ - l^-} (\bar{N}_e - l^-) \right] , \tag{3.13}$$

becomes a straight line as a function of the mean electron concentration $\bar{N}_e$. Therefore, we can determine $J = J_{PS}$ by setting $l^+ = N$ in Eq. (3.13) and varying the parameter J until $F(\bar{N}_e)$ shows a linear dependence on the electron density $(\bar{N}_e/N)$. Let us emphasize that the free energy in Eq. (3.13) is calculated in the limit $T \to 0$ from the related grand canonical potential $\Omega(\mu, T)$, $F(\bar{N}_e) = \Omega(\mu) + \mu\bar{N}_e$, where fluctuations of the electron number N_e are taken into account (see Sec. 3.2 below). To avoid even–odd oscillations, we separately compared our results with $l^- = 2$ and 4, and with $l^- = 3$ and 5 electrons. Thus we obtained two slightly different transition values J_{PS}^{24} and J_{PS}^{35}, respectively (see Fig. 3.9). With the exception of the 4×4 unit cell, which has been proved to be special because of its additional symmetries from an equivalence to a 2^4 hypercube, all other results clearly display an increase of J_{PS} with the size of the lattice. We tried different extrapolations of our finite–size results to the thermodynamic limit. The best agreement was found by a least–square fit to the curve $J_{PS} = b_0 + b_1/L$, with $L = \sqrt{N}$, where L is measured in units of the lattice constant. This fit results in the values $b_0 = 4.07$ (± 0.01) and $b_1 = -8.08$ (± 0.01) (see Fig. 3.9). When we fitted our data for J^{24}_{PS} (or J^{35}_{PS}) separately, the results for the critical value of the infinite system $b_0 = J_{PS}(L \to \infty) = 4.12$ (or 4.01) only changed within an error bar of ±0.1. We also tried a least–square fit to an $1/N$–dependence (yielding a smaller value for $J_{PS}(N \to \infty) \simeq 3.2$), but our data did not fit as well as for the extrapolation with $1/L$. The same $1/L$–dependence has been justified recently by Lin [231] from the prevailing $1/L$–dependence of the kinetic energy. Our final result $J_{PS} = 4.1$ (± 0.1) for the transition to the fully phase separated state is in good agreement with the previous results $J_{PS} = 3.8$ [246] and $J_{PS} = 4$ [245] for the 2D t–J model, which were obtained by completely different methods.

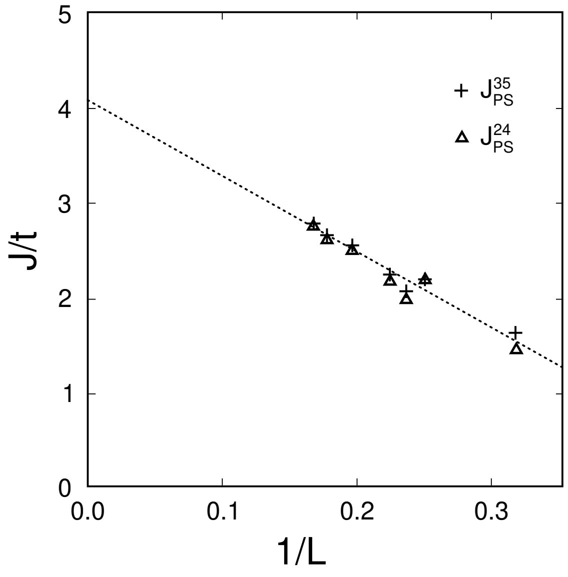

Figure 3.9: The critical exchange interaction J_{PS}, obtained for different unit cells as a function of $1/L = 1/\sqrt{N}$. For $J > J^{24}_{PS}$ ($J > J^{35}_{PS}$) we find complete phase separation according to Eq. (3.13).

3.2 Thermodynamic properties [201]

The standard (numerical) approach to the problem of studying thermodynamical properties of the Hubbard or t–J model is the Monte Carlo simulation technique based on a discrete formulation of the functional integral approach [252, 253]. Unfortunately, Monte Carlo simulations become difficult at large values of the Hubbard interaction U and cannot be extended to very low temperatures T due to the sign problem. Exact diagonalization calculations on finite lattices can, in principle, close this gap, but the computational effort increases drastically since, at finite temperatures, all or at least a considerable number of low–lying eigenvalues must be obtained. Thus ED work is restricted to fairly small systems and finite–size effects are the major difficulty of obtaining definite results for infinite systems [254]. In order to reduce the finite–size effects [255] we study the thermodynamics of the t–J model on a ten–site lattice using the *grand canonical ensemble*. Working in the grand canonical ensemble also allows for a continuous variation of the average electron density $\bar{N}_e$ even for small lattices by solving the equation $\bar{N}_e = \beta^{-1}\partial_\mu \ln \mathcal{Z}_{GC}$ for the chemical potential μ. $\mathcal{Z}_{GC}$ is the grand canonical partition function defined as

$$\mathcal{Z}_{GC} = \sum_{N_e=0}^{2N} \mathrm{e}^{\beta\mu N_e} \mathcal{Z}_C(N_e) \tag{3.14}$$

with the canonical partition function $\mathcal{Z}_C = \sum_{\vec{K},S_z} \sum_{m(\vec{K},S_z)} g_m \mathrm{e}^{-\beta E_m}$ and g_m being the degeneracy of the eigenvalue E_m.

In contrast to conventional exact diagonalization studies, where only the ground state is calculated, grand canonical thermodynamics requires the calculation of all eigenvalues for all numbers of holes. We first used as good quantum numbers S^z and $\vec{K}$ to block diagonalize the Hamiltonian. The resulting blocks were then diagonalized using an EISPACK routine. The finite–size dependence has been checked by comparing against the results of the eight–site lattice. For small hole densities, thermodynamic quantities are relatively size independent [255, 256]. When the hole concentration approaches quarter–filling, the results become more size dependent due to the small number of eigenvalues for the few–electron systems. Therefore, we restrict our calculation to electron densities larger than quarter–filling.

The chemical potential μ as a function of the electron density n is plotted in Fig. 3.10 for three different temperatures. For $J/t = 0.4$ at higher temperatures, the variation of μ with n is smooth. At very low temperatures, μ jumps at densities corresponding to integer electron numbers closely resembling the zero–temperature variation. At $J/t = 4.0$, we have a smooth curve for all temperature approaching a constant chemical potential as a function of electron density for $T = 0$ which indicates phase separation (see below). First of all this shows that the grand canonical calculation allows for a continuous variation of particle concentration for temperatures larger than the ones set by the scale of finite–size gaps (c.f., Fig. 3.10 (a)).[13] Note, however, that the finite–size dependence, which is seen as $T \to 0$ for $J/t = 0.4$, is reduced compared to the free–electron case as reported in [257]. The second point to be emphasized is that the abrupt change of n with μ for $J/t = 4.0$ as $T \to 0$ is not caused by finite–size effects because it extends over the whole concentration regime. The smaller plateau seen for $J/t = 0.4$ up to $n = 0.2$ is a different case caused by the low energy of the two–hole ground state and will disappear as the system increases [198, 200]. We have qualitative agreement with $n(\mu)$–curves obtained by Moreo *et al.* [258] for the Hubbard model using QMC on larger lattices.

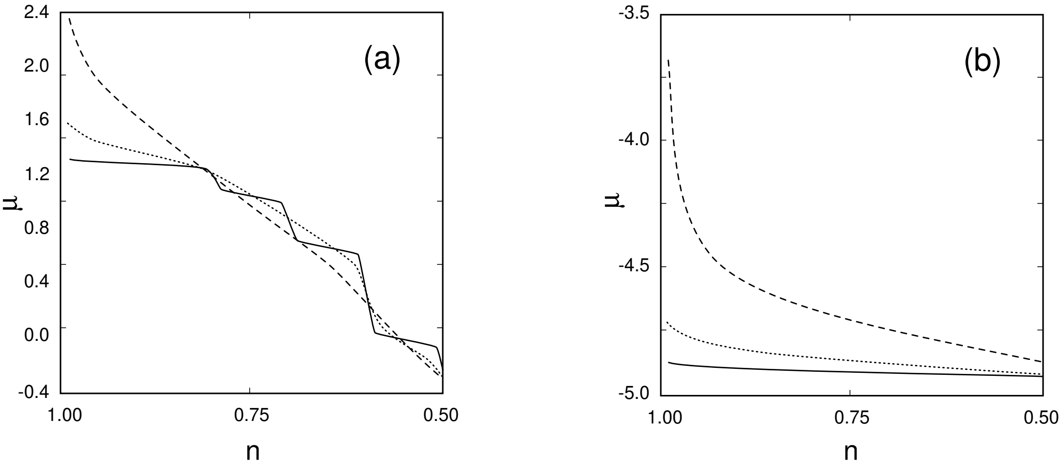

Figure 3.10: The chemical potential μ as a function of electron density n for $J/t = 0.4$ (a) and $J/t = 4.0$ (b) and $T = 0.025$ (full line), $T = 0.1$ (dotted line) and $T = 0.25$ (dashed line). All energies are measured in units of the hopping matrix element t. In this section all figures were calculated from data obtained for the ten–site lattice.

---

[13] At very low temperature there are always finite–size gaps which lead to an activated shape of the specific heat [256].

Their zero–temperature plateau corresponds to the sharp drop of μ from the Heisenberg value ($\mu_H = \infty$).

Having obtained the chemical potential for a given concentration of holes and for a given temperature, we show the specific heat per site,

$$c_v/k_B = \beta^2 \left[(\overline{H^2} - \overline{H}^2) - \frac{(\overline{HN_e} - \overline{H}\,\overline{N_e})^2}{\overline{(N_e - \overline{N_e})^2}} \right] , \tag{3.15}$$

for $J/t = 0.4$ (strong–correlation limit of the Hubbard model) and $J/t = 4.0$ (strong AFM spin interaction [211]) in Figs. 3.11 (a) and 3.11 (b). Here overbars denote averages in the grand canonical ensemble. The second part in (3.15) arises from fluctuations in the particle number which are inherent in the grand canonical approach. The qualitative peak structure remains the same apart from a rescaling of the temperature axis by $J = 4t^2/U$. It consists of two peaks: one around J/t and one around $J/4t$. The peak around J/t survives in the Heisenberg limit and, as shown in Ref. [256], is caused by spin–wave–like excitations with a renormalized coupling constant. At large J and for moderate hole doping, the height of the peak around $J/4t$ is proportional to the concentration of holes. It may be caused by the destruction of (hole) bound states, or due to local spin rearrangements [254] (of course, in the t–J model we do not see the excitations across the Mott–Hubbard gap).[14]

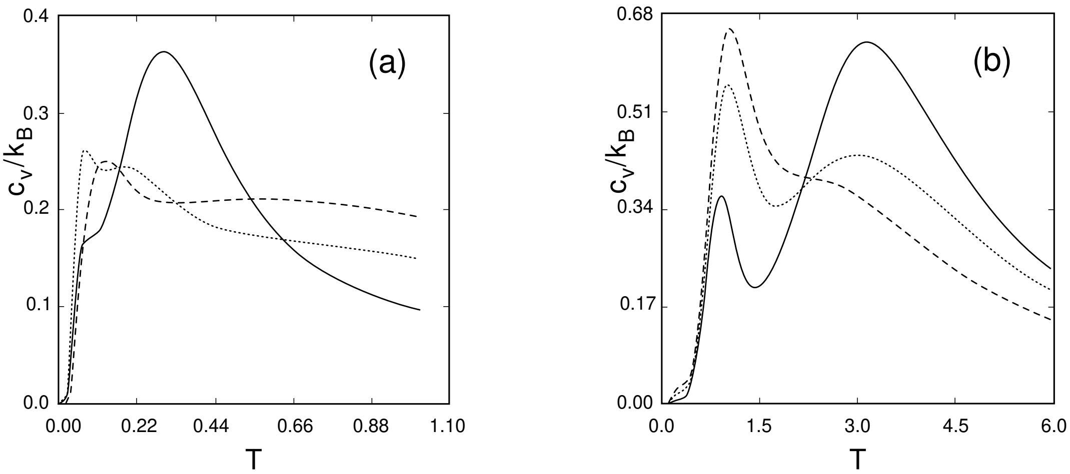

Figure 3.11: The specific heat per site as a function of temperature for $J/t = 0.4$ (a) and $J/t = 4.0$ (b) and electron densities $n = 0.95$ (full line), $n = 0.85$ (dotted line) and $n = 0.75$ (dashed line).

In the magnetic susceptibility per site we find, for $J > J_N$, a tendency towards antiferromagnetic behaviour, i.e., the paramagnetic Curie temperature Θ_D obtained by a fit to the high–temperature points is negative and decreases with increasing J (see Fig. 3.12). Here $J_N = 0.138(1)$ denotes the Nagaoka value for the ten–site cluster, i.e., for $J < J_N$ the ground state of the one–hole sector has maximal total spin S. Due to the use of the grand canonical ensemble, our data are smooth as a function of hole density and do not jump as erratically as seen in the canonical calculation of Ref. [259]. For very small values of J, smaller than the Nagaoka value, the susceptibility shows a tendency towards ferromagnetic behaviour around $0.85 < n < 0.95$, i.e., Θ_D becomes positive. Finite–size effects, however, become large, maybe

---

[14] It is not due to the term $\frac{J}{4}\tilde{n}_i\tilde{n}_j$ since we observe the same two–peak structure if we set this term to zero.

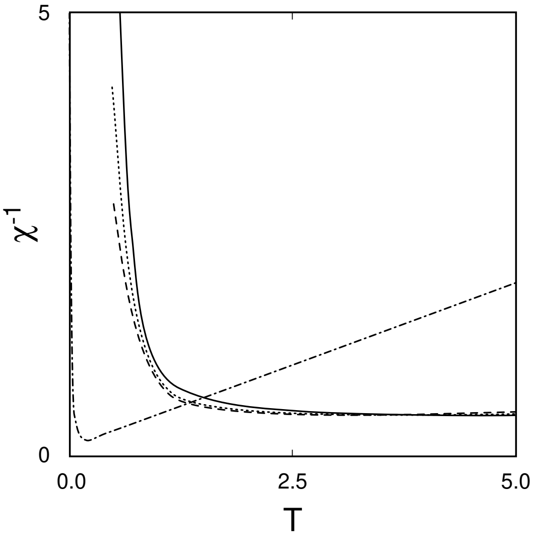

Figure 3.12: The inverse susceptibility per site as a function of temperature for $J/t = 4.0$ and electron densities $n = 0.95$ (full line), $n = 0.85$ (dotted line) and $n = 0.75$ (dashed line), and for $J/t = 0.2$ at $n = 0.95$ (dashed–dotted line).

indicating the existence of a phase of quasi–non–interacting particles like spinless fermions. Therefore we cannot decide on the existence of ferromagnetic phases apart from the one–hole Nagaoka limit.

At finite, nonzero temperature, the question of phase separation into a hole–rich and an antiferromagnetic phase arises again. It is not clear whether the phase separation observed in the t–J model at $T = 0$ extends to nonzero temperature. In a finite–size study, the results for various thermodynamic quantities may differ using the canonical or the grand canonical description.

Using the canonical ensemble, the natural extension of Emery's function $e(\delta)$ defined in the previous section is $e(\delta, T) = (f_C(\delta, T) - f_C(\delta, T))/\delta$, where f_C is the canonical free energy per site, and a minimum in $e(\delta, T)$ can be taken as an indication of phase separation at $T > 0$. At low T, we indeed find a minimum of $e(x, T)$ as a function of δ which disappears at a J–dependent temperature T_{PS}. In Fig. 3.13 we show the variation of T_{PS} with J. At $T = 0$, phase separation vanishes at the Nagaoka value J_N. Below $T_{PS}(J)$, a phase separated state gives a lower free energy value than the f_C's of the homogeneous phases. Calculating $e(\delta, T)$ with a 'grand canonical' free energy $f_{GC} = \Omega/N + \mu n$, i.e., via a Legendre transform of the grand

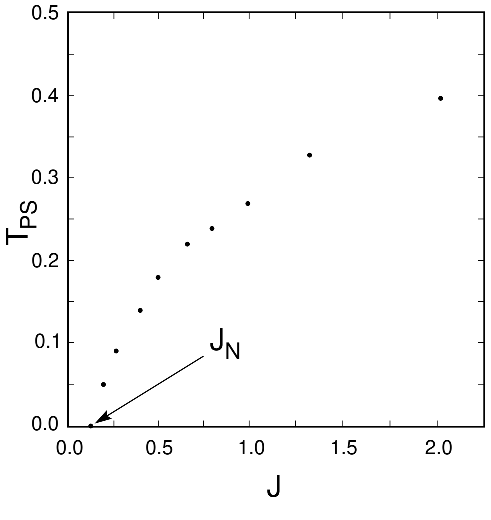

Figure 3.13: The curve $T_{PS}(J)$ as defined in the text. J_N is the Nagaoka value for the ten–site system.

canonical potential $\Omega = -\beta^{-1} \ln \mathcal{Z}_{GC}$, we do not find a minimum at any finite temperature even for $J/t = 4$. Note, however, that f_{GC} in the phase separated state is the free energy obtained from the canonical ones using the Maxwell construction. Therefore, it should be a straight line as a function of concentration. In Figs. 3.14 (a) and 3.14 (b) we show both f_C and f_{GC} for $J/t = 0.4$, 4 and at low temperatures. For $J/t = 0.4$, we see the instability of f_C due to the two–hole state. f_{GC} is just convex, which shows that there is no phase separation. For $J/t = 4$, f_C is concave and therefore unstable, whereas f_{GC} is nearly a straight line over the whole concentration axis. Here we discuss the free energy to show the dependence on the mean electron density. The related grand canonical potential as a function of μ exhibits a discontinuity in slope, which is related to the abrupt change of $n(\mu)$ (c.f., Fig. 3.10(b)). The system therefore exhibits phase separation into Heisenberg antiferromagnet and a hole–rich phase without electrons. The slight convexity of f_{GC} gives additional indication that phase separation may be unstable at any *finite* temperature.

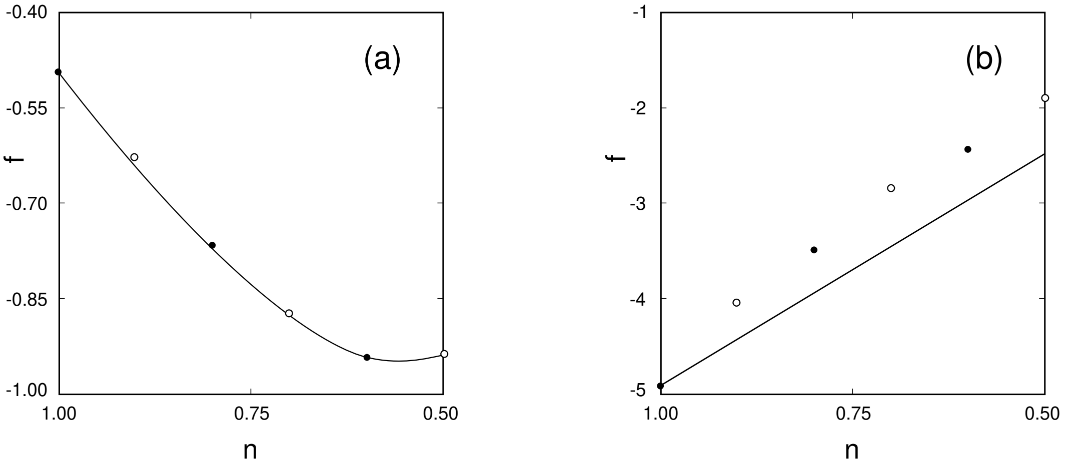

Figure 3.14: The free energy per site as a function of electron density for $J/t = 0.4$ (a), $J/t = 4.0$ (b) and $T = 0.1$. The full (open) circles are the values of f_C for even (odd) numbers of electrons; the solid line is f_{GC}.

Summarizing, we have used the grand canonical ensemble to calculate thermodynamic properties of the 2D t–J model on a ten–site lattice. This allowed us to vary the density continuously. The specific heat was shown to exhibit a double–peak structure rescaled by J. One peak could clearly be identified as being due to usual antiferromagnetic spin–wave–like excitations. Antiferromagnetic behaviour of the susceptibility was found for all concentrations apart from J smaller than the Nagaoka value. Finally, phase separation was shown to be indicated by the straight–line behaviour of f_{GC}.

Chapter 4

Slave–boson study of the 2D extended t–J model

Apart from numerical techniques, the slave–particle methods have been employed extensively in studying the effects of electron–electron correlation in the (extended) t–J model [151, 154, 260, 99, 261, 152, 165, 262, 263, 264]. For this model the two commonly used approaches, the NZA slave–boson [87, 151] and slave–fermion [154] schemes (cf. Sec. 2.4), yield quite different results concerning the (mean–field) ground–state phase diagram and the spin/charge excitations [265]. As yet, the relationship between both types of slave–field theories is not well understood. Within the NZA formulation, for example, the Hamiltonian can be solved by a mean–field approximation with the (uniform) resonating–valence–bond (RVB) order parameter. A serious difficulty of this approach is the absence of AFM correlations [154, 163], e.g., in the half–filled case, the lowest energy state, the energy of which is considerable higher than numerical estimates indicate, does not satisfy the Marshall sign rule [266] and fails to show the expected long–range Néel order [267]. On the other hand, the mean–field slave–fermion schemes [154, 261] are known to give reasonable results for the spin susceptibility as well as for the spin correlation length [265, 264], but also suffer from neglecting important correlation effects, especially the fermion charge degrees of freedom are not described sufficiently well. In contrast, the four–field SB technique (cf. Sec. 2.4), introduced by Kotliar and Ruckenstein [156] in the context of the Hubbard model, has the advantage of treating spin and charge degrees of freedom on an equal footing. Starting from the scalar KR SB representation of the Hubbard model, one may 'generate' an intersite exchange interaction via a loop expansion in the coherent–state functional integral [165]. However, the effective t–J Lagrangian, derived in this way, contains only an Ising interaction term, i.e., important spin–flip exchange processes are neglected. As we shall see below, to bosonize the complete exchange interaction term of the original t–J model, one has to use the spin–rotation–invariant extension of the KR SB theory from the beginning [158, 268].

4.1 Spin–rotation–invariant slave–boson approach to the t–t'–J model [126, 268]

4.1.1 SU(2)–invariant slave–particle representation

For the sake of definiteness, we return to the t–J Hamiltonian (2.7), that may be cast into the form

$$\mathcal{H}_{t-J} = \sum_{i,j} t_{ij}\, \tilde{\Psi}_i^{\dagger} \tilde{\Psi}_j - \frac{J}{4} \sum_{\langle ij \rangle} \left(\tilde{\Psi}_i^{\dagger} \underline{\tau}^{\mu} \tilde{\Psi}_i \right) \left(\tilde{\Psi}_j^{\dagger} \underline{\tau}_{\mu} \tilde{\Psi}_j \right) . \tag{4.1}$$

In order to bring out the $SU(2)$ symmetry of the system, we have used in (4.1) a spinor representation, where the one–row [one–column] matrices $\tilde{\Psi}_i^{\dagger} = (\tilde{\Psi}_{i\sigma}^{\dagger}, \tilde{\Psi}_{i-\sigma}^{\dagger})$ $[\tilde{\Psi}_i]$ are built up by the projected fermion creation [annihilation] operators $\tilde{\Psi}_{i\sigma}^{\dagger} \equiv \tilde{c}_{i\sigma}^{\dagger}$ $[\tilde{\Psi}_{i\sigma} \equiv \tilde{c}_i]$. $\underline{\tau}^{\mu}$ $[\underline{\tau}_{\mu}]$ denotes the kontravariant [kovariant] four–component vector $(\mu = 0, x, y, z)$ of Pauli matrices. To preserve SRI, we apply to $\mathcal{H}_{t-J}$ the manifest $[SU(2) \otimes U(1)]$ invariant SB scheme [268] based on the SRI SB approach developed for the Hubbard model by Li, Wölfle and Hirschfeld [166]. Accordingly, we define scalar boson fields $e_i^{(\dagger)}$ and bosonic matrix operators $\underline{p}_i^{(\dagger)}$ (representing empty and singly occupied sites, respectively) and pseudofermion spinor fields $\Psi_i^{(\dagger)}$ in the following way:

$$\begin{aligned} |\, 0_i \rangle &= e_i^{\dagger}\, |vac\rangle\, , \\ |\, \sigma_i \rangle &= \sum_{\rho} \Psi_{i\rho}^{\dagger} p_{i\rho\sigma}^{\dagger}\, |vac\rangle\, . \end{aligned} \tag{4.2}$$

Then the local operator constraints (2.26) becomes

$$\begin{aligned} C_i^{(1)} &= e_i^{\dagger} e_i + 2\, \mathrm{Tr}\, \underline{p}_i^{\dagger} \underline{p}_i - 1 = 0 \qquad \text{(completeness)}, \\ \underline{C}_i^{(2)} &= \Psi_i \otimes \Psi_i^{\dagger} + 2 \underline{p}_i^{\dagger} \underline{p}_i - \underline{\tau}_o = 0 \qquad \text{(1–1–correspondence)}. \end{aligned} \tag{4.3}$$

Obviously, double occupancy has been projected out. In the transformation of the fermionic spinor fields analogous to (2.27),

$$\tilde{\Psi}_i \longrightarrow \underline{z}_i \Psi_i\, , \tag{4.4}$$

the nonlinear bosonic hopping operators

$$\underline{z}_i = \underline{L}_i e_i^{\dagger} M_i \underline{p}_i \underline{N}_i\ , \tag{4.5}$$

with

$$\underline{L}_i = [\underline{\tau}_o - 2 \underline{p}_i^{\dagger} \underline{p}_i]^{-1/2}\ , \quad M_i = [1 + e_i^{\dagger} e_i + 2\, \mathrm{Tr}\, \underline{p}_i^{\dagger} \underline{p}_i]^{1/2}, \quad \underline{N}_i = [(1 - e_i^{\dagger} e_i) \underline{\tau}_o - 2 \underline{\tilde{p}}_i^{\dagger} \underline{\tilde{p}}_i]^{-1/2}\ , \tag{4.6}$$

yield a correlation–induced band renormalization. Exploiting the $SU(2) \leftrightarrow O(3)$ homomorphism, the decomposition of

$$\underline{p}_i^{(\dagger)} = \frac{1}{2} \sum_{\mu} \underline{\tau}_{\mu} p_{i\mu}^{(\dagger)} \tag{4.7}$$

into scalar (singlet) $p_o^{(\dagger)}$ and vector (triplet) $\vec{p}_i = (p_{ix}, p_{iy}, p_{iz})$ components is given as

$$\begin{aligned} p_{i\rho_1\rho_1}^{(\dagger)} &= \frac{1}{2} \left(p_{io}^{(\dagger)} + p_{iz}^{(\dagger)} \right)\ , \qquad p_{i\rho_1\rho_2}^{(\dagger)} = \frac{1}{2} \left(p_{ix}^{(\dagger)} - i p_{iy}^{(\dagger)} \right)\ , \\ p_{i\rho_2\rho_1}^{(\dagger)} &= \frac{1}{2} \left(p_{ix}^{(\dagger)} + i p_{iy}^{(\dagger)} \right)\ , \qquad p_{i\rho_2\rho_2}^{(\dagger)} = \frac{1}{2} \left(p_{io}^{(\dagger)} - p_{iz}^{(\dagger)} \right)\ . \end{aligned} \tag{4.8}$$

Here, the $p_{i\rho\rho'}$ and $p_{i\mu}$ obey the usual Bose commutation rules: $[p_{i\rho_1\rho_2}, p^\dagger_{j\rho_3\rho_4}] = \frac{1}{2}\,\delta_{ij}\,\delta_{\rho_1\rho_4}\,\delta_{\rho_2\rho_3}$ and $[p_{i\mu}, p^\dagger_{j\mu'}] = \delta_{ij}\delta_{\mu\mu'}$. Consequently, the pseudofermions $\varPsi_i = (\varPsi_{i\rho}, \varPsi_{i-\rho})^T$ satisfy anticommutation relations of the form $\{\varPsi_{i\rho}, \varPsi^\dagger_{j\rho'}\} = \delta_{ij}\,\delta_{\rho\rho'}$.

This way the interaction term is converted due to

$$\tilde{\varPsi}_i^\dagger \underline{\tau}_\mu \tilde{\varPsi}_i \longrightarrow 2\,\mathrm{Tr}\,\underline{p}_i^\dagger \underline{\tau}_\mu \underline{p}_i\,, \tag{4.9}$$

where, more explicitly, the locally defined particle number and spin operators are just

$$\begin{aligned} \tilde{n}_i &= \sum_\sigma \tilde{c}^\dagger_{i\sigma}\tilde{c}_{i\sigma} && \longrightarrow \quad \tilde{n}_i(p_{i\mu}) = 2\,\mathrm{Tr}\,\underline{p}_i^\dagger \underline{p}_i = \sum_\mu p^\dagger_{i\mu} p_{i\mu}\,, \\ \vec{S}_i &= \frac{1}{2}\sum_{\sigma\sigma'} \tilde{c}^\dagger_{i\sigma}\vec{\tau}_{\sigma\sigma'}\tilde{c}_{i\sigma'} && \longrightarrow \quad \vec{S}_i(p_{i\mu}) = \mathrm{Tr}\,\underline{p}_i^\dagger \vec{\underline{\tau}}\,\underline{p}_i = \frac{1}{2}\left(p^\dagger_{io}\vec{p}_i + \vec{p}_i^{\,\dagger} p_{io} - i\,\vec{p}_i^{\,\dagger} \times \vec{p}_i\right)\,. \end{aligned} \tag{4.10}$$

Actually, the components of the bosonized SB spin operator act as generators of rotations in spin space, i.e., $\vec{S}_i(p_{i\mu})$ satisfies the spin algebra. Since $C_i^{(1)}$ and $\underline{C}_i^{(2)}$ commute with the SB t–J Hamiltonian, the constraints (4.3) can be ensured by introducing the *time–independent* Lagrange multipliers $\lambda_i^{(1)}$ and $\underline{\lambda}_i^{(2)} = \sum_\mu \underline{\tau}_\mu \lambda^{(2)}_{i\mu}$. As a consequence, the Hamiltonian of the t–J model (4.1) in terms of the slave–boson and pseudofermion operators has to be replaced by[1]

$$\mathcal{H}^{SB}_{t-J} = \sum_{i,j} t_{ij}\varPsi_i^\dagger \underline{z}_i^\dagger \underline{z}_j \varPsi_j - J\sum_{\langle ij\rangle}\left(\mathrm{Tr}\,\underline{p}_i^\dagger \underline{\tau}^\mu \underline{p}_i\right)\left(\mathrm{Tr}\,\underline{p}_j^\dagger \underline{\tau}_\mu \underline{p}_j\right) + \sum_i (\lambda_i^{(1)} C_i^{(1)} + \mathrm{Tr}\,\underline{\lambda}_i^{(2)} \underline{C}_i^{(2)})\,. \tag{4.11}$$

In the physical subspace, $\mathcal{H}^{SB}_{t-J}$ posses the same matrix elements for the basis states (4.2) as the original t–J Hamiltonian (4.1) for the purely fermionic states. To verify this directly, special attention has to be paid to the bosonization of AFM exchange interaction term,

$$\left(\tilde{\varPsi}_i^\dagger \underline{\tau}^\mu \tilde{\varPsi}_i\right)\left(\tilde{\varPsi}_j^\dagger \underline{\tau}_\mu \tilde{\varPsi}_j\right) = 2\sum_\sigma \left(\tilde{c}^\dagger_{i\sigma}\tilde{c}^\dagger_{j-\sigma}\tilde{c}_{j\sigma}\tilde{c}_{i-\sigma} - \tilde{c}^\dagger_{i\sigma}\tilde{c}^\dagger_{j-\sigma}\tilde{c}_{j-\sigma}\tilde{c}_{i\sigma}\right), \tag{4.12}$$

which includes besides the Ising exchange contributions ($|\downarrow_i\,\uparrow_j\rangle \leftrightarrow |\downarrow_i\,\uparrow_j\rangle$) the spin–flip processes ($|\downarrow_i\,\uparrow_j\rangle \leftrightarrow |\uparrow_i\,\downarrow_j\rangle$). Let us emphasize that the matrix elements of the spin–flip terms are *not* reproduced in the scalar KR SB approach [165]. By contrast, within the SRI SB approach it is a straightforward exercise to show that these contributions can be expressed in terms of the $p^{(\dagger)}_{i\rho\rho'}$:

$$\sum_{\rho\rho'} p^\dagger_{i\rho\sigma}\, p^\dagger_{j\rho'-\sigma}\, p_{j\sigma\rho'}\, p_{i-\sigma\rho}\,|-\sigma_i\;\sigma_j\rangle = \frac{1}{4}\,|\sigma_i\;-\sigma_j\rangle\,. \tag{4.13}$$

Thus our SRI SB scheme (4.2)–(4.11) provides a consistent bosonization of the t–J model.

4.1.2 Functional–integral formulation

We pass now to the functional–integral representation of the redefined Hamiltonian (4.11). Using (2.30) and (2.31), the grand canonical partition function of the constrained system can be written as an imaginary time path integral (cf. Sec. 2.4)

$$\mathcal{Z} = \int \mathcal{D}[\bar{\varPsi}_\rho, \varPsi_\rho]\,\mathcal{D}[e^*, e]\,\mathcal{D}[p^*_\mu, p_\mu]\,d[\lambda^{(1)}]\,d[\lambda^{(2)}_\mu]\,e^{-\int_0^\beta d\tau\,\mathcal{L}(\tau)}\,, \tag{4.14}$$

---

[1] Note that additional constraints do not exist. Especially, if the constraint $\vec{p}_i \times \vec{p}_i = 0$ is added [269], the spin algebra is not satisfied.

with the Lagrangian

$$\begin{aligned}\mathcal{L}(\tau) &= \sum_i \left\{ e_i^* \left(\partial_\tau + \lambda_i^{(1)}\right) e_i + 2\,\mathrm{Tr}\,\underline{p}_i^{*T} \left((\partial_\tau + \lambda_i^{(1)})\underline{\tau}_o - \underline{\lambda}_i^{(2)^T} \right) \underline{p}_i^{\,T} - \lambda_i^{(1)} \right\} + \\ &\quad + J \sum_{\langle ij \rangle} \left(\mathrm{Tr}\,\underline{p}_i^* \vec{\underline{\tau}} \underline{p}_i \cdot \mathrm{Tr}\,\underline{p}_j^* \vec{\underline{\tau}} \underline{p}_j - \ \mathrm{Tr}\,\underline{p}_i^* \underline{p}_i \,\mathrm{Tr}\,\underline{p}_j^* \underline{p}_j \right) \\ &\quad + \sum_i \bar{\Psi}_i \left((\partial_\tau - \mu)\underline{\tau}_o + \underline{\lambda}_i^{(2)} \right) \Psi_i + \sum_{i,j} t_{ij} \bar{\Psi}_i \underline{z}_i^* \underline{z}_j \Psi_j \,. \end{aligned} \tag{4.15}$$

Apart from the above symmetry considerations the SB functional–integral formalism reveals additional global and local gauge invariances [176, 158, 182]. The action $\mathcal{S} = \int_0^\beta d\tau \mathcal{L}(\tau)$ is invariant under the following site– and time–dependent phase transformations $(\theta_i(\tau)\ \underline{\chi}_i(\tau))$, i.e., under the local symmetry group $SU(2) \otimes U(1)$,

$$\begin{aligned}\Psi_i &\rightarrow e^{-i\theta_i}\, e^{i\underline{\chi}_i}\, \Psi_i \,, \\ e_i &\rightarrow e_i\, e^{-i\theta_i} \,, \\ \underline{p}_i &\rightarrow \underline{p}_i\, e^{-i\underline{\chi}_i} \,, \end{aligned} \tag{4.16}$$

provided that the (five) Lagrange parameters act as *time–dependent* gauge fields, $\lambda_i^{(1)}(\tau)$ and $\underline{\lambda}_i^{(2)}(\tau)$, absorbing the time derivatives of the phase factors:

$$\begin{aligned}\lambda_i^{(1)} &\rightarrow \lambda_i^{(1)} + i\dot{\theta}_i \,, \\ \underline{\lambda}_i^{(2)} &\rightarrow e^{i\underline{\chi}_i}\, \underline{\lambda}_i^{(2)}\, e^{-i\underline{\chi}_i} - i\dot{\underline{\chi}}_i + i\dot{\theta}_i \underline{\tau}_o \,. \end{aligned} \tag{4.17}$$

Next, in the continuum limit, the radial gauge is introduced by representing the Bose fields by modulus and phase,

$$\begin{aligned} e_i &= |e_i| e^{i\varphi(e_i)} \,, \\ \underline{p}_i &= \frac{1}{2} \sum_\mu \underline{\tau}_\mu |p_{i\mu}| e^{i\underline{\phi}(\underline{p}_i)} \,, \end{aligned} \tag{4.18}$$

at each lattice site i and for any imaginary time (for a time–discretized version of this gauge fixing, see [182]). Exploiting the gauge freedom of the action, we can now fix the five real–valued coefficients $\theta_i(\tau)$, $\chi_{i\mu}(\tau)$ to remove five phases $(\varphi_i(\tau),\ \phi_{i\mu}(\tau))$ of the Bose fields e_i, $p_{i\mu}$ in the radial gauge. As a consequence *all* the Bose fields $\{e_i,\, p_{i\mu}\}$ become *real*, in contrast to the Hubbard model, where one SB field remains complex (cf. Sec. 2.4). At this point one should notice that the particle number and spin operators are changed into

$$\begin{aligned} \tilde{n}_i(p_{i\mu}) &= \sum_\mu p_{i\mu}^2 \,, \\ \vec{S}_i(p_{i\mu}) &= p_{io} \vec{p}_i \end{aligned} \tag{4.19}$$

(the previous notations e_i, p_{io} and $\vec{p}_i$ now denote the radial parts of the corresponding Bose fields). Then, using the familiar identity for Gaussian integrals over Grassmann fields [171],

$$\int \mathcal{D}[\bar{\Psi}_\rho, \Psi_\rho]\, e^{-\sum \bar{\Psi}_\rho [-G^{-1}]_{\rho\rho'} \Psi_\rho} = e^{\,\mathrm{Tr} \ln [-\underline{G}^{-1}]} \,, \tag{4.20}$$

the fermionic degrees of freedom can be integrated out, and we obtain the following exact representation of the grand canonical partition function

$$\mathcal{Z} = \int \mathcal{D}[\Phi]\, e^{-\mathcal{S}_{eff}} \tag{4.21}$$

in terms of the real–valued bosonic fields $\phi_{i\alpha}$ $(\alpha = 1...10)$:

$$\Phi_i(\tau) = (\{\phi_{i\alpha}(\tau)\}) = (e_i, p_{io}, \lambda_{io}^{(2)}, \lambda_i^{(1)}; p_{ix}, \lambda_{ix}^{(2)}; p_{iy}, \lambda_{iy}^{(2)}; p_{iz}, \lambda_{iz}^{(2)}) \,. \tag{4.22}$$

In Eq. (4.21), the Bose fields e_i, p_{io} and $\vec{p}_i$ are integrated like radial parts of complex fields from 0 to ∞, whereas the gauge fields $\lambda_i^{(1)}$ and $\lambda_{i\mu}^{(2)} = (\lambda_{io}^{(2)}, \vec{\lambda}_i^{(2)})$ have to be integrated parallel to the imaginary axis (cf. Eq. (2.31)). The effective bosonic action $\mathcal{S}_{eff}$ takes the form

$$\begin{aligned} \mathcal{S}_{eff} \;\; = \;\; & \int\limits_0^\beta d\tau \Big\{ \sum_i \Big[\lambda_i^{(1)} e_i^2 + \sum_\mu \left(\lambda_i^{(1)} - \lambda_{io}^{(2)} \right) p_{i\mu}^2 - 2 p_{io} \vec{p}_i \cdot \vec{\lambda}_i^{(2)} - \lambda_i^{(1)} \Big] \\ & + J \sum_{\langle ij \rangle} \Big[p_{io} \vec{p}_i \cdot \vec{p}_j p_{jo} - \frac{1}{4} \left(p_{io}^2 + \vec{p}_i^{\,2} \right) \left(p_{jo}^2 + \vec{p}_j^{\,2} \right) \Big] \Big\} \\ & - \mathrm{Tr}_{ij,\rho\rho',\tau\tau'} \, \ln \Big[- G_{ij,\rho\rho'}^{-1}(\tau,\tau') \Big] \,, \end{aligned} \tag{4.23}$$

where the (inverse) SB Green propagator is given by

$$G_{ij,\rho\rho'}^{-1}(\tau,\tau') = \Big[\left(-\partial_\tau + \mu - \lambda_{io}^{(2)} \right) \delta_{\rho\rho'} - \vec{\lambda}_i^{(2)} \cdot \vec{\tau}_{\rho\rho'} \Big] \delta_{ij} \, \delta(\tau - \tau') \; - \; t_{ij} \, (\underline{z}_i^\dagger \underline{z}_j)_{\rho\rho',\tau\tau'} (1 - \delta_{ij}) \,. \tag{4.24}$$

It may be remarked that since the bosons $e_i(\tau)$ and $p_{i\mu}(\tau)$ are taken to be real, their kinetic terms, being proportional to the time derivatives in Eq. (4.15), drop out due to the periodic boundary conditions imposed on Bose fields $(\phi_{i\alpha}(\beta) = \phi_{i\alpha}(0))$. Strictly speaking it follows from this property that *all* the Bose fields do no longer have dynamics of their own [158].

4.2 Saddle–point approximation

Using the formalism, developed so far, in the simplest approximation one can investigate the saddle–point solutions of the partition function as a starting point of a loop expansion of the collective action. Mean–field approximations to the functional integral are achieved by replacing the bosonic fields by their time–averaged values [168]. For the Hubbard model, a comparison of the paramagnetic and antiferromagnetic SB solutions with QMC results shows that such a mean–field like approach yields an excellent quantitative agreement for local observables [180] and therefore can give a qualitative correct picture with relatively little effort. Within the framework of the SRI SB representation it is possible to study, besides the simple uniform or (π, π)–ordered states, broken–symmetry mean–field solutions with more complicated spin structures like incommensurate spiral magnetic order. Along this line, the magnetic properties and, in particular, the magnetic ground–state phase diagram of the Hubbard model have been under intense investigation [167, 270, 168, 271, 272]. In this section, we report on our analytical and numerical results concerning the ground–state properties of the t–t'–J model [126, 268].

4.2.1 Incommensurate magnetic order

The evaluation of (4.23) proceeds via the saddle–point expansion, where at the first level of approximation we look for an extremum $\overline{\mathcal{S}}(\overline{\Phi}_i)$ of the bosonized action $\mathcal{S}_{eff}$ with respect to the Bose and Lagrange multiplier fields $\phi_{i\alpha}$:

$$\frac{\partial \mathcal{S}_{eff}}{\partial \phi_{i\alpha}} \overset{!}{=} 0 \quad \Longrightarrow \quad \overline{\mathcal{S}} = \mathcal{S}_{eff} \Big|_{\Phi_i = \overline{\Phi}_i} \,. \tag{4.25}$$

The physically relevant saddle–point $\overline{\Phi}_i$ is determined to give the lowest *free energy* (per site)

$$\overline{f}_{t-J} = \overline{\Omega}/N + \mu n\,, \tag{4.26}$$

where at given mean electron density n, the chemical potential μ is fixed by the requirement

$$n = -\frac{1}{N}\frac{\partial\overline{\Omega}}{\partial\mu} \tag{4.27}$$

($\overline{\Omega} = \overline{\mathcal{S}}/\beta$ denotes the grand canonical potential). Obviously, an unrestricted minimization of the free–energy functional is impossible for an infinite system. To keep the problem tractable, we use the ansatz

$$\vec{m}_i = m\vec{u}_i\,, \qquad \vec{u}_i = (\cos\vec{Q}\vec{R}_i, \sin\vec{Q}\vec{R}_i, 0) \tag{4.28}$$

for the local magnetization $\vec{m}_i = -2\vec{S}_i = -2p_{io}\vec{p}_i$. Following earlier analyses of spiral states for the Hubbard model [167, 270, 273] the unit vector $\vec{u}_i$ is chosen as a local spin quantization axis pointing in opposite directions on different sublattices. Thereby, the 'order parameter' wave–vector $\vec{Q}$ is introduced as a new 'variational' parameter to describe several magnetic ordered states: PM, FM ($\vec{Q} = 0$), AFM ($\vec{Q} = (\pi,\pi)$), and incommensurate (1,1)–spiral ($\vec{Q} = (Q,Q)$), $(1,\pi)$–spiral ($\vec{Q} = (Q,\pi)$) and (0,1)–spiral ($\vec{Q} = (0,Q)$) states (see Fig. 4.1). Note that since fluctuations of the charge density are not incorporated, the scalar Bose fields are homogeneous: $e_i = e$, $p_{io} = p_o$, $\lambda_i^{(1)} = \lambda^{(1)}$, and $\lambda_{io}^{(2)} = \lambda_o^{(2)}$. The vector fields exhibit the same spatial variation as the magnetization: $\vec{p}_i = p\vec{u}_i$ and $\vec{\lambda}_i^{(2)} = \lambda^{(2)}\vec{u}_i$. Then, transforming (4.23) in the $(\vec{k},\omega_n)$–representation,[2] the trace in $\mathcal{S}_{eff}$ can be easily performed to give the free–energy functional

$$\begin{aligned} f_{t-J} &= \lambda^{(1)}\left(e^2 + p_o^2 + p^2 - 1\right) - \lambda_o^{(2)}\left(p_o^2 + p^2\right) - 2\lambda^{(2)}p_o p + \mu n \\ &\quad + J\left[p_o^2p^2\left(\cos Q_x + \cos Q_y\right) - \frac{1}{2}\left(p_o^2 + p^2\right)^2\right] + \frac{1}{\beta N}\sum_{\vec{k}\nu}\ln\left[1 - n_{\vec{k}\nu}\right], \end{aligned} \tag{4.29}$$

where

$$n_{\vec{k}\nu} = \left[\exp\{\beta(E_{\vec{k}\nu} - \mu)\} + 1\right]^{-1} \tag{4.30}$$

holds with the renormalized single–particle energies ($\nu = \pm$)

$$\begin{aligned} E_{\vec{k}\nu} &= \frac{1}{2}(z_+^2 + z_-^2)(\varepsilon_{\vec{k}} + \varepsilon_{\vec{k}-\vec{Q}}) + \lambda_o^{(2)} \\ &\quad + \nu\frac{1}{2}\left[(z_+^2 - z_-^2)^2(\varepsilon_{\vec{k}} - \varepsilon_{\vec{k}-\vec{Q}})^2 + 4(z_+z_-(\varepsilon_{\vec{k}} + \varepsilon_{\vec{k}-\vec{Q}}) + \lambda^{(2)})^2\right]^{1/2}. \end{aligned} \tag{4.31}$$

Here, $\varepsilon_{\vec{k}} = \frac{1}{N}\sum_{\vec{R}_i-\vec{R}_j} t_{ij}\, e^{i\vec{k}(\vec{R}_i-\vec{R}_j)}$, and the $z_\pm = z_1 \pm z_2$ are obtained from the eigenvalues of the bosonic hopping operator $\underline{z}$ by diagonalizing the kinetic part. Requiring that f_{t-J} be stationary with respect to the variation of the magnetic order vector, the wave–vector $\vec{Q}$ can be obtained from the 'extremal' condition

$$\sin Q_{x,y} = \frac{1}{J\,p_o^2p^2}\,\frac{1}{N}\sum_{\vec{k}\nu} n_{\vec{k}\nu}\,\frac{\partial E_{\vec{k}\nu}}{\partial Q_{x,y}}\,. \tag{4.32}$$

---

[2] $\omega_n = 2(n+1)\pi/\beta$ [$\omega_m = 2m\pi/\beta$] denote the fermionic [bosonic] Matsubara frequencies

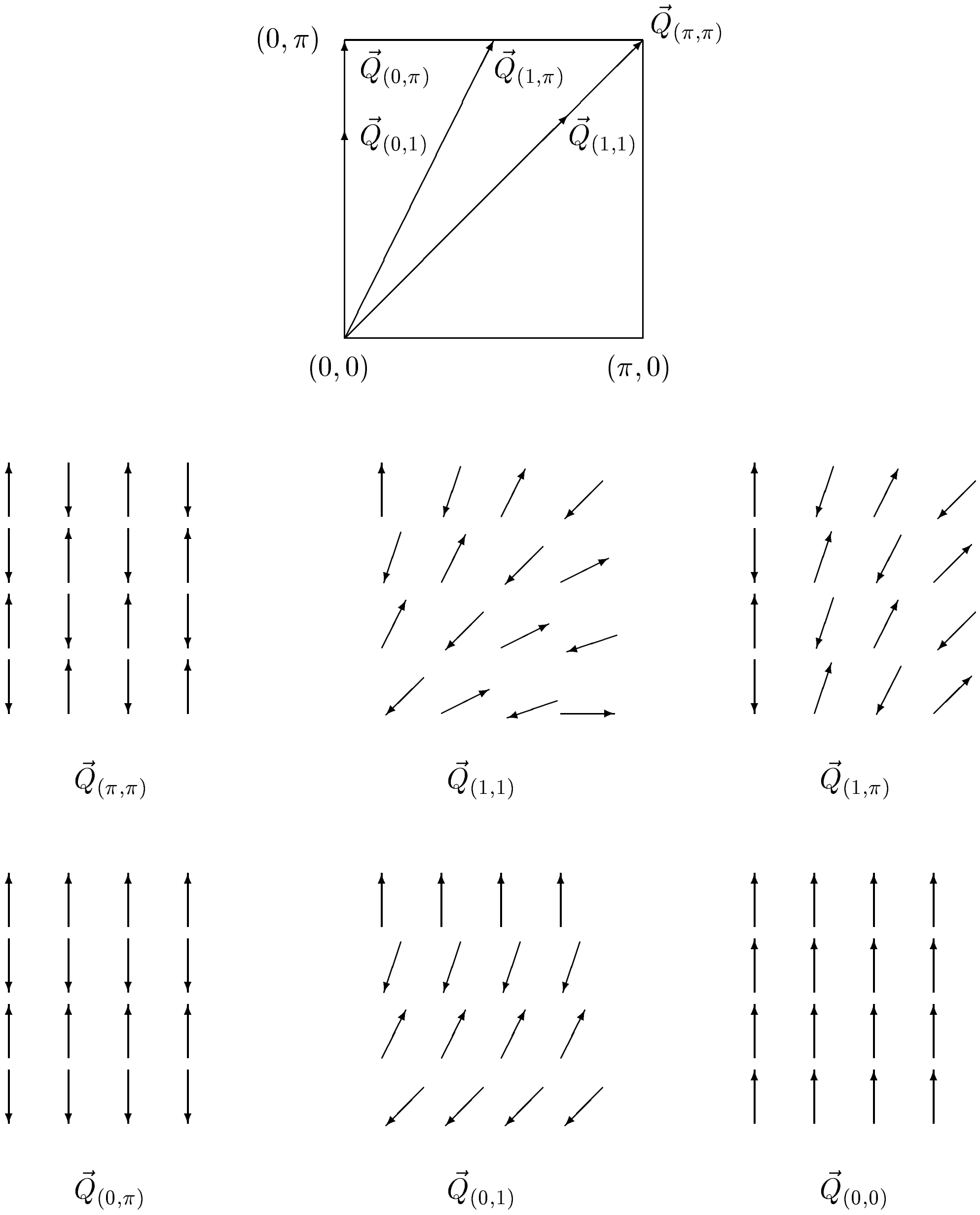

Figure 4.1: Examples of typical spiral spin patterns illustrating the nomenclature of the incommensurate magnetic wave–vectors $\vec{Q}$. For further explanation see text.

Furthermore, to determine the saddle–point values of the Bose and Lagrange multiplier fields, one has to solve the following two sets of coupled self–consistency equations:

$$\begin{aligned}
(\mathrm{I}): \qquad e^2 &= \delta = 1 - n \,, \\
p_o^2 &= \frac{n}{2} + \frac{1}{2}\sqrt{n^2 - m^2} \,, \\
p^2 &= \frac{n}{2} - \frac{1}{2}\sqrt{n^2 - m^2} \,,
\end{aligned} \tag{4.33}$$

where

$$n = \frac{1}{N}\sum_{\vec{k}\nu} n_{\vec{k}\nu} \,, \tag{4.34}$$

$$m = \frac{1}{N}\sum_{\vec{k}\nu} n_{\vec{k}\nu}\frac{\partial E_{\vec{k}\nu}}{\partial \lambda^{(2)}} \,, \tag{4.35}$$

and

$$\begin{aligned}
\text{(II):} \qquad \lambda^{(1)} &= -\frac{1}{2e}\,\frac{1}{N}\sum_{\vec{k}\nu} n_{\vec{k}\nu}\frac{\partial E_{\vec{k}\nu}}{\partial e} \,, \\
\lambda_o^{(2)} &= \frac{1}{2(p_o^2-p^2)}\left\{\frac{1}{N}\sum_{\vec{k}\nu} n_{\vec{k}\nu}\frac{\partial E_{\vec{k}\nu}}{\partial p_o}\,p_o - \frac{1}{N}\sum_{\vec{k}\nu} n_{\vec{k}\nu}\frac{\partial E_{\vec{k}\nu}}{\partial p}\,p\right\} \\
&\quad + J\left(p_o^2+p^2\right) + \lambda^{(1)} \,, \\
\lambda^{(2)} &= \frac{1}{4\,p_o\,p}\left\{\frac{1}{N}\sum_{\vec{k}\nu} n_{\vec{k}\nu}\frac{\partial E_{\vec{k}\nu}}{\partial p_o}\,p_o + \frac{1}{N}\sum_{\vec{k}\nu} n_{\vec{k}\nu}\frac{\partial E_{\vec{k}\nu}}{\partial p}\,p\right\} \\
&\quad + J\left(p_o\,p\left(\cos q_x + \cos q_y\right) - \frac{\left(p_o^2+p^2\right)^2}{2\,p_o\,p}\right) \\
&\quad + \left(\lambda^{(1)} - \lambda_o^{(2)}\right)\frac{(p_o^2+p^2)}{2\,p_o\,p} \,.
\end{aligned} \tag{4.36}$$

If one substitutes the saddle–point solutions into (4.29), the free energy is obtained as

$$\overline{f}_{t-J} = \frac{J}{4}\left[m^2\left(\cos Q_x + \cos Q_y\right) - 2n^2\right] + \lambda^{(2)}m + (\mu - \lambda_o^{(2)})n - \frac{1}{\beta N}\sum_{\vec{k}\nu}\ln\left[1 + e^{-\beta(E_{\vec{k}\nu}-\mu)}\right] \,, \tag{4.37}$$

where the quasiparticle energy $E_{\vec{k}\nu}$ takes the form

$$E_{\vec{k}\pm} = \delta(1+\delta)(\varepsilon_{\vec{k}}+\varepsilon_{\vec{k}-\vec{Q}})/y + \lambda_o^{(2)} \pm \left[\delta^2(\varepsilon_{\vec{k}}-\varepsilon_{\vec{k}-\vec{Q}})^2/y + [m(\varepsilon_{\vec{k}}+\varepsilon_{\vec{k}-\vec{Q}})/y + \lambda^{(2)}]^2\right]^{1/2} \,, \tag{4.38}$$

with $y = (1+\delta)^2 - m^2$.

In particular, at the spatially uniform paramagnetic saddle–point ($m = 0$),

$$\overline{\Phi}^{(PM)} = (e, p_o, \lambda_o^{(2)}, \lambda^{(1)}; 0, 0; 0, 0; 0, 0) \,, \tag{4.39}$$

the remaining bosonic fields

$$\begin{aligned}
e^2 &= \delta \,, \\
p_o^2 &= 1 - \delta \,, \\
\lambda^{(1)} &= -\frac{2 + 3\delta - \delta^2}{1 - \delta^2}\,\tilde{\varepsilon}(0) \,, \\
\lambda_o^{(2)} &= -\frac{2}{(1+\delta)^2}\,\tilde{\varepsilon}(0) - (1-\delta)J \,,
\end{aligned} \tag{4.40}$$

are explicitly given in terms of J, δ and a single energy parameter $\tilde{\varepsilon}(0)$ defined by

$$\tilde{\varepsilon}(\vec{q}) = \frac{2}{N}\sum_{\vec{k}} \varepsilon_{\vec{k}-\vec{q}}\,\theta(\mu - E_{\vec{k}}) \tag{4.41}$$

(at $T = 0$). Here the quasiparticle energy $E_{\vec{k}}$ is

$$E_{\vec{k}} = z^2 \varepsilon_{\vec{k}} + \lambda_o^{(2)} \,, \tag{4.42}$$

with $z^2 = 2\delta/(1+\delta)$, and μ can be determined from

$$\delta = 1 - \frac{2}{N} \sum_{\vec{k}} \theta(\mu - E_{\vec{k}}) \,. \tag{4.43}$$

Finally, in this approximation, the free energy becomes simply

$$\overline{f}_{t-J}^{(PM)} = z^2 \tilde{\varepsilon}(0) - \frac{1}{2} J (1-\delta)^2 + \mu(1-\delta) \,. \tag{4.44}$$

4.2.2 Magnetic phase diagram of the t–t'–J model

In the numerical evaluation of the self–consistency loop we proceed as follows: at given model parameters J and δ, we solve the saddle–point equations (4.35) and (4.36) for m, $\lambda^{(1)}$, $\lambda_o^{(2)}$ and $\lambda^{(2)}$ together with the integral equation (4.34) for μ using an iteration technique. Then, in an outer loop, the order parameter wave–vector $\vec{Q}$ is obtained from the extremal equation (4.32) by means of a secant method. Convergence is achieved if all quantities are determined with relative error less than 10^{-6}. Note that our numerical procedure allows for the investigation of different *metastable* symmetry broken states corresponding to *local* minima of the variational free–energy functional (4.37).

For the t–t'–J model, the transfer amplitudes t_{ij} are restricted to NN and NNN hopping processes. i.e., the bare band dispersion $\varepsilon_{\vec{k}}$, involved via $E_{\vec{k}\nu}$ in the stationary equations, takes the form

$$\varepsilon_{\vec{k}} = -2t(\cos k_x + \cos k_y) - 4t' \cos k_x \cos k_y \,. \tag{4.45}$$

As discussed in Sec. 2.3, the tight–binding parameters t and t' alone are able to reproduce the main qualitative features of the band structure and Fermi surface (FS) results for both electron– and hole–doped systems, e.g., a ratio $t'/t \simeq -0.16$ (-0.4) has been found to be appropriate for the hole–doped LSCO (YBCO) family [50, 124, 273, 125]. In the electron–doped case, the ratio t'/t is again negative, however, the signs of t and t' are reversed with respect to the hole–doped case [274]. In fact, the sign of t is of less importance because the transformation $t \to -t$ is equivalent to a phase shift of the hopping term by (π, π). If we use only positive t hereafter, the case $t' > 0$ together with a shift of the momentum $\vec{k} \to \vec{k} + (\pi, \pi)$ implies electron doping in terms of the t–t'–J model [275]. As can be seen from Fig. 4.2, this convention yields a FS shrinking around the $(0, 0)$ or Γ point ((π, π) or M point) with increasing doping in the hole–doped (electron–doped) case, which is consistent with recent ARPES measurements for YBCO [276] (NCCO [24]).

Let us first consider the case $t' = 0$, i.e., the pure t–J model. The resulting ground–state phase diagram in the J–δ plane is shown in Fig. 4.3.

For the case $\delta = 0$ (Heisenberg model), we obtain an AFM ground state. At $J = 0$, the FM is lowest in energy up to a hole concentration of 0.327, where a first–order transition to the $(1, \pi)$–spiral takes place; above $\delta = 0.39$, we find a degenerate ground state with wave–vector $(0,\pi)$. At $\delta = 0.63$ the PM is the lowest energy state (second–order transition). This coincides with the $U \to \infty$ SB results of the Hubbard model ($J = 4t^2/U$), given in [271]. The PM–FM instability occurs at $\delta_{PM-FM} = 0.33$ [177]. In contrast, the slave–fermion phase diagram [262] exhibits a much larger ferromagnetic region. This can be taken as an indication that correlation

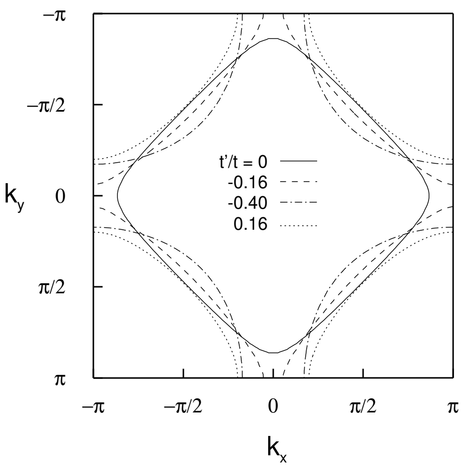

Figure 4.2: Tight–binding Fermi surfaces for the square lattice with NN (t) and NNN (t') hopping at fillings $\delta = \pm 0.1$. The curves with $t'/t = 0, -0.16, -0.4$ and $t'/t = 0.16$ correspond to hole doping ($\delta > 0$) and electron doping ($\delta < 0$), respectively.

effects are treated less accurate within the slave–fermion mean–field scheme [262, 277]. For finite exchange interaction J the (1,1)–spiral is the ground state at small doping. With increasing δ a transition to the FM takes place, which becomes unstable against the $(1,\pi)$–spiral at larger doping concentrations. For $J/t > 0.08$, we find a transition from (1,1)– to $(1,\pi)$–spirals at about $\delta \approx 0.2$. In Fig. 4.3, the dotted line separates the $(1,\pi)$–spiral state from the region, where the $(1,\pi)$– and $(0,\pi)$–states are degenerate. If we admit only homogeneous phases, the phase boundaries

$$\begin{array}{rcll} \text{(1,1)–spiral} & \leftrightarrow & (1,\pi)\text{–spiral} & \delta \approx 0.2 \\ (1,\pi)\text{–spiral} & \leftrightarrow & (1,\pi)\text{–}(0,\pi)\text{ degenerancy} & \delta \approx 0.6 \\ (1,\pi)/(0,\pi)\text{–phase} & \leftrightarrow & \text{PM} & \delta \approx 0.63 \end{array}$$

remain nearly unchanged at larger values of J. However, analyzing the thermodynamic stability of the saddle–point solutions (i.e., the curvature of $\overline{f}_{t-J}(\delta)$), one observes a tendency towards phase separation into hole–rich and AFM regions above the 'diagonal' solid curve in the left upper part of the J–δ phase diagram. This two–phase region and, more general, the problem of phase separation will be discussed in more detail below.

Figure 4.4 displays the variation of the 'extremal' spiral wave–vector $\vec{Q}$ and the corresponding amplitude of the local magnetization m as functions of doping. At $\delta = 0$, $\vec{Q} = (\pi,\pi)$ indicates the AFM order. At low doping the (1,1)–spiral order vector decreases approximately linear. With decreasing J the AFM exchange is weakened, consequently the deviation of the order vector from (π,π) increases. The discontinuities reflect the first–order transition from (1,1)– to $(1,\pi)$–spirals. For $J/t = 0.05$ the transition to the FM state takes place, with Q_x jumping down to zero. The $(1,\pi)$–spiral wave–vector shows a monotonous decrease of Q_x until at $\delta = 0.63$ the transition to the PM ($Q_x = 0$) occurs. Comparing the magnitude of the theoretical order vector of the spiral solutions to results from inelastic neutron scattering experiments on $\mathrm{La_{2-x}Sr_xCuO_4}$ [44], we find good agreement for an exchange interaction strength of $J/t = 0.4$ (which seems to be a reasonable value with respect to the strong electron correlations observed in the high–T_c's (cf. Sec. 2.3)).

Next, we investigate the ground–state properties of the t–t'–J model. In the numerical work, we take $J/t = 0.4$. Comparing the free energies of several (homogeneous) symmetry broken states, we obtain the SB phase diagram of the t–t'–J model shown in the t'/t–δ plane in Fig. 4.5. We can distinguish two regimes in the phase diagram. In the parameter regime $|t'/t| \lesssim 0.2$, Fig. 4.5 resembles the ground–state phase diagram of the pure t–J model (Fig. 4.3), i.e., we found large regions with incommensurate spiral order. However, compared to the

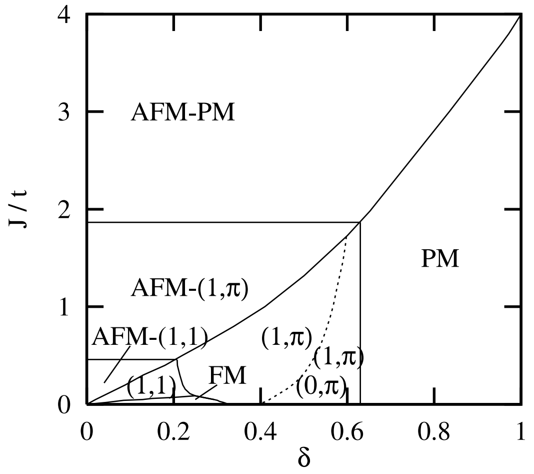

Figure 4.3: SB ground–state phase diagram of the t–J model.

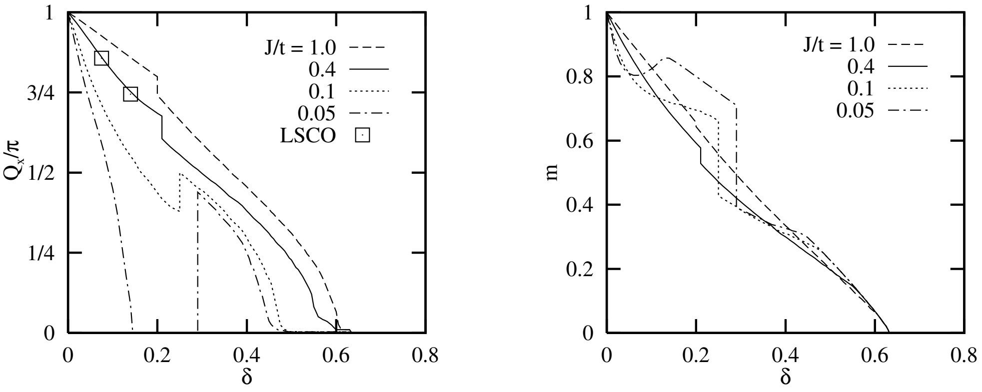

Figure 4.4: The x–component of the spiral wave–vector $\vec{Q}$ (left panel) and the magnetization m (right panel) as a function of doping δ (compared with experiments [□] on LSCO [44]).

pure t–J model, the t'–term stabilizes Néel order in a finite δ–region near half–filling. The increasing stability of AFM configurations can be intuitively understood because the t'–term moves electrons without disturbing the Néel–like background [275]. For larger ratios $|t'/t|$ we have a completely different situation. In this parameter regime only commensurate states (AFM, FM, PM) occur, where for $t' < t'_c = -1.4t$ we obtain the AFM state for all δ. Note the rather large differences to the value of t'_c obtained within a semiclassical $1/N$–expansion [278]. By varying the exchange coupling J the phase boundaries in the t'/t–δ plane are not much affected, e.g. for $J/t = 1$ and $t'/t = -0.4$, the transitions AFM$\rightleftharpoons$(1,1)–spiral and (1,1)–spiral$\rightleftharpoons$FM take place at $\delta = 0.17$ and $\delta = 0.6$, respectively. We would like to point out here that the main *qualitative* features of our SB phase diagram confirm recent studies of magnetic long–range order in the t–t'–J model [278, 279].

In Fig. 4.6 we plot the order parameter wave–vector as a function of doping at $t'/t = \pm 0.16$ and $t'/t = -0.4$. The behaviour of Q_x reflects a series of transitions AFM$\rightleftharpoons$(1,1)–spiral$\rightleftharpoons$ $(1,\pi)$–spiral$\rightleftharpoons$PM. The corresponding (sublattice) magnetization abruptly changes at the (1,1)–spiral$\rightleftharpoons$ $(1,\pi)$–spiral first–order transition. From Fig. 4.6 the asymmetry between hole ($t' < 0$) and electron doping ($t' > 0$) becomes evident. In contrast to recent Hartree–Fock results for the Hubbard model [273] we found the AFM phase near half–filling for both electron–doped and hole–doped cases (provided $t' \neq 0$). In the absence of t'–hopping, for arbitrarily small doping the AFM is found to be unstable against the (1,1)–spiral phase (cf.

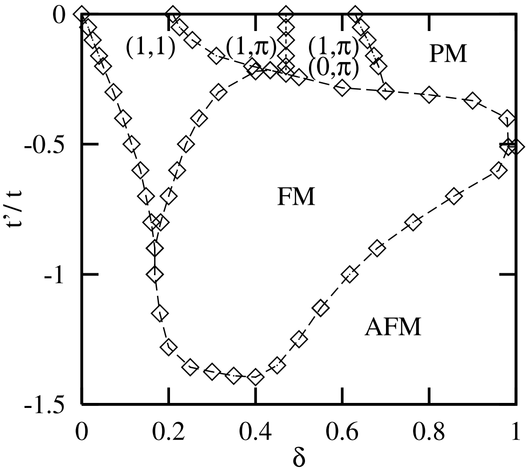

Figure 4.5: Restricted SB ground–state phase diagram of the 2D t–t'–J model at $J/t = 0.4$.

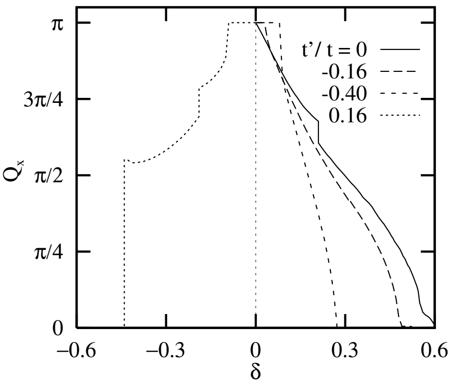

Figure 4.6: The x–component of the SB spiral wave–vector $\vec{Q}$ away from half–filling for the negative values $t'/t = -0.16$ (solid) and $t'/t = -0.4$ (long–dashed), i.e., hole doping ($\delta > 0$), and for the positive one $t'/t = 0.16$ (dashed), i.e., electron doping.

Fig. 4.5). Obviously, the AFM correlations are strongly enhanced by a positive t'–term, which is also in qualitative agreement with exact diagonalization studies of the t–t'–J model [275] and confirms the experimental findings for the electron–doped system NCCO [280, 281]. Note that the stability region of the AFM phase agrees surprisingly well with the combined phase diagram for $La_{2-x}Sr_xCuO_4$ and $Nd_{2-x}Sr_xCuO_4$ (Fig. 1.2) obtained from neutron scattering [282] and muon spin relaxation measurements [283], respectively. For the YBCO–parameter $t'/t = -0.4$, the AFM disappears around $\delta = 0.1$ whereas in the phase diagram of YBCO, determined by neutron diffraction [54], this transition takes place at about $x = 0.4$ *oxygen* content. However, there exits strong evidence that at least up to $x = 0.2$ *no holes* are transferred from Cu–O chains to CuO_2–planes (cf. also the discussion in Sec. 4.3 below).

As we have already noted, the phase diagrams presented in Figs. 4.3 and 4.5 result from the relative stability of various *homogeneous* states. On the other hand, there are arguments for the existence of *inhomogeneous*, e.g., phase–separated states in the t–J and related models [72]. Using very different methods, it was realized by several groups [78, 198, 200, 245, 284], that at large J/t the ground state of the t–J model separates into hole–poor (AFM) and hole–rich regions. Unfortunately, in the physically interesting regime of small exchange coupling ($J/t \sim$ 0.2–0.4) and low doping level this point is still controversial. To gain more insight into the phenomenon of phase separation in t–J–type models of strongly correlated electrons it seems to be important to investigate the effect of an additional NNN hopping term t' as well. Therefore we study the free energy as a function of hole density δ, where a (concave) convex curvature indicates local thermodynamic (in)stability implying a (negative) positive inverse isothermal compressibility

$$\kappa^{-1} = n^2 \frac{\partial^2 f}{\partial n^2} \, . \tag{4.46}$$

If $\kappa^{-1} < 0$, the domain of the two–phase regime is determined performing a Maxwell construction for the anomalous increase of the chemical potential μ by doping [270].

The results of our analysis of thermodynamic stability are depicted in Figs. 4.7 (a) and 4.7 (b) for the t–J and t–t'–J model, respectively.

The boundary of phase separation for the t–J model is given by the solid curve in the J–δ plane shown in Fig. 4.7 (a). As can be seen from Fig. 4.3, the different phase separated domains are built up by the (AFM) states at half–filling ($\delta = 0$) and the corresponding hole–rich state on the right boundary of the respective region. At $J = 0$, where we recover the $U \to \infty$ result of the Hubbard model [177], the free energy is a convex function $\forall\delta$, i.e., our SRI SB theory does not support recent arguments [78] for phase separation in this limit. In the opposite limit of large J, *complete* charge separation takes place for $J/t > J_{PS}/t = 4.0$, which seems to be an essentially classical result. From ED we obtain $J_{PS}/t = 4.1(\pm 0.1)$ [202], to be compared with $J_{PS}/t = 3.8$ derived by means of a high–temperature expansion [246]. We note that the homogeneous magnetic phases are always unstable close to half–filling (provided $J/t > 0$). This is in qualitative agreement with results obtained from exact diagonalization studies [78] as well as from semiclassical [245] or renormalization–group calculations [284]. Also plotted in Fig. 4.7 (a) are the results of the high–temperature expansion method [246], where phase separation may occur only above a critical exchange $J/t = 1.2$ as $\delta \to 0$, contrary to all the other approaches. The line separating the two–phase region from the stable states was determined by Marder et al. [245] within a semiclassical theory to vary as $J/t = 4\delta^2$, whereas our theory yields an approximately linear dependence at small δ. We believe that due to an improved treatment of spin correlations in our approach, the region of *incomplete* phase separation is reduced. The instability towards phase separation at small J can be taken as an indication that charge correlations may play an important role as well.

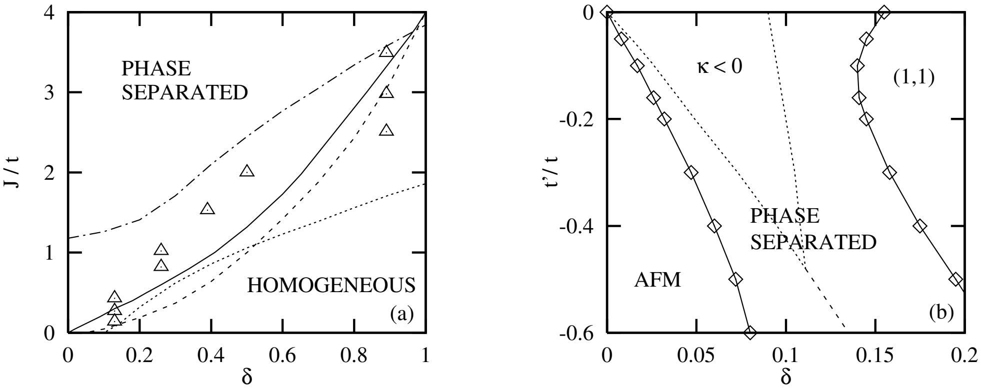

Figure 4.7: Phase diagram of the t–(t')–J model including phase separated states. The phase separation boundary (solid curve) for the t–J model is shown in the J–δ plane (a). We include the transition lines of Refs. [245] (dashed), [284] (dotted), and [246] (chain dashed). The triangles are the Lanczos results of Ref. [78]. The phase diagram of the t–t'–J is calculated in the t'/t–δ plane at $J/t = 0.4$ (b). Here the two–phase region consists of AFM and (1,1)–spiral states. For further explanation see text.

The dotted lines of zero inverse compressibility in Fig. 4.7 (b) show that also for $|t'/t| > 0$ there is a finite range of δ over which the (1,1)–spiral is locally unstable. Similar results were recently obtained by Psaltakis and Papanicolaou [278]. But it is important to stress that in our theory the AFM state is *locally* stable for *both* signs of t'. In addition, based on the Maxwell construction, we can show that near half–filling the AFM state remains also *globally* stable against phase separation for the t–t'–J model (cf. Fig. 4.7 (b), where the two–phase region is bounded by the solid lines). At larger values of $|t'/t|\gtrsim 0.5$, the phase–separated region is due to the first–order nature of the transition AFM$\rightleftharpoons$(1,1)–spiral (dashed curve) [278].

Finally to demonstrate the quality of our SRI SB approach, for the t–J model, the expectation value of the kinetic energy is compared with the results from ED for a finite 16–site [200] (36–site [202]) lattice in Fig. 4.8. We find an excellent agreement between SB results and ED data. Obviously, this result does not depend on the interaction strength J, i.e., the SB theory well describes important correlation effects. Note that $\langle \mathcal{H}_t \rangle_{t-J}/t$ is directly related to the effective transfer amplitude of the renormalized quasiparticle band, which is taken as input for the calculation of transport coefficients in the following section.

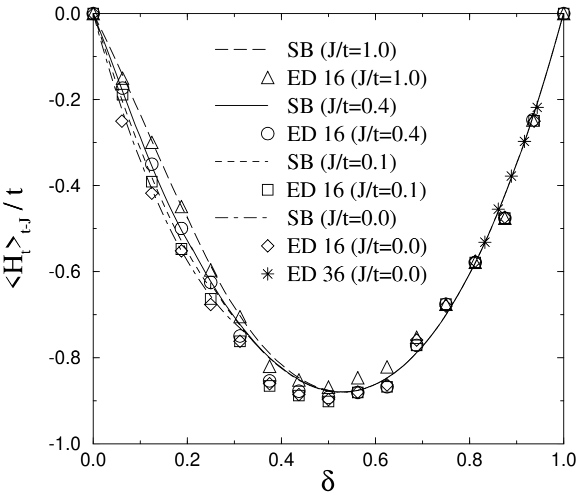

Figure 4.8: Expectation value of the kinetic energy as a function of doping at several interaction strengths J in comparison to ED results for the 16– (36–) site lattice [200, 202].

4.3 Comparison with experiments

4.3.1 Normal–state transport properties [268, 285]

As one of the main normal–state puzzles of the CuO_2 based high–T_c superconductors, the anomalous transport properties, in particular the temperature (T) and doping (δ) dependence of the Hall resistivity $R_H(T,\delta)$ [286, 287, 5, 288], has been under extensive experimental and theoretical study. Quasiparticle transport measurements suggest a small density of charge carriers and hence a *small* 'pocket-like' Fermi surface (FS) [67]. On the other hand, direct (angle–resolved photoemission (ARPES)) probes of the FS [276, 24] yield a *large* FS which satisfies Luttinger's theorem and might be well described by (LDA) band structure calculations. In principle, this contrasting behaviour is found for hole– ($La_{2-x}Sr_xCuO_4$, $YBa_2Cu_3O_{6+x}$) and electron–doped ($Nd_{2-x}Ce_xCuO_4$) copper oxides as well. Ito, Takenaka, and Uchida [65] have recently emphasized that the charge transport in the CuO_2 plane is determined by dominant spin scattering, i.e., the spin dynamics are clearly manifest in the extraordinary transport properties of the high-T_c cuprates. Then, adopting the hypothesis of Trugman [289], most of the normal–state properties of the cuprates may be explained by the dressing of quasiparticles due to magnetic interactions and the subsequent modification of their dispersion relation.

Once the quasiparticle band $E_{\vec{k}\nu}$ has been obtained, the Hall resistivity

$$R_H = \sigma_{xyz}/\sigma_{xx}\sigma_{yy} \tag{4.47}$$

and the thermopower

$$S = -(\sigma)^{-1}_{\alpha\gamma}\, \nu_{\gamma\beta} \tag{4.48}$$

can be calculated in the relaxation time approximation, using standard formulas for the transport coefficients $\sigma_{\alpha\beta}$, $\sigma_{\alpha\beta\gamma}$ and $\nu_{\alpha\beta}$:

$$\begin{aligned}
\sigma_{\alpha\beta} &= -\frac{e^2\tau}{\hbar^2 V}\sum_{\vec{k}\nu} v_{\alpha\vec{k}\nu} v_{\beta\vec{k}\nu} \frac{\partial n_{\vec{k}\nu}}{\partial E_{\vec{k}\nu}}\ , \\
\sigma_{\alpha\beta\gamma} &= -\frac{e^3\tau^2}{\hbar^4 cV}\sum_{\vec{k}\nu} v_{\alpha\vec{k}\nu}\epsilon_{\lambda\kappa\gamma} v_{\lambda\vec{k}\nu} \frac{\partial v_{\beta\vec{k}\nu}}{\partial k_\kappa}\frac{\partial n_{\vec{k}\nu}}{\partial E_{\vec{k}\nu}}\ , \\
\nu_{\alpha\beta} &= -\frac{e\tau}{\hbar^2 VT}\sum_{\vec{k}\nu} v_{\alpha\vec{k}\nu} v_{\beta\vec{k}\nu}\, E_{\vec{k}\nu} \frac{\partial n_{\vec{k}\nu}}{\partial E_{\vec{k}\nu}}\ .
\end{aligned} \tag{4.49}$$

Here $n_{\vec{k}\nu}$ is given by Eq. (4.30), V denotes the volume of the unit cell, $\epsilon_{\lambda\kappa\gamma}$ is the completely antisymmetric tensor, and $v_{\alpha\vec{k}\nu} = \partial E_{\vec{k}\nu}/\partial k_\alpha$. Note that both R_H and S do not depend on the relaxation time τ.

Along this line, the transport coefficients of various strong–coupling models have been investigated [289, 22, 290, 291]. Of course, the main problem is to determine the quasiparticle band $E_{\vec{k}}$ that forms when holes are doped into a AFM Mott insulator. To obtain $E_{\vec{k}}$, Trugman [289] solved exactly the strong–coupling Hubbard Hamiltonian (2.9) in a variational space in which a single hole can have several nearby spin flips with respect to the Néel state. Then, for the infinite system, the quasiparticles are assumed to fill this *rigid* band dispersion $E_{\vec{k}}$. The doping and temperature dependences of R_H, χ, and S calculated in that way agree surprisingly well with experiments on $\mathrm{La_{2-x}Sr_xCuO_4}$. On the other hand, Sá de Melo *et al.* [292] showed that a systematic treatment of the strong AFM correlations within the spinon holon picture leads to $\vec{k}$–dependent corrections of the quasiparticle self energy. This effect is also sufficient to reproduce the experimentally observed sign change in the Hall coefficient.

Here we will examine mainly the doping dependence of R_H (S) in terms of the t–(t')–J model using the saddle–point and relaxation time approximations, where FS and correlation effects are involved via the renormalized SB band $E_{\vec{k}\nu}$ (4.38). Let us emphasize that in our approach the SB quasiparticle band dispersion $E_{\vec{k}\nu}$ has to be determined in a self–consistent way at each doping level $\delta\,(\leftrightarrow \mu - \lambda_o^{(2)})$ by an iterative solution of the remaining nonlinear stationary equations for m, $\lambda^{(2)}$ and $\vec{Q}$. This should be contrasted to the NZA SB mean–field approach to the t–t'–J model of Chi and Nagi [291], where, in the $J\to 0$ limit, the calculation of transport properties is based on the simple replacement $\varepsilon_{\vec{k}} \to \tilde{\varepsilon}_{\vec{k}} = -2t\delta\,[(\cos k_x + \cos k_y) + 2t'/t\,\cos k_x \cos k_y]$ of the noninteracting band dispersion (4.45).

We consider first the results obtained for the t-J model.[3] The Hall resistivity $R_H(\delta)$ and the thermopower $S(\delta)$ are shown in Fig. 4.9 at fixed temperatures for different values of the exchange interaction J together with the experimental Hall data of Tagaki *et al.* [286] and the thermopower measurements of Cooper *et al.* [293]. In addition, applying Trugman's rigid–band approximation [289], we have included results based on the single–hole band dispersion (3.6) obtained from our exact diagonalization (ED) data [200] for the strong–coupling model (2.9).

---

[3] In the numerical work we take t (=0.3 eV) as the energy unit. The $\vec{k}$–summations in Eq. (4.49) are done numerically over the whole Brillouin zone of the square lattice, using a 1000 × 1000 grid.

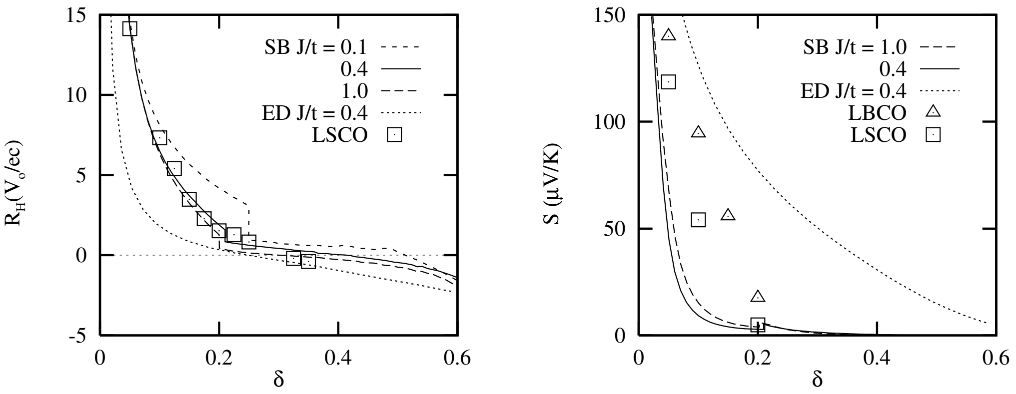

Figure 4.9: Hall resistivity at 80 K (left panel) and thermopower at 300 K (right panel) as a function of doping. Assuming $\delta = x$, our SB and ED results are compared with the experiments on $\mathrm{La_{2-x}Sr_xCuO_4}$ (R_H) [286], (S) [293] and $\mathrm{La_{2-x}Ba_xCuO_4}$ (S) [293].

As can be seen from Fig. 4.9, the calculated doping dependences of the Hall coefficient[4] and the thermopower[5] are in good qualitative agreement with the experiments. For small doping the structure of the Fermi surface yields to a hole-like sign of R_H. The change of sign, as experimentally observed at about $\delta \approx 0.3$ for $\mathrm{La_{2-x}Sr_xCuO_4}$, depends on the strength of the exchange interaction J and occurs at $\delta \approx 0.5$, 0.4 and 0.3 for $J/t = 0.1$, 0.4 and 1.0, respectively.

To discuss the band structure effects on $R_H(\delta)$, the theoretical (SB) Hall resistivity as a function of carrier density is shown in Fig. 4.10 for the t–t'–J model in comparison to experiments on LSCO [286], YBCO [287], and NCCO [5, 288]. In the LSCO and NCCO systems, the concentration of chemically doped charge carriers in the $\mathrm{CuO_2}$ planes (δ) definitely agrees with the composition (x) of the substitutes Sr and Ce. This simple relation, however, no longer holds for YBCO, i.e., the number of 'holes' transferred into the planes does not increase linearly with the oxygen content. Indeed, the magnetic properties indicate $\delta \simeq 0$ up to $x = 0.2$ [54]. In order to compare our theoretical model with the $R_H(x)$ data found on oxygen doped YBCO, we use the relation $\delta = (x - 0.2)/2$ (also, using (4.49), it has to be kept in mind that YBCO has two $\mathrm{CuO_2}$ layers per unit cell). Fig. 4.10 clearly demonstrates the importance of the NNN transfer term t' for a consistent theoretical description of the experimental Hall data. For $J/t = 0.4$, an excellent agreement with experiments on LSCO and NCCO, including the sign change of $R_H(\delta)$ at a very similar value, can be achieved using the parameter values $t'/t = 0$ and $t'/t = 0.16$, respectively. It should be noted that in the case of LSCO we obtain $t'/t = 0$ from $R_H(\delta)$ while LDA calculations yield a ratio $t'/t = -0.16$ [124, 11]. For $\mathrm{YBa_2Cu_3O_{6+x}}$, where the experiments [287] give $R_H > 0$ up to $x = 1$, a negative t'–term suffices to give the correct tendency to $R_H(\delta)$. Using $t'/t = -0.4$, our theory yields a sign change of R_H at $\delta \sim 0.7$. The strong increase (decrease) of the positive (negative) Hall coefficient as $\delta \to 0$ can be attributed to the formation of small hole (electron) pockets in the FS (see below). Obviously, this is a correlation effect. A recent analysis of resistivity saturation in LSCO [67], based on Boltzmann transport, has been taken as an indication of a small FS as well, however, the existence of a pocket–like FS is still a subtle

---

[4] The discontinuities, occurring in the SB curves at various δ, are related to changes of the magnetic structure of the ground state (cf. the magnetic phase diagram of the t–(t')–J model in Sec. 4.2.2).

[5] For $S(\delta)$, in view of the high experimental temperature (300 K), the saddle–point approximation is expected to be less accurate.

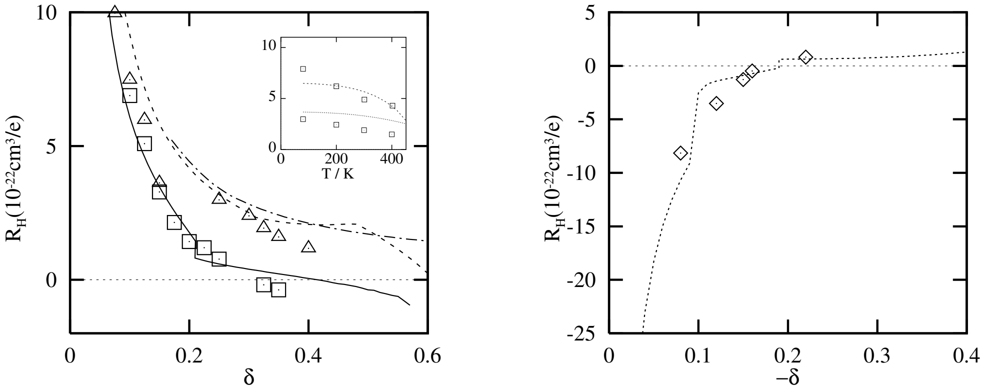

Figure 4.10: Doping dependence of the Hall resistivity for hole– (left panel) and electron–doped (right panel) systems. The slave–boson results for $J/t = 0.4$ and different ratios $t'/t = 0$ (solid), -0.16 (dashed), -0.4 (chain dotted) and $t'/t = 0.16$ (dotted) are compared with experiments on LSCO [286] (□) [at 80 K], YBCO (△) [287] [at 100 K] and NCCO (◇) [5, 288] [at 80 K], respectively. The inset shows the temperature dependence of R_H for $t'/t = 0$ at $\delta = 0.1$ (short dashed) and $\delta = 0.15$ (dotted).

and unresolved issue. We found that the temperature dependence of $R_H(\delta, T)$ is at least in qualitative agreement with experiments on LSCO (see inset Fig. 4.10 (left panel)). Note that the quasiparticle dispersion $E_{\vec{k}\pm}$ exhibits extremely *flat* minima implying the presence of a new small energy scale $\mathit{\Delta}$. Therefore, when the temperature becomes comparable to $\mathit{\Delta}$ the hole pockets are washed out and a sign change of R_H occurs (cf. Fig. 4.10 at fixed δ (inset)).[6]

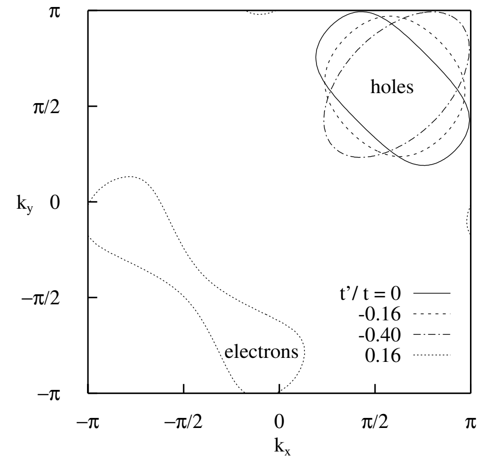

Figure 4.11: Quasiparticle Fermi surface in the (1,1)–spiral phase at $J/t = 0.4$ for $\delta = 0.1$ (hole–doped system) and $\delta = -0.1$ (electron–doped system).

The FS of the interacting system are shown in Fig. 4.11 for the same typical ratios t'/t as in Fig. 4.2 at $J/t = 0.4$ and $\delta = \pm 0.1$, where the diagonal (1,1)–spiral phase becomes lowest in energy. As observed for t–J and Hubbard models as well [294], we obtain small hole (or electron) pockets with a volume $\propto |\delta|$. The calculated FS are very anisotropic. As $|\delta|$ increases, the pockets grow, until the FS topology changes completely at a critical doping value δ_c ($R_H(\delta_c) = 0$; cf. Fig 4.10), reflecting the transition from hole to electron carriers for $t'/t < 0$ and vice versa for $t'/t > 0$.

---

[6] We recently learned of a related exact diagonalization study of Dagotto, Nazarenko, and Boninsegni [22], where, similar in conclusion, the doping and temperature dependence of R_H was calculated using a strongly renormalized *flat* quasiparticle dispersion.

To illustrate the $\vec{k}$–dependence of the SB quasiparticle dispersion relation, e.g., for the electron–doped system, in more detail, in Fig. 4.12 the $E_{\vec{k}-}$–contour is shown at 10 % doping in the (1,1)–spiral state. We point out here that $E_{\vec{k}-}$ corresponds to the *upper* quasiparticle band (in electron notation). At $J/t = 0.4$ and $\delta = -0.1$, we have $\mu - \lambda_o^{(2)} = 0.309$, $\lambda^{(2)} = -0.667$, $m = 0.757$ and $\vec{Q} = (-2.789, -2, 789)$. In contrast to the hole–doped case, $E_{\vec{k}-}$ exhibits two minima. We stress that at still lower doping level ($|\delta| \leq 0.02$), where the ground state is antiferromagnetically ordered [126], the minima of $E_{\vec{k}-}$ are located around $(\pm\pi, 0)$ and $(0, \pm\pi)$ ((0,0) and $(\pm\pi, \pm\pi)$) in the case of electron doping [$t'/t > 0$] (hole doping [$t' \leq 0$]).

The renormalization of the quasiparticle band strongly depends on both electronic correlation (*J*) and doping level (δ), which, in fact, calls the frequently used rigid–band approximation into question. Due to the strong coupling of spin and charge dynamics the characteristic energy scale for the coherent motion of the charge carriers is *J* and not *t* (provided $t > J$).

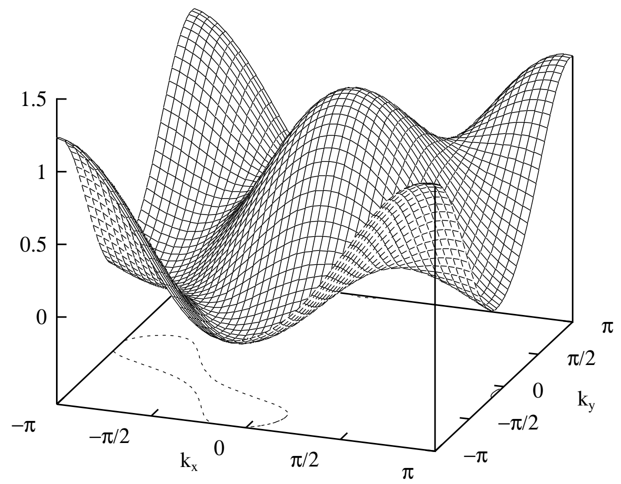

Figure 4.12: Quasiparticle dispersion relation $E_{\vec{k}-}$ for $\delta = -0.1$ and $J/t = 0.4$ (see text for further explanation).

In conclusion, we have shown that our calculation of the Hall resistivity in the relaxation–time approximation, combined with a SB based treatment of strong electronic correlations and band structure (FS) effects on the basis of the t–t'–J model, provides a reasonable explanation of the experimentally observed doping dependence of R_H on both hole– ($La_{2-x}Sr_xCuO_4$, $YBa_2Cu_3O_{6+x}$) and electron–doped ($Nd_{2-x}Ce_xCuO_4$) copper oxides.

4.3.2 Magnetic correlations and spin dynamics [51, 295]

The nature of spin excitations of the high–T_c cuprates has been experimentally studied by means of nuclear magnetic/quadrupole resonance (NMR/NQR) and inelastic neutron scattering (INS) techniques clarifying the persistence of strong antiferromagnetic correlations in the normal and superconducting states [31, 35] (cf. Sec. 1.3.1). Detailed investigations of the wave–vector dependence of the low–frequency spin fluctuation spectrum have revealed remarkable differences between the $YBa_2Cu_3O_{6+x}$ and $La_{2-x}Sr_xCuO_4$ families at low doping level x; the dynamic structure factor $S(\vec{q}, \omega)$ keeps its maximum at (π, π) in the YBCO system, while in LSCO, the peaks are displaced from the commensurate position to the four incommensurate wave–vectors $\pi(1 \pm q_o, 1)$, $\pi(1, 1 \pm q_o)$, where $q_o \sim 2x$. On the other hand, the analyses of the

NMR data show that the relaxation rates on the planar Cu sites are similar in all materials. Two striking features are associated with ${}^{63}T_1^{-1}$: (i) as a result of strong local spin fluctuations on ^{63}Cu sites it is enhanced by an order of magnitude over the oxygen rate ${}^{17}T_1^{-1}$; and (ii) in sharp contrast to the Korringa–like behavior at the planar ^{17}O sites, its temperature dependence does not follow the Korringa law. The physical origin of the contrasting $\vec{q}$–dependence of the spin fluctuation spectrum is still under discussion, and several scenarios have been proposed to analyze theoretically the neutron and nuclear relaxation data in the cuprates. Millis and Monien [296] have argued that the spin dynamics and, in particular, the temperature dependence of the spin susceptibility $\chi_s(T)$ in LSCO are caused by a spin–density–wave instability, whereas in the YBCO family they are due to in–plane AFM fluctuations and a novel 'non–Fermi–liquid' spin singlet pairing of electrons in adjacent planes. On the other hand, the magnetic properties are intimately related to the band dispersion of the noninteracting system within a Fermi liquid based framework, i.e., in this way the observed spin dynamics can be attributed to different FS geometry of LSCO type and YBCO type, respectively. Along this line, details of the spin fluctuation spectrum are studied using a nearly antiferromagnetic Fermi liquid approach by Monthoux and Pines [297] and within a large Coulomb–U auxiliary boson scheme by Si *et al* [49]. It is interesting to note, that a simple band structure model of LSCO together with 'marginal–Fermi–liquid' self–energy corrections [298], i.e., without strong AFM exchange enhancement as in the models [297, 49], can give energy and momentum dependences of the magnetic structure factor in parallel to Refs. [297, 49]. Therefore Littlewood *et al.* [298] are lead to the conclusion that the peaks seen in neutron scattering derive primarily from FS geometry. From a more microscopic point of view, the important effects of FS shape on the magnetic properties were confirmed by Fukuyama and co–workers [152, 50, 123, 299] using a (RVB) SB mean–field approach to the extended t–J model.

RPA approach

In this section, we try to understand the INS and NMR experiments on the basis of the SRI SB mean–field theory. Using a generalized RPA expression for the spin susceptibility and assuming that the AFM correlations are spatially filtered by various $\vec{q}$–dependent hyperfine form factors, we focus, in particular, on the spin *dynamical* properties in the *paraphase* of the t–t'–J model.

Our starting point is an RPA–like form for the exchange–enhanced spin susceptibility [50, 300, 45]

$$\chi_s(\vec{q},\omega) = \frac{\overline{\chi}_0(\vec{q},\omega)}{1+\frac{J}{2}(\cos q_x + \cos q_y)\,\overline{\chi}_0(\vec{q},\omega)}\ . \tag{4.50}$$

The irreducible part

$$\overline{\chi}_0(\vec{q},i\omega_m) = -\frac{2}{\beta N}\sum_{\vec{k},n} \overline{G}(\vec{k},i\omega_n)\,\overline{G}(\vec{k}+\vec{q},i\omega_{n+m}) \tag{4.51}$$

contains the (dressed) SB Green propagators $\overline{G}(\vec{k},i\omega_n) = [i\omega_n - E_{\vec{k}} + \tilde{\mu}]^{-1}$ describing noninteracting electrons with the *renormalized* band structure $E_{\vec{k}}$ (4.42). Note that the band renormalization varies strongly with hole concentration δ.

Once the dynamic spin susceptibility has been obtained, both INS measurements and NMR/NQR experiments can be explored. From the fluctuation–dissipation theorem the $\vec{q}$– and ω–dependent spin structure factor

$$S(\vec{q},\omega) = \frac{1}{\pi}\,\frac{1}{1-\exp(-\beta\hbar\omega)}\ Im\ \chi_s(\vec{q},\omega) \tag{4.52}$$

probed by INS is related to the dynamical susceptibility. On the other hand, the nuclear spin–lattice relaxation rate, ${}^{a}T_{1\alpha}^{-1}$ ($\alpha = \perp, \|$), e.g. for a field H_α applied parallel to the c–axis, given by [93]

$$\left({}^{a}T_{1\|}T\right)^{-1} = \frac{1}{2}\,\frac{k_B}{\mu_B^2\hbar}\,\lim_{\omega\to 0}\,\frac{1}{N}\sum_{\vec{q}}\,{}^{a}F_{\perp}^{2}(\vec{q})\,\frac{Im\ \chi_s(\vec{q},\omega)}{\hbar\omega} \tag{4.53}$$

and the transverse spin–spin relaxation rate, T_{2G}^{-1}, for the RKKY coupling of the nuclear Cu spins given by [301]

$$T_{2G}^{-2} = \frac{c}{8\hbar^2}\,\frac{1}{(2\mu_B)^4}\left\{\frac{1}{N}\sum_{\vec{q}}\,\left(F_{\|}^{2}(\vec{q})\,\chi_s(\vec{q})\right)^2 - \left(\frac{1}{N}\sum_{\vec{q}}\,F_{\|}^{2}(\vec{q})\,\chi_s(\vec{q})\right)^2\right\} \tag{4.54}$$

provide local, atomic site ($a = \{63,\,17\}$) specific information. Here μ_B denotes the Bohr magneton and the constant $c = 0.69$ is the natural–abundance fraction of the ^{63}Cu isotope. The form factors are given for ^{63}Cu and the planar ^{17}O nucleus as [302]

$$\begin{aligned} {}^{63}F_\alpha(\vec{q}) &= X_\alpha + 2Y(\cos q_x + \cos q_y)\,, \\ {}^{17}F_\alpha(\vec{q}) &= 2\,Z\,\cos\tfrac{q_x}{2}\,. \end{aligned} \tag{4.55}$$

Together with the anisotropy of the Cu relaxation rates, the measurements of the Knight shift

$${}^{a}K_\alpha = \frac{1}{2}\,\frac{1}{\mu_B{}^{a}\gamma_n\hbar}\,\lim_{\vec{q}\to 0}\,{}^{a}F_\alpha(\vec{q})\,\chi_s(\vec{q},\omega=0) \tag{4.56}$$

have been used to determine the hyperfine coupling constants X_α, Y and Z on the basis of the Mila–Rice Hamiltonian [303]. Following Ref. [93] we take $X_\| \approx -4Y$, $X_\perp \approx 0.84Y$, $Z \approx 0.87Y$ and $Y \approx 3.3\ 10^{-7}$ eV, where ${}^{63}\gamma\hbar = 7.5\ 10^{-24}$ erg/G and ${}^{17}\gamma\hbar = 3.8\ 10^{-24}$ erg/G. Again we take $t = 0.3eV$ as the energy unit.

As we know, the RPA susceptibility contains an unphysical instability of the paramagnetic phase at some particular wave–vector $\vec{q}$ below a critical doping δ_c as signaled by the zero in the denominator of (4.50) at $\omega = 0$ (Stoner condition). Therefore the use of (4.50) only makes sense if the system is far from the magnetic instability, i.e., $\delta > \delta_c$, where for $J = 0.4$ we have $\delta_c(t'/t = -0.16) \simeq 0.27$ and $\delta_c(-0.4) \simeq \delta_c(0) \simeq 0.17$.

Inelastic neutron scattering measurements

We begin with a discussion of the RPA dynamical spin structure factor $S(\vec{q},\omega)$. The $\vec{q}$–dependence of $S(\vec{q},\omega)$ along the main symmetry axes of the Brillouin zone is shown in Fig. 4.13 for different ratios t'/t, $J = 0.4$ and hole density $\delta = 0.3$. Here the temperature is $T = 35$ K and the frequency $\hbar\omega = 10$ meV. For LSCO–type parameters ($t'/t = 0$, -0.16) we found four pronounced incommensurate peaks located at the points $\pi(1 \pm q_o, 1)$, $\pi(1, 1 \pm q_o)$. The incommensurate modulation wave–vectors move with increasing doping level δ away from the corner of the Brillouin zone along the directions $(1,\pi)$ or $(\pi,1)$ (square lattice notation). Note that while the incommensurate peak position obtained from a three–band RPA calculation of $S(\vec{q},\omega)$ [49] can be parameterized consistent with the experimental observation that $q_o \simeq 2x$ [44], all the effective one–band RPA approaches [50, 299, 124] yield an incommensurability scaling rather as $q_o \simeq \delta$. A more detailed investigation of the LSCO–type $\vec{q}$–scans show that the $\vec{q}$–variation of $S(\vec{q},\omega)$ is mainly governed by that of $\overline{\chi}_0(\vec{q},\omega)$ and, in accordance with experiments [43], the incommensurate peaks considerably broaden as temperature or energy transfer are increased [295] (see Fig. 4.14 (left panel)). By contrast, the same plot for YBCO–type ($t'/t = -0.4$) parameters shows a broad, nearly T–independent (cf. Fig 4.14 (right panel)), maximum around the (π,π)–point [304] (see Fig. 4.13) which, due to the flat topology of $\overline{\chi}_0$, mainly reflects the $\vec{q}$–dependence of $J(\vec{q}) = J(\cos q_x + \cos q_y)$ (cf. Eq. (4.50)). In this way, our

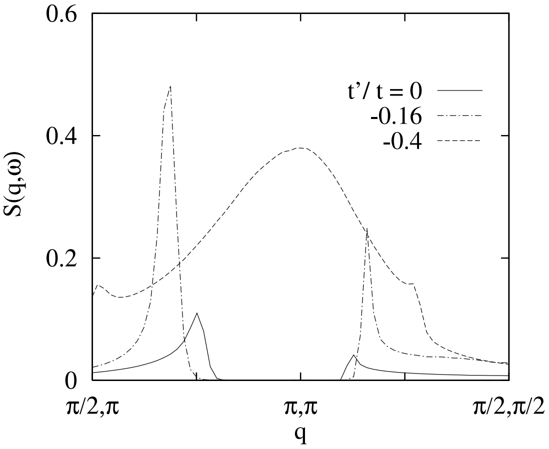

Figure 4.13: Dynamic magnetic structure factor $S(\vec{q},\omega)$ plotted along the (1,1)– and $(1,\pi)$–directions of the Brillouin zone for different ratios t'/t.

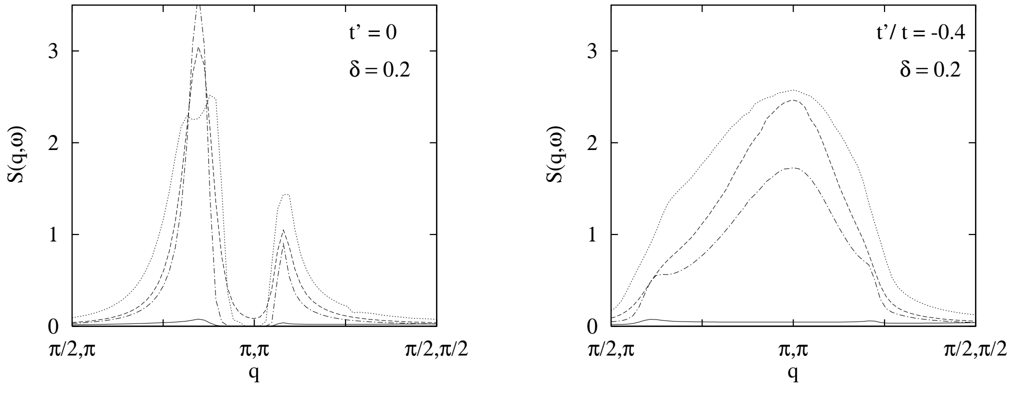

Figure 4.14: $S(\vec{q},\omega)$ for $J/t = 0.4$ at {ω [meV]; T [K]}={10; 35} (chain dotted), {10; 100} (dashed), {30; 35} (dotted) compared to the case $J = 0$ at {10; 35} (solid).

calculations confirm recent arguments [49, 298, 50] for the importance of band structure (Fermi surface geometry) effects in explaining the difference between observed LSCO and YBCO spin dynamics. Nevertheless, whether the incommensurate signals arise from an intrinsic magnetic structure or whether they result from the formation of domains (charge superstructures) in the LSCO system remains unanswered by INS [35, 302].

Nuclear spin relaxation rates

In a next step, we calculate the longitudinal or spin–lattice relaxation rate, T_1^{-1}, using the hyperfine form factors (4.55). In Fig. 4.15 the temperature dependences of ${}^{63}T_{1\|}^{-1}$ and ${}^{17}T_{1\|}^{-1}$ (inset) are shown for $\delta = 0.35$ and $t'/t = -0.4$ in comparison to experiments [305] on fully oxygenated YBCO materials ($x = 1$). Although our theory does not succeed in giving the correct amplitude of ${}^{a}T_{1\|}^{-1}$ the qualitative features of the NMR data are described surprisingly well. Obviously the broad magnetic peak in $S(\vec{q},\omega)$ at the AFM wave–vector $\vec{Q}_{AFM} = (\pi,\pi)$ strongly enhances the relaxation rate on Cu sites while, due to a geometrical cancelation (${}^{17}F_\alpha(\vec{q} \simeq \vec{Q}_{AFM}) \simeq 0$), the corresponding oxygen rate is rather insensitive to nearly commensurate AFM fluctuations, and therefore is governed by the long–wavelength part $\vec{q} \simeq 0$ of the spin susceptibility [35]. For ^{63}Cu the nominal Korringa ratio $S \equiv (1/T_1 T K_S^2)$ (K_S denotes the spin part of the Knight shift) is at least one order of magnitude larger. As can be seen from Fig. 4.15, for $YBa_2Cu_3O_7$–type parameters, a Korringa ($1/T_1 \propto T$) dependence (dotted line) holds at both Cu and O sites below $T^* \sim 120$ K, demonstrating the existence of a characteristic temperature T^* as well as in all other near–optimum–T_c compounds [35, 306]. T^* is in good agreement with the coherence energy scale suggested experimentally [306]. Above T^* the ^{17}O NMR relaxation remains linear whereas the ^{63}Cu relaxation time does not follow the Korringa law. Similar results are found for the LSCO system [307].

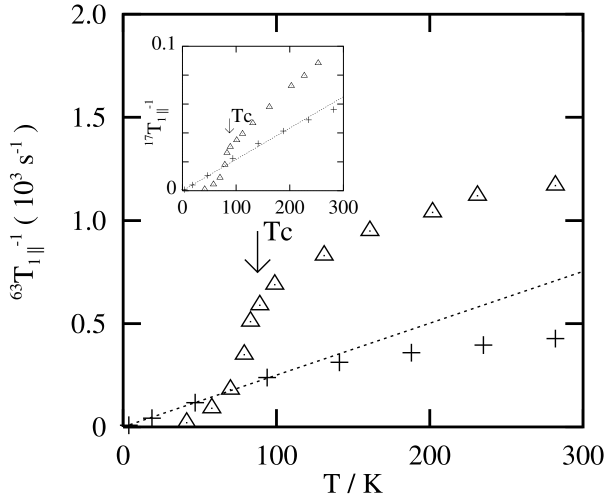

Figure 4.15: Spin–lattice relaxation rates ${}^{63}T_{1\|}^{-1}$ and ${}^{17}T_{1\|}^{-1}$ (inset) as a function of temperature. SB results ((+); $t'/t = -0.4$, $\delta = 0.35$) are compared with experiments (△) on $YBa_2Cu_3O_7$ [305].

In the oxygen–deficient compound $YBa_2Cu_3O_{6.6}$, $1/({}^{63}T_{1\|}T)$ shows a broad maximum at about 150 K (see Fig. 4.16), which reflects a strong deviation from the canonical Korringa behaviour. In the normal state regime the theoretical results agree even quantitatively with the experimental ^{63}Cu–NMR data [308]. At this point it is important to stress that the present theory incorporates considerable band renormalization effects already via $\overline{\chi}_0(\vec{q},\omega)$, especially at low doping level. Thus a rather moderate strength $J = 0.4$ of the AFM exchange interaction yields the experimentally observed enhancement of ${}^{63}T_{1\|}$. In striking contrast to the optimally doped YBCO system, the Korringa relation is no longer satisfied for the planar ^{17}O nucleus sites in the underdoped material (cf. inset Fig. 4.16). Instead, a different behaviour

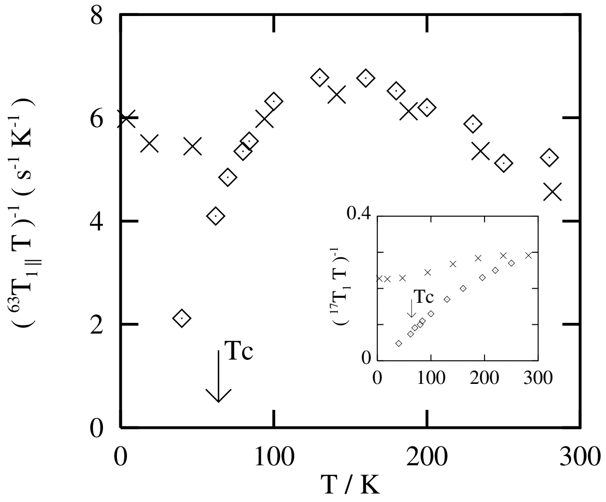

Figure 4.16: ^{63}Cu and planar ^{17}O relaxation data (◇) for underdoped $YBa_2Cu_3O_{6.6}$ [308] are plotted *vs* temperature. Theoretical results (×) are given at $t'/t = -0.4$, and $\delta = 0.2$.

$^{17}T_{1\|}T^{17}K_S = const$ was suggested to hold down to T_c [308]. The unconventional T–scaling of $^{17}T_{1\|}$ has been taken as a signature for another important feature of the normal–state spin dynamics, the so–called spin–gap phenomenon [35].

Complementary measurements of the transverse spin–spin relaxation rate, T_{2G}^{-1}, have provided further insights into the drastic change in the magnetic properties when passing from the overdoped to the underdoped regime [301, 309]. As experimentally observed, we found that T_{2G}^{-1} increases (decreases) with increasing (decreasing) hole doping (temperature) [307]. In order to detect the opening of a spin–pseudogap as a function of T, a powerful technique is to measure the ratio T_{2G}/T_1T [55] which is nearly constant above ~ 200 K for desoxygenated $YBa_2Cu_3O_{6.6}$ [301]. The calculated temperature dependence of this quantity is shown in Fig. 4.17 together with recent experimental results [301]. Most noticably, the opening of a

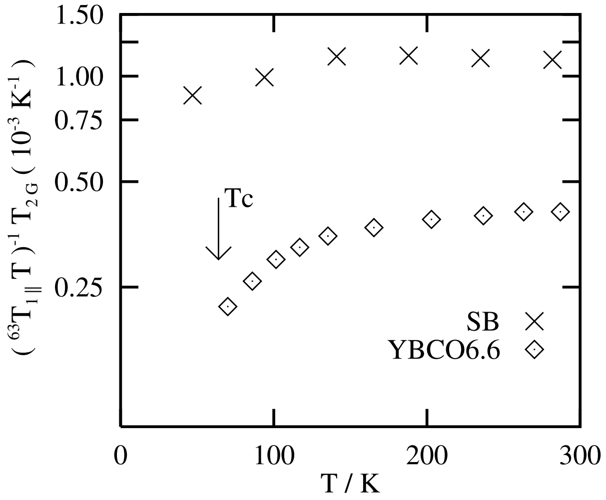

Figure 4.17: $T_{2G}/(^{63}T_{1\|}T)$ in underdoped $YBa_2Cu_3O_{6.6}$ (◇) as measured by Takigawa [301] compared with the SB data (×) at $t'/t = -0.4$, and $\delta = 0.2$.

spin–pseudo gap at $T^\star \simeq 135$ K [55], i.e. well above T_c, is clearly seen as a decrease of T_{2G}/T_1T below $T^\star$. Note that for $YBa_2Cu_3O_7$, as predicted by Fermi liquid theories, the ratio T_{2G}^2/T_1T is approximately constant above ~ 150 K [35].

To conclude, we have shown that our SB treatment of the spin dynamics in terms of the t–t'–J model may provide a reasonable explanation of the basic features of both INS and NMR experiments on LSCO and YBCO high–T_c compounds.

4.4 Gaussian fluctuations

4.4.1 Dynamic response functions in the SRI SB approach [310]

In this section we want to improve on the previous (non-conserving) RPA–like form of the dynamical spin susceptibility (4.50) by accounting for quadratic terms (Gaussian fluctuations) in the fluctuation expansion ($\Phi_{i\alpha} = \overline{\Phi}_{\alpha}^{(PM)} + \delta\overline{\Phi}_{i\alpha}$) of the collective action (4.23),

$$\mathcal{S}_{\text{Gauss}} = \overline{\mathcal{S}}^{(PM)} + \sum_{q;\alpha,\beta} \delta\phi_{\alpha}(-q)\, \mathcal{S}_{\alpha\beta}(q)\, \delta\phi_{\beta}(q) \ , \tag{4.57}$$

in order to derive the complete set of dynamical response functions for the t–t'–J model at the paramagnetic saddle point $\{\overline{\mathcal{S}}^{(PM)}, \overline{\Phi}^{(PM)}\}$. The fluctuation matrix $\mathcal{S}_{\alpha\beta}$ can be calculated according to

$$\mathcal{S}_{\alpha\beta}(q,q') = \mathcal{S}_{\alpha\beta}(q)\delta(q+q') = \frac{1}{2\mathcal{N}} \sum_{R_i,R_j} e^{-iqR_i} \left.\frac{\partial^2 \mathcal{S}_{eff}}{\partial\phi_{i\alpha}\partial\phi_{j\beta}}\right|_{\substack{\Phi_i=\Phi_j=\overline{\Phi}^{(PM)} \\ \delta(\tau-\tau')}} e^{-iq'R_j} \ , \tag{4.58}$$

where the shorthand notations $q = (\vec{q},\omega_m)$, $k = (\vec{k},\omega_n)$, $R_i = (\vec{R}_i,\tau)$, $\mathcal{N} = \beta N$, and $\sum_{R_i} = \sum_i \int_0^{\beta} d\tau$ are introduced. It is easy to see that at the PM saddle point the 10 × 10 fluctuation matrix $\underline{\mathcal{S}}$ decomposes into a 4 × 4 matrix $\underline{\mathcal{S}}_c$ (connected to charge fluctuations $(\delta e_i, \delta p_{io}, \delta\lambda_{io}^{(2)}, \delta\lambda_i^{(1)})$) and three identical 2 × 2 matrices $\underline{\mathcal{S}}_x = \underline{\mathcal{S}}_y = \underline{\mathcal{S}}_z =: \underline{\mathcal{S}}_s$ (connected to spin fluctuations, e.g., upon the elements $(\delta p_{ix}, \delta\lambda_{ix}^{(2)})$):

$$\underline{\mathcal{S}} = \begin{pmatrix} \boxed{\quad\underline{\mathcal{S}}_c\quad} & & & 0 \\ & \boxed{\underline{\mathcal{S}}_x} & & \\ & & \boxed{\underline{\mathcal{S}}_y} & \\ 0 & & & \boxed{\underline{\mathcal{S}}_z} \end{pmatrix} . \tag{4.59}$$

The non-vanishing matrix elements of $\underline{\mathcal{S}}_c$ and $\underline{\mathcal{S}}_s$ are found to be

$$\begin{aligned} \mathcal{S}_{ee}(q) &= \lambda^{(1)} - \overline{\chi}_2(q) \left(z_+ \frac{\partial z_+}{\partial e} \right)^2 + \tilde{\varepsilon}(\vec{q}) \left(\frac{\partial z_+}{\partial e} \right)^2 + \tilde{\varepsilon}(0)\ z_+ \frac{\partial^2\, z_+}{\partial e^2} \ , \\ \mathcal{S}_{ep_o}^{(2)}(q) &= -\overline{\chi}_2(q)\ z_+^2 \frac{\partial z_+}{\partial e} \frac{\partial z_+}{\partial p_o} + \tilde{\varepsilon}(\vec{q}) \frac{\partial z_+}{\partial e} \frac{\partial z_+}{\partial p_o} + \tilde{\varepsilon}(0)\ z_+ \frac{\partial^2\, z_+}{\partial e \partial p_o} \ , \\ \mathcal{S}_{e\lambda_o^{(2)}}^{(2)}(q) &= -\overline{\chi}_1(q)\ z_+ \frac{\partial z_+}{\partial e} \ , \\ \mathcal{S}_{e\lambda^{(1)}}(q) &= e \ , \end{aligned}$$

$$\begin{aligned}
\mathcal{S}_{p_o p_o}(q) &= \lambda^{(1)} - \lambda_o^{(2)} - Jp_o^2(1 + cosq_x + cosq_y) \ , \\
&\quad -\overline{\chi}_2(q) \left(z_+ \frac{\partial z_+}{\partial p_o} \right)^2 + \tilde{\varepsilon}(\vec{q}) \left(\frac{\partial z_+}{\partial p_o} \right)^2 + \tilde{\varepsilon}(0) \ z_+ \frac{\partial^2 \, z_+}{\partial p_o^2} \ , \\
\mathcal{S}_{p_o \lambda_o^{(2)}}(q) &= -p_o - \overline{\chi}_1(q) \ z_+ \frac{\partial z_+}{\partial p_o} \ , \\
\mathcal{S}_{p_o \lambda^{(1)}}(q) &= p_o \ , \\
\mathcal{S}_{\lambda_o^{(2)} \lambda_o^{(2)}}(q) &= -\chi_0(q) \ ,
\end{aligned} \tag{4.60}$$

and

$$\begin{aligned}
\mathcal{S}_{p_x p_x}(q) &= \lambda^{(1)} - \lambda_o^{(2)} - Jp_o^2(1 - cosq_x - cosq_y) \ , \\
&\quad -\overline{\chi}_2(q) \left(z_+ \frac{\partial z_-}{\partial p_x} \right)^2 + \tilde{\varepsilon}(\vec{q}) \left(\frac{\partial z_-}{\partial p_x} \right)^2 + \tilde{\varepsilon}(0) \ z_+ \frac{\partial^2 \, z_+}{\partial p_x^2} \ , \\
\mathcal{S}_{p_x \lambda_x^{(2)}}(q) &= -p_o - \overline{\chi}_1(q) \ z_+ \frac{\partial z_-}{\partial p_x} \ , \\
\mathcal{S}_{\lambda_x^{(2)} \lambda_x^{(2)}}(q) &= -\overline{\chi}_0(q) \ ,
\end{aligned} \tag{4.61}$$

respectively. The generalized Lindhard functions $\overline{\chi}_n(q)$ are given by

$$\overline{\chi}_n(q) = -\frac{2}{\mathcal{N}} \sum_k \left(\varepsilon_{\vec{k}} + \varepsilon_{\vec{k}+\vec{q}} \right)^n \overline{G}(k) \, \overline{G}(k+q) \quad , \quad n = 0, 1, 2 \, , \tag{4.62}$$

with the single–particle Green function

$$\overline{G}(k) = \frac{1}{i\omega_n - 2\varepsilon_{\vec{k}} \delta/(1+\delta) - \lambda_o^{(2)} + \mu} \ . \tag{4.63}$$

Following Li, Sun and Wölfle [311] the spin and charge susceptibilities defined by

$$\chi_s(q) = \sum_{\sigma\sigma'} \sigma\sigma' \langle \delta n_\sigma(-q) \delta n_{\sigma'}(q) \rangle \tag{4.64}$$

$$\chi_c(q) = \sum_{\sigma\sigma'} \langle \delta n_\sigma(-q) \delta n_{\sigma'}(q) \rangle \ , \tag{4.65}$$

may be rewritten as functional integrals over the corresponding SB fields:

$$\chi_s(q) = 4p_o^2 \langle \delta p_z(-q) \delta p_z(q) \rangle \ , \tag{4.66}$$

$$\chi_c(q) = 4e^2 \langle \delta e(-q) \delta e(q) \rangle \ . \tag{4.67}$$

Here the two–point correlation functions are related to the inverse fluctuation matrix by

$$\langle \delta\phi_\alpha(-q) \delta\phi_\beta(q) \rangle = \frac{1}{2} \left(\mathcal{S}^{-1} \right)_{\alpha\beta} \ . \tag{4.68}$$

More explicitly, we have

$$\chi_s(q) = 2p_o^2 \left(\mathcal{S}_s{}^{-1} \right)_{p_x p_x} = \frac{2p_o^2}{det\underline{S}_s} \mathcal{S}_{\lambda_x^{(2)} \lambda_x^{(2)}} \ , \tag{4.69}$$

$$\chi_c(q) = 2e^2 \left(\mathcal{S}_c{}^{-1} \right)_{ee} = \frac{-2e^2 p_o^2}{det\underline{S}_c} \mathcal{S}_{\lambda_o^{(2)} \lambda_o^{(2)}} \ . \tag{4.70}$$

Then, after a lengthy but straightforward calculation, we can the derive following concise expression for both the dynamic spin and charge susceptibility of the t–t'–J model:

$$\chi_{s,c}(q) = \frac{\overline{\chi}_0(q)}{1 + A_{s,c}(\vec{q})\,\overline{\chi}_0(q) + B_{s,c}\overline{\chi}_1(q) + \frac{1}{4}B_{s,c}^2\left\{\overline{\chi}_1^2(q) - \overline{\chi}_0(q)\overline{\chi}_2(q)\right\}}\ , \tag{4.71}$$

where

$$\begin{aligned} A_s(\vec{q}) &= \frac{\delta}{(1+\delta)^3}\Big\{\tilde{\varepsilon}(\vec{q}) + 3\tilde{\varepsilon}(0)\Big\} + \frac{1}{2}J(\vec{q})\ , \\ A_c(\vec{q}) &= \frac{1}{\delta(1+\delta)^3}\Big\{\tilde{\varepsilon}(\vec{q}) - (4\delta+1)\tilde{\varepsilon}(0)\Big\} - \frac{1}{2}J(\vec{q})\ , \\ B_s &= \frac{2\delta}{(1+\delta)^2}\ , \qquad B_c = -\frac{2}{(1+\delta)^2}\ , \end{aligned} \tag{4.72}$$

and

$$J(\vec{q}) = J\left(\cos q_x + \cos q_y\right)\ . \tag{4.73}$$

The response functions (4.71), which exhibit a similar analytical structure as for the Hubbard model [311, 312], do not have the standard RPA form (4.50) since higher–order Lindhard functions $\overline{\chi}_n(\vec{q})$ are involved. Note that for the t–(t')–J model the coefficients $A_{s,c}$ and $B_{s,c}$ are given in a much simpler and more explicit form.

4.4.2 Numerical results [126, 310]

To make the discussion of (4.71) more quantitative, we have numerically evaluated the wave–vector– and frequency–dependent spin susceptibility $\chi_s(\vec{q},\omega) = \chi_s'(\vec{q},\omega) + \chi_s''(\vec{q},\omega)$ for different band fillings and model parameters t'/t, J/t. Let us first consider the static susceptibility $\chi_s(\vec{q})$, where we are primarily interested in the instability line of the paraphase against magnetic structures (determined from the poles of $\chi_s(\vec{q})$ in $\vec{q}$ space), as suggested from the magnetic phase diagram (Figs. 4.3 and 4.5).

Static spin susceptibility

Starting with the t–J model, we show some representative results for $\chi_s(\vec{q})$ (a,c,e) and the response functions $\overline{\chi}_n(\vec{q})$ (b,d,f) along the high–symmetry directions of the square lattice Brillouin zone in Fig. 4.18. For low electron densities ($\delta = 0.75$, Fig. 4.18 (a,b)), the SB renormalized quasiparticle band structure has a nearly circular Fermi surface. In the small–$\vec{q}$ region, the weak dependence on $\vec{q}$ of $\overline{\chi}_0$ and χ_s (for small J/t) is in accord with the flatness of the response function $\overline{\chi}_0(\vec{q})$ for the 2D parabolic band dispersion up to the Kohn anomaly at $2k_F$ [313]. Note that for small wave–numbers, the enhancement of χ_s with respect to $\overline{\chi}_0$ decreases with increasing J. The Kohn anomalies at $\vec{Q}_K = 2\vec{k}_F$ (joining two points on the FS with anti-parallel Fermi velocities) are reflected in maxima of $\overline{\chi}_0$ and χ_s. In the (0,1)– and (1,1)–directions the anomalies occur at $\vec{Q}_{K1} = (0, 2.56)$ and $\vec{Q}_{K2} = (1.74, 1.74)$, respectively, where $|\vec{Q}_{K1}|/|\vec{Q}_{K2}| = 1.04$ expresses the very small FS anisotropy (for the square FS in the $\delta = 0$ case, we have $|\vec{Q}_{K1}|/|\vec{Q}_{K2}| = \sqrt{2}$). Let us point out that for $J/t = 4$, at $\delta_c^{(1,1)} = 0.69$ the paraphase is unstable against the $(1,1)$–spiral state (see the sharp structure in χ_s at $\vec{Q}_{K2} = (1.85, 1.85)$). However, this transition is not realized since the AFM–PM phase separated state is lower in energy (cf. Fig. 4.7). The instability against phase separation cannot be seen in $\chi_s(\vec{q})$.

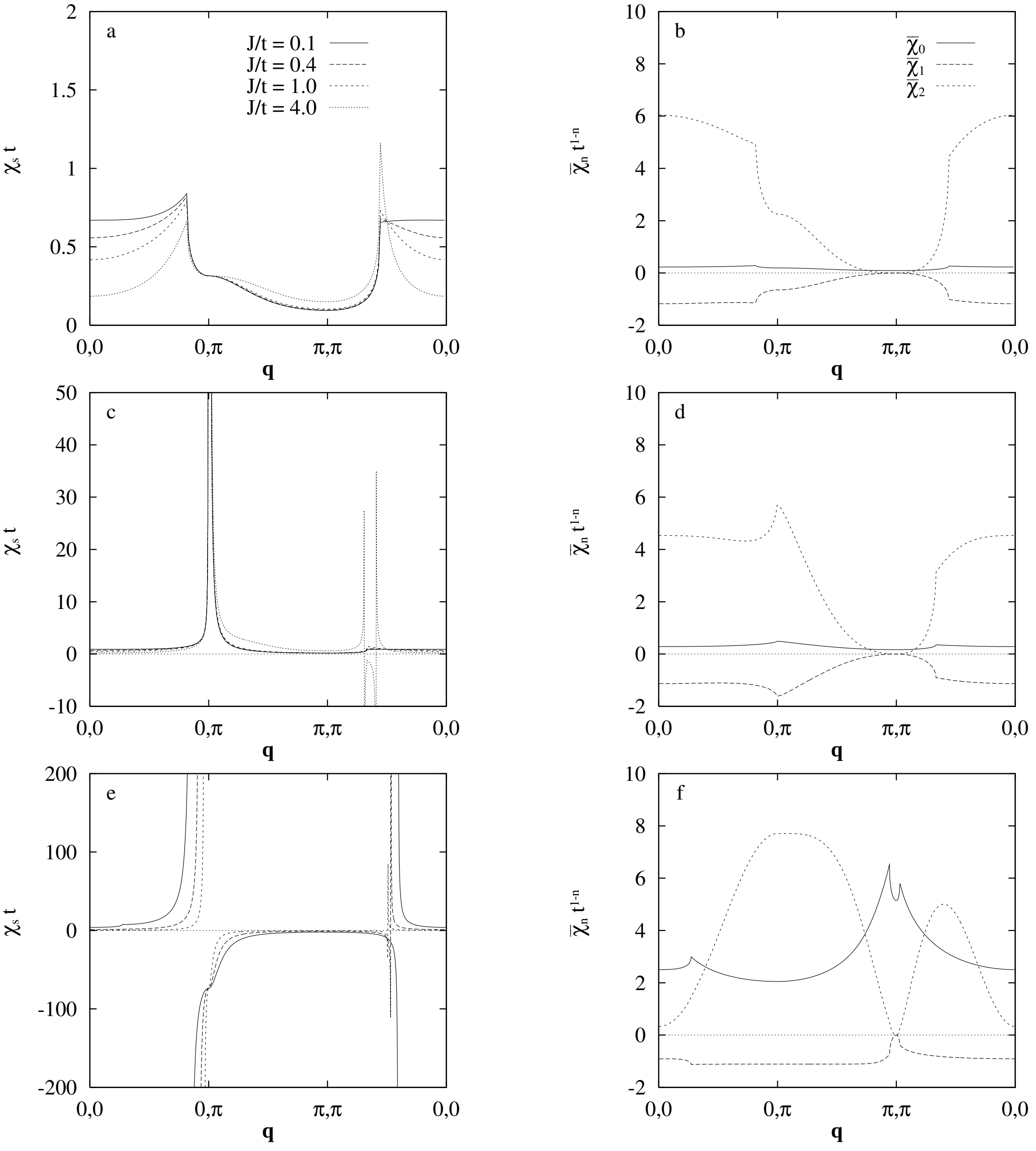

Figure 4.18: Static spin susceptibility as a function of $\vec{q}$ for different band fillings $\delta = 0.75$ (a), $\delta^{(1,\pi)} = 0.6294$ (c), and $\delta = 0.1$ (e). For comparison, the corresponding response functions $\overline{\chi}(\vec{q})$ are shown in (b), (d), and (f), respectively.

In Fig. 4.18 (c) and (d) the results at the critical hole concentration $\delta_c^{(1,0)} = 0.6294$ for the second–order PM-$(0,\pi)$- $[(1,\pi)$-] state phase transition (which is nearly independent of J [268], cf. Fig. 4.3) are depicted. Along the (0,1)–direction, the Kohn anomaly of $\overline{\chi}_n(\vec{q})$ occurs at $\vec{Q}_{K1} = (0,\pi)$ which results in a divergence of χ_s at $\vec{Q}_{K1}$. Let us emphasize that this instability is mainly governed by the pronounced $\vec{q}$–dependence of the function $\overline{\chi}_2(\vec{q})$ (on the contrary, $\overline{\chi}_0(\vec{q})$ for larger δ is nearly constant in the whole Brillouin zone). Thus the instability line determined from the poles of the paramagnetic spin susceptibility coincides with the phase boundary between the paraphase and the $(0,\pi)$– $[(1,\pi)$–] state calculated by the saddle–point solution. Note that $\vec{Q}_{K2} = (2.1, 2.1)$ and $|\vec{Q}_{K1}|/|\vec{Q}_{K2}| = 1.06$ expresses the increasing FS anisotropy with decreasing δ. For $J/t = 0.4$, the sharp structures in the *paramagnetic* susceptibility $\chi_s(\vec{q})$ near $\vec{Q}_{K2}$ reveal that the system has passed the PM–(1,1)–spiral instability point.

For comparison with the above results and with the spin fluctuation theory by Tanamoto *et al.* [152], in Fig. 4.18 we have plotted $\chi_s(\vec{q})$ for $\delta = 0.1$ lying far in the instability region (cf. Figs. 4.3, 4.18 (a,c)), where magnetically ordered states are realized. At $\delta = 0.1$ ('rounded–square' FS), the Kohn anomalies in $\overline{\chi}_0(\vec{q})$ appear at $\vec{Q}_{K1} = (0, 2\pi - 2k_F)$, where $2k_F = 5.4 > \pi$ and the q_x–component is reduced into the first Brillouin zone (Umklapp scattering), and at the 'pseudo–nesting' vector $\vec{Q}_{K2} = (3.0, 3.0)$ $(2k_F/|\vec{Q}_{K2}| = 1.27)$ (see Fig. 4.18 (f)). In addition, a sharp incommensurate peak occurs at $(\pi - \eta, \pi)$, $\eta \simeq 0.2$, which is higher in magnitude than the Kohn peak. A similar behaviour of $\overline{\chi}_0(\vec{q})$ in the small–doping region was also found in previous RPA–like fluctuation theories for the t–J [152] (cf. Sec. 4.3.2) and Hubbard models (see, e.g., Refs. [314, 124]). Whereas in the spinon–holon theory by Tanamoto *et al.* [152], $\chi_s(\vec{q})$ behaves qualitatively similar as $\overline{\chi}_0(\vec{q})$ and the maximum of $\overline{\chi}_0(\vec{q})$ at $(\pi - \eta, \pi)$ may give rise to a spiral order for small δ $(0 < \eta \ll \pi)$, in our SB approach the situation is quite different. The instability occurs, at much larger values of δ against the $(0, \pi)$ $[(1, \pi)]$ ordered state which is due to the predominant role of $\overline{\chi}_2(\vec{q})$ near $(0, \pi)$.

Let us now consider the t–t'–J model. As shown in Fig. 4.19 for different ratios t'/t, the saddle–point phase boundary PM$\rightleftharpoons$ $(1, \pi)/(0, \pi)$–spiral (cf. Fig. 4.5) coincides with a divergence of $\chi_s((0, \pi), 0)$ proving again the consistency of both approaches. Obviously, the deviation of $\chi_s(q)$ from the standard RPA form (4.50), $\chi_s(\vec{q}, \omega) = \chi_o(\vec{q}, \omega)/[1 + J(\vec{q})\chi_o(\vec{q}, \omega)/2]$ [50, 300, 45], is necessary to reproduce the phase boundaries in our SB phase diagram. To elucidate the influence of t' on the detailed $\vec{q}$–dependence of the response functions $\overline{\chi}_n(\vec{q})$, in Fig. 4.20 we have plotted $\overline{\chi}_n(\vec{q})$ along the path Γ–X–M–Γ in the square lattice Brillouin zone.

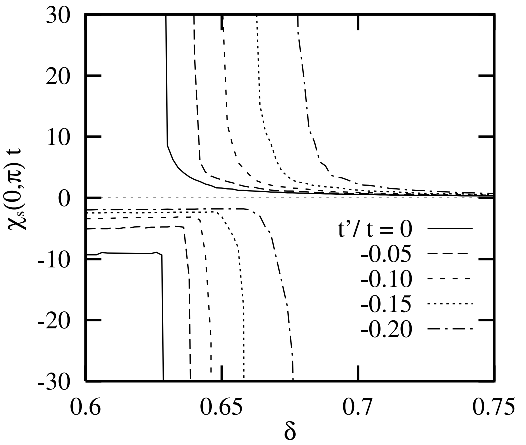

Figure 4.19: Doping dependence of the static spin susceptibility $\chi_s((0, \pi), 0)$ near the PM$\rightleftharpoons$ $(0, \pi)$–spiral phase transition for $J/t = 0.4$ and different ratios t'/t.

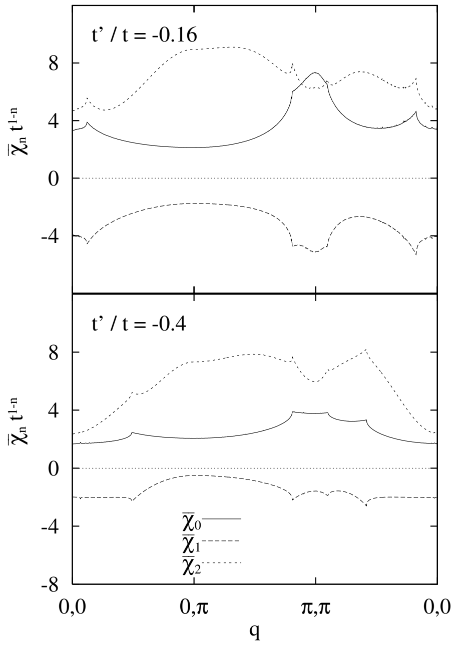

Figure 4.20: Response functions $\overline{\chi}_n(\vec{q})$ along the highly symmetric directions of the Brillouin zone at doping level $\delta = 0.1$.

The point we would like to emphasize here is the predominant role of $\overline{\chi}_1(\vec{q})$ and $\overline{\chi}_2(\vec{q})$ with increasing ratio $|t'/t|$. The higher–order Lindhard functions $\overline{\chi}_1(\vec{q})$ and $\overline{\chi}_2(\vec{q})$ differ in their $(\vec{q},\ \omega)$–dependence significantly from the ordinary Lindhard function $\overline{\chi}_0(\vec{q})$. Recent work for the 1D Hubbard model [312] shows the importance of these extended Lindhard functions for a consistent treatment of the dynamical charge correlations as well.

Although to be fully consistent one has to calculate $\chi_s(\vec{q})$ also for the magnetically ordered phases, the behaviour of the *paramagnetic* susceptibility can be taken as an indication that spiral states are good approximate candidates for the ground state of the t–t'–J model near half–filling.

Dynamic spin susceptibility

To study the spin dynamics in the paraphase, in Fig. 4.21 the results for $\chi_s'(\vec{q},\omega)$ (a) and $\chi_s''(\vec{q},\omega)$ (b) of the t–J model with $\delta = 0.63$ at fixed $\omega/t = 0.1$ versus $\vec{q}$ are shown. For finite frequencies, the sharp Kohn peak in $\chi_s'(\vec{q},\omega = 0)$ at $\vec{Q}_{K1}$ near $(0,\pi)$ is split into two incommensurate maxima. This may be interpreted as follows. The small energy transfer ω/t creates an effective momentum of the particle–hole pairs which slightly deviates from $\vec{Q}_{K1}$ resulting in an incommensurate peak structure of $\chi_s'(\vec{q},\omega)$ (analogous to that found for $\overline{\chi}_0(\vec{q})$ in the case of Fig. 4.18 (f)). In correspondence with this, the spectral weight $\chi_s''(\vec{q},\omega)$ has a pronounced structure near $(0,\pi)$. The vanishing of χ_s'' in some $\vec{q}$–region is also known from the Lindhard function for the free electron gas. With increasing frequency the separation between the incommensurate peaks in χ_s' increases and the structure is smeared out (especially, the ratio of the maximum height to the minimum at $(0,\pi)$ decreases [310]). At the same time, the features in χ_s'' near $(0,\pi)$ become less pronounced. For $J/t = 4$, in passing the PM$\rightleftharpoons$(0,π)–state transition point with increasing ω, $\chi_s'(\vec{q},\omega)$ at $\vec{q} = \vec{Q}_{max}^{(0,\pi)}(\omega)$ develops similar structures as for the δ–driven transition at $\omega = 0$ (cf. Fig. 4.18). The imaginary part reveals a pronounced absorption.

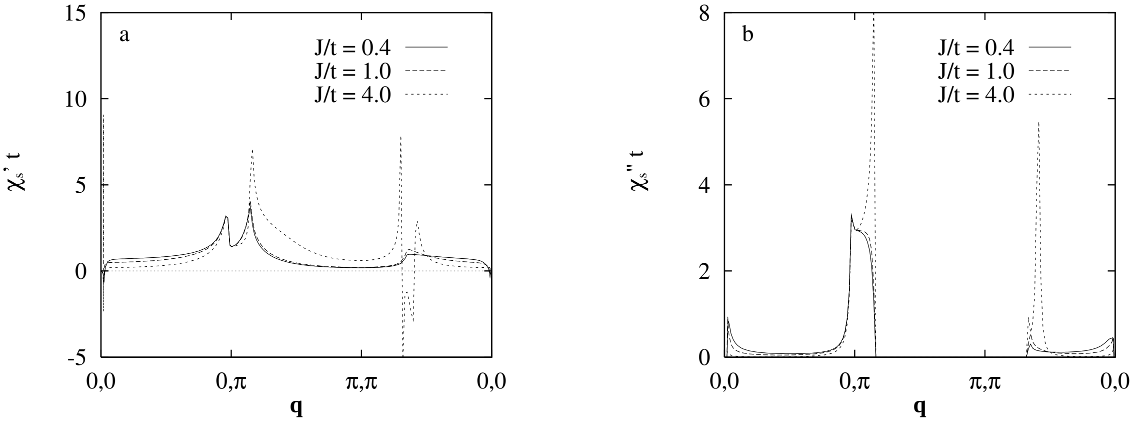

Figure 4.21: Real (a) and imaginary (b) parts of the dynamic spin susceptibility for the t–J model as a function of $\vec{q}$ for $\delta = 0.63$ and $\omega/t = 0.1$.

To investigate this transition region in more detail, in Fig. 4.22 the real (a) and the imaginary (b) part of $\chi_s((0,\pi),\omega)$ are shown as functions of ω for various doping levels $\delta \gtrsim \delta_c^{(0,\pi)}(\omega = 0)$. Approaching $\delta_c^{(0,\pi)}(\omega = 0)$ from above, a sharp maximum in χ_s' and χ_s'' develops at $\delta_c^{(0,\pi)}(\omega_c)$. The pronounced absorption maxima at $\omega_c/t = 0.0112$ describes the excitation of a collective mode ((0,π)–paramagnon). Note that $\delta_c^{(0,\pi)}(\omega > 0) \gtrsim \delta_c^{(0,\pi)}(\omega = 0)$. For

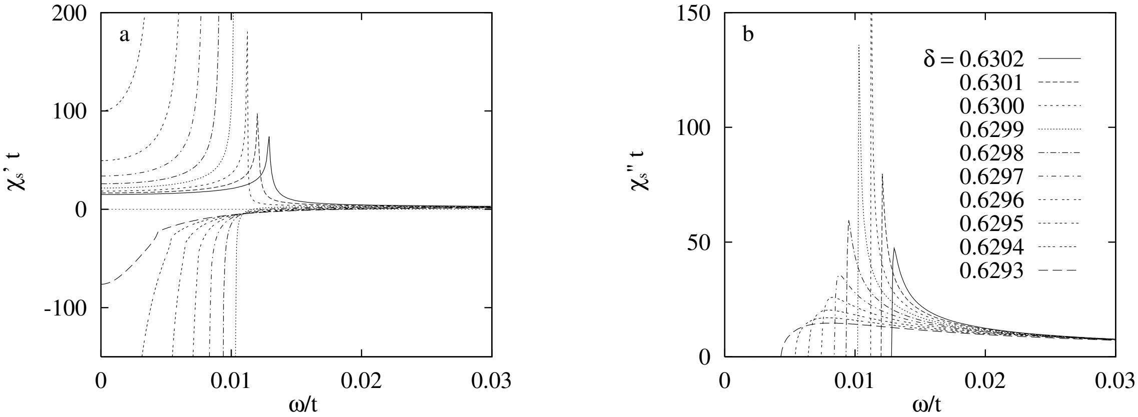

Figure 4.22: Frequency dependences of the real (a) and imaginary (b) parts of the spin susceptibility near the PM$\rightleftharpoons$ $(0,\pi)$–state phase transition for $J/t = 0.4$, $\vec{q} = (0,\pi)$ and different band fillings around $\delta_c^{(0,\pi)}$.

$\delta \lesssim \delta_c^{(0,\pi)}(\omega_c)$, $\chi_s'((0,\pi),\omega)$ exhibits, as a function of ω, a similar structure as $\chi_s'(\vec{q},\omega = \text{const.})$ below the transition point (cf. Figs. 4.18 and 4.21). If, for a given value of δ, the wave–vector deviates from the Kohn anomaly value, there occurs a kinetic gap in the spectral weight χ_s'' (Fig. 4.22 (b); compare the discussion given in Refs. [124]). The gap formation may be explained by the excitations of particle–hole pairs with an effective momentum $\vec{Q}_{K1}$ spanning the FS and with a finite spectral weight. In Fig. 4.23 the frequency dependences of $\chi_s'(\vec{q},\omega)$ and $\chi_s''(\vec{q},\omega)$ for larger doping ($\delta = 0.75$), $J/t = 0.4$ ($t' = 0$) and at different fixed $\vec{q}$–values are shown. They exhibit the characteristic behaviour of response functions (in accordance with Kramers–Kronig relations), e.g., the zero–crossing of χ_s' at the maximum of χ_s''. At $\vec{q} = \vec{Q}_{K1} = (0, 2.56)$, where $\chi_s(\vec{q})$ has a maximum (cf. Fig. 4.18 (a)), the spectral weight describes the particle–hole continuum. As seen in Fig. 4.23, the kinetic gap increases with increasing deviation of q_x from the anomaly value.

To summarize, in this section we have calculated the two–point dynamic response functions in the t–t'–J model within the SRI SB approach taking into account the Gaussian fluctuations around the paramagnetic saddle point. Our main results are the following:

(i) For the spin and charge susceptibilities, we have derived explicit analytical expressions going beyond the standard RPA form.

(ii) We have performed a detailed numerical evaluation of the spin susceptibility for arbitrary frequencies, wave–vectors, band fillings and exchange interactions. The static and dynamic susceptibilities are found to be qualitatively affected by the SB–renormalized Fermi surface geometry.

(iii) The instability line of the paraphase against incommensurate magnetic order, determined by a divergence in the static susceptibility, is in agreement with the phase boundary in the saddle–point phase diagram.

(iv) Near the PM$\rightleftharpoons$ $(0,\pi)$–state phase transition, we have found a collective spin–fluctuation mode ((0,π)–paramagnon), where the spectral weight has a kinetic gap followed by a sharp peak structure.

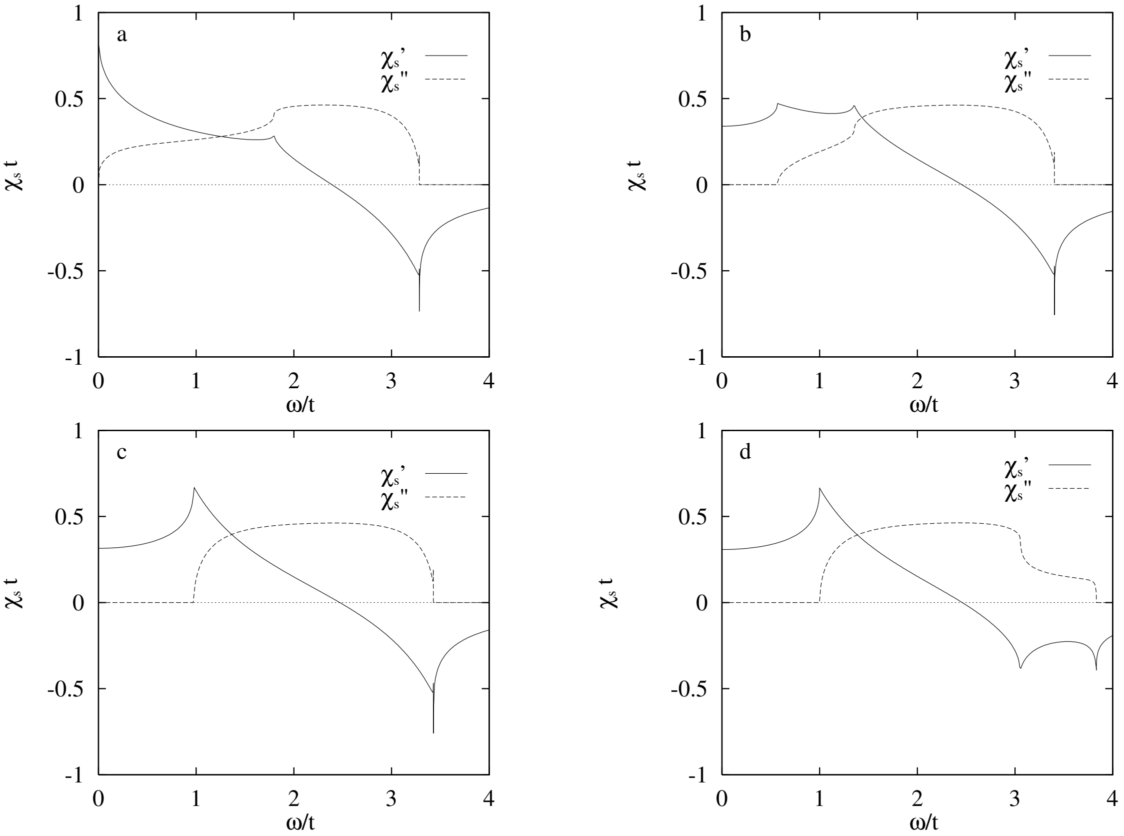

Figure 4.23: Frequency dependence of the spin susceptibility for $J/t = 0.4$, $\delta = 0.75$ and different wave–vectors $\vec{q} = (0, 2.56)$ (a), $\vec{q} = (0, 2.9)$ (b), $\vec{q} = (0, \pi)$ (c), and $\vec{q} = (0.24, \pi)$ (d).

Chapter 5

Theory of magnetic short–range order for the Hubbard model

As revealed by neutron scattering [315] and nuclear magnetic resonance [316, 317, 318] experiments, in the normal state of high–T_c superconductors there exist pronounced antiferromagnetic spin correlations which are ascribed to the electronic interactions within the CuO_2 planes. In particular for the slightly doped cuprates, the strong Coulomb correlations on the Cu sites are believed to result in a considerable AFM short–range order (SRO) [36, 38]. Knight–shift [318] and bulk measurements [318, 41, 40] of the spin susceptibility $\chi(T,\delta)$ in $La_{2-x}Sr_xCuO_4$ show a maximum in the doping dependence as well as, for moderate hole doping ($\delta \leq 0.21$), in the temperature dependence, where the temperature of the maximum decreases with increasing doping (cf. Sec. 1.3.1). Such a behaviour, also observed in $YBa_2Cu_3O_{6+x}$ ($x \leq 0.92$) [319, 320], may be qualitatively understood as an effect of AFM short–range order which decreases with increasing doping and temperature.

Up to now there have been only a few attempts, based on one–band [289, 92, 152, 321] and three–band [38] correlation models, to describe the unusual doping and temperature dependence of the normal–state susceptibility. In the t–t'–J model, a maximum in χ was obtained for the Pauli susceptibility of a strongly renormalized quasiparticle band [289] or for the RPA slave–boson susceptibility [152] showing a cusp in the temperature dependence at the transition to the singlet RVB state. In a semi–phenomenological weak–coupling approach to the one–band Hubbard model [321], the zero–temperature susceptibility was found to increase upon doping. The role played by SRO in explaining the normal–state susceptibility was investigated on the basis of a slave–boson CPA (coherent potential approximation) approach to the three–band Hubbard model [38]. This theory, however, is self-consistent only at the single–site level and does not hold at very low temperatures. Thus, an improved treatment of SRO in the paraphase of itinerant correlation models, which is valid also at $T = 0$, is highly desirable.

In this chapter we present the main features of a self–consistent slave–boson theory of magnetic SRO in the one–band Hubbard model, which has been proposed recently by Trapper, Ihle, and Fehske [39, 322].

5.1 Magnetic SRO versus LRO in the 2D Hubbard model [39]

In spite of the numerous analytical approaches to the description of magnetic correlations in the Hubbard model, there are only a few methods designed for the investigation of SRO. For example, in previous Hubbard–Stratonovich/CPA theories the free–energy functional can be transformed to an effective Ising model [323, 324], where the SRO is treated in the Bethe cluster approximation [323]. At $T = 0$, however, those theories reduce to the Hartree–Fock approximation in both the weak– and strong–coupling limits [325] and therefore neglect important correlations.

On the other hand, as pointed out in the preceding section, in the scalar [156] and spin–rotation–invariant [166] SB approaches, an appreciable part of the correlations is taken into account even at the saddle point. At this level of approximation, the resulting SB mean–field theory of the Hubbard model has been explored by many authors [156, 180, 270, 167, 177, 271] by allowing for a variety of (translational–invariant) symmetry broken solutions corresponding to different magnetic *long–range ordered* (LRO) states. Typical results for the magnetic ground–state phase diagram of the 2D Hubbard model are shown in Fig. 5.1 [177, 271]. Clearly, the stability region of LRO phases is overestimated in such mean–field–like approaches. Attempts to include non–uniform spin arrangements (e.g. domain walls [327]) or the effects of magnetic SRO [328] give strong evidence that the region of magnetic LRO is drastically

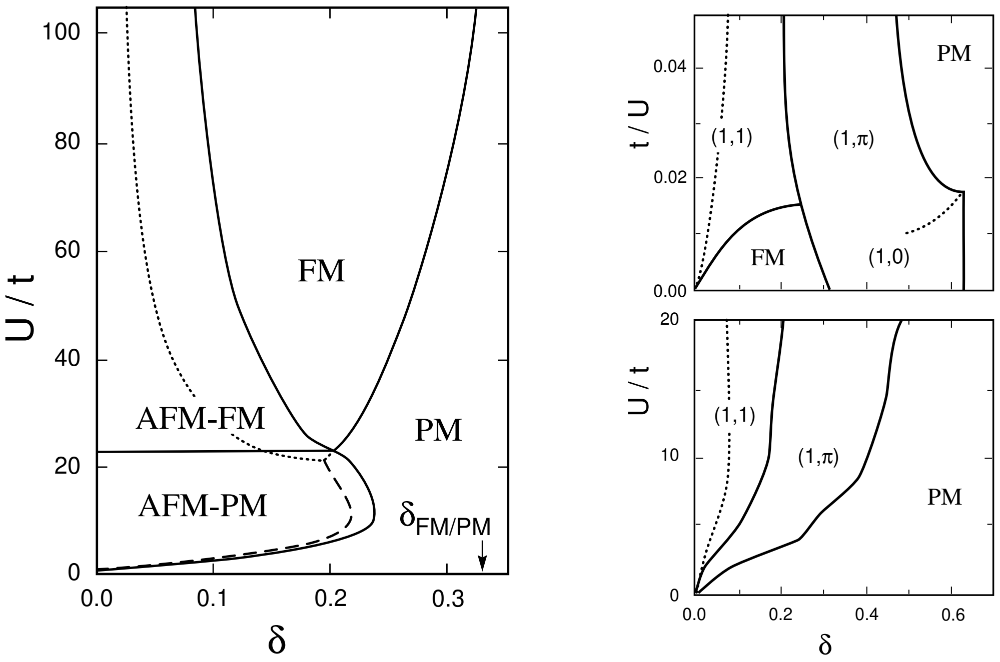

Figure 5.1: Magnetic phase diagram of the 2D Hubbard model as obtained from scalar two–sublattice KR (left panel [177]) and SRI KR (right panels, re-drawn from [146]) slave–boson mean–field theories. The restricted phase diagram to the left contains homogeneous PM, FM and, at $\delta = 0$, AFM states. The AFM to FM (PM) transition line is given by the dotted (dashed) curve. The AFM as well as the FM are not fully polarized below a critical value of U. Allowing for phase–mixing, regions with AFM–FM and AFM–PM phase separation occur. Let us emphasize the qualitative agreement with the phase diagram calculated by Fazekas *et al.* [326] using the Gutzwiller variational method for the infinite–dimensional Hubbard model. Contrary to their results, however, we found that the FM–PM transition is always of first order. Taking incommensurate magnetic phases into consideration it is found that the AFM state at half–filling develops into an (1,1)–spiral state upon doping (see right panel). Although the inclusion of spiral solutions decreases the concave curvature of $f(\delta)$, an instability towards phase separation (dotted line) still exists.

reduced [146]. However, as yet all previous SB theories do not take into consideration SRO effects in a fully self–consistent way.

Therefore, including magnetic SRO via a *nonlocal* saddle–point solution of the SB functional integral, we expect to obtain qualitatively new results concerning the stability of magnetic LRO versus SRO, the problem of phase separation, and the doping dependence of the spin susceptibility.

5.1.1 Transformation to an effective Ising model

We start from the scalar KR SB representation (2.16)–(2.19) of the Hubbard model

$$\mathcal{H} = \sum_{i,j,\sigma} t_{ij} z^{\dagger}_{i\sigma} f^{\dagger}_{i\sigma} f_{j\sigma} z_{j\sigma} + U \sum_{i} d^{\dagger}_{i} d_{i} - h \sum_{i,\sigma} \sigma f^{\dagger}_{i\sigma} f_{i\sigma} \tag{5.1}$$

in an uniform external magnetic field h. The bosonic hopping operators $z^{(\dagger)}_{i\sigma}$ are given by Eqs. (2.23) and (2.24). Integrating out the pseudofermionic fields $(f^{(\dagger)}_{i\sigma})$ in the functional–integral representation of the partition function and using the radial gauge and the static approximation for the Bose fields ($p_{i\sigma}$, d_i, $\lambda^{(2)}_{i\sigma}$, where the e_i fields are eliminated by the saddle–point approximation for $\lambda^{(1)}_i$ [325]), we get

$$\begin{aligned} \mathcal{Z} &= \int [\mathcal{D}d][\mathcal{D}d^*][\mathcal{D}n][\mathcal{D}\nu][\mathcal{D}m][\mathcal{D}\xi] \exp\left\{-\beta \Psi(\{d, d^*, n, \nu, m, \xi\})\right\} , && (5.2)\\ \Psi &= \sum_{i} (U d^*_i d_i - n_i \nu_i + m_i \xi_i) + \tfrac{1}{\pi} \int d\omega f(\omega - \mu) \mathrm{Im}\ \mathrm{Tr} \ln \left[-G^{-1}_{ij\sigma}(\omega)\right] , && (5.3)\\ G^{-1}_{ij\sigma}(\omega) &= [\omega - \nu_i + \sigma(\xi_i + h)]\delta_{ij} - z^*_{i\sigma} z_{j\sigma} t_{ij} , && (5.4) \end{aligned}$$

where

$$m_i = \sum_{\sigma} \sigma p^2_{i\sigma} , \qquad \xi_i = -\tfrac{1}{2} \sum_{\sigma} \sigma \lambda^{(2)}_{i\sigma} , \tag{5.5}$$

$$n_i = \sum_{\sigma} p^2_{i\sigma} + 2 d^*_i d_i , \quad \nu_i = \tfrac{1}{2} \sum_{\sigma} \lambda^{(2)}_{i\sigma} , \tag{5.6}$$

and

$$z_{i\sigma} = \frac{\sqrt{2}\left[\sqrt{(n_i + \sigma m_i - 2 d^*_i d_i)(1 - n_i + d^*_i d_i)} + d_i \sqrt{n_i - \sigma m_i - 2 d^*_i d_i}\,\right]}{\sqrt{(n_i + \sigma m_i)(2 - n_i - \sigma m_i)}} . \tag{5.7}$$

In Eqs. (5.5) and (5.6), m_i and n_i are the bosonic representations of the local magnetization and particle number defined analogously to its fermionic counterparts $m^f_i = \sum_\sigma \sigma f^\dagger_{i\sigma} f_{i\sigma}$ and $n^f_i = \sum_\sigma f^\dagger_{i\sigma} f_{i\sigma}$, respectively. Since ξ_i couples to m_i as a magnetic field we denote ξ_i by ‘internal magnetic field’.

To proceed, we remove the non–diagonal randomness in the transfer term of (5.4) along the lines indicated by Shiba [329]. Here we introduce the modified Shiba transformation

$$G_{ij\sigma} \rightarrow \hat{G}_{ij\sigma} = \sum_{lm} \hat{z}^*_{il\sigma} G_{lm\sigma} \hat{z}_{mj\sigma} , \tag{5.8}$$

where

$$\hat{z}_{ij\sigma} = z_{i\sigma} \delta_{ij} , \qquad q_{i\sigma} = |z_{i\sigma}|^2 . \tag{5.9}$$

Then, under the trace operation in (5.3), $G^{-1}_{ij\sigma}(\omega)$ can be replaced exactly by

$$\hat{G}^{-1}_{ij\sigma}(\omega) = \frac{\omega - \nu_i + \sigma(\xi_i + h)}{q_{i\sigma}}\delta_{ij} - t_{ij} \ . \tag{5.10}$$

Next, we aim to incorporate the SRO by going beyond the PM saddle point. To this end we perform an expansion in terms of the *local* perturbation

$$V_{i\sigma}\delta_{ij} = -\hat{G}^{-1}_{ij\sigma} + \hat{G}^{o-1}_{ij\sigma} \ , \tag{5.11}$$

where $\hat{G}^{o-1}_{ij\sigma}(\omega)$ is the inverse PM saddle–point propagator obtained from (5.10) by replacing $q_{i\sigma} \to q^o_\sigma$, $\nu_i \to \nu^o$ and $\xi_i \to \xi^o$ (in this chapter, the supersript '^{o}' denotes the *uniform paramagnetic saddle–point value* without SRO).

For further approximations, it is convenient to separate $\hat{G}^o_{ij\sigma}$ into the diagonal ($\hat{G}^o_{ii\sigma}$) and off-diagonal components ($\hat{G}^{o\prime}_{ij\sigma}$) given by

$$\hat{G}^o_{ii\sigma}(\omega) = \frac{1}{N}\sum_{\vec{k}} \frac{q^o_\sigma}{\omega - E^o_{\vec{k}\sigma}} \ , \quad \hat{G}^{o\prime}_{ij\sigma}(\omega) = \frac{1-\delta_{ij}}{N}\sum_{\vec{k}} \frac{q^o_\sigma \, e^{i\vec{k}(\vec{R}_i - \vec{R}_j)}}{\omega - E^o_{\vec{k}\sigma}} \ , \tag{5.12}$$

where

$$E^o_{\vec{k}\sigma} = q^o_\sigma \varepsilon_{\vec{k}} + \nu^o - \sigma(\xi^o + h) \ , \tag{5.13}$$

and $\varepsilon_{\vec{k}} = -2t\sum_{i=1}^{D}\cos k_i$ is the unrenormalized tight–binding band in D dimensions. Returning to (5.3), we can rewrite

$$\begin{aligned} \mathrm{Tr}\ \ln\left[-\hat{G}^{-1}_{ij\sigma}(\omega)\right] &= \mathrm{Tr}\ \ln\left[-\hat{G}^{o-1}_{ij\sigma}(\omega)\right] + \mathrm{Tr}\ \ln\left[(1 - \hat{G}^o_{ii\sigma}(\omega)V_{i\sigma}(\omega))\delta_{ij}\right] \\ &\quad + \mathrm{Tr}\ \ln\left[\delta_{ij} - \hat{G}^{o\prime}_{ij\sigma}(\omega)T_{j\sigma}(\omega)\right] \end{aligned} \tag{5.14}$$

with the scattering matrix

$$T_{i\sigma}(\omega) = \frac{V_{i\sigma}(\omega)}{1 - \hat{G}^o_{ii\sigma}(\omega)V_{i\sigma}(\omega)} \ . \tag{5.15}$$

The second term on the r.h.s. of (5.14) yields a single–site fluctuation contribution to the functional (5.2), whereas the third term describes the coupling between the fluctuations at all sites and is responsible for SRO effects.

Treating the fluctuations of the local magnetizations m_i and the internal magnetic fields ξ_i on an equal footing, we express those fields by their amplitude and direction according to

$$m_i = \bar{m}_i s_i \ , \quad \xi_i = \bar{\xi}_i s_i \ , \text{ with } \ s_i = \pm \ . \tag{5.16}$$

Furthermore, we make the ansatz

$$b_i \to b_{s_i} \text{ with } \ b \in \{\bar{m}, \bar{\xi}, n, \nu, d^*, d\} \ , \tag{5.17}$$

which becomes relevant for the calculation of the uniform static spin susceptibility (Sect. 5.2); for $h = 0$, we have $b_{s_i} = b$. Then the partition function is given as

$$\mathcal{Z} = \sum_{\{s_i\}} \int [\mathcal{D}d_{s_i}][\mathcal{D}d^*_{s_i}][\mathcal{D}n_{s_i}][\mathcal{D}\nu_{s_i}][\mathcal{D}\bar{m}_{s_i}][\mathcal{D}\bar{\xi}_{s_i}] \exp\{-\beta\Psi(\{s_i\})\} \ . \tag{5.18}$$

Now we transform the free–energy functional $\varPsi$ to an effective Ising model along the lines indicated by Kakehashi [323]. By the identity

$$\varPsi(\{s_i\}) = \sum_{\{\alpha_i=\pm 1\}} \left(\prod_i \frac{1+s_i\alpha_i}{2} \right) \varPsi(\{\alpha_i\}) \tag{5.19}$$

we get

$$\varPsi(\{s_i\}) = \bar{\varPsi} - \sum_i \bar{h}_i s_i - \sum_{(ij)} \bar{J}_{ij} s_i s_j - \sum_{(ijk)} \dots \tag{5.20}$$

with

$$\bar{\varPsi} = \left(\tfrac{1}{2}\right)^N \sum_{\{\alpha_i\}} \varPsi(\{\alpha_i\}) \ , \tag{5.21}$$

$$\bar{h}_i = -\left(\tfrac{1}{2}\right)^N \sum_{\{\alpha_i\}} \alpha_i \varPsi(\{\alpha_i\}) \ , \tag{5.22}$$

$$\bar{J}_{ij} = -\left(\tfrac{1}{2}\right)^N \sum_{\{\alpha_i\}} \alpha_i \alpha_j \varPsi(\{\alpha_i\}) \ . \tag{5.23}$$

In the pair approximation, all terms of (5.14) involving more than two sites are neglected so that

$$\mathrm{Tr}\ \ln\left[\delta_{ij} - \hat{G}^{o\prime}_{ij\sigma} T_{j\sigma}(\alpha_j)\right] = \sum_{(ij)\sigma} \ln\left[1 - \hat{G}^{o\prime}_{ij\sigma} T_{j\sigma}(\alpha_j) \hat{G}^{o\prime}_{ji\sigma} T_{i\sigma}(\alpha_i)\right] \ , \tag{5.24}$$

and the higher–order terms in (5.20) vanish. Restricting ourselves to NN pairs $\langle ij \rangle$ only, the functional $\varPsi$ takes the form

$$\varPsi(\{s_i\}) = \bar{\varPsi} - \bar{h} \sum_i s_i - \bar{J} \sum_{\langle ij \rangle} s_i s_j \tag{5.25}$$

with

$$\begin{aligned}
\bar{\varPsi} &= -\tfrac{1}{\beta} \sum_{\vec{k}\sigma} \ln\left[1 + \mathrm{e}^{-\beta(E^o_{\vec{k}\sigma} - \mu)}\right] \\
&\quad + \tfrac{N}{2} \sum_{\alpha} \left\{ U d^*_\alpha d_\alpha - n_\alpha \nu_\alpha + \bar{m}_\alpha \bar{\xi}_\alpha + \sum_\sigma \left[\varPhi_{\alpha\sigma} + \tfrac{z}{4}\left(\varPhi_{\alpha\alpha\sigma} + \varPhi_{-\alpha\alpha\sigma}\right)\right] \right\} \ ,
\end{aligned} \tag{5.26}$$

$$\bar{h} = -\tfrac{1}{2} \sum_\alpha \alpha \left[U d^*_\alpha d_\alpha - n_\alpha \nu_\alpha + \bar{m}_\alpha \bar{\xi}_\alpha + \sum_\sigma \left(\varPhi_{\alpha\sigma} + \tfrac{z}{2} \varPhi_{\alpha\alpha\sigma}\right) \right] \ , \tag{5.27}$$

$$\bar{J} = -\tfrac{1}{4} \sum_{\alpha\sigma} \left(\varPhi_{\alpha\alpha\sigma} - \varPhi_{-\alpha\alpha\sigma}\right) \ , \tag{5.28}$$

where $\varPhi_{\alpha\sigma} = \varPhi_{i\sigma}(\alpha_i)|_{\alpha_i=\alpha}$ and $\varPhi_{\alpha\alpha'\sigma} = \varPhi_{\langle ij \rangle\sigma}(\alpha_i, \alpha_j)\Big|_{\substack{\alpha_i=\alpha \\ \alpha_j=\alpha'}}$, z is the coordination number, and

$$\varPhi_{i\sigma} = \tfrac{1}{\pi} \int d\omega f(\omega - \mu) \mathrm{Im}\ \ln\left[1 - \hat{G}^o_{ii\sigma} V_{i\sigma}(\alpha_i)\right] \ , \tag{5.29}$$

$$\varPhi_{\langle ij \rangle\sigma} = \tfrac{1}{\pi} \int d\omega f(\omega - \mu) \mathrm{Im}\ \ln\left[1 - \hat{G}^{o\prime}_{\langle ij \rangle\sigma} T_{j\sigma}(\alpha_j) \hat{G}^{o\prime}_{\langle ji \rangle\sigma} T_{i\sigma}(\alpha_i)\right] \ . \tag{5.30}$$

Let us emphasize that the parameters of the effective Ising model (5.25), in particular the Ising–exchange integral $\bar{J}$, are complicated functions of all SB fields and have to be determined self–consistently at each given interaction strength U and hole doping $\delta = 1 - n$.

5.1.2 Slave–boson saddle–point with SRO

To calculate the partition function (5.18) with the functional (5.25) in the saddle–point approximation incorporating SRO, we proceed in two steps. First, we perform the s_i–sum by means of the Bethe cluster approximation, i.e., we take into account only the nearest–neighbour SRO. Thereafter, we adopt the saddle–point approximation for all Bose fields b_α (Eq. (5.17)). Correspondingly, contrary to CPA approaches [38, 323], our theory incorporates SRO at the saddle–point in a fully self–consistent way at the pair approximation level.

In the Bethe approximation, the lattice is divided into $N/2$ clusters consisting of a central site (s_0) and its z nearest neighbours (s_l) which also belong to the surrounding clusters. Accordingly, the external–field term in (5.25) is weighted by a factor of z^{-1}. The Ising coupling to the neighbouring clusters is approximately taken into account by the effective Bethe field h^*. Thus, we have

$$\Psi = \bar{\Psi} + \frac{N}{2}\left(-\bar{h} s_0 - \left(\tfrac{1}{z}\bar{h} + h^* \right) \sum_{l=1}^{z} s_l - \bar{J} \sum_{l=1}^{z} s_0 s_l \right) \ . \tag{5.31}$$

From the probability W_α for the Ising spin α at the central site,

$$W_\alpha = \frac{1}{\mathcal{Z}_c} e^{\alpha\beta\bar{h}} \left\{ 2\cosh\left[\beta(\tfrac{1}{z}\bar{h} + h^* + \alpha\bar{J}) \right] \right\}^z \ , \tag{5.32}$$

where $\sum_\alpha W_\alpha = 1$ and $\mathcal{Z}_c$ is the cluster partition function, the Ising spin averages $\langle \ldots \rangle$ can be calculated. The field h^* is determined from the Bethe condition

$$\langle s_0 \rangle = \langle s_l \rangle \ , \tag{5.33}$$

where $\langle s_l \rangle = (z\beta\mathcal{Z}_c)^{-1} \partial\mathcal{Z}_c / \partial h^*$, which yields the self–consistency equation

$$h^* = \tfrac{z-1}{z}\bar{h} + \tfrac{z-1}{2\beta} \ln \left\{ \frac{\cosh\left[\beta(\frac{1}{z}\bar{h} + h^* + \bar{J}) \right]}{\cosh\left[\beta(\frac{1}{z}\bar{h} + h^* - \bar{J}) \right]} \right\} \ . \tag{5.34}$$

For the Ising–spin correlation function we get

$$\langle s_0 s_l \rangle = \sum_\alpha \alpha W_\alpha \tanh\left[\beta(\tfrac{1}{z}\bar{h} + h^* + \alpha\bar{J}) \right] \ . \tag{5.35}$$

Finally, adding a Bogoliubov free–energy term, the effective bosonic action is given by

$$\mathcal{S} = \beta\bar{\Psi} - \tfrac{N}{2} \left\{ \ln \mathcal{Z}_c - z\beta h^* \langle s_0 \rangle \right\} \ , \tag{5.36}$$

where we have omitted a constant entropy contribution. Note that for the 2D square lattice one can also use the exact paramagnetic Onsager solution [330], where it turns out that the nearest–neighbour correlation function in the Bethe approximation (Eq. (5.35)) becomes exact at zero temperature.

Only just now, we calculate the free energy in the saddle–point approximation for the Bose fields b_α=$\{\bar{m}_\alpha$, $\bar{\xi}_\alpha$, n_α, ν_α, d_α $\}$, where we take the saddle–point solution $d_\alpha^* = d_\alpha$. From $\partial\mathcal{S}/\partial b_\alpha = 0$ and the dependences on b_α of $\bar{J}$, $\bar{h}$, and h^* we obtain the self–consistency equations determining the saddle point with SRO, which can be cast to the form

$$\bar{m}_\alpha = \alpha \sum_\sigma \sigma n_{\alpha\sigma}^f \quad , \quad \bar{\xi}_\alpha = -\sum_\sigma Q_{\alpha\sigma}^f \frac{\partial q_{\alpha\sigma}}{\partial \bar{m}_\alpha} \ , \tag{5.37}$$

$$n_\alpha = \sum_\sigma n_{\alpha\sigma}^f \quad , \quad \nu_\alpha = \sum_\sigma Q_{\alpha\sigma}^f \frac{\partial q_{\alpha\sigma}}{\partial n_\alpha} \ , \tag{5.38}$$

$$U = -\sum_{\sigma} Q^f_{\alpha\sigma} \frac{\partial q_{\alpha\sigma}}{\partial d^2_{\alpha}} \, . \tag{5.39}$$

Here the pseudofermionic expression ($n^f_{\alpha\sigma}$) for the particle density is given by

$$\begin{aligned} n^f_{\alpha\sigma} &= \frac{1}{1+\alpha K_{\bar{h}}} \sum_{\alpha'} \left\{ (1+\alpha' K_{\bar{h}}) \frac{\partial \Phi_{\alpha'\sigma}}{\partial \lambda^{(2)}_{\alpha\sigma}} \right. \\ &\qquad \left. + \tfrac{z}{4} (1 + 2\alpha' K_{\bar{h}} + K_{\bar{J}}) \frac{\partial \Phi_{\alpha'\alpha'\sigma}}{\partial \lambda^{(2)}_{\alpha\sigma}} + \tfrac{z}{4} (1 - K_{\bar{J}}) \frac{\partial \Phi_{-\alpha'\alpha'\sigma}}{\partial \lambda^{(2)}_{\alpha\sigma}} \right\} \, , \end{aligned} \tag{5.40}$$

where

$$K_{\bar{h}} = \frac{\langle s_0 \rangle}{2} - \frac{z\beta h^*}{2(1-(z-1))L_{\bar{h}}} \left[1 - (z+1)\langle s_0\rangle^2 + z\langle s_0 s_l\rangle - (z-1)L_{\bar{h}}(1-\langle s_0\rangle^2) \right], \tag{5.41}$$

$$K_{\bar{J}} = \langle s_0 s_l \rangle + \frac{z\beta h^*}{(z-1)^{-1} - L_{\bar{h}}} \left[((z-1)^{-1} - L_{\bar{h}})(1 - \langle s_0 s_l\rangle)\langle s_0\rangle + L_{\bar{J}}(\langle s_0 s_l\rangle - \langle s_0\rangle^2) \right], \tag{5.42}$$

$$L_{\bar{h}} = \frac{1}{2} \sum_{\alpha} \alpha \tanh\left[\beta(\tfrac{1}{z}\bar{h} + h^* + \alpha\bar{J})\right] , \tag{5.43}$$

$$L_{\bar{J}} = \frac{1}{2} \sum_{\alpha} \tanh\left[\beta(\tfrac{1}{z}\bar{h} + h^* + \alpha\bar{J})\right] , \tag{5.44}$$

and $\lambda^{(2)}_{\alpha\sigma} = \nu_\alpha - \alpha\sigma\bar{\xi}_\alpha$. In Eqs. (5.37) to (5.39), $Q^f_{\alpha\sigma}$ is given by (5.40) with $\partial\lambda^{(2)}_{\alpha\sigma}$ replaced by $\partial q_{\alpha\sigma}$. The chemical potential is determined from the number condition $n = \sum_\alpha W_\alpha n_\alpha$ with n_α given by (5.38). At the saddle point, we have $n^f_{\alpha\sigma} = n_{\alpha\sigma} = (n_\alpha + \alpha\sigma\bar{m}_\alpha)/2$, where $n_{\alpha\sigma}$ is the bosonic expression. In the paraphase at $T = 0$, the free energy per site is given by $\bar{f}(h=0) = \frac{1}{N}\bar{\Psi} - \frac{z}{2}|\bar{J}| + \beta + \mu n$.

For vanishing local magnetization, $\bar{m}_\alpha = 0$, we have $V_{\alpha\sigma} = 0$ and (by (5.28) and (5.30)) $\bar{J} = 0$ so that there is no SRO, and the PM saddle point (with the external field h) is recovered from (5.37) to (5.39). Accordingly, there are two possible paraphases defined, for $h = 0$, by

$$\begin{aligned} &\text{PM} \quad\;\; : \langle s_i \rangle = 0 \, , \; \langle s_i s_j \rangle = 0 \; ; \; \bar{m} = 0 \; (\bar{J} = 0) \, , \\ &\text{SRO–PM} : \langle s_i \rangle = 0 \, , \; \langle s_i s_j \rangle \neq 0 \; ; \; \bar{m} > 0 \; (\bar{J} \neq 0) \, , \end{aligned} \tag{5.45}$$

where i and j are NN sites. At $T = 0$, the paraphase with antiferromagnetic (ferromagnetic) SRO has to be distinguished from the corresponding LRO phases, denoted shortly by AFM (FM): $\langle s_i \rangle = -\langle s_j \rangle = 1$, $\langle s_i s_j \rangle = -1$, $\bar{J} < 0$ $\quad$ ($\langle s_i \rangle = \langle s_j \rangle = 1$, $\langle s_i s_j \rangle = 1$, $\bar{J} > 0$). In the AFM phase there is a *finite* sublattice magnetization ($m_A = p^2_{A\uparrow} - p^2_{A\downarrow} = -m_B$) obtained from the A–B–saddle–point solution [180, 268]. Of course, the local–magnetization amplitude $\bar{m}$ of the SRO-PM phase differs from m_A; in particular, we found $\bar{m} \neq 0$ in parameter regions, where $m_A = 0$ (compare Fig. 5.1 with Fig. 5.3 (below)). Let us further stress that the characteristics of $\bar{J}$ have to be contrasted with the effective Ising–exchange energy $\tilde{J}$ occurring in previous Hubbard–Stratonovich/CPA approaches [323, 324], where $\tilde{J}$ couples thermally induced local moments and is finite also in the paraphase without SRO.

5.1.3 Phase diagram of the 2D Hubbard model

In Fig. 5.2 the ground–state energies of various phases are plotted as functions of δ at $U/t = 8$, where the 2D tight–binding unperturbed density of states is used. For comparison, we have also depicted the results obtained by the SRI SB saddle–point solution for incommensurate spiral LRO states [168] and by exact diagonalizations on a 4×4 lattice [229]. Most notably, in the doping region $0.045 \lesssim \delta \lesssim 0.21$ the ground–state energy of the SRO–PM phase is lower than that of the spiral phases and, moreover, lies very close to the exact data. At very small and higher dopings, where the $(1,1)$– and $(1,\pi)$–spirals become the ground state, respectively, our PM–SRO solution behaves less favourably. We suggest that the inclusion of spiral SRO within a spin–rotation–invariant SB theory may further improve the results in both doping regions. Next, let us discuss the stability of the PM, SRO–PM, and AFM phases in more detail. As shown in Fig. 1, for $U/t = 8$ we obtain an AFM $\rightleftharpoons$ SRO-PM phase transition of first order at the critical hole doping $\delta_{c_1} \simeq 0.04$ and a SRO–PM $\rightleftharpoons$ PM transition of second order at $\delta_{c_2} \simeq 0.26$. We would like to point out that in the SRO-PM phase the energy is a convex function of the particle density, so that this phase is locally stable against phase separation. There is much controversy about the problem of phase separation in the Hubbard model [71, 78, 331]. Whereas exact diagonalization [229] (see Fig. 5.2) and QMC studies [258] do not yield evidence of phase separation, in mean–field–like theories [168, 177, 332] the lowest energy state has a negative compressibility over a wide doping region ($\delta \lesssim 0.15$, cf. Figs. 5.1 and 5.2). In contrast, our SRO–PM state has a positive compressibility also at very low dopings ($\delta > \delta_{c_1} \simeq 0.04$). For $\delta \lesssim \delta_{c_1}$, both the AFM and $(1,1)$–spiral phases are locally unstable. Correspondingly, the existence of phase separation for $\delta \to 0$ remains an open problem. However, from our results we argue that an extended SRO theory which, e.g., includes a longer than nearest–neighbour ranged SRO may yield a convex free energy for all δ.

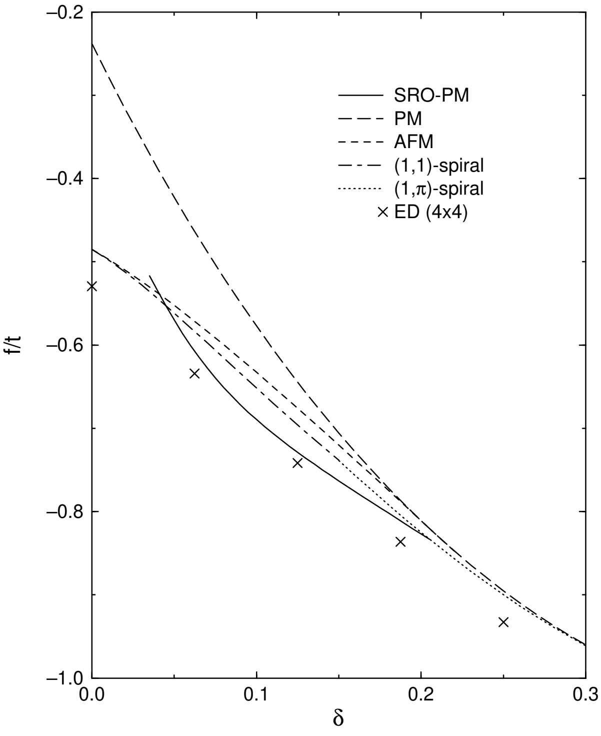

Figure 5.2: Ground–state energies of the 2D Hubbard model as functions of doping at $U/t = 8$. The energy of the SRO-PM phase is compared with SB [168] and ED [229] results.

Having established the quality of our method, in Fig. 5.3 the ground–state phase diagram is mapped out, where for numerical simplification we have used a semi–elliptic unperturbed density of states. Note that for $U/t = 8$, the critical dopings at the phase transitions, $\delta_{c_1} \simeq 0.03$ and $\delta_{c_2} \simeq 0.23$, nearly coincide with those given above. At large enough U/t ratios, the LRO is strongly suppressed in favour of SRO. For values of U/t being realistic for high–T_c cuprates ($U/t \simeq 8$, [112]), the AFM phase is destroyed at the critical hole doping $\delta_{c_1} \simeq 0.03$, which agrees with the experimentally observed value in $La_{2-x}Sr_xCuO_4$. Thus, the rapid disappearance of antiferromagnetism in high–T_c cuprates at very low hole dopings may be related to the

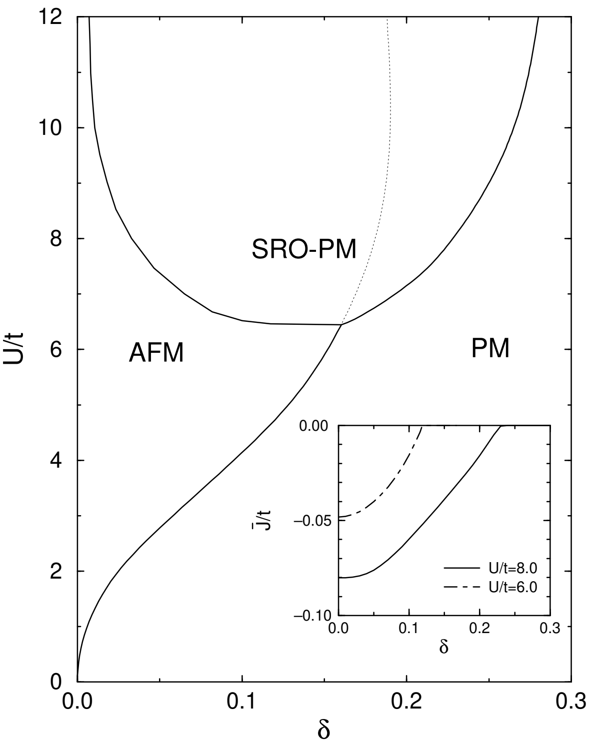

Figure 5.3: Ground–state phase diagram of the 2D Hubbard model, where AFM, PM, and SRO–PM denote the antiferromagnetic LRO phase, the paraphase without SRO, and the paraphase with SRO, respectively. The dotted line marks the well–known AFM$\rightleftharpoons$PM transition (cf. Fig. 5.1 [156, 180, 177]) which is suppressed by the SRO–PM phase. The effective antiferromagnetic exchange interaction ($\bar{J} < 0$) is shown in the inset.

persistence of a pronounced AFM SRO in the paraphase. The stability region of the SRO–PM phase at $U/t \simeq 8$, $0.03 \lesssim \delta \lesssim 0.23$, nearly coincides with the doping regime of $\mathrm{La_{2-x}Sr_xCuO_4}$ compounds, where, above T_c, the so–called 'strange metal' phase occurs. Correspondingly, the unconventional normal–state behaviour of high–T_c cuprates may be due to the presence of a considerable degree of SRO. The effective Ising–exchange integral $\bar{J}(\delta, U)$, shown in the inset of Fig. 5.3, is intimately related to the existence of SRO and reflects the interplay of local and itinerant magnetic behaviour. With decreasing magnetic correlations, i.e., with increasing δ and decreasing U/t, $|\bar{J}|$ decreases, as expected.

The behaviour of the local–magnetization amplitude $\bar{m}$ governing the degree of SRO in the paraphase according to $\langle m_0 m_1 \rangle = \bar{m}^2 \langle s_0 s_1 \rangle$ is shown in Fig. 5.4 (a). Note that $\bar{m}$ has to be conceptually distinguished from the local magnetic moment $m_{loc} = \frac{3}{4}(n - 2d^2)$ (Fig. 5.4 (b))

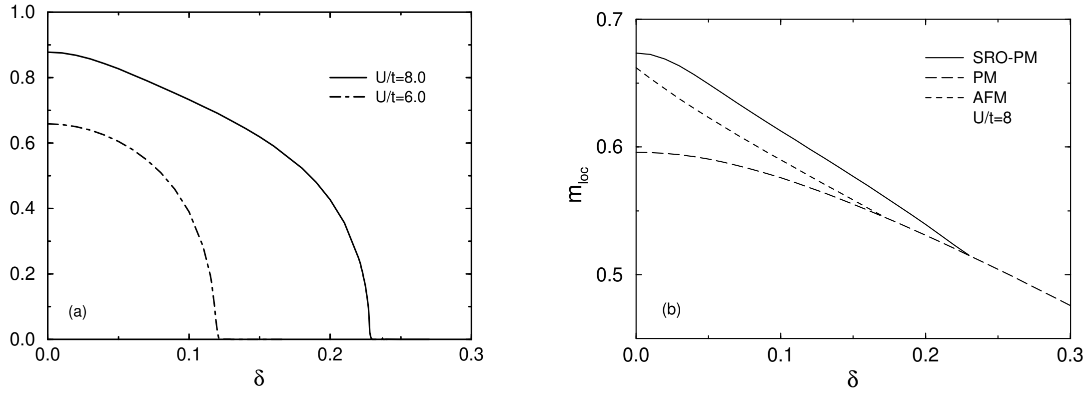

Figure 5.4: Amplitude of the local magnetization (a) compared with the local magnetic moment (b).

which exists independently from SRO. The higher values of m_{loc} in the SRO–PM phase compared with the local moment in the AFM LRO phase (Fig. 5.4 (b)) may be explained by the reduced itinerancy due to SRO spin correlations.

To conclude, the main result of our theory concerning the ground–state properties of the Hubbard model is that the magnetic LRO phases make way to a paraphase with SRO in a wide doping region. This SRO–PM phase is locally stable against phase separation.

5.2 Uniform static spin susceptibility [322]

5.2.1 Theory

The uniform static spin susceptibility $\chi(T,\delta)$ is of particular interest in the investigation of magnetic correlation effects. It is defined as

$$\chi = \lim_{h\to 0} \frac{dm}{dh} \quad \text{with} \quad m = \sum_{\alpha} W_\alpha m_\alpha \;, \tag{5.46}$$

where $m = \langle m_{s_i} \rangle$ ($m_{s_i} = \bar{m}_{s_i} s_i$ according to (5.16), (5.17); $s_i \to \alpha_i$) is the averaged magnetization, and W_α is given by (5.32). Thus, we have

$$\chi = \lim_{h\to 0} \sum_{\alpha} \left(W_\alpha \frac{dm_\alpha}{dh} + m_\alpha \frac{dW_\alpha}{dh} \right) \,. \tag{5.47}$$

The first term in (5.47) describes the change of the magnetization–amplitude with the applied magnetic field and gives mainly the ‘itinerant’ contribution to χ. The second term describes directional fluctuations of the local magnetizations and is called the ‘local’ contribution being finite only in the presence of SRO. Note that the ‘itinerant’ and ‘local’ properties are interrelated and determine *both* contributions to the spin susceptibility. By $W_\alpha = W_\alpha(\bar{h}, h^*, \bar{J})$ we obtain

$$\frac{dW_\alpha}{dh} = \frac{\alpha\beta}{\Theta_{\mathrm{I}}} \frac{d\bar{h}}{dh} \tag{5.48}$$

with

$$\Theta_{\mathrm{I}} = z \exp\{-2\beta \bar{J}\} - z + 2 \,. \tag{5.49}$$

The structure of (5.48), for $z = 4$, coincides with that derived by Baumgärtel et al. [38]. Calculating $d\bar{h}/dh$ we take care of the dependence $\bar{h} = \bar{h}(\{\bar{m}_\alpha\}, \{\bar{\xi}_\alpha\}, m^o, \xi^o, h)$ which differs from that in the CPA approach of Ref. [38], where instead of m^o and ξ^o, W_α appears. Moreover, we take into account the symmetry relations in the paraphase, $\frac{d\bar{m}_+}{dh}\Big|_{h=0} \equiv \bar{m}_{+_h} = -\bar{m}_{-_h}$, $\frac{d\bar{\xi}_+}{dh}\Big|_{h=0} \equiv \bar{\xi}_{+_h} = -\bar{\xi}_{-_h}$, and $\frac{dW_+}{dh}\Big|_{h=0} \equiv W_{+_h} = -W_{-_h}$. According to the saddle–point equations (5.37) for $\bar{m}_+$ and $\bar{\xi}_+$, resulting from $\partial\mathcal{S}/\partial\bar{\xi}_+ = 0$ and $\partial\mathcal{S}/\partial\bar{m}_+ = 0$, respectively, we have $\bar{m}_+ = \bar{m}_+(\{\bar{m}_\alpha\}, \{\bar{\xi}_\alpha\}, m^o, \xi^o, h)$ and the analogous dependence of $\bar{\xi}_+$. Taking into consideration the full dependence on the external field h of W_+, $\bar{m}_+$, $\bar{\xi}_+$, m^o, and ξ^o, for the derivatives of those quantities in the limit $h \to 0$ we obtain the linear system of equations

$$\begin{pmatrix} \frac{1}{\beta}\Theta_{\mathrm{I}} & -\bar{h}_{\bar{m}_{[+,-]}} & -\bar{h}_{\bar{\xi}_{[+,-]}} & -\bar{h}_{m^o} & -\bar{h}_{\xi^o} \\ \mathcal{S}_{W_{[+,-]}\bar{\xi}_+} & \mathcal{S}_{\bar{m}_{[+,-]}\bar{\xi}_+} & \mathcal{S}_{\bar{\xi}_{[+,-]}\bar{\xi}_+} & \mathcal{S}_{m^o\bar{\xi}_+} & \mathcal{S}_{\xi^o\bar{\xi}_+} \\ \mathcal{S}_{W_{[+,-]}\bar{m}_+} & \mathcal{S}_{\bar{m}_{[+,-]}\bar{m}_+} & \mathcal{S}_{\bar{\xi}_{[+,-]}\bar{m}_+} & \mathcal{S}_{m^o\bar{m}_+} & \mathcal{S}_{\xi^o\bar{m}_+} \\ 0 & 0 & 0 & \mathcal{S}^o_{m^o\xi^o} & \mathcal{S}^o_{\xi^o\xi^o} \\ 0 & 0 & 0 & \mathcal{S}^o_{m^o m^o} & \mathcal{S}^o_{\xi^o m^o} \end{pmatrix} \begin{pmatrix} W_{+_h} \\ \bar{m}_{+_h} \\ \bar{\xi}_{+_h} \\ m^o_h \\ \xi^o_h \end{pmatrix} = \begin{pmatrix} \bar{h}_h \\ -\mathcal{S}_{h\bar{\xi}_+} \\ -\mathcal{S}_{h\bar{m}_+} \\ -\mathcal{S}^o_{h\xi^o} \\ -\mathcal{S}^o_{hm^o} \end{pmatrix} \,, \tag{5.50}$$

where

$$X_y = \frac{\partial X}{\partial y}\,, \quad X_{x_{[+,-]}} = \left(\frac{\partial}{\partial x_+} - \frac{\partial}{\partial x_-}\right) X\,, \text{ and } \quad X_{xy} = \frac{\partial^2 X}{\partial x \partial y}\,. \tag{5.51}$$

In the paraphase without SRO, from the lower block of (5.50), the susceptibility is obtained as

$$\chi^o = m_h^o = \frac{\chi_0^o}{1 + A\,\chi_0^o + B\,\chi_1^o + \frac{1}{4}B^2(\chi_1^{o2} - \chi_0^o\chi_2^o)} \tag{5.52}$$

with

$$A = \sum_\sigma \frac{\partial^2 q_\sigma^o}{\partial m^{o2}}\,, \quad B = \frac{1}{2}\sum_\sigma \sigma \frac{\partial q_\sigma^o}{\partial m^o}\,, \tag{5.53}$$

and

$$\chi_n^o = -\frac{1}{N}\sum_{\vec{k}\sigma} (2\varepsilon_{\vec{k}})^n \frac{\partial f(E_{\vec{k}\sigma}^o - \mu)}{\partial E_{\vec{k}\sigma}^o}\,. \tag{5.54}$$

Let us point out that our result for the spin susceptibility χ^o agrees with the static and uniform limit of the dynamic spin susceptibility derived, within the SRI SB scheme [166], from the Gaussian fluctuation matrix at the PM saddle point [311]. Contrary, the uniform static spin susceptibility given in Ref. [175] within the scalar four–field SB approach disagrees with the result of Li *et al.* [311] away from half–filling.

To calculate the influence of SRO on the spin susceptibility in the SRO–PM phase, we insert the solutions for m_h^o and ξ_h^o into the system (5.50), where the corresponding terms appear in the inhomogeneities of the equations for W_{+_h}, $\bar{m}_{+_h}$, and $\bar{\xi}_{+_h}$. From the solution of (5.50), we finally obtain the spin susceptibility as

$$\chi = \frac{\Theta_\mathrm{I}\,\chi_\mathrm{I} + \chi_\mathrm{II}}{\Theta_\mathrm{I} + \Theta_\mathrm{II}} \tag{5.55}$$

with

$$\chi_\mathrm{I} = \Delta\left[\Xi\,\mathcal{S}_{\bar{m}_{[+,-]}\bar{\xi}_+} - \Lambda\mathcal{S}_{\bar{\xi}_{[+,-]}\bar{\xi}_+}\right], \tag{5.56}$$

$$\begin{aligned}\chi_\mathrm{II} = {} & 2\beta\bar{m}_+\Gamma + \beta\Delta\Big\{\Big[2\bar{m}_+\left(\Xi\,\bar{h}_{\bar{m}_{[+,-]}} + \Lambda\,\bar{h}_{\bar{\xi}_{[+,-]}}\right) - \Gamma\mathcal{S}_{W_{[+,-]}\bar{\xi}_+}\Big]\mathcal{S}_{\bar{m}_{[+,-]}\bar{\xi}_+} \\ & -\bar{h}_{\bar{\xi}_{[+,-]}}\left(\Lambda\mathcal{S}_{W_{[+,-]}\bar{\xi}_+} - \Xi\mathcal{S}_{W_{[+,-]}\bar{m}_+}\right) - 2\bar{m}_+\Xi\bar{h}_{\bar{\xi}_{[+,-]}}\mathcal{S}_{\bar{m}_{[+,-]}\bar{m}_+} \\ & + \left(\Gamma\mathcal{S}_{W_{[+,-]}\bar{m}_+} - 2\bar{m}_+\Lambda\bar{h}_{\bar{m}_{[+,-]}}\right)\mathcal{S}_{\bar{\xi}_{[+,-]}\bar{\xi}_+}\Big\}\,, \end{aligned} \tag{5.57}$$

and

$$\begin{aligned}\Theta_\mathrm{II} = {} & \beta\Delta\Big[\left(\mathcal{S}_{W_{[+,-]}\bar{\xi}_+}\,\bar{h}_{\bar{m}_{[+,-]}} + \mathcal{S}_{W_{[+,-]}\bar{m}_+}\,\bar{h}_{\bar{\xi}_{[+,-]}}\right)\mathcal{S}_{\bar{m}_{[+,-]}\bar{\xi}_+} \\ & -\bar{h}_{\bar{\xi}_{[+,-]}}\mathcal{S}_{W_{[+,-]}\bar{\xi}_+}\mathcal{S}_{\bar{m}_{[+,-]}\bar{m}_+} - \bar{h}_{\bar{m}_{[+,-]}}\mathcal{S}_{W_{[+,-]}\bar{m}_+}\mathcal{S}_{\bar{\xi}_{[+,-]}\bar{\xi}_+}\Big]\,, \end{aligned} \tag{5.58}$$

where

$$\Delta = [\mathcal{S}^2_{\bar{m}_{[+,-]}\bar{\xi}_+} - \mathcal{S}_{\bar{\xi}_{[+,-]}\bar{\xi}_+}\mathcal{S}_{\bar{m}_{[+,-]}\bar{m}_+}]^{-1}\,, \tag{5.59}$$

$$\Xi = -S_{h\bar{\xi}_+} - \mathcal{S}_{m^o\bar{\xi}_+}m_h^o - \mathcal{S}_{\xi^o\bar{\xi}_+}\xi_h^o\,, \tag{5.60}$$

$$\Lambda = -S_{h\bar{m}_+} - \mathcal{S}_{m^o\bar{m}_+}m_h^o - \mathcal{S}_{\xi^o\bar{m}_+}\xi_h^o\,, \tag{5.61}$$

$$\Gamma = \bar{h}_h + \bar{h}_{m^o}m_h^o + \bar{h}_{\xi^o}\xi_h^o\,. \tag{5.62}$$

Here we are primarily interested in the zero–temperature susceptibility. Equations (5.55) to (5.58) then lead to

$$\lim_{T\to 0}\chi = \begin{cases} \chi_{\mathrm{I}} & \text{for antiferromagnetic SRO} \quad (\bar{J}<0) \\ \dfrac{\chi_{\mathrm{II}}}{\Theta_{\mathrm{II}}} & \text{for ferromagnetic SRO} \quad (\bar{J}>0). \end{cases} \tag{5.63}$$

Let us emphasize that, in contrast to the theory by Baumgärtel *et al.* [38], we get a *finite* susceptibility at $T=0$. Hereafter we consider the case of antiferromagnetic SRO (ferromagnetic SRO can be realized only at large values of U/t being unrealistic for the cuprates). For this case, the coefficients $\mathcal{S}_{xy}$ in (5.50) occurring in χ_{I} become

$$\begin{aligned} \mathcal{S}_{\bar{m}_{[+,-]}\bar{\xi}_+} &= \mathcal{S}_{\bar{\xi}_{[+,-]}\bar{m}_+} = 1+\sum_\eta q_\eta^{-1} q_\eta^{(\bar{m})}\left\{n_\eta^f - a_\eta^2 \mathit{\Phi}_{1,\eta}^{(0,2)} + a_\eta b_\eta \mathit{\Phi}_{0,\eta}^{(0,2)}\right. \\ &\left. -z\left[a_{-\eta}^2\mathit{\Phi}_{1,-\eta\eta}^{(0,1,1)} + a_\eta^2 \mathit{\Phi}_{1,-\eta\eta}^{(0,0,2)} - a_{-\eta}b_{-\eta}\mathit{\Phi}_{0,-\eta\eta}^{(0,1,1)} - a_\eta b_\eta \mathit{\Phi}_{0,-\eta\eta}^{(0,0,2)}\right]\right\} , \end{aligned} \tag{5.64}$$

$$\mathcal{S}_{\bar{\xi}_{[+,-]}\bar{\xi}_+} = \sum_\eta q_\eta^{-1}\left\{a_\eta \mathit{\Phi}_{0,\eta}^{(0,2)} + z\left(a_{-\eta}\mathit{\Phi}_{0,-\eta\eta}^{(0,1,1)} + a_\eta\mathit{\Phi}_{0,-\eta\eta}^{(0,0,2)}\right)\right\} , \tag{5.65}$$

$$\begin{aligned} \mathcal{S}_{m^o\bar{\xi}_+} &= -\sum_\eta q_\eta^{-1} q^{o(m)}\left\{a_\eta^{-1} n_\eta^f + q^o \mathit{\Phi}_{1,\eta}^{(1,1)} - a_\eta \mathit{\Phi}_{1,\eta}^{(0,2)}\right. \\ &\left. +z\left[q^o\mathit{\Phi}_{1,-\eta\eta}^{(1,0,1)} - a_{-\eta}\mathit{\Phi}_{1,-\eta\eta}^{(0,1,1)} - a_\eta \mathit{\Phi}_{1,-\eta\eta}^{(0,0,2)}\right]\right\} , \end{aligned} \tag{5.66}$$

$$\mathcal{S}_{\xi^o\bar{\xi}_+} = \mathcal{S}_{h\bar{\xi}_+} - \mathcal{S}_{\bar{\xi}_{[+,-]}\bar{\xi}_+} , \tag{5.67}$$

$$\mathcal{S}_{h\bar{\xi}_+} = \sum_\eta a_\eta\left\{\mathit{\Phi}_{0,\eta}^{(1,1)} + z\mathit{\Phi}_{0,-\eta\eta}^{(1,0,1)}\right\} , \tag{5.68}$$

$$\begin{aligned} \mathcal{S}_{\bar{m}_{[+,-]}\bar{m}_+} &= \sum_\eta\left\{\left[q_\eta^{(\bar{m}^2)} - 2q_\eta^{-1}\left(q_\eta^{(\bar{m})}\right)^2\right]Q_\eta^f + q_\eta^{-1}\left(q_\eta^{(\bar{m})}\right)^2\left\{a_\eta^3\mathit{\Phi}_{2,\eta}^{(0,2)} - 2a_\eta^2 b_\eta \mathit{\Phi}_{1,\eta}^{(0,2)}\right.\right. \\ & +a_\eta b_\eta^2 \mathit{\Phi}_{0,\eta}^{(0,2)} + z\left[a_\eta a_{-\eta}^2 \mathit{\Phi}_{2,-\eta\eta}^{(0,1,1)} + a_\eta^3 \mathit{\Phi}_{2,-\eta\eta}^{(0,0,2)} - a_{-\eta}(a_{-\eta}b_\eta + a_\eta b_{-\eta})\mathit{\Phi}_{1,-\eta\eta}^{(0,1,1)}\right. \\ &\left.\left.\left. -2a_\eta^2 b_\eta \mathit{\Phi}_{1,-\eta\eta}^{(0,0,2)} + a_{-\eta}b_\eta b_{-\eta}\mathit{\Phi}_{0,-\eta\eta}^{(0,1,1)} + a_\eta b_\eta^2 \mathit{\Phi}_{0,-\eta\eta}^{(0,0,2)}\right]\right\}\right\} , \end{aligned} \tag{5.69}$$

$$\begin{aligned} \mathcal{S}_{m^o\bar{m}_+} &= \sum_\eta q_\eta^{-1} q_\eta^{(\bar{m})} q^{o(m)}\left\{z\left[a_\eta\left(2\mathit{\Phi}_{1,-\eta\eta}^{(0,0,1)} + q^o\mathit{\Phi}_{2,-\eta\eta}^{(1,0,1)} - a_{-\eta}\mathit{\Phi}_{2,-\eta\eta}^{(0,1,1)} - a_\eta \mathit{\Phi}_{2,-\eta\eta}^{(0,0,2)}\right)\right.\right. \\ &\left. -b_\eta\left(\mathit{\Phi}_{0,-\eta\eta}^{(0,0,1)} + q^o\mathit{\Phi}_{1,-\eta\eta}^{(1,0,1)} - a_{-\eta}\mathit{\Phi}_{1,-\eta\eta}^{(0,1,1)} - a_\eta\mathit{\Phi}_{1,-\eta\eta}^{(0,0,2)}\right)\right] \\ &\left. +a_\eta\left(2\mathit{\Phi}_{1,\eta}^{(0,1)} + q^o\mathit{\Phi}_{2,\eta}^{(1,1)} - a_\eta\mathit{\Phi}_{2,\eta}^{(0,2)}\right) - b_\eta\left(\mathit{\Phi}_{0,\eta}^{(0,1)} + q^o\mathit{\Phi}_{1,\eta}^{(1,1)} - a_\eta \mathit{\Phi}_{1,\eta}^{(0,2)}\right)\right\} , \end{aligned} \tag{5.70}$$

$$\begin{aligned} \mathcal{S}_{\xi^o\bar{m}_+} &= \mathcal{S}_{h\bar{m}_+} - \sum_\eta q_\eta^{-1}q_\eta^{(\bar{m})}\left\{a_\eta\left(\mathit{\Phi}_{0,\eta}^{(0,1)} - a_\eta\mathit{\Phi}_{1,\eta}^{(0,2)}\right) + a_\eta b_\eta \mathit{\Phi}_{0,\eta}^{(0,2)}\right. \\ &\left. +z\left[a_\eta\left(\mathit{\Phi}_{0,-\eta\eta}^{(0,0,1)} - a_{-\eta}\mathit{\Phi}_{1,-\eta\eta}^{(0,1,1)} - a_\eta\mathit{\Phi}_{1,-\eta\eta}^{(0,0,2)}\right) + b_\eta\left(a_{-\eta}\mathit{\Phi}_{0,-\eta\eta}^{(0,1,1)} + a_\eta\mathit{\Phi}_{0,-\eta\eta}^{(0,0,2)}\right)\right]\right\} \end{aligned} \tag{5.71}$$

$$\mathcal{S}_{h\bar{m}_+} = -\sum_\eta a_\eta q_\eta^{(\bar{m})}\left\{a_\eta\mathit{\Phi}_{1,\eta}^{(1,1)} - b_\eta\mathit{\Phi}_{0,\eta}^{(1,1)} + z\left[a_\eta\mathit{\Phi}_{1,-\eta\eta}^{(1,1)} - b_\eta\mathit{\Phi}_{0,-\eta\eta}^{(1,1)}\right]\right\} , \tag{5.72}$$

with the abbreviations:

$$q^{o(m)} = \sigma\left.\frac{\partial q_\sigma^o}{\partial m^o}\right|_{m^o=0} \quad , \quad q_\eta^{(\bar{m})} = \eta\frac{\partial q_\eta}{\partial\bar{m}} \quad , \quad q_\eta^{(\bar{m}^2)} = \frac{\partial^2 q_\eta}{\partial\bar{m}^2} , \tag{5.73}$$

$$\varPhi_{n,\eta}^{(k,l)} = \frac{1}{q^o} \frac{\partial^{k+l} \varPhi_{n,\eta}}{\partial(\sigma h)^k \, \partial b_\eta^l} \quad , \quad \varPhi_{n,\eta\eta'}^{(k,l,m)} = \frac{1}{q^o} \frac{\partial^{k+l+m} \varPhi_{n,\eta\eta'}}{\partial(\sigma h)^k \partial b_\eta^l \partial b_{\eta'}^m} \,, \tag{5.74}$$

$$\varPhi_{n,\eta} \quad = \quad \tfrac{1}{\pi} \int d\omega \, \omega^n f(\omega - \mu) \mathrm{Im} \;\; \ln \left[1 - G^o V_\eta \right] \,, \tag{5.75}$$

$$\varPhi_{n,\eta\eta'} \quad = \quad \tfrac{1}{\pi} \int d\omega \, \omega^n f(\omega - \mu) \mathrm{Im} \;\; \ln \left[1 - G^{o\prime} T_\eta G^{o\prime} T_{\eta'} \right] \;, \tag{5.76}$$

and $a_\eta = \frac{q^o}{q_\eta}$, $b_\eta = \frac{\lambda_\eta^{(2)} - \lambda^o}{q_\eta}$, where $\eta = \alpha\sigma = \pm$.

5.2.2 Numerical results and comparison with experiments

To evaluate the doping dependence of the uniform static spin susceptibility at $T = 0$, all quantities (eqs. (5.52) to (5.54), (5.56), and (5.64) to (5.72)) have to be calculated in the $h = 0$ limit from the solution of the self–consistency equations (5.37) to (5.39). In the involved numerical evaluation of the integrals (5.29) and (5.30) and of their derivatives (5.74), particular attention has to be paid to the analytical behaviour of the complex logarithm.

Fig. 5.5 shows the doping dependence of the zero–temperature susceptibility for the 2D Hubbard model, where the realistic values $U/t = 8$ and $t = 0.3$ eV for $\mathrm{La}_{2-\delta}\mathrm{Sr}_\delta\mathrm{CuO}_4$ [112] are used. As found in Sec. 5.1, for $U/t = 8$ there occurs a first–order (1,1)–spiral⇌SRO–PM transition at $\delta_{c_1} = 0.04$ and a SRO–PM⇌PM transition of second order at $\delta_{c_2} = 0.26$. In the PM phase ($\delta > \delta_{c_2}$) the SB band–renormalized Pauli susceptibility (5.52) has a pronounced doping dependence in two dimensions. In the SRO–PM phase ($\delta_{c_1} < \delta < \delta_{c_2}$), where the finite local–magnetization amplitude $\bar{m}$ results in an effective Ising–exchange interaction $\bar{J} < 0$ and antiferromagnetic SRO, the Pauli susceptibility consisting of interrelated 'itinerant' and 'local' parts is suppressed due to the SRO–induced spin stiffness against the orientation along the homogeneous external field. Accordingly, at $\delta_{c_2} = 0.26$ a cusp in $\chi(0, \delta)$ appears. Since, for $\delta_{c_1} < \delta < \delta_{c_2}$, $|\bar{J}|$ decreases with increasing δ (cf. Fig. 5.3 (inset)), the susceptibility increases upon doping.

The peak in $\chi(0, \delta)$ only appears at sufficiently high ratios U/t ($U/t > 6$ [39], for which a SRO–PM⇌PM transition may occur. According to the phase diagram, given in Sec. 5.1 (cf. Fig. 5.3), in the region $6 < U/t < 12$ the SRO–PM⇌PM transition shifts to higher doping values with increasing U/t. Correspondingly, the peak position in $\chi(0, \delta)$ reveals the same U/t dependence. In Fig. 5.5 we have also depicted the experimental data on $\mathrm{La}_{2-\delta}\mathrm{Sr}_\delta\mathrm{CuO}_4$ at 50 K [41] showing a pronounced maximum at a hole doping of about 25%. Let us underline that we have *not* performed any fit procedure of our theoretical zero–temperature results. That means, using the commonly accepted value $U/t = 8$ for the Hubbard model applied to high–T_c cuprates, we obtain the position of the susceptibility maximum in excellent agreement with the value observed in Ref. [41]. Moreover, our theory correctly describes the variation of χ with doping below δ_{c2}. For $\delta \gtrsim \delta_{c2}$, the large drop in $\chi(\delta)$ can be attributed to a density of states effect.

Finally, we notice that the increase of the susceptibility upon doping obtained within our theory for moderate Coulomb repulsions ($U/t > 6$) is in qualitative accord with recent QMC data [333] and with a semi–phenomenological and non–selfconsistent approach to the Hubbard model [37]. However, in those works a maximum in the spin susceptibility was found even at a smaller coupling ($U/t = 4$).

From our results we conclude that the concept of magnetic SRO in strong–correlation models may play the key role in the explanation of many unconventional normal–state properties of high–T_c compounds. The theory may be extended in several directions. In particular, as

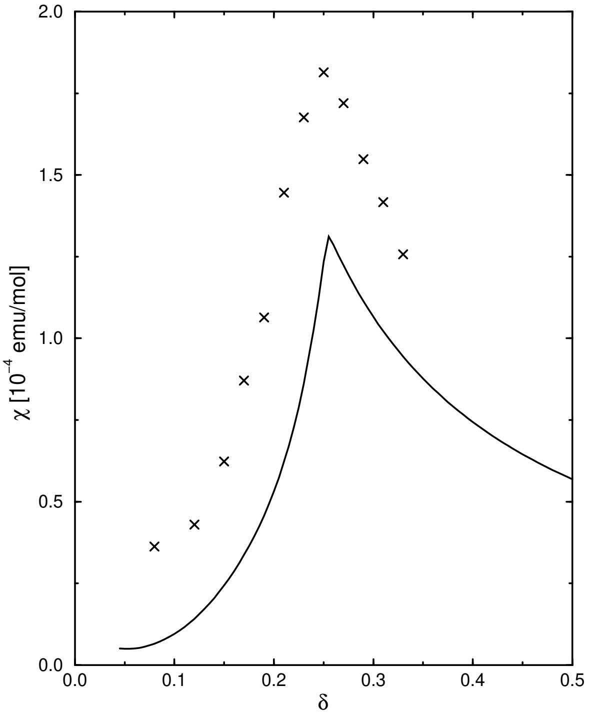

Figure 5.5: Uniform static spin susceptibility as a function of doping. The theoretical result obtained for the 2D Hubbard model at $U/t = 8$, $t = 0.3$ eV, and $T = 0$ K, is compared with experiments (×) on $La_{2-\delta}Sr_\delta CuO_4$ at $T = 50$ K [41]. Note that the experimental data have to be corrected for the diamagnetic core (-9.9×10^{-5} emu/mol) and Van Vleck (2.4×10^{-5} emu/mol) contributions; however, χ^{core} and χ^{VV} can be taken to be independent of doping and temperature over the limited parameter region studied here [40].

motivated by neutron scattering experiments [315] probing the AFM correlation length over several lattice spacings, the effects of a longer than nearest–neighbour ranged SRO (which may be described beyond the nearest–neighbour pair approximation) should be investigated.

Chapter 6

Ground–state properties of the 2D half-filled extended Hubbard model

Long–range Coulomb interactions are expected to play an important role in a variety of low–dimensional materials, such as 1D conducting polymers [334] and charge transfer salts [335]. From a more theoretical point of view the incorporation of interatomic Coulomb interaction may be desirable to exclude phase separated states which are discussed frequently for the Hubbard and t-J models [78]. In one spatial dimension the half–filled extended Hubbard model including nearest–neighbour interaction has been intensively investigated using, among other techniques, renormalization group methods [336, 337, 338], exact Lanczos diagonalization [339, 340, 341] and Monte Carlo simulation [342, 343]. The ground–state phase diagram of the extended Hubbard shows a surprising richness. For repulsive on– and inter–site Coulomb interactions ($U, V > 0$) the ground state of the system can be a spin–density–wave (SDW) with continuous symmetry or a truly long–range ordered charge–density–wave (CDW) phase. Monte Carlo [343] and Lanczos results [340, 344] indicate that the SDW–CDW transition occurs slightly above the $U = 2V$ line given by renormalization group [338, 345] and Hartree–Fock [346] calculations. A quantum Monte Carlo simulation of the 2D extended Hubbard model shows that the 1D and 2D cases are qualitatively similar, where the SDW–CDW transition is found for the square lattice near the line $U = 4V$ [347]. The extended Hubbard model with on–site and/or inter–site attractive interaction has been studied as a theoretical model of local electron pairing in the context of superconductivity (for an overview see Micnas *et al.* [348]). The negative–U Hubbard model describes the crossover from a BCS–like superconductivity to the superfluidity of charged bosons. In the strong–attraction limit one observes preformed local pairs (bipolarons). The interatomic Coulomb interaction will stabilize CDW ordering ($V > 0$) or singlet (on–site) superconductivity ($V < 0$). The negative–V extended Hubbard model ($U > 0$) is expected to lead to anisotropic superconducting states for weak on-site correlations and to a SDW phase in the strong–coupling U–limit (cf. [348], and references therein). At large negative V, a first–order transition to a charge separated state is found by Monte Carlo [343] and Lanczos [340] techniques. A physical mechanism leading to such type of effective short–range electron–electron attraction can be, among others, a strong local electron–phonon coupling [348, 349, 350].

6.1 Two–sublattice slave–boson saddle–point approach [179]

Motivated by the above findings the goal of this chapter is to investigate the ground–state properties of the 2D extended Hubbard model

$$\mathcal{H} = -t \sum_{\langle ij \rangle,\sigma} \left(c^{\dagger}_{i\sigma} c_{j\sigma} + \text{H.c.} \right) + U \sum_{i} n_{i\uparrow} n_{i\downarrow} + V \sum_{\langle ij \rangle} n_i n_j \,, \tag{6.1}$$

in particular in the physically most interesting half–filled band sector. In (6.1) the first two terms together define the standard Hubbard model with an on–site electron interaction U. V measures the Coulomb interaction between electrons on NN sites.

Using the scalar four–field KR SB representation (2.16)–(2.19) of the partition function at the two–sublattice saddle–point level of approximation, the free energy (per site) follows as [272]

$$\begin{aligned} \overline{f} \;=\; & \frac{1}{2} \sum_{\eta} \left\{ \lambda^{(1)}_{\eta} \left(e^2_{\eta} + p^2_{\eta\uparrow} + p^2_{\eta\downarrow} + d^*_{\eta} d_{\eta} - 1 \right) - \sum_{\sigma} \lambda^{(2)}_{\eta\sigma} \left(p^2_{\eta\sigma} + d^*_{\eta} d_{\eta} \right) + \; U d^*_{\eta} d_{\eta} \right. \\ & \left. + \, V \sum_{\sigma,\sigma'} \left(p^2_{\eta\sigma} + d^*_{\eta} d_{\eta} \right) \left(p^2_{-\eta\sigma} + d^*_{-\eta} d_{-\eta} \right) \right\} + \frac{1}{\beta N} \sum_{\vec{k},\nu,\sigma} \ln \left(1 - n_{\vec{k}\nu\sigma} \right) + \mu n \,, \end{aligned} \tag{6.2}$$

where

$$n_{\vec{k}\nu\sigma} = \frac{1}{\mathrm{e}^{\beta(E_{\vec{k}\nu\sigma} - \mu)} + 1} \tag{6.3}$$

with

$$E_{\vec{k}\nu\sigma} = \lambda^{(+)}_{\sigma} + \varepsilon_{\vec{k}\nu\sigma} \,, \quad \varepsilon_{\vec{k}\nu\sigma} = \nu \sqrt{[\lambda^{(-)}_{\sigma}]^2 + \varepsilon^2_{\vec{k}} \, |z_{A\sigma}|^2 \, |z_{B\sigma}|^2} \tag{6.4}$$

holds, and $\lambda^{(\pm)}_{\sigma} = (\lambda^{(2)}_{A\sigma} \pm \lambda^{(2)}_{B\sigma})/2$. Here $\eta = A, B$ denotes the sublattice index and $\nu = \pm 1$, i.e., the $\vec{k}$–summations are restricted to the magnetic Brillouin zone of the square lattice. The Bose fields e_{η}, $d^*_{\eta} = d_{\eta}$, $p_{\eta\sigma}, \lambda^{(1)}_{\eta}$, and $\lambda^{(2)}_{\eta\sigma}$ are obtained from the solution of 14 coupled self–consistency equations given in Ref. [272]. The bipartite nature of the lattice plays an essential role for the appearance of a broken symmetry state [180]. At half–filling we are mainly interested in spin (SDW) and charge (CDW) ordered states with vanishing net magnetization ($m = 0$). Therefore we introduce the following 'order parameters':

$$\Delta_{SDW} \;=\; \frac{1}{2}(m_A - m_B) = \sum_{\vec{k},\nu,\sigma} \sigma \, \lambda^{(-)}_{\sigma} \frac{n_{\vec{k}\nu\sigma}}{\varepsilon_{\vec{k}\nu\sigma}} \,, \tag{6.5}$$

$$\Delta_{CDW} \;=\; \frac{1}{2}(n_A \,-\, n_B) \,=\, \sum_{\vec{k},\nu,\sigma} \lambda^{(-)}_{\sigma} \frac{n_{\vec{k}\nu\sigma}}{\varepsilon_{\vec{k}\nu\sigma}} \,. \tag{6.6}$$

In the above equations, $m_{\eta} = n_{\eta\uparrow} - n_{\eta\downarrow}$ are the sublattice magnetizations, where the sublattice particle numbers (per spin) are defined by $n_{\eta\sigma} = p^2_{\eta\sigma} + d^2_{\eta}$. Accordingly, the different phases with (SDW, CDW) and without (PM) long–range order can be specified as:

$$\begin{array}{lll} \text{PM} & \Delta_{SDW} = 0 & \Delta_{CDW} = 0 \\ \text{SDW (AFM)} & \Delta_{SDW} \neq 0 & \Delta_{CDW} = 0 \\ \text{CDW (PM)} & \Delta_{SDW} = 0 & \Delta_{CDW} \neq 0 \end{array} \quad .$$

6.2 Numerical results [272]

After establishing the various symmetry broken states, we determine the phase diagram of the 2D extended Hubbard model (see Fig. 6.1). In the plane of U and V, the phase boundaries are indicated by solid lines. Let us first discuss the repulsive case with $U, V > 0$. The physics in this region is dominated by the competition between U and V, which favour SDW and CDW states, respectively. The SB phase boundary between CDW and SDW (AFM) states is sligthly shifted from the Hartree–Fock [346] and 1D renormalization group [338, 345] result $U = zV$ (z denotes the number of NN sites). Obviously, this is an effect of the Coulomb correlations which are included in our the SB mean–field treatment. The deviation from the line $U = zV$ was indicated by Lanczos [340, 344] and Monte Carlo [341, 343, 347] calculations as well. Using the 'local Ansatz' approach [351], Oleś *et al.* [352] found a qualitatively similar behaviour. The shift of the transition line towards the CDW phase is somewhat smaller than the Lanczos result obtained by Waas *et al.* [340] for finite chains up to eight sites. At this point it should be mentioned, that our mean–field approximation contains the dimensionality of the problem only via the unperturbed density of states. A comparison with the 2D Monte Carlo data of Zhang and Callaway [347] yields, e.g., at $U = 4$: $V_{CDW \to SDW} \cong 1.02$ (Fig. 6.1) and $V_{CDW \to SDW} \cong 1.05$ (Ref. [347]). We next consider the region, where U or V becomes negative.

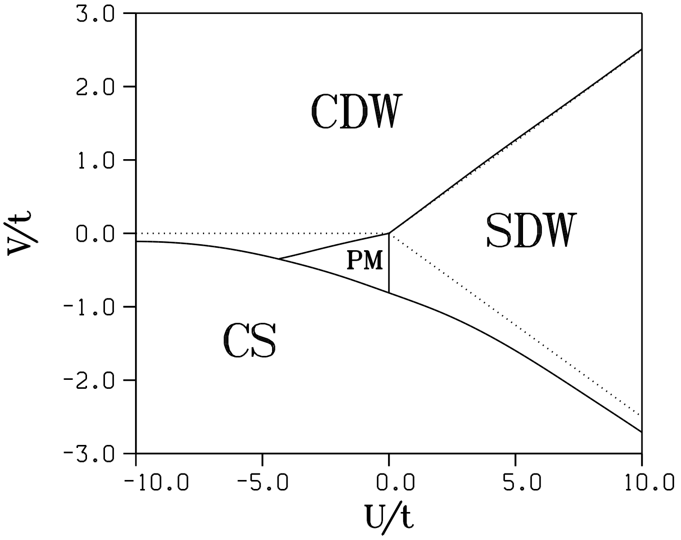

Figure 6.1: SB phase diagram of the 2D extended Hubbard model in the half–filled band sector. The dotted lines show the results of asymptotic expansions (see text).

Unfortunately, the SB scheme presented above does not contain superconducting correlations which may be of importance in this regime [343, 348]. Restricting us to the normal state, we obtain four different phases. Besides CDW and SDW order, the phase diagram exhibits at $U \leq 0$ and $V < 0$ (but $|V|$ not too large) a metallic paramagnetic phase. It is interesting to note, that the CDW and SDW correlation functions, obtained in this parameter regime from finite–lattice Lanczos calculations, have the same order of magnitude. At the same time the kinetic part of ground–state energy becomes strongly enhanced [205]. This may be interpreted as a tendency towards metallic behaviour. The magnetic susceptibility is evidently suppressed by an attractive interaction [348]. For large negative V the system shows a transition to an inhomogeneous charge separated state (CS). The position of the boundary towards complete phase separation agrees well with the Monte Carlo results of Lin and Hirsch [343]. In the charge separated state, the equilibrium configuration consists of two separated regions with different electron densities n_1 and n_2. To determine the phase boundary, we compare the free energy of several homogeneous states with the free energy of the two phase system performing the usual Maxwell construction. The ground–state energy of the CS state can be easily calculated when the charge separation becomes complete (i.e., $n_1 = 0$ and $n_2 = 2$). Equating the free energies of charge separated and SDW (CDW) states in the limit $U, V \to \infty$ ($|V| \ll 1$, $U \to \infty$), one gets the asymtotic behaviour marked in Fig. 6.1 by dotted lines. We found that the transitions SDW⇌CDW and SDW, CDW, PM⇌CS are of first order, whereas the transitions CDW, SDW⇌PM are of second order. Our SB treatment yields no evidence for a crossover from a continuous to a first–order SDW⇌CDW transition with increasing U and V. The crossover behaviour has been controversy discussed for the 1D systems [336, 337, 338, 339, 340, 341, 342].

The variation of CDW and SDW order parameters along characteristic lines in the parameter space is illustrated in Figs. 6.2 and 6.3. In Fig. 6.2 we show Δ_{CDW} as a function of V for the CDW⇌PM⇌CS transition ($U/t = -4, 0$) as well as for the CDW⇌SDW⇌CS transition ($U/t = 2, 4, 6$). The jump of Δ_{CDW} for $U > 0$ corresponds to an intersection of the free energies of CDW and SDW states, which is an indication of the first–order transition behaviour. Increasing the Hubbard interaction U at constant V, we obtain the expected reduction of Δ_{CDW}, where at $V < 0$ the CDW order parameter goes continuously to zero (cf. Fig. 6.3 (a)). Note that for $U > 0$ the sublattice magnetization is independent of the interatomic Coulomb interaction V. Thus we observe a monotonous increase of Δ_{SDW} with U for the SDW solution even in their instability region. Above (below) the transition point CDW⇌SDW Δ_{CDW} (Δ_{SDW}) breaks abruptly down. In the PM regime both quantities vanish. In order to discuss the mobility of the charge carriers we have calculated the effective transfer amplitude $t_{eff} =< \sum c^{\dagger}_{i\sigma} c_{j\sigma} > / < \sum c^{\dagger}_{i\sigma} c_{j\sigma} >_{(U,V)=0}$. This quantity was used by Lilly *et al.* [180] to demonstrate the excellent quantitative agreement of SB and QMC results for the Hubbard model. As can be seen from Fig. 6.3 (b), the electronic correlations lead to a reduction of t_{eff} compared to the free–electron case. However, it is interesting to notice that t_{eff} becomes enhanced in the PM state and reaches its free–electron value even at finite negative V (cf. the chain dotted curve in Fig. 6.3 (b)). For the repulsive case ($U, V > 0$), t_{eff} exhibits a cusp–structure at the CDW⇌SDW transition point, where the electronic gap is minimal. Due to the large number of doubly occupied sites on one sublattice, the effective hopping matrix element is reduced in the CDW phase compared to the SDW state.

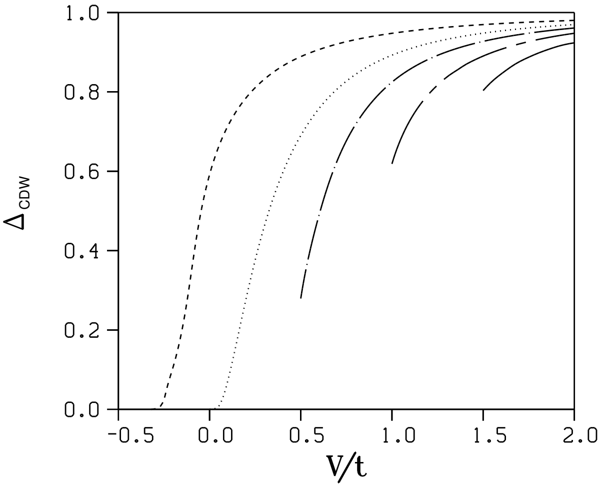

Figure 6.2: CDW order parameter Δ_{CDW} as a function of the interatomic Coulomb interaction V. The curves are given at various Hubbard interactions $U/t = -4$ (dashed), $U/t = 0$ (dotted), $U/t = 2$ (chain dotted), $U/t = 4$ (chain dashed), and $U/t = 6$ (solid).

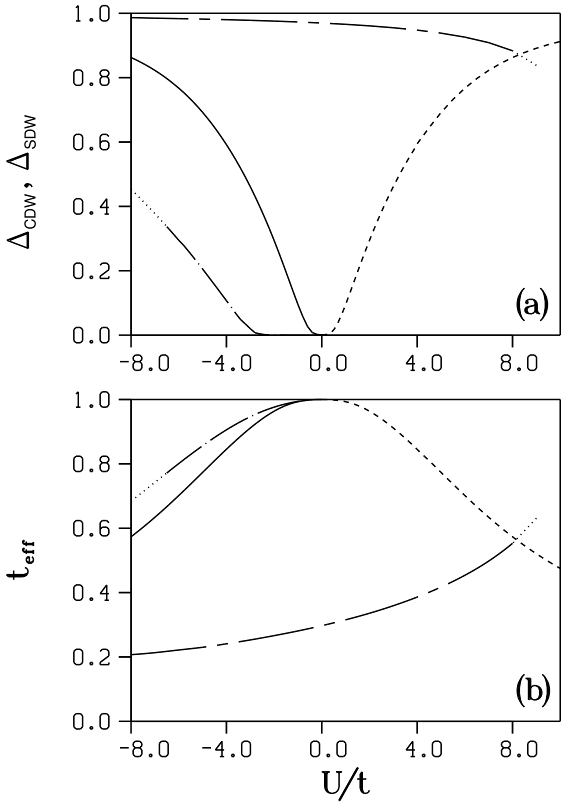

Figure 6.3: Order parameters Δ_{SDW}, Δ_{CDW}, and the effective hopping amplitude t_{eff} are given as functions of U in (a) and (b), respectively. Δ_{CDW} and t_{eff} are presented in the CDW phase at $V/t = -0.2$ (chain dotted line), $V/t = 0$ (solid), and $V = 2/t$ (chain dashed). The dashed curves denote Δ_{SDW} and t_{eff} in the SDW state, where the results are independent of V. Note that this solution becomes energetically stable only below the CDW$\rightleftharpoons$SDW transition line. Dotted lines corresponds to a metastable CDW solution.

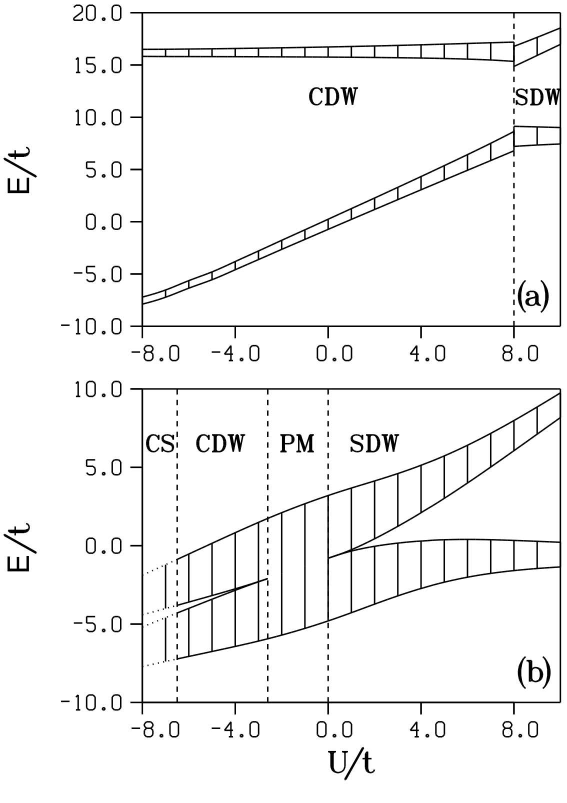

Figure 6.4: Renormalized quasiparticle bandwidths in dependence on the intraatomic Coulomb interaction strength U at $V/t = 2$ (a) and $V/t = -0.2$ (b).

Results showing the renormalized quasiparticle bandwidth versus U for repulsive ($V > 0$) and attractive ($V < 0$) NN interactions are presented in Figs. 6.4 (a) and (b), respectively. For the CDW and SDW states, the chemical potential μ is situated in the mid of the insulating gap. The band narrowing with increasing correlations is clearly visible. Note that at the CDW$\rightleftharpoons$SDW transition, the insulating gap of the SDW state is smaller than the corresponding CDW gap. As function of U the position of lower (upper) Hubbard band remains nearly unchanged in the SDW (CDW) phase, whereas the upper (lower) band varies almost linearly with U (see Fig. 6.4 (a)). This can be understood performing the well–known attraction–repulsion transformation [255]. For the PM phase the gap disappears and we obtain metallic behaviour. In addition, the local magnetic moment $m_{loc;\eta} = \frac{3}{4}(n_\eta - 2d_\eta^2)$ takes roughly the value of the band limit, i.e., $m_{loc;\eta} \simeq 3/8$. m_{loc} is a measure for the 'localization' of the electronic spin. In the SDW state $m_{loc;\eta}$ grows gradually to the atomic limit value $m_{loc;\eta}(U \to \infty) = 3/4$.

The analysis of the ground–state properties of the extended Hubbard model away from half–filling is much more elaborate. In this case, Varma [353] has investigated the extended Hubbard model in the ($U < 0,\ V > 0$) sector by mapping it onto an anisotropic Heisenberg model in the presence of an external field. Alternatively, Laad *et al.* [354] performed in the strong–coupling limit a canonical transformation onto a field–free XX–Z model at half–filling. Upon doping, they found evidence for singlet superconducting and long–range ordered magnetic phases. More recently, the weak–coupling limit of the extended Hubbard model on a D–dimensional hypercubic lattice ($D \geq 3$) has been studied by van Dongen [355] using a $1/D$–expansion. The main result of this work is that, close to half–filling, the ground–state of the extended Hubbard model is phase separated rather than incommensurate (for $D \geq 3$), where the phase separated state consists of SDW or CDW ordered high–density and disordered low–density regions. Results similiar in conclusion were obtained earlier in the framework of our two–sublattice SB approach for the two–dimensional case (cf. the detailed analysis of the ground–state phase diagram presented in Ref. [272]). In the SDW domain, our results away from half–filling indicate only a weak tendency towards phase separation compared to the findings for the pure Hubbard model. For this case the critical doping δ_c, where the isothermal compressibility κ diverges, is shifted to smaller values with increasing V. On the other hand, for the CDW-like state (especially at $V/U > 0.5$) the effect of V is to *enhance* the concave curvature of the free energy, so that the formation of a phase separated ground state is favoured even more.

Part II

Lattice Instabilities and Polaronic Effects in Strongly Coupled Electron–Phonon Systems

Chapter 7

Selected phenomena in interacting electron–phonon systems

The interplay of electron–electron and electron–phonon (EP) interactions is of fundamental importance in determining the electronic properties of strongly correlated fermion systems currently of great interest in condensed matter physics. Especially research on high–T_c superconductivity has spurred intense investigations of the competition or, if possible, of the cooperation of these two fundamental interactions [356, 357]. Even if should turn out that the EP coupling is not the relevant pairing interaction in high–T_c compounds, EP effects need to be reconsidered for the case of strong electron–electron interaction and low effective dimensionality as realized in these materials. For example, in the presence of strong Coulomb correlations, a rather weak EP coupling can cause polaronic band narrowing [358, 359] and might, therefore, drive the system further into the strongly correlated regime.

Unfortunately, for strongly coupled EP systems exact results exist only in a few special cases and limits [360, 361, 362, 363]. Whereas, in an approximative treatment, the weak–coupling regime is well understood and dealt with by perturbation theory, the standard strong–coupling Migdal–Eliashberg theory [364, 365] based on the adiabatic Migdal theorem might break down for strong enough EP interactions due to the familiar polaronic band collapse [366]. From a theoretical point of view, the nature of the so–called 'self–trapping' transition, which describes the transformation of a band of quasi–free charge carriers to one of heavily dressed polaronic quasiparticles is one of the most challenging problems in strongly interacting EP systems. Although since Landau's early suggestion of a delocalization–localization transition in 1933 [367] numerous studies have been performed to tackle the formation of bi–/polarons (see Refs. [361, 366, 368, 369] for recent reviews), we still lack a complete understanding of this transition and even of the basic features of the polaronic or bipolaronic state (cf. the heated debates concerning the question whether small bi–/polarons can move itinerantly [356]).

Motivated by this situation, the purpose of our work is to address several issues in investigating interacting EP systems, which are relevant, both on general reasons as well as in the framework of high–T_c superconductivity. Using variational slave–boson and exact diagonalization techniques, we are particularly interested to study the problem of (bi)polaron formation and transport in terms of probably the simplest microscopic models proposed for a description of polaronic effects in systems with strong Coulomb correlations, the Holstein Hubbard model and the Holstein t–J model.

7.1 Polaronic effects in the copper and nickel oxides

Whereas it is widely believed that most of the unusual normal–state properties of the high-T_c oxide systems may be related to strong electronic correlations, the importance of EP coupling is still a heavily debated issue [356]. Many experiments have indicated substantial EP coupling in the bismuthates [350, 370] and recently in the copper oxides as well (cf. the Raman [371] and IR data [372, 373]). In addition, elaborate density functional calculations [374, 375] have demonstrated that the EP coupling is strong for several modes in $\mathrm{YBa_2Cu_3O_7}$ and $\mathrm{La_{2-x}(Ba,Sr)_xCuO_4}$. The relevance of EP coupling can be seen from the experimental observation of phonon renormalization in the cuprates [376]. For these materials, ion channeling [377, 378], neutron scattering [379] and photo-induced absorption measurements [380] also give evidence for large anharmonic lattice fluctuations, which may be responsible for local phonon–driven charge instabilities in the planar $\mathrm{CuO_2}$ electron system [381, 358]. Therefore polaronic effects are suggested to play a non–negligible role in the copper–based materials $\mathrm{La_{2-x}Sr_xCuO_{4+y}}$ [382, 366, 383, 384, 369, 385] and even more in the isostructural nickel–based charge transfer oxides $\mathrm{La_{2-x}Sr_xNiO_{4+y}}$ [384, 386]. Experimentally, photo-induced absorption experiments [387], infrared spectroscopy [388] and infrared reflectivity measurements [389] unambiguously indicate the formation of ‘self–localized’ polaronic states (small polarons) in the *insulating* parent compounds $\mathrm{La_2CuO_{4+y}}$ and $\mathrm{Nd_2CuO_{4-y}}$ of the hole– and electron–doped superconductors $\mathrm{La_{2-x}Sr_xCuO_{4+y}}$ and $\mathrm{Nd_{2-x}Ce_xCuO_{4-y}}$, respectively. On the other hand, the anomalous mid-infrared optical absorption band, observed in the normal *metallic* state of the doped LSCO and NCCO materials, has been interpreted in terms of photon–assisted hopping of small polarons as well [387, 390, 384]. Based on these experimental findings, several theoretical groups [391, 383, 392, 366, 393, 394, 395, 396, 369, 397, 398] propagate a (bi)polaronic scenario for high–T_c superconductivity.[1] Although there are many indications that at least part of the charge carriers in high–T_c compounds have characteristics of (bi)polarons [382], the present experimental situation certainly does not permit to draw any definite conclusion concerning the microscopic origin of high–T_c superconductivity in copper–oxide–based materials.

The strongest evidence for polaron formation in doped charge transfer oxides is provided by recent experiments on $\mathrm{La_{2-x}Sr_xNiO_4}$ [384, 386]. The isostructural compounds $\mathrm{La_2CuO_4}$ and $\mathrm{La_2NiO_4}$ show a remarkable difference upon the substitution of La by Sr. Both materials become metallic upon doping, but in the nickelates a nearly total substitution of La for Sr is necessary. Also in $\mathrm{La_{2-x}Sr_xNiO_{4+y}}$ no superconductivity is found for any x. A resolution of this problem might be given by extended LDA calculations [375], which show that the nickelates are much more susceptible to a breathing polaron instability than the cuprates. The reason is the much stronger magnetic confinement effect of additional holes and nickel spins. These low–spin composite holes are nearly entirely prelocalized and the EP coupling becomes much more effective in forming polarons. As a result a complex variety of (incommensurate) charge– and spin–ordering phenomena, related to magnetic and transport anomalies, have recently been observed at the doping level $x \approx 1/3$ [386, 399, 400, 401, 402] (see Fig. 7.1). At low doping, the incommensurate charge order due to the ‘quasi–frozen’ arrangements of carriers in $\mathrm{La_{2-x}Sr_xNiO_{4+y}}$ has a dramatic effect on the magnetic properties, replacing the Néel order of pure $\mathrm{La_2NiO_4}$ by a spin glass with incommensurate magnetic correlations peaked at the wave–vectors $\pi(1 \pm q_o, 1 \pm q_o)$ and $\pi(1 \pm q_o, 1 \mp q_o)$, where $q_o = 0.16$ for $x = 0.2$ [400, 401]. This has to be contrasted with the situation in the cuprates (cf. Sec. 1.3.1). For the composition $\mathrm{La_{1.5}Sr_{0.5}NiO_4}$ (quarter filling, $x = 0.5$), the electron diffraction measurements

---

[1] Note, however, that there is a lot of controversy [356] about the question of whether bipolaronic superconductivity requires the existence of ‘large’ [383] or ‘small’ [369] bipolarons.

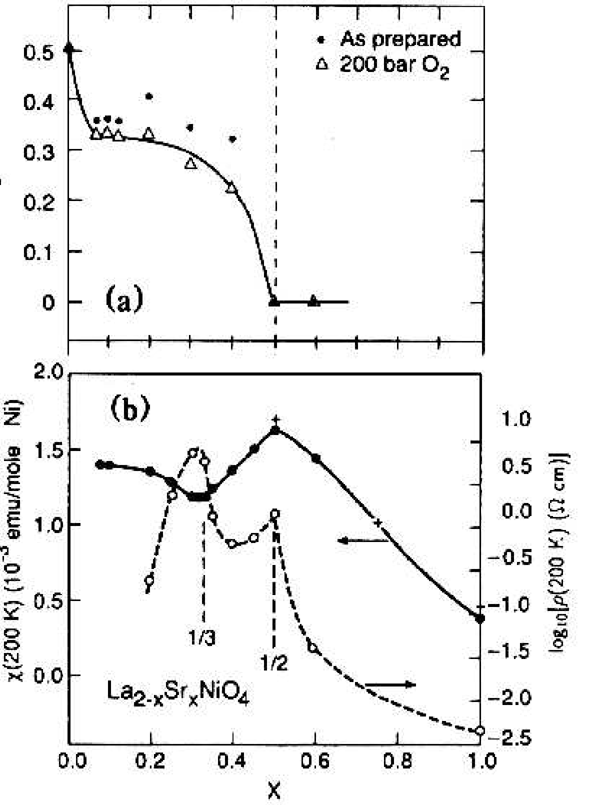

Figure 7.1: Charge modulation wave–vector δ of the superlattice modulation measured from the (π, π)–point at 93 K [(a), taken from [386]], spin susceptibility χ and logarithmic resistivity $\log \rho$ at 200 K [(b), taken from [399]] as a function of Sr doping x for $\mathrm{La}_{2-\mathrm{x}}\mathrm{Sr}_{\mathrm{x}}\mathrm{NiO}_{4+\mathrm{y}}$.

show a commensurate superstructure spot at the (π, π)–point, which has been interpreted as a sign of truly 2D ordering of breathing type polarons, i.e., as a polaronic superlattice. The difference between the polaronic behaviour of the cuprates and the nickelates is also seen in the infrared optical response [384].

7.2 Basic interactions and model Hamiltonians

Let us consider a system of correlated electrons coupled to phonons. The simplest models are then of the Holstein– (or Peierls–) Hubbard variety, where the electron–phonon interaction is incorporated in the Hamiltonian by a local Holstein term:

$$\mathcal{H} = \mathcal{H}_{el} + \mathcal{H}_{el-ph} + \mathcal{H}_{ph} \ , \tag{7.1}$$

with

$$\mathcal{H}_{el} = -t \sum_{\langle ij \rangle \sigma} \left(c^{\dagger}_{i\sigma} c_{j\sigma} + \mathrm{H.c.} \right) + U \sum_{i} n_{i\uparrow} n_{i\downarrow} \ , \tag{7.2}$$

$$\mathcal{H}_{el-ph} = -\bar{\lambda} \sum_{i\sigma} q_i n_{i\sigma} \ , \tag{7.3}$$

$$\mathcal{H}_{ph} = \sum_{i} \left(\frac{p_i^2}{2M} + \frac{K}{2} q_i^2 \right) \ . \tag{7.4}$$

The first term (7.2) represents the standard Hubbard model on a D–dimensional hypercubic lattice. The second term (7.3) couples the electronic system via the EP interaction constant $\bar{\lambda}$ locally to an internal optical degree of freedom of the effective lattice i. $\mathcal{H}_{ph}$ takes into account the elastic energy of a harmonic lattice with spring constant K and mass M.

In the context of an effective single–band description of the copper/nickel oxides, the collective Holstein coordinates q_i may be thought of as representing *local* apical out–of–plane [358] or bond–parallel in–plane [403] breathing–type displacements of the oxygen atoms.[2] At half–filling the EP coupling may lead to a Peierls instability (in competition to the AFM instability triggered by U), which is connected to a static (π, π)–distortion of the square lattice (frozen phonon mode).

In terms of K and M we define a reference phonon frequency $\omega = \sqrt{K/M}$. Introducing as usual phonon creation $b_i^\dagger$ and destruction operators b_i

$$q_i = \sqrt{\frac{\hbar}{2M\omega}}\left(b_i^\dagger + b_i\right) , \qquad p_i = i\sqrt{\frac{\hbar\omega M}{2}}\left(b_i^\dagger - b_i\right) . \tag{7.5}$$

for a quantum mechanical description of lattice vibrations, the Holstein Hubbard Hamiltonian (7.1) takes the form

$$\mathcal{H}_{H-H} = \hbar\omega \sum_i \left(b_i^\dagger b_i + \frac{1}{2}\right) - \sqrt{\varepsilon_p \hbar\omega} \sum_{i\sigma} \left(b_i^\dagger + b_i\right) n_{i\sigma} - t \sum_{\langle ij \rangle \sigma} \left(c_{i\sigma}^\dagger c_{j\sigma} + \text{H.c.}\right) + U \sum_i n_{i\uparrow} n_{i\downarrow} , \tag{7.6}$$

where $\varepsilon_p = \bar{\lambda}^2/2K$.

The physics of the Holstein Hubbard model is governed by three competing effects: the itinerancy of the electrons, their Coulomb repulsion and the local EP interaction. Once the energy scale has been extracted, there are two dimensionless ratios of energies, U/t and ε_p/t, which mainly determine the tendency of the itinerant quantum mechanical system to establish a magnetic or charge ordered state, respectively. Since, however, the EP coupling is retarded in nature, the ratio between phonon frequency and electronic hopping amplitude $\hbar\omega/t$ defines a third relevant energy scale of the problem. Obviously, the significance of the different effects depends on the electron density n, which is the fourth crucial parameter involved in the Holstein Hubbard model.

For the pure (1D) Holstein model, the different energy regimes and the corresponding approximations were classified by Feinberg *et al.* [407] in terms of ε_p/t, $\hbar\omega/t$, and $\sqrt{\varepsilon_p/\hbar\omega}$. The condition $\varepsilon_p/t \gg 1$ ($\ll 1$) refers to the strong–coupling (weak–coupling) case. On the other hand $\sqrt{\varepsilon_p/\hbar\omega} > 1$ (< 1) means that multi-phonon (single–phonon) processes are involved in the electron dynamics [407]. The adiabatic regime is then characterized by the relations $\hbar\omega \ll t, \varepsilon_p$ *and* $\sqrt{\hbar\omega\varepsilon_p} \ll t$, i.e., if $t < \sqrt{\hbar\omega\varepsilon_p}$ is fulfilled, non–adiabatic effects becomes important even for $\hbar\omega < t$ [407]. The non–adiabatic strong–coupling case may lead to polaron formation and, provided an attractive interaction is induced, to polaronic or bipolaronic superconductivity [350, 408]. In the opposite adiabatic limit, the competition between CDW states and standard BCS–like superconductivity takes place.

In the single–electron case, the Holstein Hamiltonian has been studied extensively as a paradigmatic model for polaron formation [366]. The principal result is that the effective mass of a single charge carrier coupled strongly to the local lattice vibrations becomes very heavy,

---

[2] For the planar breathing mode characterized by the wave–vector $\vec{Q} = (\pi, \pi)$ the Holstein coordinates take the form $q_i = \left(x_{i_x,i_y} - x_{i_x-1,i_y} + y_{i_x,i_y} - y_{i_x,i_y-1}\right)/4$, where the displacements of both oxygens in the unit cell $i = (i_x, i_y)$ are related by $x_{i_x,i_y} = -x_{i_x-1,i_y} = y_{i_x,i_y} = -y_{i_x,i_y-1}$. Obviously, a small distortion along the bonding direction leads to significant changes in the $\mathrm{Cu}_{3\mathrm{d}_{\mathrm{x}^2-\mathrm{y}^2}} - \mathrm{O}_{2\mathrm{p}_{\mathrm{x,y}}}$ overlap integral or hybridization [404]. As discussed in Sec. 2.1, upon doping the additional holes are mostly localized on the four oxygens surrounding the central Cu atom and may build up the Zhang–Rice singlets. Moving the in–plane oxygens towards the Cu this binding is enhanced ($q_i < 0$). The calculation of the planar EP coupling constant within a frozen–phonon procedure yields large values for this frequently discussed breathing–mode distortion [403, 405, 406, 375, 179].

making the particle susceptible to ‘self–trapping’. Monte Carlo simulations [409] indicate that the transition from a wide–band Fermi liquid to narrow–band polaronic system is *continuous* but *rather sharp* and takes place in the intermediate region of EP coupling. As stated above, the Migdal theorem is violated under this polaronic band collapse driven by the instability of the phonon vacuum [366]. Depending on the ratio $\hbar\omega/t$, there are two completely different types of approximations in the strong–coupling region [369]. The first approach, based on the Lang–Firsov canonical transformation [410] followed by the zero–phonon approximation, yields exact results in the antiadiabatic limit $\hbar\omega \to \infty$. It describes the case of (small) non-adiabatic Lang–Firsov polarons (NLFP). The second approach is based on an expansion in $\hbar\omega/t$, which has been worked out by Holstein [411, 412] for the two–site model only and yields another type of (heavy) polarons, the so–called ‘adiabatic’ Holstein polarons (AHP). Note that in the adiabatic limit $\hbar\omega \ll t, \varepsilon_p$, the procedure of averaging over phonons to obtain the renormalized polaronic bandwidth is doubtful [413, 359, 414]. Recently Kabanov and Mashtakov [415] have obtained the main results of the adiabatic approach from a functional–integral method, which takes the extremal displacement field configurations into account. We would like to emphasize that the situation becomes much less clear if the energy scales are not well separated, e.g., in the intermediate regime $\varepsilon_p \sim \hbar\omega \sim t$. Furthermore, in the many–particle system, the Coulomb correlations give rise to collective phenomena which may result in a variety of phases as a function of band filling and interaction strengths including, e.g., (incommensurate) charge– and spin–density–wave, bipolaronic or superconducting ground states.

Chapter 8

Theoretical analysis of the Holstein Hubbard model

In spite of the amazingly rich physics contained in the Holstein Hubbard model, it was tailored to investigate a large variety of long–standing problems in coupled EP systems, e.g., the Peierls charge–density–wave (CDW) formation [416, 417, 406, 418, 419], the dynamics of the self–trapping transition [350], polaronic superconductivity [395, 420] or the appearance of long–periodic (incommensurate) phases in quasi one-dimensional systems such as MX–chain compounds [421].

Neglecting the Coulomb interaction term, the molecular crystal or Holstein model [411] has been investigated with respect to pairing and Peierls CDW correlations using (quantum) Monte Carlo simulations in one spatial dimension [422] and recently in two dimensions in the half–filled band sector [423] as well as away from half–filling [424, 425]. Based on the concept 'transition by breaking of analyticity', Aubry *et al.* [426] argued that the CDW state in the Holstein model can be viewed as an superposition of bipolaronic states pinned to the lattice. The spinless Holstein model was treated by CPA [427], MC [428] and variational methods [429, 430] to discuss the self–trapping transition in the limit of low electron density ($n \ll 1$) and for the half–filled band case [407].

In the presence of Hubbard interaction U, the phase diagram of the half–filled 1D Holstein Hubbard model was obtained from Monte Carlo calculations [416]. For this model, the effects of quantum lattice fluctuations on the Peierls dimerization are worked out by means of a variational polaron wave function, where the electronic correlations are treated within the Hartree–Fock approximation [418] or using a modified Gutzwiller approach [419]. To discuss the polaronic properties in the strong EP coupling regime, a complete numerical solution was performed for the two–site Holstein Hubbard model by Ranninger and Thibblin [431] and for an O(4)–Cu(1)–O(4) cluster Hamiltonian by Mustre de Leon *et al.* [432]. For the 2D Holstein Hubbard model most of the calculations are done in the adiabatic limit ($\hbar\omega = 0$). The stability of the 2D Holstein Hubbard model against static Peierls distortions was investigated at and near half–filling by several authors using Hartree–Fock [417], quantum Monte Carlo [406] and exact diagonalization [358] methods.

In this chapter, we analyze the main features of the ground–state phase diagram of the 2D Holstein Hubbard model by means of a variational slave–boson scheme, which extends the variational treatment of the phonon dynamics proposed by Zheng *et al.* [433]. Our approach facilitates a unique treatment of electron–electron and electron–phonon interaction, and allows, to some extent, an interpolation between weak– and strong–coupling regimes as well as between adiabatic and antiadiabatic limits.

8.1 Variational treatment of the phonon subsystem

Let us now set up an effective electronic Hamiltonian for the Holstein Hubbard model. As a first step, we perform an *inhomogeneous modified variational Lang–Firsov transformation* (IMVLF) [359]

$$\tilde{\mathcal{H}} = \mathcal{U}^{\dagger}\,\mathcal{H}_{H-H}\,\mathcal{U}\,, \qquad \mathcal{U} = \mathrm{e}^{-\mathcal{S}_1(\Delta_i)}\,\mathrm{e}^{-\mathcal{S}_2(\bar{\gamma},\gamma)}\,\mathrm{e}^{-\mathcal{S}_3(\alpha)} \tag{8.1}$$

with

$$\mathcal{S}_1(\Delta_i) = -\frac{1}{2\sqrt{\hbar\omega\varepsilon_p}}\sum_i \Delta_i(b_i^{\dagger} - b_i)\,, \tag{8.2}$$

$$\mathcal{S}_2(\bar{\gamma},\gamma) = -\sqrt{\varepsilon_p/\hbar\omega}\sum_{i\sigma}(\bar{\gamma}/2 + \gamma n_{i\sigma})(b_i^{\dagger} - b_i)\,, \tag{8.3}$$

$$\mathcal{S}_3(\alpha) = -\alpha\sum_i(b_i^{\dagger}b_i^{\dagger} - b_i b_i)\,, \tag{8.4}$$

where $\sum_i \Delta_i = 0$. The unitary transformation $\mathcal{U}$ contains $N+2$ variational parameters.

Here, the first canonical transformation $\mathcal{S}_1(\{\Delta_i\})$ introduces a set of static *site–dependent* displacement fields Δ_i, i.e., there is a priori no restriction to a special type of CDW order. $\mathcal{S}_1$ is designed to describe static *local* lattice distortions and ensures the correct behaviour of our theory in the strong–coupling *adiabatic* limit (see Chap. 10). The special cases

$$\Delta_i = 0 \qquad\qquad \text{(UMVLF)} \tag{8.5}$$

and

$$\Delta_i = (-1)^i\Delta \qquad \text{(SMVLF)} \tag{8.6}$$

refer to *uniform* [434] and *staggered* [433] distributions of the displacement fields, respectively. It is in the spirit then, that the former transformation is ‘correct’ at low densities in the non–adiabatic regime while the latter one should be appropriate near half–filling in the adiabatic limit (here Δ is a measure of static phonon–staggered ordering related to a frozen–in (π,π)–dimerization of the lattice [433]).

To describe polaronic effects at arbitrary band fillings, a second unitary transformation $\mathcal{S}_2(\gamma,\bar{\gamma})$ was performed, where the variational parameter γ measures the degree of the polaron effect ($0 \le \gamma \le 1$), which becomes most important in the low–carrier–density *antiadiabatic* limit. For $\gamma \equiv 1$ and $\bar{\gamma} \equiv 0$, S_2 becomes the well–known Lang–Firsov (LF) transformation [410]. The parameter $\bar{\gamma}$ may be obtained from $\langle\tilde{b}_i\rangle_{\tilde{\mathcal{H}}} = \langle b_i\rangle_{\mathcal{H}} = \sqrt{\varepsilon_p/\hbar\omega}\,n$ $(\tilde{b}_i = \mathcal{U}^{\dagger}b_i\mathcal{U})$ with $\langle b_i\rangle_{\tilde{\mathcal{H}}} = 0$ or by minimization of the free–energy functional with respect to $\bar{\gamma}$ yielding $\bar{\gamma} = n - \gamma n$ (see next section). Thus in S_2, the first contribution of $\bar{\gamma}$ results in a mean shift of the equilibrium position of the local oscillators while the second contribution, together with the second term of S_2, couples the polaronic distortion to the density fluctuation $n_i - n$. As will be shown in Sec. 8.4 [434], the transformation (8.3) describes finite–density effects much more correctly than the variational Lang–Firsov (VLF) approach ($\bar{\gamma} \equiv 0$) used by Feinberg *et al.* [407].

To take into account for the anharmonicity of the phonon modes we perform the squeezing transformation $\mathcal{S}_3$, proposed by Zheng *et al.* [433, 435], generating a new type of Glauber coherent lattice states, the two–phonon state [436]. The squeezing effect, which becomes relevant at finite electron densities, counteracts the polaronic band narrowing. The inclusion of squeezing phenomena is a first step towards the understanding of the multi–phonon regime at intermediate coupling strengths, where $1 \lesssim \varepsilon_p/t < \sqrt{\varepsilon_p/\hbar\omega}$. More recently, the squeezing approach has been generalized by taking into account the correlations between different squeezed phonon states [437].

As a result of (8.2) to (8.4), the transformed Hamiltonian (8.1) is given by

$$\begin{aligned}\tilde{\mathcal{H}} \;=\;& \bar{\gamma}^2\varepsilon_p N + \frac{1}{4\varepsilon_p}\sum_i \Delta_i^2 + \tilde{\lambda}\sum_i \Delta_i \\ &+\frac{\hbar\omega}{2}\left(\tau^2+\tau^{-2}\right)\sum_i (b_i^\dagger b_i + \frac{1}{2}) + \frac{\hbar\omega}{4}\left(\tau^2-\tau^{-2}\right)\sum_i (b_i^\dagger b_i^\dagger + b_i b_i) \\ &+\sqrt{\varepsilon_p\hbar\omega}\,\bar{\gamma}\tau^{-1}\sum_i (b_i^\dagger + b_i) + \sqrt{\hbar\omega/\varepsilon_p}\,(2\tau)^{-1}\sum_i \Delta_i(b_i^\dagger + b_i) \\ &-(1-\gamma)\sum_{i\sigma}\Delta_i n_{i\sigma} - \sqrt{\varepsilon_p\hbar\omega}\,(1-\gamma)\,\tau^{-1}\sum_{i\sigma}(b_i^\dagger + b_i)n_{i\sigma} \\ &-\tilde{\varepsilon}_p\sum_{i\sigma} n_{i\sigma} - t\sum_{<ij>\sigma}\left(\tilde{\Phi}_{ij}c_{i\sigma}^\dagger c_{j\sigma} + \text{H.c.}\right) + \tilde{U}\sum_i n_{i\uparrow}n_{i\downarrow}\,, \end{aligned} \tag{8.7}$$

where

$$\tilde{\varepsilon}_p = \varepsilon_p\left[\gamma(2-\gamma) + 2(1-\gamma)\bar{\gamma}\right]\,, \tag{8.8}$$

$$\tilde{U} = U - 2\varepsilon_p\gamma(2-\gamma)\,, \tag{8.9}$$

$$\tilde{\Phi}_{ij} = \exp\left\{-\gamma\tau\sqrt{\varepsilon_p/\hbar\omega}\left(b_i^\dagger - b_i - b_j^\dagger + b_j\right)\right\}\,, \tag{8.10}$$

and the squeezing parameter $\tau^2 = \exp\{-4\alpha\}$ were introduced. The Lagrange parameter $\tilde{\lambda}$ enforces the constraint $\sum_i \Delta_i = 0$.

As a next step in our variational approach, the eigenstates $|\tilde{\Psi}\rangle$ of $\tilde{\mathcal{H}}$ are approximated by the variational states $|\tilde{\Psi}_V\rangle$ taking the ansatz

$$|\tilde{\Psi}_V\rangle = |\tilde{\Psi}_{ph}\rangle \otimes |\tilde{\Psi}_{el}\rangle\,. \tag{8.11}$$

Eq. (8.11) corresponds to the decoupling of the *transformed* phonon and electron subsystems described by $\tilde{\mathcal{H}}$.

Finally, averaging over the transformed phonon vacuum, $\overline{\mathcal{H}}_{H-H} \equiv \langle\tilde{\Psi}_{ph}^0|\tilde{\mathcal{H}}|\tilde{\Psi}_{ph}^0\rangle$, we obtain the effective electronic Hamiltonian

$$\begin{aligned}\overline{\mathcal{H}}_{H-H} \;=\;& \frac{\hbar\omega}{4}N(\tau^2+\tau^{-2}) + \bar{\gamma}^2\varepsilon_p N + \frac{1}{4\varepsilon_p}\sum_i \Delta_i^2 + \tilde{\lambda}\sum_i \Delta_i - (1-\gamma)\sum_{i\sigma}\Delta_i n_{i\sigma} \\ &-\tilde{\varepsilon}_p\sum_{i\sigma} n_{i\sigma} - \rho t\sum_{<ij>\sigma}\left(c_{i\sigma}^\dagger c_{j\sigma} + \text{H.c.}\right) + \tilde{U}\sum_i n_{i\uparrow}n_{i\downarrow}\,. \end{aligned} \tag{8.12}$$

Here

$$\rho = \overline{\tilde{\Phi}_{ij}} = \langle\tilde{\Psi}_{ph}^0|\tilde{\Phi}_{ij}|\tilde{\Psi}_{ph}^0\rangle = \exp\{-\varepsilon_p\gamma^2\tau^2/\hbar\omega\} \tag{8.13}$$

is the polaronic band narrowing factor, where, for $\gamma^2 = \tau^2 = 1$, ε_p denotes the small–polaron binding energy in the atomic limit ($t = 0$). Note that in this approach the dynamic part of the residual polaron–multi-phonon interaction is neglected (cf. Sec. 8.5). Furthermore, let us emphasize that the transformed phonon vacuum is not an eigenstate of the phonon number operators. Since the generators $\mathcal{S}_1$ and $\mathcal{S}_2$ do not commute with $\mathcal{S}_3$, the state $|\tilde{\Psi}\rangle$ with minimal uncertainty was obtained in applying first the squeezing transformation [407].

As can be seen from the first term of $\overline{\mathcal{H}}_{H-H}(\Delta_i, \bar{\gamma}, \gamma, \tau^2)$, the squeezing transformation leads via a frequency renormalization to an increase of the zero–point energy of the phonons. On the other hand, the reduction of the hopping integral is weakened by τ^2, i.e., the phonon squeezing decreases the zero–point fluctuations of the conjugated momentum. Therefore one can expect a maximal squeezing effect somewhere between the weak– and strong–coupling limits [407]. With respect to the interplay of the dynamic polaron effect and the static CDW formation near half–filling, Zheng's SMVLF approach [433, 435] incorporates the interference of both contributions (cf. the fifth term of (8.12)). This effect was omitted in the variational treatment of Nasu [438]. Obviously, in the effective Hubbard model $\overline{\mathcal{H}}_{H-H}$, the bare Hubbard repulsion becomes renormalized ($U \to \tilde{U}$), which raises the probability of a phonon–induced attractive interaction $\tilde{U} < 0$.

8.2 Slave–boson theory for the effective electronic Hamiltonian [179, 439]

In order to treat the correlation effects incorporated in the effective model (8.12) in a non–perturbative way, we use the scalar slave–boson approach introduced by Kotliar and Ruckenstein [156]. Their SB scheme provides a symmetric representation of spin and charge degrees of freedom and therefore should be an appropriate starting point for a treatment of the 2D Holstein Hubbard model as well. Since a detailed presentation of the KR SB theory applied to the Hubbard and extended Hubbard models has been given in Sec. 2.4 and Chap. 6, we restrict us to list the essential steps and equations.

We evaluate the theory at the saddle–point level where all Bose fields become real variables. Of course, an unrestricted minimization of the corresponding free–energy functional is impossible for the infinite system. Therefore, we will use the SMVLF transformation ($\Delta_i = (-1)^i \Delta$) and adopt the two–sublattice SB mean–field approximation [180], i.e., the Bose fields are considered as static and uniform on a sublattice $\eta = A, B$ which also implies that the constraints are satisfied on each sublattice only on average. This approximation allows for a description of the paramagnetic (polaronic) phase and of long–range ordered states such as antiferro– (AFM), ferro– (FM), and ferrimagnetic (FIM) phases with or without a CDW ((π,π)–dimerization). The perfect Fermi surface nesting of 2D tight-binding band structure points towards the occurrence of A–B symmetry broken states at least at half–filling.

Then, the free–energy functional can be represented as

$$\begin{aligned} f(\Delta, \bar{\gamma}, \gamma, \tau^2) \;=\;& \frac{1}{2}\sum_{\eta}\left[-\lambda_{\eta}^{(1)} + \lambda_{\eta}^{(1)} e_{\eta}^2 + \sum_{\sigma}(\lambda_{\eta}^{(1)} - \lambda_{\eta\sigma}^{(2)}) p_{\eta\sigma}^2 + [\lambda_{\eta}^{(1)} - \sum_{\sigma}\lambda_{\eta\sigma}^{(2)} + \tilde{U}] d_{\eta}^2\right] \\ & + \frac{\hbar\omega}{4}\left(\tau^2 + \tau^{-2}\right) + \frac{\Delta^2}{4\varepsilon_p} + \bar{\gamma}^2 \varepsilon_p + \mu\, n + \frac{1}{\beta N}\sum_{\vec{k}\nu\sigma}\ln\left\{1 - n_{\vec{k}\nu\sigma}\right\}, \end{aligned} \tag{8.14}$$

where

$$n_{\vec{k}\nu\sigma} = \left[\exp\left\{\beta(E_{\vec{k}\nu\sigma} - \mu)\right\} + 1\right]^{-1} \tag{8.15}$$

with

$$E_{\vec{k}\nu\sigma} = \lambda_{\sigma}^{(+)} - \tilde{\varepsilon}_p + \varepsilon_{\vec{k}\nu\sigma}\,, \qquad \varepsilon_{\vec{k}\nu\sigma} = \nu\sqrt{\left(\lambda_{\sigma}^{(-)} - \Delta(1-\gamma)\right)^2 + \rho^2 q_{A\sigma} q_{B\sigma} \varepsilon_{\vec{k}}^2}\,, \tag{8.16}$$

$q_{\eta\sigma} = |z_{\eta\sigma}|^2$, and $\lambda_{\sigma}^{(\pm)} = (\lambda_{A\sigma}^{(2)} \pm \lambda_{B\sigma}^{(2)})/2$.

Requiring the free–energy functional (8.14) to be stationary with respect to variations of the bosonic fields e_η, d_η, $p_{\eta\sigma}$, $\lambda_\eta^{(1)}$, and $\lambda_{\eta\sigma}^{(2)}$, one has to solve self–consistently the set of 14 coupled saddle–point equations

$$\lambda_\eta^{(1)} e_\eta = \sum_{\sigma'} q_{-\eta\sigma'} \frac{4x_{\eta\sigma'}}{1-4\delta_{\eta\sigma'}^2} \left(\frac{2e_\eta x_{\eta\sigma'}}{1+2\delta_{\eta\sigma'}} - p_{\eta\sigma'} \right) \rho^2 I_{\sigma'}^{(2)} \,, \tag{8.17}$$

$$[\lambda_\eta^{(1)} - \sum_\sigma \lambda_{\eta\sigma}^{(2)} + \tilde{U}] d_\eta = \sum_{\sigma'} q_{-\eta\sigma'} \frac{4x_{\eta\sigma'}}{1-4\delta_{\eta\sigma'}^2} \left(\frac{2d_\eta x_{\eta\sigma'}}{1-2\delta_{\eta\sigma'}} - p_{\eta-\sigma'} \right) \rho^2 I_{\sigma'}^{(2)} \,, \tag{8.18}$$

$$\begin{aligned} &[\lambda_\eta^{(1)} - \lambda_{\eta\sigma}^{(2)}] p_{\eta\sigma} = \\ &\quad \sum_{\sigma'} q_{-\eta\sigma'} \frac{4x_{\eta\sigma'}}{1-4\delta_{\eta\sigma'}^2} \left[\left(\frac{2p_{\eta\sigma'} x_{\eta\sigma'}}{1-2\delta_{\eta\sigma'}} - e_\eta \right) \delta_{\sigma\sigma'} + \left(\frac{2p_{\eta-\sigma'} x_{\eta\sigma'}}{1+2\delta_{\eta\sigma'}} - d_\eta \right) \delta_{\sigma-\sigma'} \right] \rho^2 I_{\sigma'}^{(2)} \,, \end{aligned} \tag{8.19}$$

$$e_\eta^2 + d_\eta^2 + \sum_\sigma p_{\eta\sigma}^2 = 1 \,, \tag{8.20}$$

$$d_\eta^2 + p_{\eta\sigma}^2 = \frac{1}{N} \sum_{k\nu} n_{k\nu\sigma} \left(1 + \xi_\eta \frac{\lambda_\sigma^{(-)} - \Delta(1-\gamma)}{\varepsilon_{\vec{k}\nu\sigma}} \right) \,, \tag{8.21}$$

together with the following extremal equations for the variational parameters Δ, $\bar{\gamma}$, γ, and τ^2 :

$$\Delta = 2\varepsilon_p (1-\gamma) \sum_\sigma \left[\lambda_\sigma^{(-)} - \Delta(1-\gamma) \right] I_\sigma^{(0)} \,, \tag{8.22}$$

$$\bar{\gamma} = (1-\gamma)(1-\delta) \,, \tag{8.23}$$

$$\begin{aligned} &2\varepsilon_p (1-\gamma) \left[(1-\delta) + d_A^2 + d_B^2 \right] - 2\varepsilon_p \bar{\gamma} (1-\delta) \\ &\quad = \Delta \sum_\sigma \left[\lambda_\sigma^{(-)} - \Delta(1-\gamma) \right] I_\sigma^{(0)} - 2\tau^2 \rho^2 \gamma \frac{\varepsilon_p}{\hbar\omega} \sum_\sigma q_{A\sigma} q_{B\sigma} I_\sigma^{(2)} \,, \end{aligned} \tag{8.24}$$

$$\frac{\hbar\omega}{4} (1-\tau^{-4}) = \gamma^2 \rho^2 \frac{\varepsilon_p}{\hbar\omega} \sum_\sigma q_{A\sigma} q_{B\sigma} I_\sigma^{(2)} \,. \tag{8.25}$$

In the above equations, we use the abbreviations

$$I_\sigma^{(0)} := \frac{1}{N} \sum_{\vec{k}\nu} n_{\vec{k}\nu\sigma} \frac{1}{\varepsilon_{\vec{k}\nu\sigma}} \,, \tag{8.26}$$

$$I_\sigma^{(2)} := \frac{1}{N} \sum_{\vec{k}\nu} n_{\vec{k}\nu\sigma} \frac{\varepsilon_{\vec{k}}^2}{\varepsilon_{\vec{k}\nu\sigma}} \,, \tag{8.27}$$

$$x_{\eta\sigma} := e_\eta p_{\eta\sigma} + p_{\eta-\sigma} d_\eta \,, \tag{8.28}$$

$$\delta_{\eta\sigma} := 1/2 - p_{\eta\sigma}^2 - d_\eta^2 \,, \tag{8.29}$$

as well as the conventions $\xi_\eta = 1\,(-1) \Leftrightarrow \eta = A\,(B)$ and $\sigma = 1\,(-1) \Leftrightarrow \sigma = \uparrow (\downarrow)$.

Furthermore, we introduce the charge– (Δ_{CDW}) and spin–density–wave (Δ_{SDW}) order parameters

$$\Delta_{CDW} = \frac{1}{2} \sum_{\eta\sigma} \xi_\eta n_{\eta\sigma} = \frac{\Delta}{2\varepsilon_p(1-\gamma)} \,, \tag{8.30}$$

$$\Delta_{SDW} = \frac{1}{2} \sum_{\eta\sigma} \xi_\eta \sigma n_{\eta\sigma} \,, \tag{8.31}$$

and the net magnetization

$$m = \frac{1}{2}\left(m_A + m_B\right) = \frac{1}{2}\sum_{\eta\sigma} \sigma n_{\eta\sigma}\,, \tag{8.32}$$

where the sublattice particle numbers (per spin) are given by $n_{\eta\sigma} = p_{\eta\sigma}^2 + d_\eta^2$. Finally, we define the local magnetic moment m_{loc} and the effective hopping amplitude t_{eff} according to:

$$m_{loc} = \frac{3}{8}\sum_\eta \left(n_\eta - 2d_\eta^2\right)\,, \tag{8.33}$$

$$t_{eff} = \frac{< \sum c_{i\sigma}^\dagger c_{j\sigma} >}{< \sum c_{i\sigma}^\dagger c_{j\sigma} >_{(U,\varepsilon_p,\hbar\omega)=0}}\,. \tag{8.34}$$

8.3 Charge and spin correlations in the weak–coupling regime [179, 272, 439]

In the numerical evaluation of the self–consistency loop (8.17)–(8.25) we proceed as follows: eliminating the variables e_η^2, $p_{\eta\sigma}^2$, $\lambda_\eta^{(1)}$ and $\bar{\gamma}$, we solve the six remaining saddle–point equations for d_η^2 and $\lambda_\sigma^{(\pm)}$ together with the integral equation for μ using an iteration technique. At given model parameters ε_p, U, ω and n (all energies are measured in units of t, and $\hbar = 1$) this is done for a fixed initial set of variational parameters $\{\Delta^{(i)}, \gamma^{(i)}, \tau^{2\,(i)}\}$. Then, in an outer loop, the new set $\{\Delta^{(i+1)}, \gamma^{(i+1)}, \tau^{2\,(i+1)}\}$ is obtained from a fix–point iteration of the variational equations (8.22)–(8.25) at the point where the bosonic fields are stationary. Convergence is achieved if order and variational parameters are determined with a relative error $\leq 10^{-6}$. In this iteration process, the $\vec{k}$–summations were performed at $T = 0$ using the unperturbed 2D tight–binding density of states $N(\varepsilon) = K(1-\varepsilon^2/16)/2\pi^2$, where $K(m)$ denotes the complete elliptic integral of the first kind.

The theory developed so far allows the investigation of the whole parameter range of EP coupling strengths. In this section we will restrict the numerical calculations to the case of moderate EP interaction, where polaronic effects lead only to a weak mass renormalization of the charge carriers, i.e., we consider the light–polaron regime. Since the critical coupling strength for the transition from 'light' to 'heavy' polarons was found to be $\varepsilon_{p,c}(n)/t \sim 4$–6 for the Holstein Hubbard model [434], we chose as a typical EP coupling $\varepsilon_p = 1.8$ throughout this section.

8.3.1 Special limits of the Holstein Hubbard model

The adiabatic limit $\omega = 0$

First we recapitulate the basic features of the ground–state phase diagram of the Holstein Hubbard model at $\omega = 0$ [179, 177]. The domains of stability of several homogeneous ground states are shown in Fig. 8.1 in the U–δ plane. Here the different phases are classified according to the order parameters (8.30)–(8.32). For the states with vanishing net magnetization ($m = 0$) we have:

PM	$\Delta_{CDW} = 0$	$\Delta_{SDW} = 0$
PM/CDW	$\Delta_{CDW} \neq 0$	$\Delta_{SDW} = 0$
AFM	$\Delta_{CDW} = 0$	$\Delta_{SDW} \neq 0\,.$

The various FIM states ($m \neq 0$) can be specified with respect to the relative importance of SDW and CDW correlations (cf. Ref. [177]):

$$\begin{array}{ll} \text{FIM} & \Delta_{CDW} \approx \Delta_{SDW} \\ \text{FIM/SDW} & \Delta_{CDW} \ll \Delta_{SDW} \\ \text{FIM/CDW} & \Delta_{CDW} \gg \Delta_{SDW} \,. \end{array}$$

(For the pure Hubbard model, away from half–filling, FIM solutions were considered first by Oleś [440] using the Local ansatz [351]). In addition, there is the FM state with $m > 0$ and $\Delta_{CDW} = \Delta_{SDW} = 0$.

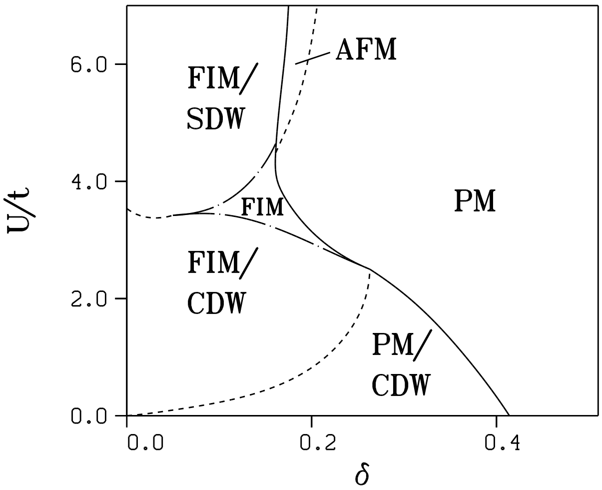

Figure 8.1: Ground–state phase diagram of the 2D Holstein Hubbard model in the adiabatic limit ($\omega = 0$) at $\varepsilon_p = 1.8$. The solid line separates states with finite lattice distortion from 'undimerized' states. For further explanation see text.

At half–filling we obtain a stable PM/CDW state below a critical Hubbard interaction U_c, where the 'dimerization' of the square lattice is related via (8.30) to the CDW order parameter. Increasing the Coulomb interaction the gap parameter Δ decreases up to the abrupt breakdown at the first–order transition to the AFM state. Note that U_c is only slightly reduced from its Hartree–Fock value $U_c^{HF} = 2\varepsilon_p$ [179].

Off half–filling, solutions with finite Peierls distortions are lowest in energy for a large parameter range of U and δ. Depending on the relative strength U/ε_p, one observes a CDW and SDW dominated regime. The dashed phase boundary between FIM/CDW and FIM/SDW denotes a first–order transition, whereas both Δ_{CDW} and Δ_{SDW} vary continuously along the FIM/CDW$\rightleftharpoons$ FIM $\rightleftharpoons$ FIM/SDW transition. It has to be noted that the FM state is absent within this parameter range.

The case $\tilde{U}$=0

At finite frequencies, the effective Coulomb repulsion $\tilde{U} = U - 2\varepsilon_p(2\gamma - \gamma^2)$ is reduced by polaronic effects. In particular, for $U < 2\varepsilon_p$, an attractive interaction $\tilde{U} < 0$ appears at high enough frequencies. It is just this phenomenon which gives rise to the possibility of bipolaron formation. In the standard polaron theories, the interaction term is usually neglected. This is certainly correct in the extreme dilute limit $n \ll 1$. For finite electron densities, however, the effective electron interaction becomes important. Putting $\tilde{U}$ equal to zero before the variation of the ground–state energy (8.14) with respect to $\bar{\gamma}$, γ, τ^2 and d^2, we obtain, e.g., for the self–trapping transition an unphysical large critical coupling strength $\varepsilon_{pc} \propto (1-n)^{-1}$ near half–filling [434].

The approximation $\tilde{U} \equiv 0$ was used by Weber and Büttner [441] to investigate electronic correlations in Peierls systems. The main problem of this approach lies in the fact, that the advantage of an exact diagonalization of the transfomed Hamiltonian (which is strictly valid only for one special point in the parameter space), is accompanied by a loss of variational degrees of freedom.

To determine the hyperplane where $\tilde{U} = 0$ is actually fulfilled, we solve the complete set of self–consistency equations (8.17)–(8.25), ensuring the constraint

$$\gamma_0 = 1 - \sqrt{1 - U/2\varepsilon_p}\,. \tag{8.35}$$

Then the extremal free energy is obtained as

$$\begin{aligned} \overline{f}(\tilde{U} = 0) &= \frac{\hbar\omega}{4}\left(\tau_0^2 + \tau_0^{-2}\right) + \frac{\Delta^2}{4\varepsilon_p} - \varepsilon_p\, n\left[1 - (1-n)(1-\gamma_0)^2\right] \\ &+ \frac{2}{N}\sum_{\vec{k}\nu} \nu\sqrt{\Delta_0^2(1-\gamma_0)^2 + \rho_0^2\,\varepsilon_{\nu\vec{k}}^2}\;\Theta\left(\mu - \varepsilon_{\nu\vec{k}}\right)\,. \end{aligned} \tag{8.36}$$

Figure 8.2 shows the corresponding ($\tilde{U} = 0$) contour plot as a function of U in the ω–δ plane at $\varepsilon_p = 1.8$. The solid line separates the Peierls distorted state from the pure PM. In the antiadiabatic limit the ‘dimerization’ vanishes asymptotically even at $\delta = 0$ where $\tilde{U} = 0$ is reached for $U = 2\varepsilon_p$ independent of δ. Figure 8.2 clearly indicates that, including even a moderate Hubbard interaction, bipolaron formation becomes unlikely in the low–frequency regime.

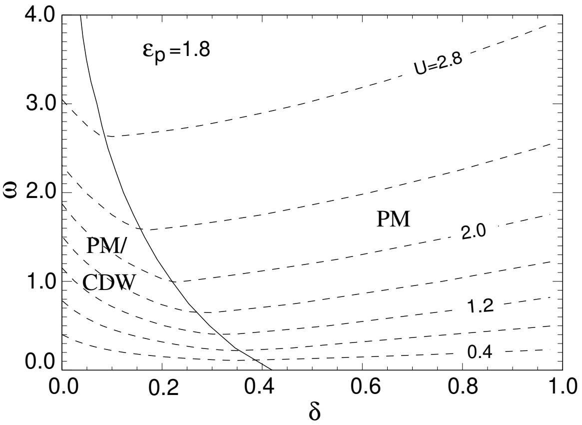

Figure 8.2: Lines of constant U on the $\tilde{U} = 0$ hyperplane.

The pure Holstein model

In proceeding to investigate the solutions of the extremal equations (8.17)–(8.25), it is useful to consider first the special case $U = 0$, i.e., the Holstein model. Our numerical results are summarized in Figs. 8.3 and 8.4.

The stability region of the state with finite Peierls distortion is shown in Fig. 8.3 (a). Doping the system away from half–filling, a second–order phase transition PM/CDW$\rightleftharpoons$PM takes place, where the transition point $\delta_c(\omega)$ is shifted to lower values increasing the phonon frequency. To analyze this transition and the main features of the ground–state solution, in Fig. 8.3 (b)–(d)

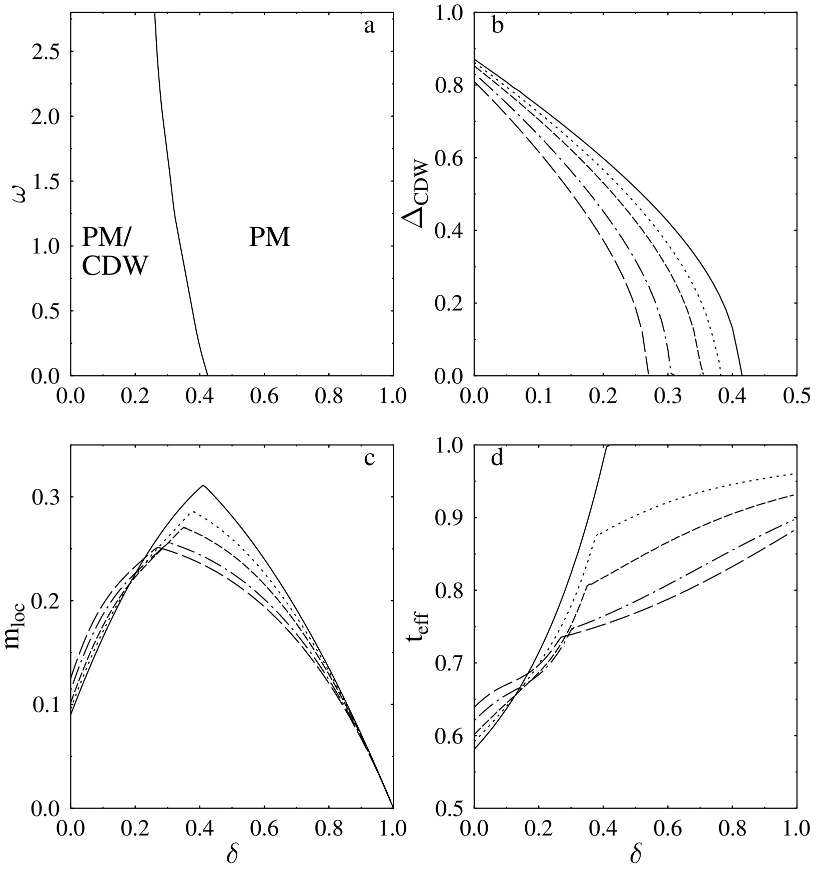

Figure 8.3: Phase diagram of the pure Holstein model ($U \equiv 0$), CDW order parameter Δ_{CDW}, local magnetic moment m_{loc}, and effective hopping amplitude t_{eff} are shown as a function doping δ in **a**, **b**, **c** and **d**, respectively. The results are given at $\varepsilon_p = 1.8$ for various phonon frequencies $\omega = 0$ (solid), 0.4 (dotted), 0.8 (dashed), 1.6 (chain dotted), and 2.4 (long dashed).

we present Δ_{CDW}, m_{loc} and t_{eff} as a function of doping at various frequencies. As can be seen from Fig. 8.3 (b), the CDW order parameter goes continuously to zero with increasing δ. Let us emphasize that the static Peierls distortion is suppressed by two effects acting in combination. The δ–effect, which exists at $\omega = 0$ as well, can be attributed to an increasing asymmetry in the occupation numbers d_A^2 and e_B^2 upon doping (recall that the on–site energies are lowered (raised) on the A– (B–) sublattice in the CDW state, thus one has $d_A^2 = e_B^2 > d_B^2 = e_A^2$ at half–filling). The inclusion of phonon dynamics yields a further reduction of the CDW long–range order. Obviously, the finite–ω effects, which in our variational approach are mainly realized via the ability to polaron formation, become more important at larger hole concentrations. The destruction of the PM/CDW structure leads to the occurrence of a larger number of single occupied sites and therefore to an enhancement of the local magnetic moment (see Fig. 8.3 (c)). At the same time, the mobility of the charge carriers is increased, so we get a considerably enhanced effective hopping amplitude t_{eff} (cf. Fig. 8.3 (d)). In the PM state, one observes with decreasing electron density a decrease [increase] of m_{loc} [t_{eff}].

For a more detailed discussion of the non–adiabatic effects, we have plotted the polaron band narrowing ρ, the variational parameters γ and τ^2, and the effective interaction $\tilde{U}$ in Fig. 8.4 (a)–(d). First of all, as displayed in Fig. 8.4 (b), the main effect of the quantum

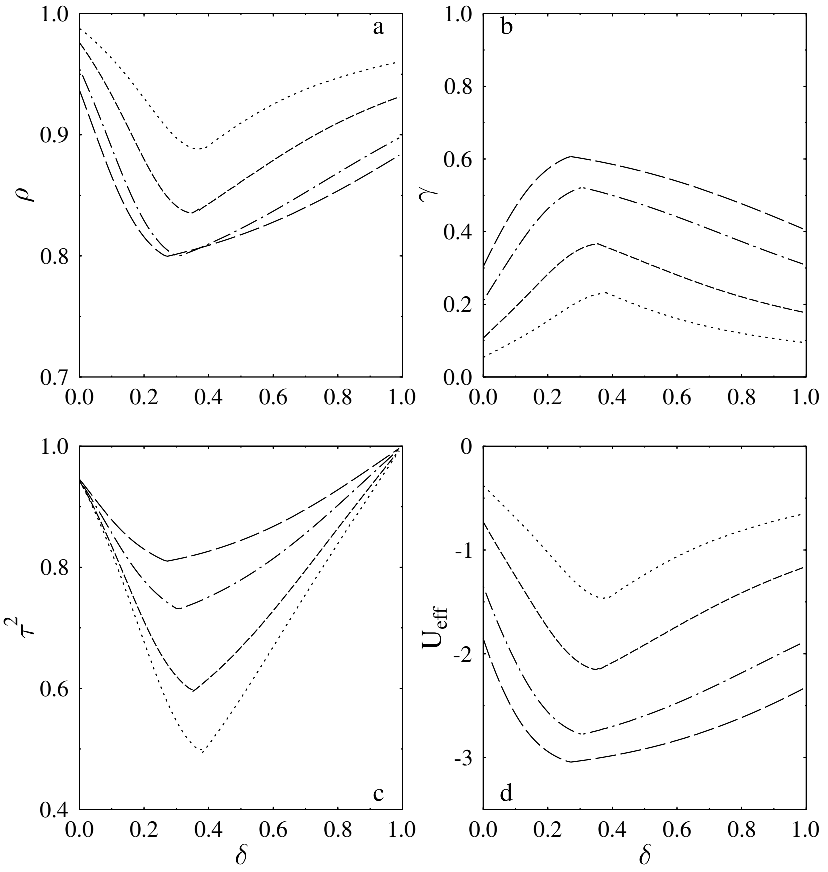

Figure 8.4: Polaron band narrowing ρ **a**, polaron γ **b** and squeezing τ^2 **c** variational parameters, as well as the effective Coulomb interaction $U_{eff} := \tilde{U}$ **d** as a function of doping at various frequencies. The notation is the same as in Fig. 8.3 (a)–(d).

fluctuations is to enhance the tendency towards polaron formation. That means, the movement of the charge carriers and its concomitant lattice distortion creates large anomalous fluctuations of the lattice coordinates and the local charge density. It follows that the (adiabatic) CDW ordering is suppressed with respect to the case $\omega = 0$ (cf. the interference term $\propto (-1)^i\Delta(1-\gamma)$ in (8.12)). As pointed out by Feinberg *et al.* [407], in a many–polaron system, the coherent motion of polarons implies by a quantum mechanical effect a squeezing of the conjugated momentum fluctuations which counteracts the polaronic band renormalization (Fig. 8.4 (c)). Including this squeezing phenomena, the net result for ρ is shown in Fig. 8.4 (a). Let us stress that our variational treatment yields a rather weak polaron band narrowing ($\rho \sim 0.8 - 0.9\ \forall\delta$ compared to $\rho \sim 10^{-4}$ in the normal small–polaron theory [411]), i.e., even for $\varepsilon_p/t \sim 2\ldots4$ the polarons are 'light' quasiparticles [434, 442]. At low doping the loss of mobility due to the reduction of ρ is overcompensated by the gain of kinetic energy when the long–range order (CDW) goes down and t_{eff} increases with ω (cf. Fig. 8.3 (d)). At larger (but fixed) δ, i.e., in particular in the PM region, t_{eff} is reduced by the polaron band narrowing (note that now $t_{eff}(\omega = 0) = 1$ holds). Of course, for the Holstein model, the effective Hubbard interaction $\tilde{U}$ is always negative (Fig. 8.4 (d)). This attractive on–site interaction would favour bipolaron formation if the EP coupling is strong enough ($\varepsilon_p/t \sim 3$ [442]). (Contrary to the CDW state the bipolaronic state may be characterized by an enhanced probability for double occupancy on *both* sublattices). In the weak–coupling regime, however, the probability of single occupancy becomes only somewhat weakened and as a result the local magnetic moment is slightly reduced with increasing ω (cf. Fig. 8.3 (c)). Clearly, these correlation effects are of minor importance at low particle densities. Therefore, t_{eff} increases with δ. In the limit $\delta \to 1$, we have $\gamma = \hbar\omega/(\hbar\omega + 4\rho t)$, $\tau^2 = 1$ and $t_{eff} = \rho$.

8.3.2 Phase diagram of the Holstein Hubbard model

The $\delta = 0$ case

At half–filling, the unperturbed 2D tight–binding band structure gives rise to perfect (π, π) Fermi surface nesting. Then, depending on the relative interaction strengths of ε_p and U, the system shows an instability towards the formation of a CDW or SDW (AFM) state modulated with the same wave–vector.

The phase boundary between the PM/CDW and the AFM states, shown in Fig. 8.3 (a), was determined from the points of intersection of the corresponding free energies. The critical

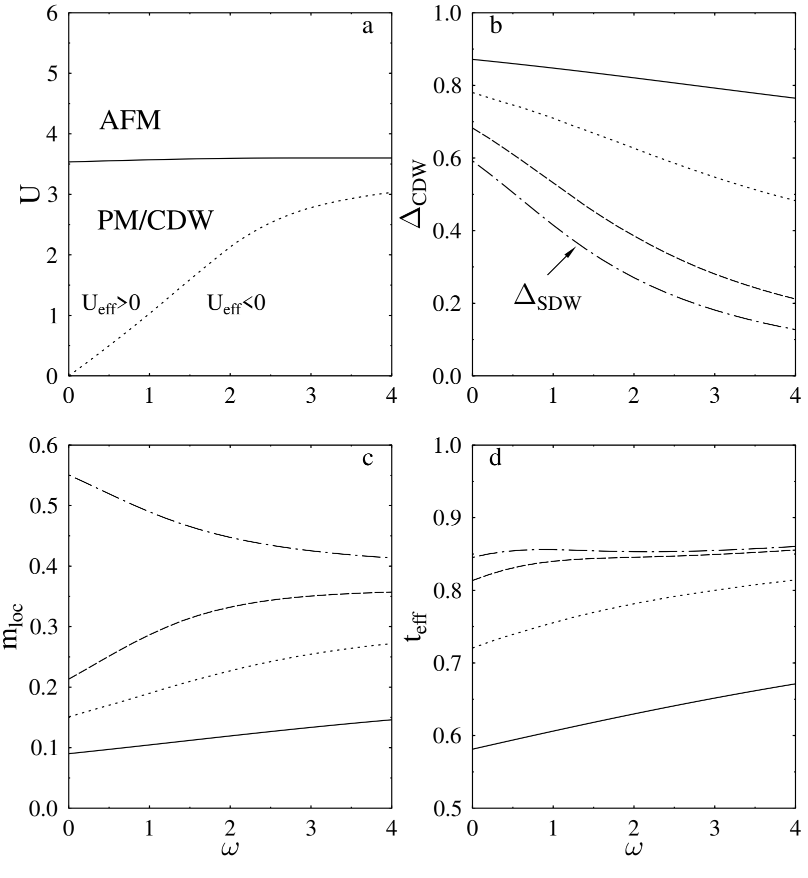

Figure 8.5: The domains of stability of AFM and PM/CDW states in the U–ω plane are depicted in **a** for the half–filled band case. The dotted line indicates the boundary $\tilde{U} = 0$. The CDW (SDW) order parameter Δ_{CDW} (Δ_{SDW}), the local magnetic moment m_{loc} and the effective hopping t_{eff} *vs* phonon frequency ω are given in **b**, **c** and **d** respectively. We show results for different values of Hubbard interaction $U = 0$ (solid), 2 (dotted), 3 (dashed), and 4 (chain dotted). The EP coupling is $\varepsilon_p = 1.8$.

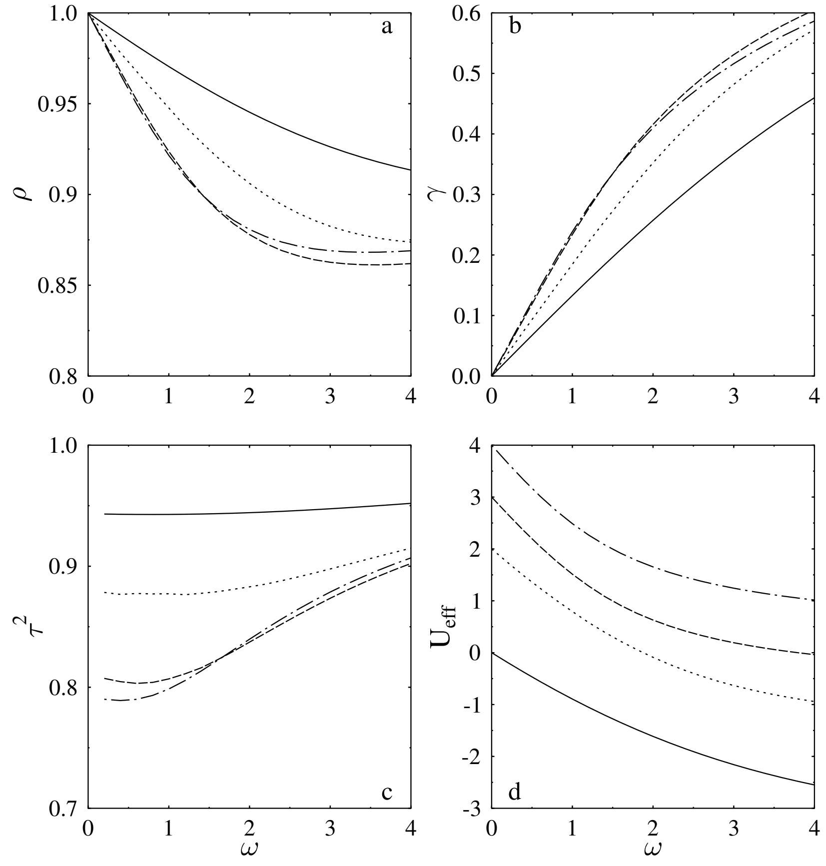

Figure 8.6: Shown are the frequency dependences of ρ **a**, γ **b**, τ^2 **c**, and $U_{eff}(=\tilde{U})$ **d** for the same model parameters as in Fig. 8.5.

value U_c, where the first order phase transition PM/CDW$\rightleftharpoons$AFM takes place, is approximately independent of ω ($U_c(\omega) \lesssim U_c^{HF}$). In the antiadiabatic limit, we obtain the Hartree–Fock result $U_c(\omega \to \infty) \to U_c^{HF}$. The dependence of the CDW (SDW) order parameter on the phonon frequency is displayed in Fig. 8.5 (b) for different characteristic Coulomb interaction strengths, which corresponds to CDW ($U = 0, 2, 3$) and AFM solutions ($U = 4$) at half–filling. Obviously, the long–range order is weakened when the frequency of the lattice vibrations is raised (cf. $\Delta_{CDW}(\omega)$ and $\Delta_{SDW}(\omega)$ in Fig. 8.5 (b)). As a result the local magnetic moment goes down (up) in the CDW (AFM) phase (Fig. 8.5 (c)). At fixed ω, the Peierls distortion becomes rapidly suppressed if the on–site Coulomb interaction is taken into account. Increasing U, the energy cost at doubly occupied sites starts to dominate the energy gain on one sublattice (A) owing to static 'dimerization'. At the same time we found that the gain of kinetic energy ($\propto t_{eff}$) becomes more important until the AFM is established at U_c (Fig. 8.5 (d)). Then, in the AFM phase, t_{eff} is a monotonous decreasing function of U as in the static case [180, 179].

Figures 8.6 (a)–(d) show the band narrowing factor ρ, the variational parameters γ and τ^2, and $\tilde{U}$ as a function of frequency for U = 0, 2, 3 and 4. First of all, we obtain again a very modest polaronic band narrowing (Fig. 8.6 (a)), even for sizeable values of γ (that means strong polaron effect; cf. Fig. 8.6 (b)). This is in agreement with the previous findings for the 1D Holstein Hubbard model [419]. At low frequencies, the optimal value of the variational parameter γ grows approximately linear with ω. As already stated, in our system the non–

adiabaticity is mainly connected to the polaron effect. Thus, γ is a monotonically increasing function of ω [419]. Interpolating to the antiadiabatic limit, one gets $\gamma(\omega \to \infty) = 1$. Compared to the case $U = 0$, in the CDW state, the polaron effect is enhanced increasing U. This is clearly related to the suppression of the CDW long–range order. In the AFM state, the U–dependence of γ is reversed.

The squeezing parameter τ^2 shows a non-monotonous behaviour as a function of ω (Fig. 8.6 (c)). As remarked in Sec. 8.1, the squeezing phenomenon is most pronounced in the regime where $t \sim \omega \sim \varepsilon_p$. In this region the energy loss due to the enhanced zero–point energy of the phonon subsystem can be overcompensated by the gain of kinetic energy in the electronic (polaronic) system (squeezing of the momentum fluctuations). There is no squeezing effect ($\tau^2 = 1$) in the antiadiabatic limit [419] as well as for very large couplings ($\varepsilon_p \gg t$; heavy–polaron limit [434]). Figure 8.6 (d) shows the reduction of the effective Hubbard interaction with increasing polaron effect. This tells us why, in the AFM state, Δ_{SDW} and m_{loc} goes down at higher frequencies (cf. Figs. 8.6 (b) and 8.6 (c)).

Summarizing this section, we reiterate the important point that our variational treatment of the phonon dynamics yields a significant ω–dependence of the polaron (γ), squeezing (τ^2) and correlation ($\tilde{U}$) effects. This should be contrasted to the results of the standard polaron theory [411, 429] where, of course, $\gamma \equiv 1$, $\tau^2 \equiv 1$, and $\tilde{U} = U - 2\varepsilon_p$.

Finally, let us notice that Zheng *et al.* [419] have studied the effect of finite phonon frequency on the Peierls dimerization using a modified Gutzwiller approach for the Holstein Hubbard model. However, their calculations are restricted to the half–filled band case, the PM/CDW state and one spatial dimension. In this limit, we are able to verify their numerical results within the framework of our variational SB scheme.

The $\delta \neq 0$ case

We now work out the finite ω–effects on the ground–state phase diagram of the 2D Holstein Hubbard model. Analyzing the stability of the various homogeneous phases, we obtain the shift of the phase boundaries as function of ω shown in Fig. 8.7 (cf., the $\omega = 0$ phase diagram presented in Sec. 8.3.1, Fig. 8.1). The results are given at two characteristic Hubbard interaction strengths $U = 2$ (Fig. 8.7 (a)) and $U = 4$ (Fig. 8.7 (b)), which, with respect to the ratio U/ε_p, refer to the CDW and SDW dominated region of the δ–U phase diagram (see Fig. 8.1), respectively. As reported in the previous section, at half–filling, we obtain a PM/CDW (AFM) state $\forall\omega$ at $U = 2$ ($U = 4$). Upon doping we observe a transition from states with finite static Peierls distortion (PM/CDW (a); FIM/SDW (b)) to 'undimerized' states (PM (a); AFM, PM (b)) at a critical hole concentration $\delta_c(\omega)$. Increasing the frequency of the lattice vibrations this transition is shifted to lower values of δ_c, i.e., at large enough ω, the long–range order (CDW, SDW) is destroyed by quantum fluctuations connected to polaron formation and squeezing effects (cf. also the discussion in Sec. 8.3.1). In the FIM/CDW, FIM/SDW and FIM states both charge (driven by ε_p) and spin correlations (established by $\tilde{U}$) coexist. Due to the additional weakening of the effective Coulomb interaction at higher frequencies, the states with FIM spin order become more suppressed than the states with PM/CDW order (see Fig. 8.7 (a)). Note that the transitions accompanied by a change in both SDW and CDW order are first–order phase transitions (FIM/CDW$\rightleftharpoons$PM/CDW; FIM/SDW$\rightleftharpoons$AFM, PM; FIM$\rightleftharpoons$PM), whereas the transitions PM/CDW, AFM$\rightleftharpoons$PM are of second order. In addition we would like to stress, that there is no sharp phase boundary between FIM/SDW and FIM states. We determined the transition line (chain dotted curve in Fig. 8.7 (b)) from the somewhat arbitrary requirement $\Delta_{CDW} \cong \Delta_{SDW}$. Then this transition point also corresponds to a local maximum of t_{eff}. The dotted curve in Fig. 8.7 (a) shows the line where $\tilde{U} = 0$. Above $\omega_c = 1.87$ (obtained in the

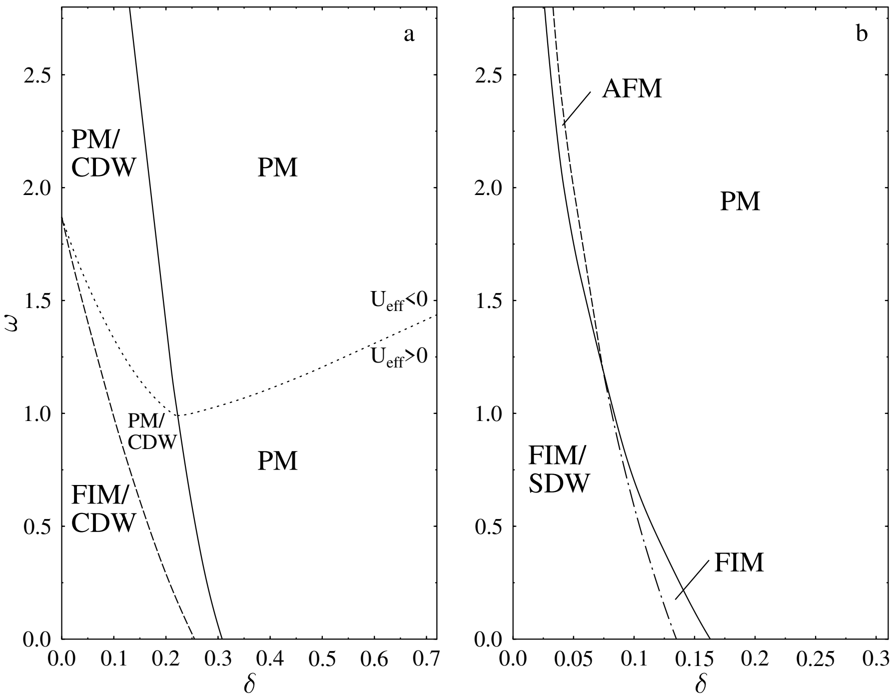

Figure 8.7: The phase diagram of the Holstein Hubbard model is displayed in the δ–ω plane for $\varepsilon_p = 1.8$ at $U = 2$ **a** and $U = 4$ **b**. Solid curves separate states with and without 'dimerization'; dashed lines denote the phase boundaries between phases with different magnetic order. The chain dotted curve corresponds to the 'transition' FIM/SDW $\rightleftharpoons$ FIM (see text). In **a** the $U_{eff} = \tilde{U} = 0$ line is marked by the dotted curve.

limit $\delta \to 0$), we have $\tilde{U} < 0 \; \forall \delta$, i.e., a magnetic solution ($\Delta_{SDW}, m \neq 0$) does not exist. At fixed frequency ω, $\tilde{U}(\delta)$ takes its minimal value at the transition point $\delta_c(\omega)$ where the polaron effect becomes strongest (see below).

The variation of the CDW and SDW order parameters is illustrated in Fig. 8.8 for the same interaction strengths $U = 2$ (a,b) and $U = 4$ (c,d) as in Fig. 8.7. Obviously, the behaviour of Δ_{CDW} and Δ_{SDW} as function of doping is reversed as one moves from the CDW to the SDW region. For $U = 2$ ($U = 4$) we have $n_A \gg n_B$ ($m_A \gg |m_B|$), where the dominance of the CDW (SDW) correlations is most pronounced in the vicinity of the half–filled band case (note the different scales of the axis of ordinate in Fig. 8.8). In the FIM states the resulting net magnetization (8.32) obeys the relation $m = \min\{\delta, 1 - \delta\}$. Let us emphasize, that for large Hubbard interactions, i.e., in the SDW region, the EP coupling causes a monotonous increase of the CDW correlations (order parameter) doping the system away from half–filling. This result is supported by QMC [406] and ED [358, 443] studies (of course, within our A–B saddle–point approximation, we are unable to describe *local* phonon–driven lattice distortions). As can be seen from Fig. 8.8, in the predominant CDW (SDW) ordered phases the static Peierls distortion (magnetic order) is strongly reduced with increasing ω, whereas Δ_{SDW} (Δ_{CDW}) shows only a weak ω–dependence. The jump–like behaviour of Δ_{CDW} (a) and Δ_{SDW} (d) at certain $\delta_c(\omega)$ is related to an intersection of the free energies for the different phases indicating a first–order phase transition.

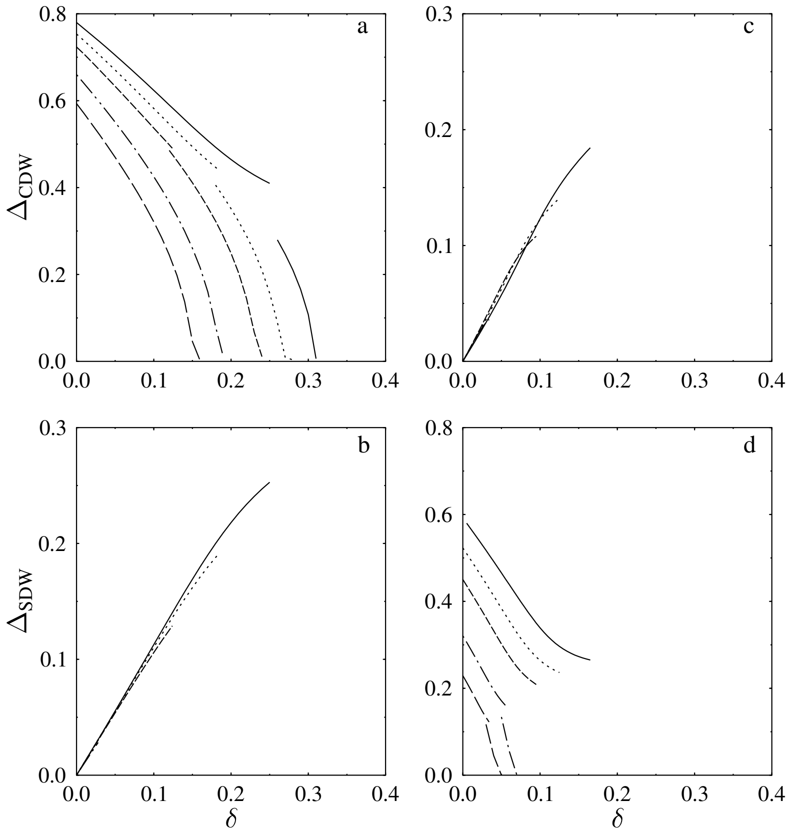

Figure 8.8: Order parameters Δ_{CDW} and Δ_{SDW} are given as a function of doping δ at $U = 2$ (**a**, **b**) and $U = 4$ (**c**, **d**), respectively. Results are shown for $\omega = 0$ (solid), 0.4 (dotted), 0.8 (dashed), 1.6 (chain dotted), and 2.4 (long dashed) at $\varepsilon_p = 1.8$.

Figure 8.9 shows the δ–dependence of ρ, τ^2 and m_{loc} at different frequencies for $U = 2$ (a)–(c) and $U = 4$ (d)–(f), respectively. Again we observe only a weak polaron band renormalization $\rho \sim 0.9$ at moderate EP coupling $\varepsilon_p = 1.8$. This can be attributed to our variational treatment of polaron and squeezing phenomena. The minimum of $\rho(\delta)$ is connected to the transition to the 'undimerized' PM state at $\delta_c(\omega)$. Since the electronic correlation ($\propto U$) becomes less important in the dilute limit (i.e., at large δ), in this region the behaviour of ρ is dominated by EP and kinetic energy effects. Increasing the Coulomb interaction U at fixed EP coupling ($\varepsilon_p = 1.8$) and phonon frequency ($\omega = 0.8$), $\rho(U)$ raises up to a maximum at about $U_{max} = 2\varepsilon_c$, where $\varepsilon_c(\delta, \omega)$ denotes the critical EP coupling strength for the transition to the heavy–polaron state [434]. Above U_{max}, we obtain a very smooth decrease of $\rho(U)$ driven by the electronic band renormalization ($\propto q_{\eta\sigma}$). The limit $U = \infty$ will be discussed in more detail in the next section. As already mentioned, the squeezing phenomenon favours the quantum mechanical tunneling of polarons and therefore enhances (suppresses) the itinerancy of the polaronic charge carriers (a static Peierls distortion). Figures 8.9 (b) and (e) show that the effect of squeezing is most pronounced at the transition PM/CDW, FIM$\rightleftharpoons$PM. At $U = 2$, the behaviour of m_{loc} as a function of δ and ω was found to be qualitatively similar to the results obtained for the Holstein model in Sec. 3.1.3 (cf. Figs. 8.3 (c) and 8.7 (c)). On the other hand, m_{loc} is strongly enhanced in the FIM/SDW phase and shows, compared to the

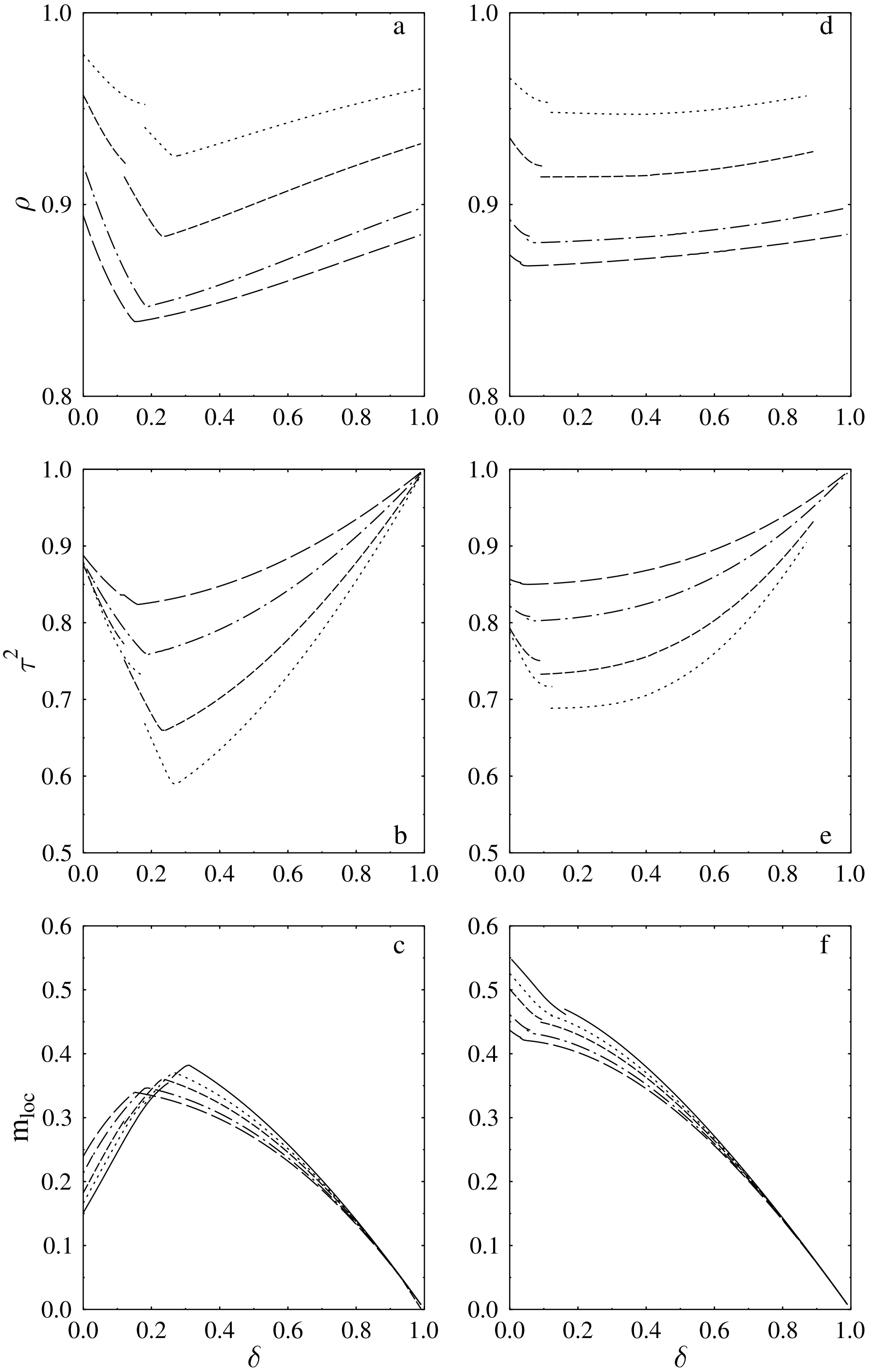

Figure 8.9: The corresponding results for the polaron band narrowing ρ **a (d)**, the squeezing effect **b (e)**, and the local magnetic moment m_{loc} **c (f)** at $U = 2\,(4)$. The notation is the same as in Fig. 8.8.

FIM/CDW case, a reversed dependence on ω and δ (see Fig. 8.7 (d)).

Summary

This section aims to address the non–adiabatic effects in a coupled EP system described by the Holstein Hubbard model. The main results of our investigations are the following.

(i) We have presented the ground–state phase diagrams of the 2D Holstein and Holstein Hubbard models for a wide class of model parameters $(U, \omega;\ \delta)$, where the EP coupling was fixed to an intermediate value $(\varepsilon_p/t = 1.8)$. At half–filling the Holstein coupling leads to a PM state with static (π, π) Peierls distortion. Incorporating the intraatomic part of the Coulomb interaction U, the 'dimerization' is a monotonous decreasing function of U up to the point U_c, where the first–order transition to the AFM state takes place. With increasing frequency of the lattice vibrations the static lattice distortion is reduced. Off half–filling, the phase diagram becomes more complex. Depending on doping level and Coulomb interaction strength, we observe Peierls distorted states with predominant charge (FIM/CDW, $\Delta_{CDW} \gg \Delta_{SDW}$; PM/CDW $\Delta_{SDW} = 0$) or magnetic (FIM/SDW, $\Delta_{CDW} \ll \Delta_{SDW}$) long–range order as well as AFM, FM and PM phases $(\Delta_{CDW} = 0)$.

(ii) In our approach, the main effect of phonon dynamics is to enhance the tendency towards polaron formation. As first pointed out by Zheng *et al.* [433], the interference between (adiabatic) frozen 'dimerization' and (antiadiabatic) polaron effect plays a very important role, in particular in the intermediate parameter region where the energy scales are not well separated. As a result, the CDW long–range order is suppressed by quantum fluctuations. Due to the additional polaronic renormalization of the Hubbard interaction, in the SDW region, the magnetic correlations are weakened as well.

(iii) In the adiabatic limit the theory yields the results obtained within a frozen–phonon approach to the Holstein Hubbard model [179, 177]. In the opposite antiadiabatic limit, we have no static Peierls distortion and, provided that $\varepsilon_p < \varepsilon_c$ (i.e., $\rho(\omega \to \infty) = 1$) [434], the theory fits the SB phase diagram for the pure Hubbard model with $\tilde{U} = U - 2\varepsilon_p$.

(iv) At finite frequencies, the central point, we would like to emphasize, is the strong ω– and δ–dependence of polaron and squeezing effects. As a result also the CDW/SDW order parameters, the local magnetic moment and the effective Hubbard interaction show a large variation with ω and δ. Note that this behaviour cannot be obtained within the frozen–phonon [177] or standard Lang–Firsov approaches [410].

(v) The variational treatment of polaron formation at finite carrier densities yields an incomplete polaron effect, i.e., 'light' polarons, even at considerable EP coupling strengths $(\varepsilon_p < 4t)$. The effective polaron mass is determined self–consistently, where the polaron narrowing $(\propto \rho)$ and the correlation induced narrowing $(\propto q_{\eta\sigma} q_{-\eta\sigma})$ are interrelated.

(vi) The squeezing effect enhances the mobility of the polaronic charge carriers $(\propto t_{eff})$ and tends to suppress the CDW long–range order. In addition, the self–trapping transition is shifted to larger EP couplings [434]. However, compared to the ρ–corrections obtained from the modified variational treatment of polaron formation, the incorporation of the squeezing phenomenon yields, roughly speaking, a much smaller effect in the order of 5–10 percent. In the light–polaron regime the polaron and squeezing effects are most pronounced at the PM/CDW$\rightleftharpoons$PM transition point.

8.4 Polaron formation in the Holstein Hubbard model at finite densities [434]

The formation of tight–binding polarons in strongly coupled EP systems is a problem of current interest [411, 429, 410, 444, 430, 428, 445, 446]. One of the basic problems in this field is the transition from quasi–free electrons to self–trapped heavy polarons with increasing coupling strength [429, 444, 430, 428, 446]. Most of the previous theories concerned with this problem adopt the single–polaron picture which is only justified in the limit of very low carrier densities (realized, e.g., in photo-induced absorption experiments). Thereby, the spinless Holstein model [411] (describing a short–range EP interaction) was treated by variational [429, 430] and Monte Carlo methods [428]. On the basis of this model, Toyozawa [429] has found, at low enough phonon frequencies, a discontinuous self–trapping transition. The previous theories of polaron transport are also based on the single–polaron picture [411, 430, 410, 447, 448, 449, 360].

The study of finite–density effects on the polaron formation and transport is of particular importance. For instance, in the high–T_c materials, the density of charge carriers introduced by doping can be varied continuously and may have appreciable values. Attempts at taking into consideration finite densities in the polaron formation were made by Feinberg *et al.* [407]. Those authors, using a variational approach and including squeezing effects, have obtained an abrupt self–trapping transition in the spinless model at half–filling. However, the density dependence of this transition was not yet studied. Moreover, until now there is no theory of polaron formation in the Holstein Hubbard model for spin–$\frac{1}{2}$ electrons at finite densities, where correlation effects become important. Recently, Suzuki *et al.* [390] have taken into account arbitrary densities in the theory of polaron conductivity on the basis of the Holstein Hubbard model using the ‘normal’ Lang–Firsov transformation [410].

To discuss the interplay of dimerization and polaronic effects near half–filling, in the preceding section we have investigated the case of moderate EP coupling, i.e., weak mass renormalization. In this section we focus our attention to the case, where due to strong EP coupling a substantial mass renormalization of the quasiparticles may take place (heavy polarons).

We treat the formation of polarons and squeezing phenomena (in terms of two–phonon coherent states) by the UMVLF approach (8.1)–(8.5), restricting ourselves to the non–dimerized paramagnetic phase (which is certainly correct far enough from half–filling [439]). Then, the effective polaronic Hubbard model becomes [434]

$$\overline{\mathcal{H}}_p^H = \sum_{\vec{k},\sigma} \left(\rho\, \varepsilon_{\vec{k}} - \tilde{\varepsilon}_p\right) c^\dagger_{\vec{k}\sigma} c_{\vec{k}\sigma} + \tilde{U} \sum_i n_{i\uparrow} n_{i\downarrow} + \bar{\gamma}^2 \varepsilon_p N + \frac{\hbar\omega}{4} \left(\tau^2 + \tau^{-2}\right) N \tag{8.37}$$

where the variational parameters (γ, τ^2) are determined by minimization of the ground–state energy $\langle \tilde{\Psi}^0_{el} | \overline{\mathcal{H}}_p^H | \tilde{\Psi}^0_{el} \rangle$.

To separate the polaron correlation effects due to $\tilde{U}$ (combined Coulomb repulsion and phonon–induced attraction), we first consider two versions of $\overline{\mathcal{H}}_p^H$ describing uncorrelated polarons.

8.4.1 Uncorrelated polarons

To study the finite–density and squeezing effects on the polaron formation, we take the spin–$\frac{1}{2}$ ($s = \frac{1}{2}$) model (8.37) in the Hartree–Fock approximation. For comparison, we also consider the spinless ($s = 0$) Holstein model resulting in the effective Hamiltonian of the form (8.37) without spin sum and interaction term.

To simplify the analytical calculations, in this section we express the $\vec{k}$–summation in terms of the square density of states. Measuring, hereafter, all energies in units of t, we obtain the variational free energy per site ($s = \frac{1}{2}$, 0) in the form

$$f(\bar{\gamma}, \gamma, \tau^2) = \bar{\gamma}^2 \varepsilon_p - n \left\{ \tilde{\varepsilon}_p + 4\rho \left(1 - \frac{n}{2s+1} \right) \right\} + s \, \frac{n^2}{2} \, \tilde{U} + \frac{\hbar\omega}{4} \left(\tau^2 + \tau^{-2} \right) . \tag{8.38}$$

In addition, we have

$$\bar{\gamma} = \left\{ \begin{array}{cc} (1-\gamma)\, n \; , & \text{UMVLF} \\ 0 \quad , & \text{VLF} \, . \end{array} \right. \tag{8.39}$$

Minimizing f, the variational parameters γ and τ^2 are determined from the equations

$$\gamma = \hbar\omega \left\{ \hbar\omega + \varepsilon_{c_1} \rho \, \tau^2 \right\}^{-1} , \tag{8.40}$$

$$\tau^2 = \hbar\omega \left\{ (\hbar\omega)^2 + \varepsilon_p \, \rho \gamma^2 \, \varepsilon_{c_1}^2 / \varepsilon_{c_2} \right\}^{-1/2} , \tag{8.41}$$

where

$$\varepsilon_{c_1} = \left\{ \begin{array}{cc} 4 \quad , & \text{UMVLF} \\ 4 \, \frac{2s+1-n}{2s+1+2sn} \; , & \text{VLF} \, , \end{array} \right. \tag{8.42}$$

and

$$\varepsilon_{c_2} = \varepsilon_{c_1}^2 \left\{ 16 \, n \left(1 - \frac{n}{2s+1} \right) \right\}^{-1} . \tag{8.43}$$

In the variational analysis, the solution of the extremal equations (8.40) and (8.41) must be used to find the absolute minimum of the free–energy functionals for both the UMVLF and the VLF.

In this chapter we characterize the polarons by their effective mass expressed in terms of the band narrowing factor, $m^*/m = \rho^{-1}$, as function of the model parameters ε_p and $\hbar\omega$ and of the polaron density n. For a detailed classification within different $\hbar\omega$–ε_p regimes we refer to Ref. [407]. In the framework of our effective band description we are not able to investigate the spatial extent of the polarons in the weak– and strong–coupling regimes. In the strong–coupling case ($\varepsilon_p \gg 1$), for 'small' (heavy) polarons we have $\rho \ll 1$.

Solving the system (8.38) to (8.43), some results are shown in Fig. 8.10 as constant–ρ contours in the $\hbar\omega$–ε_p plane for different n. We have compared the results including squeezing with those neglecting squeezing ($\tau^2 \equiv 1$). For all $\hbar\omega$, ε_p and n we have found

$$f_{UMVLF} < f_{VLF} < f_{LF} \, , \tag{8.44}$$

where, in each case, the energy is lowered by the inclusion of the squeezing effect. Neglecting squeezing effects, the ρ–contours for the UMVLF are identical in the HF solution and the spinless model and do not depend on n.

Next we consider the adiabatic limit ($\omega \to 0$). By (8.13) and a low–frequency expansion, we obtain three solutions of (8.40) and (8.41),

$$\begin{array}{llcll} \text{I} : & \gamma = \frac{\tau^{-2}}{\varepsilon_{c_1}} \, \hbar\omega & , & \tau^2 = \left(1 - \frac{\varepsilon_p}{\varepsilon_{c_2}} \right)^{\frac{1}{2}} & ; \\ \text{II} : & \gamma = 1 & , & \tau^2 = 1 & ; \\ \text{III} : & \gamma = 1 - \left(\frac{\varepsilon_{c_2}}{\varepsilon_p} \, \rho \right)^{\frac{1}{2}} & , & \tau^2 = \frac{1-\gamma}{\varepsilon_{c_1} \gamma} \, \hbar\omega & . \end{array} \tag{8.45}$$

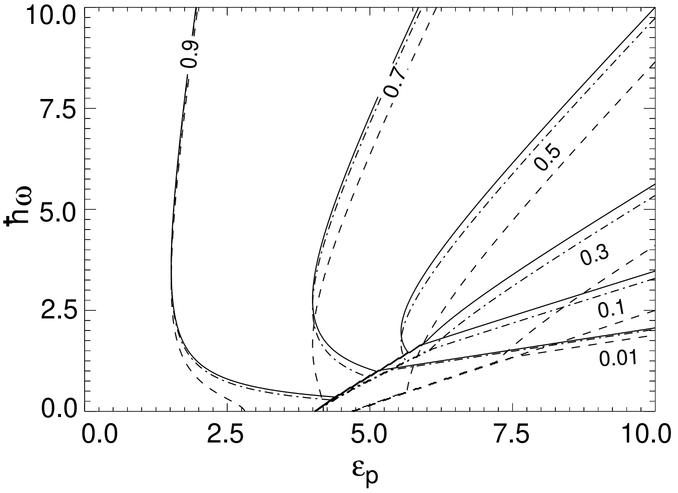

Figure 8.10: Contour plots of the polaron band narrowing factor ρ in the $\hbar\omega$–ε_p plane for the uncorrelated $s=\frac{1}{2}$ case using the UMVLF. Solid curves show the results without squeezing ($\tau^2\equiv 1$), which are independent of the polaron density n. Chain dotted (short–dashed) curves correspond to the case $\tau^2\neq 1$ for $n=0.1$ ($n=0.7$).

At $\omega=0$, we have $\rho=1$ for solution I and $\rho=0$ for solution II. For solution III, we get the relation

$$\varepsilon_p=\varepsilon_{c_2}\,\rho\left(\frac{\varepsilon_{c_1}}{\varepsilon_{c_2}}\ln\rho-1\right)^2 . \tag{8.46}$$

Let us point out that solution III, where $\tau^2\to 0$ ($\alpha\to\infty$) as $\omega\to 0$, yields a finite zero–point energy of phonons and a vanishing variance of the ion coordinates within the uncertainty principle in its minimal form [407].

Analyzing the stability of the *paramagnetic* solutions (8.45) by comparing the corresponding ground–state energies (8.38), we obtain the stability regions in the n–ε_p plane shown in Fig. 8.11. Of course, near half–filling ($0.7\lesssim n\lesssim 1.3$) symmetry broken solutions (e.g. charge or spin ordered states) may have a lower free energy (cf. Refs. [179, 177]).

For $n<n_c$ ($\varepsilon_{c_2}>\varepsilon_{c_1}$), where n_c is determined from $\varepsilon_{c_2}=\varepsilon_{c_1}$, with increasing ε_p we get an abrupt transition from the free–electron state I to the perfectly localized self–trapped

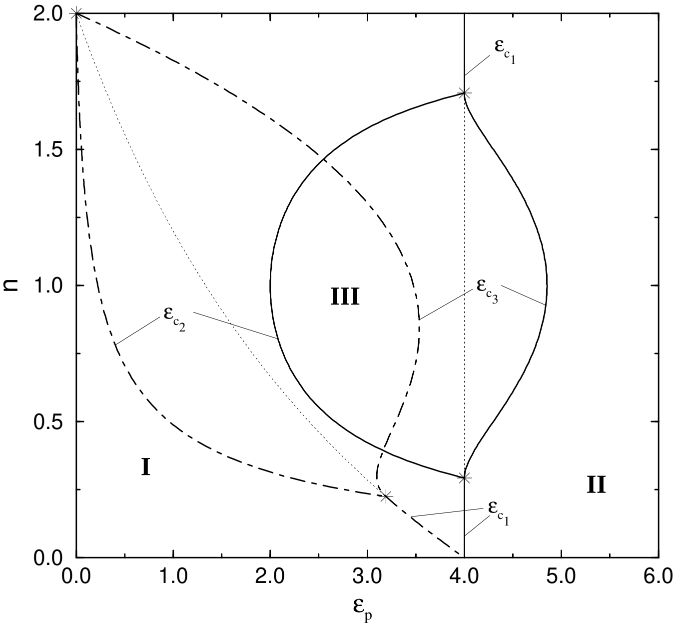

Figure 8.11: Stability regions I, II and III of the corresponding ($s=\frac{1}{2}$) Hartree–Fock solutions (8.45) in the adiabatic limit. The solid (chain dashed) curves denote the boundaries for the UMVLF (VLF), where ε_{c_1}, ε_{c_2} and ε_{c_3} are given by (8.42), (8.43) and (8.47), respectively. The symbol (∗) marks the triple point. Dotted curves indicate the transition line I⇌II neglecting the squeezing effect.

state II at the critical coupling ε_{c_1}. Such a discontinuous change in the effective mass at the self–trapping transition, well–known in single–electron theories [429, 444, 446], was also found by Feinberg *et al.* [407] (for $\omega > 0$) in the spinless half–filled band model applying the VLF. Let us stress that we get $f_{UMVLF} < f_{VLF}$, i.e., the UMVLF treats the finite–density problem more correctly. Whereas in the UMVLF the transition point does not depend on n ($\varepsilon_{c_1} = 4$), the VLF yields a decrease of ε_{c_1} with increasing n (in the limit $n = 0$ we have $\varepsilon_{c_1} = 4$ in all cases).

For $n > n_c$ ($\varepsilon_{c_2} < \varepsilon_{c_1}$), with increasing ε_p we obtain a continuous transition from I to III at ε_{c_2} and a discontinuous self–trapping transition from III to II at ε_{c_3} (see Fig. 8.11), where

$$\varepsilon_{c_3} = \frac{\varepsilon_{c_1}^2}{\varepsilon_{c_2}}\,\rho_{c_3}\,, \quad \rho_{c_3} = \exp\left\{-\left(1-\frac{\varepsilon_{c_2}}{\varepsilon_{c_1}}\right)\right\}\,, \tag{8.47}$$

and in the region $\varepsilon_{c_2} < \varepsilon_p < \varepsilon_{c_3}$ the band narrowing factor decreases from $\rho = 1$ to $\rho = \rho_{c_3}$. Note that the two successive transitions do not occur in the spinless model treated by the UMVLF, since $\varepsilon_{c_2} < \varepsilon_{c_1}$ cannot be fulfilled. The occurrence of the triple point ($\varepsilon_{c_1} = \varepsilon_{c_2} = \varepsilon_{c_2}$) is a finite–density effect realized via the squeezing effect. Neglecting squeezing ($\tau^2 \equiv 1$) we have no solution III, and only the abrupt self–trapping transition from I to II at ε_{c_1} takes place (indicated, for $n > n_c$, by the dotted lines in Fig. 8.11). As can be seen from Fig. 8.10, squeezing increases with increasing n towards half–filling and shifts the self–trapping transition to higher values of ε_p ($\varepsilon_{c_3} > \varepsilon_{c_1}$). Obviously, the best treatment of the polaron formation yields the highest value of the self–trapping transition point.

Considering the finite–frequency range, without squeezing, the sharp transition from light polarons ($\rho \lesssim 1$) to self–trapped heavy polarons ($\rho \ll 1$) takes place at $\varepsilon_{c_1}(\omega)$ increasing with ω from ε_{c_1}, given by (8.42), up to the critical point $\varepsilon_{c_1}(\omega_{c_1})$, whereby the magnitude of the discontinuity in ρ decreases. For $\omega > \omega_{c_1}$, the discontinuity disappears and we get a smooth crossover from light to heavy polarons with increasing ε_p (in qualitative agreement with previous results [429, 444, 407]). The situation is analogous to that in the gas–liquid first–order transition [429], if we let ω correspond to the temperature, ρ to the volume, and ε_p to the pressure. For $\tau^2 \equiv 1$, the critical point may be determined analytically starting from $\varepsilon_p(\rho,\omega) = -\ln\rho\,(\hbar\omega + \varepsilon_{c_1}\rho)^2/\hbar\omega$. From the conditions $\partial\varepsilon_p/\partial\rho|_{\rho_{c_1},\omega_{c_1}} = 0$ and $\partial^2\varepsilon_p/\partial\rho^2|_{\rho_{c_1},\omega_{c_1}} = 0$ we obtain $\rho_{c_1} = \exp(-3/2)$, $\hbar\omega_{c_1} = 2\,\rho_{c_1}\,\varepsilon_{c_1}$, and $\varepsilon_{c_1}(\omega_{c_1}) = \frac{27}{4}\,\rho_{c_1}\,\varepsilon_{c_1}$.

Taking into account squeezing effects, for $n < n_c$ the self–trapping transition point $\varepsilon_{c_1}(\omega)$ is shifted to higher values of ε_p, and the critical–point value ω_{c_1} becomes smaller (see Fig. 8.10). For $n > n_c$ (compare Fig. 8.11), the abrupt self–trapping transition takes place at $\varepsilon_{c_3}(\omega)$ increasing with ω (Fig. 8.10), except for the spinless model treated by the UMVLF. Because $\varepsilon_{c_3}(\omega) > \varepsilon_{c_1}(\omega)$, squeezing reduces the heavy–polaron region.

Finally, let us consider the antiadiabatic limit. Here, we get $\gamma = 1$ and $\tau^2 = 1$ for arbitrary ε_p and n. Note that, although the polaron effect is strongest, according to (8.13) we have light polarons ($\rho = 1$).

8.4.2 Correlated polarons

In the Hartree–Fock approximation to the model (8.37), the polaron formation does not depend on the effective interaction $\tilde{U}$. However, from physical arguments we suggest that a repulsive intra-site interaction $\tilde{U}$ increases the effective polaron mass and favours the self–trapping tendency. In this section, our aim is to investigate the correlation effects on the polaron formation due to the effective Coulomb repulsion $\tilde{U} > 0$, where we consider the homogeneous paraphase. To this end, we start from the effective polaronic Hubbard model (8.37) and use the KR

SB technique on the level of the paramagnetic saddle–point approximation. The free–energy functional now becomes

$$f(\bar{\gamma},\gamma,\tau^2) = \bar{\gamma}^2\varepsilon_p - n\tilde{\varepsilon}_p + q\,\rho\,\tilde{\varepsilon}(0) + \tilde{U}d^2 + \frac{\hbar\omega}{4}\left(\tau^2 + \tau^{-2}\right)\,. \tag{8.48}$$

Here,

$$\tilde{\varepsilon}(0) = \frac{2}{N}\sum_{\vec{k}} \varepsilon_{\vec{k}}\,\theta(\mu - q\,\rho\,\varepsilon_{\vec{k}}) \tag{8.49}$$

(μ is the Fermi energy obtained from $n = \frac{2}{N}\sum_{\vec{k}}\theta(\mu - q\,\rho\,\varepsilon_{\vec{k}})$),

$$q = \frac{2y - y^2 - (1-n)^2}{n\,(2-n)} \tag{8.50}$$

is the correlation–induced band narrowing factor for the (lower) Hubbard band ($n < 1$), and the probability for double site–occupancy

$$d^2 = \frac{(y+n-1)^2}{4y} \tag{8.51}$$

is given by the solution of the equation ($y > 0$)

$$\frac{\tilde{U}}{\rho} = \frac{8\,\tilde{\varepsilon}(0)}{n\,(2-n)}\,\frac{y^2\,(y-1)}{y^2 - (1-n)^2}\,. \tag{8.52}$$

Eq. (8.52) takes into account the electronic correlations which are determined by the ratio $\tilde{U}/\rho$ (instead of U for the pure Hubbard model). For the Holstein Hubbard model, in our variational method, Eq. (8.52) must be supplemented by the extremal equations for γ and τ^2 derived from Eq. (8.48). We obtain

$$\gamma = \frac{(n + 2d^2 - \bar{\gamma}n)\,\hbar\omega}{(n+2d^2)\,\hbar\omega \;-\; q\,\rho\,\tilde{\varepsilon}(0)\,\tau^2}\,, \tag{8.53}$$

$$\tau^2 = \hbar\omega\left\{(\hbar\omega)^2 - 4\,\varepsilon_p\,q\,\rho\,\tilde{\varepsilon}(0)\,\gamma^2\right\}^{-\frac{1}{2}}\,. \tag{8.54}$$

In the solution of the self–consistency equations (8.52) to (8.54) with (8.49) to (8.51) for both the UMVLF and the VLF, we have to guarantee that $\tilde{U} > 0$ in the whole parameter range of $\hbar\omega$, ε_p and n, in particular in the self–trapped heavy–polaron region (compare Fig. 8.10). Therefore, the Hubbard interaction U has to be chosen large enough. The case $\tilde{U} < 0$ may give rise to bipolaron formation.

Let us consider two limiting cases of the ground–state energy (8.48) using the square density of states which gives $\tilde{\varepsilon} = -4n\,(1 - n/2)$. Putting $\tilde{U} \equiv 0$ in Eq. (8.52) ($y = 1$), we get $q = 1$ and $d^2 = n^2/4$ so that (8.48) becomes the HF result (8.38). Considering the limit $\tilde{U}/\rho \to \infty$ (the effective interaction $\tilde{U}/\rho$ becomes extremely large in the heavy–polaron region), from (8.51) and (8.52) we have $\lim_{(\tilde{U}/\rho)\to\infty} \tilde{U}\,d^2 = 0$. By (8.52), we get $y = 1 - n$ so that

$$\lim_{(\tilde{U}/\rho)\to\infty} q = \frac{1-n}{1-n/2}\,. \tag{8.55}$$

Using the $\tilde{\varepsilon}$ value given above for the square density of states, we obtain $q\,\tilde{\varepsilon} = -4n\,(1-n)$, and (8.48) changes to the ground–state energy (8.38) for the spinless model.

We have solved numerically the coupled system of self–consistency equations (8.49) to (8.54), including the determination of the absolute minimum of the ground–state energy (8.48), and show some representative results in Figs. 8.12 to 8.4.2.

For a fixed frequency ($\hbar\omega = 0.8$), at which the self–trapping transition may occur (see Fig. 8.10), in Fig. 8.12 the dependence of the polaron narrowing factor ρ on ε_p, n, and U is illustrated. Note that above the transition point, our approach yields an extremely strong band narrowing ($\rho \lesssim 10^{-3}$). For comparison, the results obtained without squeezing and by means of the square density of states are also depicted. The large difference of the results obtained by the exact and square densities of states may be explained, according to (8.13), (8.53) and (8.54), by the exponential dependence of ρ on $\tilde{\varepsilon}(0)$. The chosen parameters permit the separation of the correlation effects from the squeezing effects. First, we obtain the result that, at fixed n, with increasing Hubbard interaction U the self–trapping transition is shifted to lower values of ε_p, whereby this effect increases with the polaron density. This is also corroborated by comparing the transition points in the Hartree–Fock approximation and the spinless model (corresponding to the limit $\tilde{U}/\rho \to \infty$) which, for $\hbar\omega = 0.8$ and $n = 0.7$, are

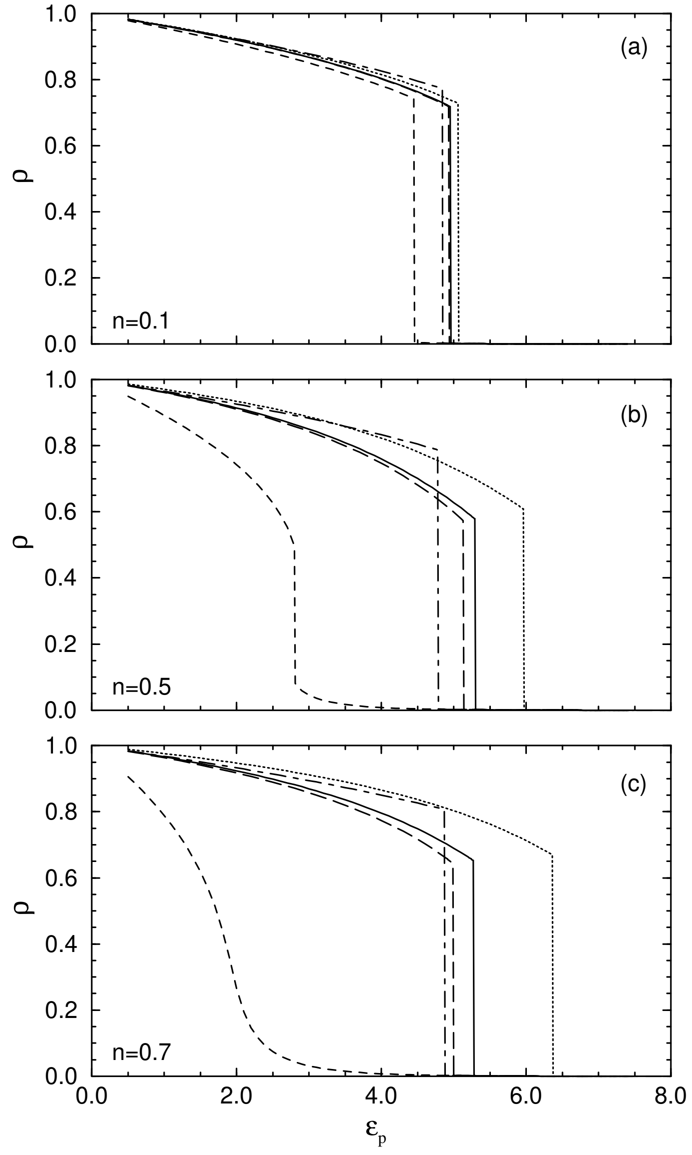

Figure 8.12: Polaron band narrowing ρ as a function of the polaron binding energy ε_p at $\hbar\omega = 0.8$ for different band fillings $n = 0.1$ (a), 0.5 (b) and 0.7 (c). Solid (long–dashed) curves denote the UMVLF results including the squeezing effect at Hubbard interaction $U = 15$ ($U = 20$). The dotted line shows ρ *vs* ε_p for $U = 15$ using the square density of states. At $U = 15$, results for the UMVLF and the VLF without squeezing are given by chain dashed and short–dashed curves, respectively.

given by 6.3 and 5.9, respectively. The lowering of the transition point may be explained by the correlation–induced carrier localization which increases with U and suppresses the double site–occupancy. Correspondingly, this localization effect supports the self–trapping of a single polaron which results in the decrease of the transition threshold. By the same reasonings, the increase of the effective polaron mass (decrease of ρ) below the transition with increasing U (see Fig. 8.12) may be understood. Let us emphasize that this behaviour holds provided that $\tilde{U} > 0$ for all ε_p up to the transition to the heavy–polaron state. For the UMVLF without squeezing, this transition is nearly independent of n (cf. the chain dashed curves in Figs. 8.12 (a)-(c)). This behaviour must be interpreted as an effect of the exact two–dimensional density of states. Using the simple square density of states, for $U = 15$ (UMVLF without squeezing) we obtain the transition points $\varepsilon_c(n)$: $\varepsilon_c(0.1) = 4.96$, $\varepsilon_c(0.5) = 5.40$, and $\varepsilon_c(0.7) = 5.84$. Obviously, with increasing electron density the kinetic energy contribution dominates the correlation energy (at fixed U), so that it becomes more difficult to localize the charge carriers.

In addition to this finite–density effect, the squeezing effect (increasing with n) also implies a shift of the self–trapping transition to higher values of ε_p. That means, the squeezing effect counteracts the correlation effect (due to U), which is also demonstrated in Fig. 8.12. Considering Figs. 8.12 (b) and 8.12 (c), the difference in ε_c, at $U = 15$, without and with squeezing is smaller for $n = 0.7$ than for $n = 0.5$. Moreover, the curves for $U = 15$ with squeezing belonging to $n = 0.5$ and $n = 0.7$ show coinciding transition points. From those results we see the counteracting tendencies of squeezing and correlation, where for certain parameter regions the squeezing effect may compensate the correlation effect.

As seen in Fig. 8.12, the VLF yields a decrease of the transition point compared with the UMVLF results (cf. also Fig. 8.11), where this deviation increases with the density.

In Fig. 8.13, the band narrowing factor is depicted for a frequency ($\hbar\omega = 3.0$), for which the sharp self–trapping transition is suppressed. However, as for $\hbar\omega = 0.8$, with increasing U the effective polaron mass is enhanced (where the correlation effect increases with n). Comparing Figs. 8.12 and 8.13, with increasing frequency the squeezing effect on the light–polaron mass is reversed: whereas for $\hbar\omega = 0.8$, ρ below the transition point is decreased by squeezing (Fig. 8.12), for higher frequencies (Fig. 8.13) squeezing leads to an increase in ρ.

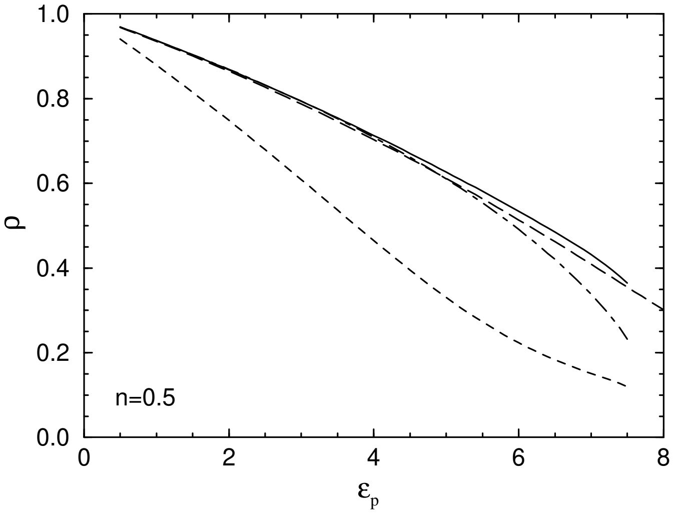

Figure 8.13: Band narrowing factor ρ *vs* ε_p for $\hbar\omega = 3.0$ and $n = 0.5$. The notations are the same as in Fig. 8.12.

In Fig. 8.14 we have plotted the ground–state energies belonging to some of the solutions shown in Figs. 8.12 and 8.13. The self–trapping transition is reflected as a kink point in the energy curves. Furthermore, it can be seen explicitly that the solution in the UMVLF has a lower energy than that in the VLF.

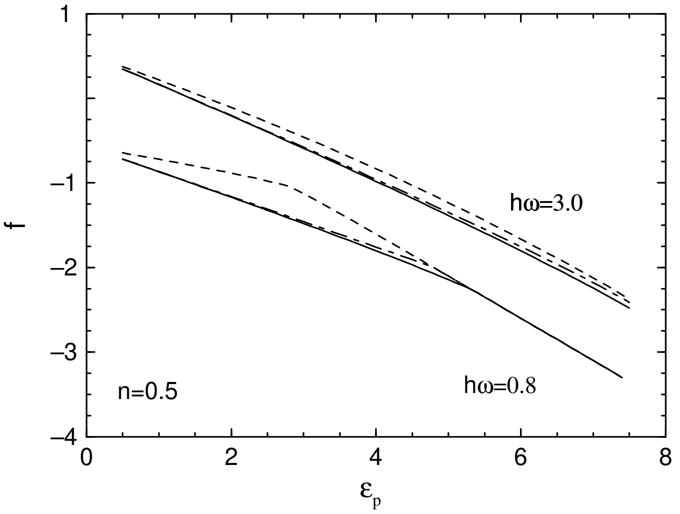

Figure 8.14: Ground–state energy f in dependence on the polaron binding energy ε_p at $U = 15$, $n = 0.5$ for $\hbar\omega = 0.8$ and 3.0. The UMVLF solution with $\tau^2 \neq 1$ (solid line) is compared with the results, where both the UMVLF (chain dashed) and the VLF (dashed) are used for $\tau^2 \equiv 1$.

In the presence of Coulomb interactions, the effective polaron mass is determined by the band narrowing factor $q\rho$, where the correlation narrowing ($q < 1$) and the polaron narrowing ($\rho < 1$) are coupled (cf. the self–consistency scheme given by Eqs. (8.48)–(8.54)). As shown in Fig. 8.4.2 (left panel), the factor q changes abruptly at the self–trapping transition from higher to lower values, in qualitative agreement with the behaviour of ρ. With increasing correlation, q below the transition is reduced, as expected. Above the transition, the ratio $\tilde{U}/\rho$ is of the order of 10^3 to 10^4 provided that $\tilde{U} > 0$. Therefore, q takes the value in the $\tilde{U}/\rho \to \infty$ limit given by (8.55). For higher frequencies ($\hbar\omega = 3.0$), q continuously increases with ε_p and, of course, we have $q \to 1$ for $\tilde{U} \to 0$.

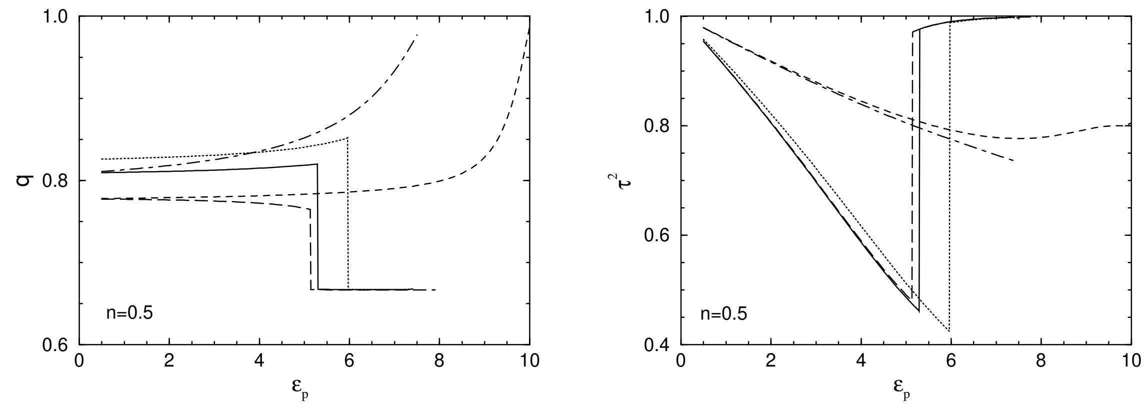

Figure 8.15: Band narrowing factor q (left panel) and squeezing variational parameter τ^2 (right panel) as a function of ε_p for the UMVLF at $n = 0.5$ with: $\hbar\omega = 0.8$ and $U = 15$ (solid), $U = 20$ (long–dashed); $\hbar\omega = 3.0$ and $U = 15$ (chain dashed), $U = 20$ (short–dashed). The dotted curve belongs to $\hbar\omega = 0.8$, $U = 15$, where the square density of states is used.

The dependence of the squeezing variational parameter τ^2 on ε_p is displayed in Fig. 8.4.2 (right panel). For $\hbar\omega = 0.8$, below the self–trapping transition, the effect of squeezing is to weaken the band narrowing forced by ε_p, i.e., the squeezing phenomenon increases with ε_p. In the heavy–polaron region, squeezing becomes negligible due to the strong localization of the polarons. At high enough ω (see the curves for $\hbar\omega = 3.0$ in Fig. 8.4.2), τ^2 shows a smooth variation with ε_p. With increasing Coulomb interaction U, the squeezing effect is reduced which becomes more pronounced with increasing n. This again elucidates the counteracting effects of squeezing and correlation.

Let us now comment on some limitations of the present theory. In our variational approach to the Holstein Hubbard model, below a critical phonon frequency, with increasing electron–phonon coupling ε_p a *discontinuous* transition at from light polarons ($\rho \lesssim 1$) to *extremely* heavy polarons ($\rho \ll 1$) takes place. Qualitatively, the same behaviour also holds for the spinless Holstein model. Concerning the nature of the self–trapping transition, it is well known that a variational calculation can induce artifacts in the critical behaviour. Indeed, more elaborate theories may rule out the discontinuous nature of this transition, but, in accord with numerical Monte Carlo [428] and ED results [450, 414], may yield a rather sharp transition from a quasi–free electron metal to a heavy–polaron metal. Next, in the spirit of the (modified) Lang–Firsov approach, we have performed the average over the transformed phonon vacuum, which is, strictly speaking, valid only in the *non–adiabatic* limit [413] (note that we have found a smooth crossover from light to heavy polarons in the non–adiabatic regime). Furthermore, our mean–field–like decoupling of the polaron and phonon subsystems neglects important correlation effects due to the residual polaron–phonon interaction and the dynamical correlation of the lattice deformations, which, e.g., give rise to the polaron hopping conductivity (cf. Sec. 8.5). A more detailed discussion of these problems will be given in the following.

8.5 Unitary–transformation scheme for bi–/polaron correlation models [451]

The aim of this section is to derive effective polaron and bipolaron models from the Holstein Hubbard model in the *large–positive* and *large–negative* interaction limits within a systematic and unified scheme of Schrieffer–Wolff–type transformations [452]. By this operator–algebraic approach, which differs from the procedure by Alexandrov *et al.* [349, 366],[1] we obtain, in the moderately heavy– and light–polaron cases, two effective polaronic t–J and bipolaron models. Methodically, the underlying approximations are detailed in all limiting cases.

Treating the polaron formation at finite densities in the non–dimerized paraphase of the Holstein Hubbard model by the variational approach outlined in Sec. 8.1 and Sec. 8.4, we perform the unitary transformation

$$\tilde{\mathcal{H}}_p = \mathcal{U}^\dagger \mathcal{H}_{H-H} \mathcal{U} \,, \quad \mathcal{U}(\gamma) = \exp\Big\{ -\sqrt{\varepsilon_p/\hbar\omega} \sum_i [n + \gamma(n_i - n)]\,(b_i - b_i^\dagger) \Big\} \,, \tag{8.56}$$

where n is the mean polaron density. By this the polaron Hamiltonian $\tilde{\mathcal{H}}_p$ is obtained as

$$\tilde{\mathcal{H}}_p = \mathcal{H}_{\tilde{U}} + \mathcal{H}_t + \mathcal{H}_\gamma + \mathcal{H}_{ph} \,, \tag{8.57}$$

$$\mathcal{H}_{\tilde{U}} = -\tilde{\varepsilon}_p \sum_i n_i + \tilde{U} \sum_i n_{i\uparrow} n_{i\downarrow} \,, \tag{8.58}$$

$$\mathcal{H}_t = -t \sum_{\langle i,j \rangle \sigma} \Phi_{ij}\, c_{i\sigma}^\dagger c_{j\sigma} \,, \tag{8.59}$$

$$\mathcal{H}_\gamma = (\gamma - 1)\sqrt{\varepsilon_p \hbar\omega} \sum_i (b_i^\dagger + b_i)(n_i - n) + (\gamma - 1)^2 n^2 \varepsilon_p N \,, \tag{8.60}$$

$$\mathcal{H}_{ph} = \hbar\omega \sum_i (b_i^\dagger b_i + \frac{1}{2}) \,, \tag{8.61}$$

---

[1] Alexandrov *et al.* [349, 366] have derived an effective bipolaron model by an unitary transformation procedure, where the bipolaron parameters are expressed in terms of dynamical multi-phonon correlation functions.

where $\Phi_{ij} = \tilde{\Phi}_{ij}(\tau^2 \equiv 1)$ is given by (8.10). For $\gamma \equiv 1$, $\tilde{\mathcal{H}}_p$ is the well–known small–polaron Hamiltonian [410].

Taking the average of $\tilde{\mathcal{H}}_p$ over the transformed phonon ground state an effective polaron model may be obtained. In this approach the residual polaron–multi-phonon interaction, proportional to $(\Phi_{ij} - \overline{\Phi_{ij}})$, is neglected. As shown by recent exact cluster diagonalizations for the Holstein Hubbard model [359, 414] (cf. Chap. 9), this is a good approximation in the light–polaron case $\rho = \overline{\Phi_{ij}} \lesssim 1$ (realized for ε_p, $\hbar\omega \ll t$ with $\gamma \ll 1$ or for $\hbar\omega \gg t$, $|\tilde{U}|$ with $\gamma \lesssim 1$ [434, 439]). On the other hand, as was pointed out by Alexandrov *et al.* [413], the adiabatic heavy Holstein polaron (realized for $\hbar\omega < t$ and $\varepsilon_p > zt$; z is the coordination number) cannot be obtained by the phonon averaging procedure. Taking into account the anharmonic lattice fluctuations, which become important at finite polaron densities and in the intermediate coupling regime, we perform the average $\overline{(\ldots)}$ of $\mathcal{H}_p$ over the squeezed phonon state [453, 433]

$$|\tilde{\Psi}^{sq}_{ph}\rangle = \exp\left\{\alpha \sum_i (b_i^\dagger b_i^\dagger - b_i b_i)\right\} |\, 0\rangle \,. \tag{8.62}$$

This yields the effective polaronic Hubbard model (8.37)

$$\overline{\mathcal{H}}_p^H = \mathcal{H}_{\tilde{U}} + \overline{\mathcal{H}}_t + \overline{\mathcal{H}}_{ph} + (\gamma - 1)^2 n^2 \varepsilon_p N \,, \tag{8.63}$$

where $\overline{\mathcal{H}}_t$ is given by (8.59) with Φ_{ij} replaced by the polaron band narrowing factor ρ (8.13).

Next, we derive effective bi–/polaron models in the strong correlation limit (large $|\tilde{U}|$) for non–adiabatic moderately heavy Lang–Firsov polarons ($t < \hbar\omega$, $0.3 \lesssim \rho < 1$; $\gamma \lesssim 1$) and for light polarons.

Let us first consider the *moderately heavy–polaron case*, where fluctuations become important [414, 450]. We separate $\mathcal{H}_t$ into contributions from polaron transitions without and with changes in the number of doubly occupied sites,

$$\mathcal{H}_t = \mathcal{T}_0 + \mathcal{V} \,, \qquad \mathcal{V} = \mathcal{T}_1 + \mathcal{T}_{-1} \,, \tag{8.64}$$

$$\mathcal{T}_0 = -t \sum_{\langle i,j \rangle \sigma} \Phi_{ij} \, (c_{i\sigma}^\dagger (1 - n_{i\bar{\sigma}}) \, c_{j\sigma} \, (1 - n_{j\bar{\sigma}}) + c_{i\sigma}^\dagger n_{i\bar{\sigma}} c_{j\sigma} n_{j\bar{\sigma}}) \,, \tag{8.65}$$

$$\mathcal{T}_1 = -t \sum_{\langle i,j \rangle \sigma} \Phi_{ij} \; c_{i\sigma}^\dagger n_{i\bar{\sigma}} c_{j\sigma} (1 - n_{j\bar{\sigma}}) \,; \quad \mathcal{T}_{-1} = \mathcal{T}_1^\dagger \,. \tag{8.66}$$

Note that

$$[\mathcal{H}_{\tilde{U}}, \mathcal{T}_m] = m \tilde{U} \mathcal{T}_m \,; \quad m = 0, \pm 1 \,. \tag{8.67}$$

In the processes described by (8.64) the on–site energy changes by $m\tilde{U}$, where multi-phonon emissions and absorptions take place. For large $|\tilde{U}|$, the transitions with $m = \pm 1$ are energetically unfavourable.

Now we apply the recursive scheme of Schrieffer–Wolff–type transformations developed by MacDonald *et al.* [128, 454] for the Hubbard model to the polaron Hamiltonian (8.57). Eliminating transitions between states with differing numbers of doubly occupied sites up to $O(\tilde{U}^{-1})$, we perform the unitary transformation

$$\tilde{\mathcal{H}}_p' = \mathrm{e}^{\mathcal{S}} \, \tilde{\mathcal{H}}_p \, \mathrm{e}^{-\mathcal{S}} \,, \qquad \mathcal{S} = \mathcal{S}^{(1)} + \mathcal{S}^{(2)} \,; \tag{8.68}$$

$$\mathcal{S}^{(1)} = \frac{1}{\tilde{U}} \, (\mathcal{T}_1 - \mathcal{T}_{-1}) \,, \qquad \mathcal{S}^{(2)} = \frac{1}{\tilde{U}^2} \, (\, [\mathcal{T}_1, \mathcal{T}_0] - [\mathcal{T}_0, \mathcal{T}_{-1}] \,) \,. \tag{8.69}$$

The generators $\mathcal{S}^{(1)}$ and $\mathcal{S}^{(2)}$ are chosen such that

$$\left[\mathcal{S}^{(1)}, \mathcal{H}_{\tilde{U}}\right] = -\mathcal{V}\,, \qquad \left[\mathcal{S}^{(2)}, \mathcal{H}_{\tilde{U}}\right] = -\left[\mathcal{S}^{(1)}, \mathcal{T}_0\right]\,. \tag{8.70}$$

Thus we get

$$\tilde{\mathcal{H}}_p' = \mathcal{H}_{\tilde{U}} + \mathcal{T}_0 + \mathcal{H}_\gamma + \mathcal{H}_{ph} + \frac{1}{2}\left[\mathcal{S}^{(1)}, \mathcal{V}\right] + \left[\mathcal{S}^{(1)}, \mathcal{H}_\gamma\right] + \left[\mathcal{S}^{(1)}, \mathcal{H}_{ph}\right] + O(\tilde{U}^{-2})\,. \tag{8.71}$$

After a somewhat lengthy but straightforward calculation we obtain

$$\frac{1}{2}\left[\mathcal{S}^{(1)}, \mathcal{V}\right] = \frac{2zt^2}{\tilde{U}}\sum_i n_{i\uparrow}n_{i\downarrow} + \frac{2t^2}{\tilde{U}}\sum_{\langle i,j\rangle} \varPhi_{ij}^2\; C_i^\dagger C_j + \frac{2t^2}{\tilde{U}}\sum_{\langle i,j\rangle}\left(\vec{S}_i\vec{S}_j - \frac{1}{4}n_i n_j\right) + \mathcal{H}_3\,. \tag{8.72}$$

$\mathcal{H}_3$ denotes the three–site contributions, and $C_i^\dagger = c_{i\uparrow}^\dagger c_{i\downarrow}^\dagger$ is the pair–creation operator.

Considering the large–positive–$\tilde{U}$ limit, we project $\tilde{\mathcal{H}}_p'$ onto the subspace with no double occupancy and thereafter take the average over the phonon state (8.62). Obviously, we have $\langle\tilde{\varPsi}_{ph}^{sq}|\mathcal{H}_\gamma|\tilde{\varPsi}_{ph}^{sq}\rangle = 0$. Moreover, we get $\langle\tilde{\varPsi}_{ph}^{sq}|\left[\mathcal{S}^{(1)}, \mathcal{H}_{ph}\right]|\tilde{\varPsi}_{ph}^{sq}\rangle = 0$. The term $\langle\tilde{\varPsi}_{ph}^{sq}|\left[\mathcal{S}^{(1)}, \mathcal{H}_\gamma\right]|\tilde{\varPsi}_{ph}^{sq}\rangle = 2\varepsilon_p\gamma(\gamma-1)(\overline{\mathcal{T}}_1 + \overline{\mathcal{T}}_{-1})/\tilde{U}$ will be neglected due to the small prefactor $\gamma - 1$. As a result, we are left with the effective polaronic t–J model

$$\begin{aligned} \mathcal{H}_p^{t-J} = \quad & -\tilde{\varepsilon}_p\sum_i \tilde{n}_i - t_p\sum_{\langle i,j\rangle\sigma}\tilde{c}_{i\sigma}^\dagger\tilde{c}_{j\sigma} + J\sum_{\langle i,j\rangle}\left(\vec{S}_i\vec{S}_j - \frac{1}{4}\tilde{n}_i\tilde{n}_j\right) \\ & -t_{p,3}\sum_{\langle ijk\rangle\sigma}\Big((\tilde{c}_{i\sigma}^\dagger\tilde{c}_{j\bar{\sigma}}^\dagger\tilde{c}_{j\bar{\sigma}}\tilde{c}_{k\sigma} + \tilde{c}_{i\bar{\sigma}}^\dagger\tilde{c}_{j\bar{\sigma}}\tilde{c}_{j\sigma}^\dagger\tilde{c}_{k\sigma}) + \text{H.c.}\Big) + \frac{\hbar\omega}{4}(\tau^2 + \tau^{-2})\,, \end{aligned} \tag{8.73}$$

where

$$t_p = \rho\, t\,, \qquad t_{p,3} = \rho\, t^2/\tilde{U}\,, \qquad J = 2t^2/\tilde{U}\,, \tag{8.74}$$

$\tilde{c}_{i\sigma} = c_{i\sigma}(1 - n_{i\bar{\sigma}})$, and the summation $\langle ijk\rangle$ extends over all NN pairs $\langle ij\rangle$ and $\langle jk\rangle$. Note that the superexchange is not influenced by the polaron formation, whereas the restricted hopping and the three–site terms are renormalized by the polaron band narrowing. This is in accordance with the results obtained for a modified Holstein t–J model, where the phonon mode couples to the empty sites [455] (see also Chap. 10).

In the large–negative–$\tilde{U}$ limit, the formation of on–site bipolarons takes place. Since in this case there are no real polarons, we project $\tilde{\mathcal{H}}_p'$ onto the subspace of empty and doubly occupied sites. After averaging over the phonon state (8.62) we get the effective bipolaron model

$$\mathcal{H}_b = -\varepsilon_b\sum_i N_i - t_b\sum_{\langle i,j\rangle} C_i^\dagger C_j + V\sum_{\langle i,j\rangle} N_i N_j + \frac{\hbar\omega}{4}(\tau^2 + \tau^{-2})N\,, \tag{8.75}$$

where the projection of n_i yields $2N_i$ with $N_i = C_i^\dagger C_i$. t_b and V denote the effective bipolaron transfer integral and the intersite repulsion, respectively, given by

$$t_b = 2\,\rho^4\, t^2/|\tilde{U}|\,, \quad V = 2t^2/|\tilde{U}|\,. \tag{8.76}$$

Besides a renormalization of the bipolaron binding energy $\varepsilon_b - 2\varepsilon_p = |\tilde{U}| + 2zt^2/|\tilde{U}|$, the polaron–multi-phonon interaction gives rise to a heavy bipolaron mass $\propto \rho^{-4}$ which is due to virtual transitions to unpaired polarons accompanied by multi-phonon emissions. The results (8.76) are in agreement with those by Alexandrov *et al.* [349, 366] derived in the limit $\hbar\omega \ll |\tilde{U}|$.

In the *light–polaron case*, we derive effective bi–/polaron models in the strong correlation limit starting from the model $\overline{\mathcal{H}}_p$ (Eq. (8.63)). Following the same steps as in the derivation of (8.73) and (8.75), one easily sees that all parameters of $O(t^2)$ are equally renormalized by ρ^2. Since the term $\langle\tilde{\Psi}^{sq}_{ph}|\left[\mathcal{S}^{(1)},\mathcal{H}_\gamma\right]|\tilde{\Psi}^{sq}_{ph}\rangle$ is proportional to $\gamma(\gamma-1)$, it can be dropped again. Therefore, in the large–positive–$\tilde{U}$ limit we get $\overline{\mathcal{H}}_p^{t-J}$ given by (8.73), where

$$\overline{t}_p = t_p\,, \qquad \overline{t}_{p,3} = \rho\, t_{p,3}\,, \qquad \overline{J} = \rho^2\, J\,. \tag{8.77}$$

Compared with the polaronic t–J model (8.73) and (8.74), in the light–polaron case the superexchange (8.77) is slightly reduced. Obviously, for $\varepsilon_p = \hbar\omega = 0$, Eq. (8.73) reduces to the standard t–J model.

Correspondingly, in the large–negative–$\tilde{U}$ limit we obtain the effective bipolaron model $\overline{\mathcal{H}}_b$, where $\overline{\varepsilon}_b = 2\varepsilon_p + |\tilde{U}| + 2z(\rho t)^2/|\tilde{U}|$ and

$$\overline{t}_b = t_b\,/\rho^2\,, \quad \overline{V} = \rho^2\, V\,. \tag{8.78}$$

Compared with the heavy–bipolaron parameters (8.76), the mass is proportional to ρ^{-2}, and the bipolaron repulsion is weakened. In this case the bipolaron motion does not involve virtual phonon processes. This is in accord with the result by Alexandrov *et al.* [349, 366] in the antiadiabatic limit $\hbar\omega \gg |\tilde{U}|$. Let us point out that the application of the phenomenological large–negative–U Hubbard model to the bipolaron problem is justified only for rather weak mass renormalization. Different versions of the negative–U Hubbard model and the resulting pairing models [456, 457] were extensively studied in the literature (see [348] and references therein), where models of the structure (8.75) are isomorphic to the quantum anisotropic pseudo-spin Heisenberg model [458, 459].

In the t–J model the polaron formation may change the ratio of the interaction versus hopping terms from $J/t < 1$ (holding for high–T_c cuprates) to $J/t_p \propto \rho^{-1} > 1$. Note that for $J > t$ the 2D t–J model shows phase separation, whereas for $J \ll t$ it does not [126]. Equally, in the heavy–bipolaronic pairing model, the ratio $V/t_b \propto \rho^{-4}$ is appreciably enhanced compared with the pairing models studied in the context of the large–negative–U Hubbard model [458]. Altogether, the bi–/polaron effects provide a microscopic foundation for a realistic extension of the t–J and pairing model parameter regions.

8.6 Polaron hopping conductivity [434]

To investigate the finite–density and correlation effects on the polaron conductivity, we start from the polaronic Hamiltonian $\tilde{\mathcal{H}}_p$ (8.56). We confine ourselves to the heavy–polaron regime ($\rho \ll 1$), where squeezing phenomena become negligible (cf. Sec. 8.4).

The real part of the electrical conductivity is given by the the Kubo formula

$$\mathrm{Re}\,\sigma(\omega) = \frac{\tanh(\beta\hbar\omega/2)}{2\Omega\hbar\omega}\int\limits_{-\infty}^{\infty} dt'\, \mathrm{e}^{i\omega t'}\left\langle\left[\tilde{J}^\nu,\,\tilde{J}^\nu(t')\right]_+\right\rangle_{\tilde{\mathcal{H}}_p}\,. \tag{8.79}$$

Ω is the crystal volume, $\beta = 1/k_BT$, and $\tilde{J}^\nu$ denotes the ν–component of the polaron current operator

$$\vec{\tilde{J}} = \frac{e}{i\hbar}\sum_i \vec{R}_i\left[n_i,\,\tilde{\mathcal{H}}_p\right]_- = \frac{iet}{\hbar}\sum_{\langle i,j\rangle\,\sigma}(\vec{R}_i - \vec{R}_j)\;\Phi_{ij}\;c^\dagger_{i\sigma}c_{j\sigma} \tag{8.80}$$

(note that in this section ω is the frequency of the optical conductivity while the bare phonon frequency is denoted by ω_0). Since we are in the heavy–polaron regime, we decouple the polaron–phonon correlation function appearing in the current correlator into a product of dynamical polaron and phonon correlation functions. Then, those functions are calculated, in the spirit of our variational approach, on the basis of $\mathcal{H}_0 = \mathcal{H}_{\tilde{t}} + \mathcal{H}_{\tilde{U}} + \mathcal{H}_{ph}$ resulting from $\tilde{\mathcal{H}}$ by decoupling the phonon and polaron subsystems. Here, $\mathcal{H}_{\tilde{t}}$ is given by (8.59) with $t\Phi_{ij}$ replaced by the polaronic reduced transfer integral

$$\begin{aligned} \tilde{t} &= t\,\langle\Phi_{ij}\rangle_0 = t\,\exp\{-\kappa\coth(\beta\hbar\omega_0/2)\}\,, \\ \kappa &= \frac{\varepsilon_p}{\hbar\omega_0}\gamma^2 \end{aligned} \tag{8.81}$$

($\langle\cdots\rangle_0$ denotes the *thermodynamic* average with respect to $\tilde{\mathcal{H}}_0$). Since we are primarily interested in the low–temperature conductivity, the variational parameter γ is taken from our ground–state analysis given in Sec. 8.4. Our main concern is the characteristics of the polaron–enhanced optical absorption by multi-phonon processes in the low–temperature regime. Therefore, we disregard the polaron band contribution and consider only the polaron hopping conductivity which is due to polaron transitions accompanied by multi-phonon absorptions and emissions. The hopping contribution is given by

$$\begin{aligned} \langle\tilde{J}^\nu\tilde{J}^\nu(t')\rangle_0 = -\left(\frac{e\,t}{\hbar}\right)^2 \sum_{\substack{\langle i,j\rangle\sigma \\ \langle l,m\rangle\sigma'}} & (R_i^\nu - R_j^\nu)\,(R_l^\nu - R_m^\nu)\,\langle c_{i\sigma}^\dagger c_{j\sigma} c_{l\sigma'}^\dagger(t') c_{m\sigma'}(t')\rangle_0 \\ & \times \Big(\langle\Phi_{ij}\,\Phi_{lm}(t')\rangle_0 - \langle\Phi_{ij}\rangle_0\langle\Phi_{lm}\rangle_0\Big)\;. \end{aligned} \tag{8.82}$$

Since in the heavy–polaron regime we have $\tilde{t} \ll \hbar\omega_0,\, U$, we calculate the hopping conductivity $\mathrm{Re}\{\sigma_h(\omega)\}$ to the lowest order in $\tilde{t}$, i.e., we take the polaron correlation function in the atomic limit. We obtain

$$\langle c_{i\sigma}^\dagger c_{j\sigma} c_{l\sigma'}^\dagger(t') c_{m\sigma'}(t')\rangle_{\mathcal{H}_{\tilde{U}}} = K_{ij}(t')\;\delta_{lj}\,\delta_{mi}\,\delta_{\sigma\sigma'}\;, \tag{8.83}$$

$$\begin{aligned} & K_{ij}(t') = K_0 + K_1\,\mathrm{e}^{\frac{i}{\hbar}\tilde{U}t'} + K_{-1}\,\mathrm{e}^{\frac{-i}{\hbar}\tilde{U}t'}\;, \\ & K_0 = \left(\frac{n}{2} - K\right)(1 - n + 2K)\;,\quad K_1 = \left(\frac{n}{2} - K\right)^2\;,\quad K_{-1} = \mathrm{e}^{-\beta\tilde{U}}K_1\;, \end{aligned} \tag{8.84}$$

where

$$K \equiv \langle n_{i\uparrow}n_{i\downarrow}\rangle_{\mathcal{H}_{\tilde{U}}} = \frac{n}{2}f(\tilde{U} - \tilde{\mu})\;. \tag{8.85}$$

Here $f(\varepsilon)$ is the Fermi function, and $\tilde{\mu} = \tilde{\varepsilon}_p + \mu$. By $\tilde{\mathcal{H}}_{ph}$ we get the phonon correlation function

$$\langle\Phi_{ij}\Phi_{ji}(t')\rangle_0 = \langle\Phi_{ij}\rangle_0^2\,\exp\Big\{2\kappa\,\Big[(p+1)\,\mathrm{e}^{i\omega_0 t'} + p\,\mathrm{e}^{-i\omega_0 t'}\Big]\Big\}\;, \tag{8.86}$$

where $p = 1/(\exp(\beta\hbar\omega_0) - 1)$.
Expanding the exponential we obtain

$$\begin{aligned} \langle\Phi_{ij}\Phi_{ji}(t')\rangle_0 - \langle\Phi_{ij}\rangle_0^2 = \langle\Phi_{ij}\rangle_0^2 \quad & \Bigg\{2\sum_{s=1}^{\infty}\sum_{k=0}^{\infty}\frac{1}{(s+k)!\,k!}\left(\frac{\eta}{2}\right)^{s+2k} \\ & \times\,\cosh(s\beta\hbar\omega_0/2 + is\omega_0 t') + \sum_{k=1}^{\infty}\frac{1}{(k!)^2}\left(\frac{\eta}{2}\right)^{2k}\Bigg\}\;, \end{aligned} \tag{8.87}$$

where $\eta = 2\kappa \sinh^{-1}(\beta\hbar\omega_0/2)$. Inserting Eqs. (8.82), (8.83), (8.87) into Eq. (8.79) we get

$$\begin{aligned}\mathrm{Re}\,\sigma_h(\omega) = \quad & 2\frac{N}{\Omega}\left(\frac{ea}{\hbar}\right)^2 \tilde{t}^2\, \frac{\tanh(\beta\hbar\omega/2)}{\hbar\omega} \int\limits_{-\infty}^{\infty} dt'\, \mathrm{e}^{i\omega t'} \Bigg\{ K_{ij}(t') \\ & \times \left[2\sum_{s=1}^{\infty} \mathrm{I}_s(\eta)\, \cosh(s\beta\hbar\omega_0/2 + is\omega_0 t') + \mathrm{I}_0(\eta) - 1 \right] + \text{c.c.} \Bigg\}\,, \qquad (8.88)\end{aligned}$$

where

$$\mathrm{I}_s(\eta) = \sum_{k=0}^{\infty} \frac{1}{\Gamma(s+k+1)\, k!} \left(\frac{\eta}{2}\right)^{s+2k} \qquad (8.89)$$

is the modified Bessel function. Taking $K_{ij}(t')$ from Eq. (8.84) and performing the time integration in (8.88) we obtain the optical absorption spectrum ($\omega > 0$)

$$\begin{aligned}\mathrm{Re}\,\sigma_h(\omega) = \quad & 8\pi\frac{N}{\Omega}\left(\frac{ea}{\hbar}\right)^2 \tilde{t}^2 \Bigg\{ \sum_{s=1}^{\infty} \mathrm{I}_s(\eta) \Bigg[K_0 \frac{\sinh(s\beta\hbar\omega_0/2)}{s\hbar\omega_0}\, \delta(\omega - s\omega_0) \\ & + K_1\, \mathrm{e}^{-\beta\tilde{U}/2} \left(\frac{\sinh\!\left(\frac{\beta}{2}(\tilde{U} + s\hbar\omega_0)\right)}{\tilde{U} + s\hbar\omega_0}\, \delta\!\left(\omega - \frac{\tilde{U}}{\hbar} - s\omega_0\right)\right. \\ & \left. + \frac{\sinh\!\left(\frac{\beta}{2}(\tilde{U} - s\hbar\omega_0)\right)}{\tilde{U} - s\hbar\omega_0} \left(\delta\!\left(\omega - \frac{\tilde{U}}{\hbar} + s\omega_0\right) + \delta\!\left(\omega + \frac{\tilde{U}}{\hbar} - s\omega_0\right)\right)\right)\Bigg] \\ & + K_1\, \mathrm{e}^{-\beta\tilde{U}/2}\, \frac{\sinh(\beta\tilde{U}/2)}{\tilde{U}}\, (\mathrm{I}_0(\eta) - 1)\, \delta\!\left(\omega - \frac{\tilde{U}}{\hbar}\right) \Bigg\}\,. \qquad (8.90)\end{aligned}$$

The δ–functions in Eq. (8.90) express the energy conservation in polaron transitions with or without changes in the number of doubly occupied sites accompanied by multi-phonon emissions and absorptions. For example, the first term in Eq. (8.90) describes processes without changes in the number of doubly occupied sites and with the net emission of s phonons. The second term gives contributions from the creation of doubly occupied sites with the net emission of s phonons, whereas the change in the number of doubly occupied sites described by the last term is accompanied by an equal number of emitted and reabsorbed phonons.

Using the envelope of the δ–functions, Eq. (8.90) can be expressed as

$$\begin{aligned}\mathrm{Re}\,\sigma_h(\omega) = \quad & 8\pi\frac{N}{\Omega}\left(\frac{ea}{\hbar}\right)^2 \frac{\tilde{t}^2}{\omega_0} \Bigg\{ \frac{\sinh(\beta\hbar\omega/2)}{\hbar\omega} \Bigg[K_0\, \mathrm{I}_{\omega/\omega_0}(\eta) + K_1\, \mathrm{e}^{-\beta\tilde{U}/2} \\ & \times \left(\mathrm{I}_{(\omega - \frac{\tilde{U}}{\hbar})/\omega_0}(\eta) + \mathrm{I}_{(\frac{\tilde{U}}{\hbar} - \omega)/\omega_0}(\eta) + \mathrm{I}_{(\omega + \frac{\tilde{U}}{\hbar})/\omega_0}(\eta) \right) \Bigg] \\ & + K_1\, \mathrm{e}^{-\beta\tilde{U}/2}\, \frac{\sinh(\beta\tilde{U}/2)}{\tilde{U}}\, (\mathrm{I}_0(\eta) - 1)\, \delta\!\left(\omega - \frac{\tilde{U}}{\hbar}\right) \Bigg\}\,. \qquad (8.91)\end{aligned}$$

Note that $\mathrm{I}_{\omega/\omega_0}(\eta)$ has meaning only for $\omega \geq \omega_0$.

Let us now consider the low–temperature limit ($k_B T \ll \hbar\omega_0, \tilde{U}$) of the absorption spectrum in the case $n < 1$. Concerning the correlation functions (8.84), in the atomic limit we have $\lim_{T\to 0} \mathrm{e}^{(-\beta\tilde{\mu})} = 2(1-n)/n$ so that $K(T=0) = 0$ and

$$K_0(T=0) = \frac{n}{2}(1-n) \quad K_1(T=0) = \frac{n^2}{4}\,. \qquad (8.92)$$

The low–temperature expansion of Eq. (8.91) gives contributions to the zero–temperature spectrum only from the first two terms. Thus, we obtain

$$\mathrm{Re}\,\sigma_h(\omega;T=0)=2\pi\frac{N}{\Omega}\left(\frac{ea}{\hbar}\right)^2\frac{\tilde{t}^2}{\omega_0}\frac{1}{\hbar\omega}\left\{n(1-n)\,B(\omega)+\frac{n^2}{2}B\Big(\omega-\frac{\tilde{U}}{\hbar}\Big)\right\}\,, \qquad (8.93)$$

where

$$B(\omega)=(2\kappa)^{\frac{\omega}{\omega_0}}\,\Gamma^{-1}(1+\omega/\omega_0)\,; \qquad \omega\geq\omega_0\,. \qquad (8.94)$$

Note that in the low–density limit $n \ll 1$ (first order in n) and in the $\tilde{U}=0$ limit, the absorption spectra (8.91) and (8.93) agree with those obtained for uncorrelated polarons and for the LF transformation by Loos [360]. In Ref. [360] the spectra are shown to reproduce the results by Reik (for $T=0$ and $\omega \gg \omega_0$) and by Reik and Heese [448] (for not too low temperatures and $\varepsilon_p > \hbar\omega_0$).

We have numerically evaluated the zero–temperature absorption spectrum (8.93) for $\varepsilon_p = 6t$, $\hbar\omega_0 = 0.8t$ and for various sets of the parameters U and $n < 1$. That is, we consider the heavy–polaron region, where multi-phonon and non-adiabatic processes take place ($\hbar\omega_0 < t < \sqrt{\hbar\omega_0\varepsilon_p}$ [407]). In addition, we take the Hubbard interaction U to be large enough so that $\tilde{U} \gg \tilde{t}$.

The absorption spectra are shown in Fig. 8.16. For $U = 30$ (Fig. 8.16 (a)) we have $\gamma \simeq 1$ for all n (e.g., $n = 0.5$: $\gamma = 0.997$, $\rho = 6.2 \times 10^{-4}$). In this regime we compare our results with the LF ($\gamma \equiv 1$) spectrum given by Suzuki *et al.* [390]. We obtain a low–energy peak at $\hbar\omega_{m1} \simeq 2(\varepsilon_p - \hbar\omega_0)$ $\forall n$, in agreement with the position of the small–polaron maximum at about $2\varepsilon_p$ found in single–polaron theories (see, e.g., Refs. [430, 447, 360]). The peak position given in Ref. [390] ($\hbar\omega_{m1} \simeq \varepsilon_p$) is incorrect. For the peak width at half height we get $\Delta_1 = 7.3$ for all n, (Ref. [390]: $\Delta_1 \simeq \sqrt{2\kappa}\hbar\omega_0 = 3.1$). The polaron correlation ($\tilde{U} = 18$) gives rise to a high–energy peak at $\hbar\omega_{m2} \simeq U - \hbar\omega_0$ (Ref. [390]: $\hbar\omega_{m2} \simeq U - \varepsilon_p$) with the same width, where the peak height increases with n. Note that the low–energy absorption is symmetric with respect to $n = 0.5$.

In order to get more insight into the correlation effects on the optical absorption, in Figs. 8.16 (b), (c) the spectra are shown for $U = 20$ and $U = 15$, respectively. The variational parameter γ has nearly the same value as for $U = 30$, since $\tilde{U}/\rho$ is of the order of 10^4 in all cases. For $U = 20$ (15) we have $\tilde{U} = 8$ (3) $\forall n$. Owing to the decreasing value of $\tilde{U}$, the second contribution to (8.93) starts to merge with the first one so that the spectrum may show only one peak at $\hbar\omega_m$. Considering the case $U = 15$ (Fig. 8.16 (c)), due to the increasing weight of the second contribution with increasing n, $\hbar\omega_m$ as well as the peak width increase with n. Thus, for not too strong polaron correlations and high enough densities it is possible to obtain a shift of the polaron absorption maximum to higher energies and a broadening of the spectrum. For fixed U, this correlation effect increases with n. On the other hand, for fixed n, the broadening of the single peak increases with $\tilde{U}$ and, for high enough values of $\tilde{U}$, a two–peak structure evolves (see Fig. 8.16 (a)).

Let us relate this behaviour to some recent attempts at interpreting the mid-infrared absorption in high–T_c materials [387, 58] in terms of polaron hopping transport [387, 384, 390]. The photo-induced absorption spectra in the insulating phase of those compounds exhibit a maximum in the mid-infrared which may be well fit by $\mathrm{Re}\{\sigma_h(\omega, T = 0)\}$ in the low–density limit [387] (where polaron interactions can be neglected). Considering, e.g., $\mathrm{YBa_2Cu_3O_{6.3}}$, the peak position observed at 0.13 eV yields a polaron binding energy of $\varepsilon_p \simeq 0.07$ eV. In the metallic samples, where we have appreciable values of the charge carrier density, the conductivity maximum is reported to shift to lower energies with increasing carrier concentration [58], in

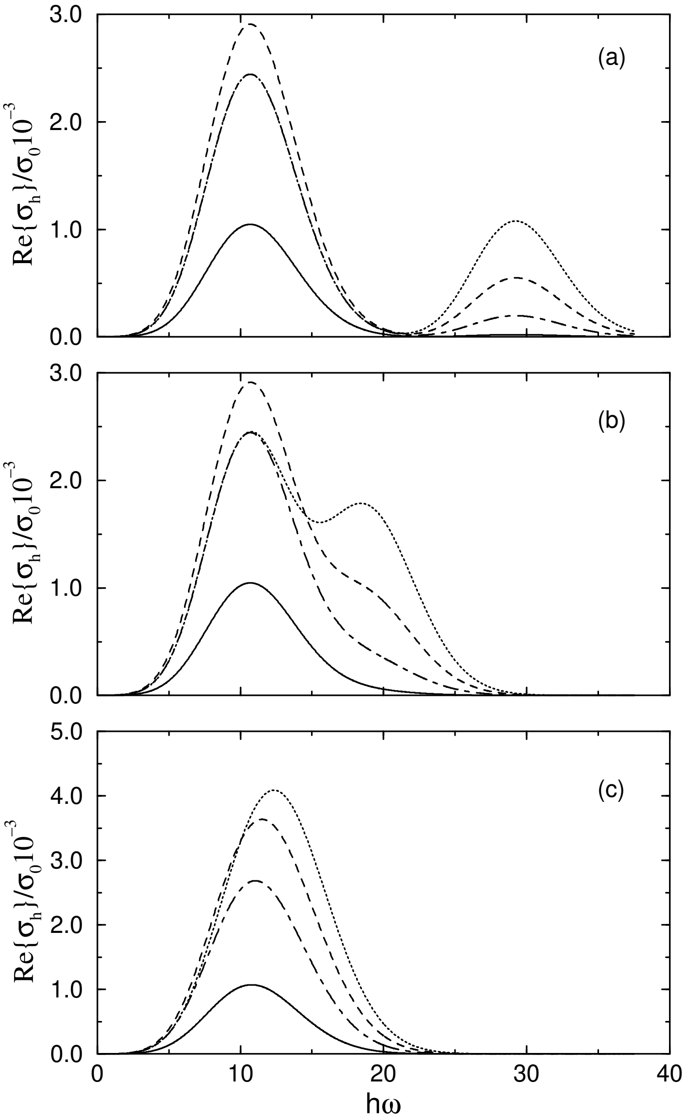

Figure 8.16: Real part of the hopping conductivity $\mathrm{Re}\{\sigma_h\}$ (in units of $\sigma_0 = 2\pi N e^2 a^2/\Omega\hbar$) as a function of frequency at $\varepsilon_p = 6$ and $\hbar\omega_0 = 0.8$. The results are shown for $U = 30$ (a), $U = 20$ (b) and $U = 15$ (c), where full, chain dashed, dashed and dotted lines correspond to $n = 0.1$, $n = 0.3$, $n = 0.5$ and $n = 0.7$, respectively.

disagreement with our polaron theory. In any case, the peak observed in the metallic samples is broader than calculated within single–polaron transport theory [387, 384]. This additional broadening (for $\omega > \omega_m$), also known from the small–polaron material TiO_2 [449], was recently suggested to be due to polaron correlations [387, 384] or to finite $\tilde{t}$ corrections to $\sigma_h(\omega)$ [390] (not included in (8.93)). As shown by our analysis, for appropriate parameter values, the broadening of the mid-infrared peak may be due to polaron correlations.

Chapter 9

Exact Lanczos results for the Holstein Hubbard model

In this chapter we analyze the 1D and partly the 2D Holstein Hubbard model on finite lattices with up to ten sites by means of direct Lanczos diagonalization, preserving the full dynamics and quantum nature of the phonons. By using direct ED techniques it is necessary to truncate the phononic Hilbert space, and hence the accessible parameter space is limited by the size of the matrix one can diagonalize. Therefore ED studies up to now were limited to either weak electron–phonon couplings ($\varepsilon_p \ll t, \hbar\omega$) [460], to the so–called frozen–phonon approximation ($\hbar\omega = 0$) [461, 462, 443, 463], or to very small systems (four or even two sites) [431, 413, 464]. Using parallel computers we were able to calculate the ground–state properties of the Holstein Hubbard model for a wide range of phonon frequencies, electron–electron and electron–phonon interaction strengths, where the emphasis is on the investigation of the transition from 'large' to 'small' polarons. In particular, we discuss the low–lying excitations (spectral functions) on large enough lattices, in order to establish the formation of a (bi)polaronic quasiparticle band in the strong–coupling case.

9.1 Computational procedure [450]

A general state of the Holstein Hubbard Hamiltonian, $\mathcal{H}_{H-H}$ (Eq. (7.6)), describing $N_{el} = N_\uparrow + N_\downarrow$ electrons on a finite D–dimensional hypercubic lattice with N sites can be written as the direct product

$$|\Psi\rangle = \sum_{l,k} c_l^k \; |l\rangle_{el} \otimes |k\rangle_{ph} \,, \tag{9.1}$$

where l and k label the basic states of the electronic and phononic Hilbert space with dimensions $D_{el} = \binom{N}{N_\uparrow}\binom{N}{N_\downarrow}$ and $D_{ph} = \infty$, respectively. Since the bosonic part of the Hilbert space is infinite dimensional we use a truncation procedure [465] restricting ourselves to phononic states with at most M phonons:

$$|k\rangle_{ph} = \prod_{i=1}^{N} \frac{1}{\sqrt{n_i^k!}} \left(b_i^\dagger\right)^{n_i^k} \; |0\rangle_{ph} \tag{9.2}$$

with

$$\sum_{i=1}^{N} n_i^k \leq M \,, \tag{9.3}$$

and $1 \leq k \leq D_{ph}^{(M)} = (M+N)!/M!N!$. To further reduce the dimension of the Hilbert space we separate out the center of mass motion by transforming to new phonon operators $B_i^{(\dagger)}$, which can be taken into account analytically as displaced harmonic oscillators.

Then the resulting Hamiltonian matrix is diagonalized using a standard Lanczos method. As the convergence of the Lanczos procedure depends on the (relative) difference of neighbouring eigenvalues, $|E_{i+1} - E_i|/|E_i|$, one needs to be very careful in resolving eigenvalues within the extremely narrow small–polaron band. To monitor the convergence of our truncation procedure as a function of M we calculate the weight of the m–phonon states in the ground state $|\Psi_0\rangle$ of $\mathcal{H}_{H-H}$:

$$|c^m|^2 = \sum_{l,k} |c_l^k|^2 \,, \qquad \text{where } m = \sum_{i=1}^{N} n_i^k \,. \tag{9.4}$$

At fixed M, the curve $|c^m|^2(m)$ is bell-shaped and its maximum corresponds to the most probable number of phonon quanta in the ground state. To illustrate the M–dependences of the ground–state energy E_0 and the coefficients $|c^m|^2$, we have shown both quantities for the single–electron Holstein model in Fig. 9.1. In the numerical work convergence is achieved if the relative error of the ground–state energy is less than 10^{-7}. In addition, we check that E_0 is smaller than the estimate obtained from the IMVLF treatment of the phonon subsystem proposed in Ref. [359] (cf. Sec. 10.3).

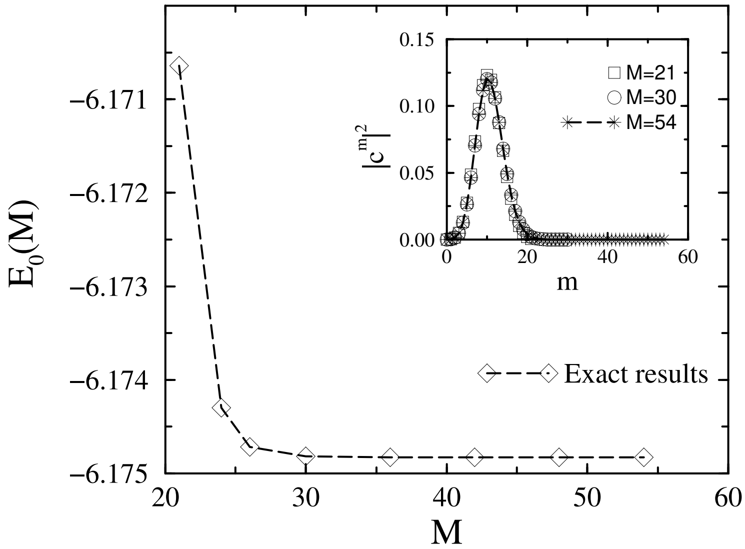

Figure 9.1: Ground–state energy E_0 and weight of the m–phonon states $|c^m|^2$ (inset) as a function of the maximal number of phonons M for the 1D single–electron Holstein model on a four–site lattice. The model parameters are: $\varepsilon_p = 6.0$, $\hbar\omega = 0.4$ (all energies are measured in units of t).

We have written the program in Fortran90 and ran it on a 64–node CM5. We were able to diagonalize Hamiltonian matrices up to a dimension of about 82 millions. Since a matrix vector multiplication for this matrix size takes less than 150 seconds, the limiting factor of our numerical algorithm is the available storage.

9.2 One–electron case [414]

In the first place, we investigate the polaron properties of the 1D Holstein model with a single electron on finite rings with up to ten sites using periodic boundary conditions. In the light of the literature over at least the last two decades [466, 428, 361, 464, 363, 362] we expect a gradual transition from a (nearly free) large–polaron solution to a small–polaron–like ground state upon increasing the EP coupling. Since, in particular in the adiabatic regime, the formation of a polaronic state is accompanied by a strong reduction of the coherent electron motion, this effect should be observable in the expectation value of the kinetic energy $E_{p,kin}/t = -\sum_{<ij>\sigma}\langle\Psi_0|(c_{i\sigma}^{\dagger}c_{j\sigma} + \mathrm{H.c.})|\Psi_0\rangle$, where $|\Psi_0\rangle$ is the ground–state wave-function. We therefore define an effective polaronic transfer amplitude [359],

$$t_{p,eff} = E_{p,kin}(\varepsilon_p, U)/E_{p,kin}(0, U)\,, \tag{9.5}$$

in order to characterize the increase in the quasiparticle mass [359]. Note that $t_{p,eff}$ substantially differs from the (exponential) polaron band renormalization factor (ρ) obtained analytically in the non–adiabatic Lang–Firsov and adiabatic Holstein cases [413] (cf. also Chap. 8).

We illustrate the dependence of this effective hopping amplitude on the EP interaction strength in Fig. 9.2, where we have plotted $t_{p,eff}$ as a function of ε_p at different phonon frequencies. First it is important to realize that there are two complementary (adiabatic and non–adiabatic) regimes for the polaronic motion. In the non–adiabatic regime, where the lattice fluctuations are fast and the phonons are able to follow immediately the electronic motion forming a non–adiabatic Lang–Firsov polaron (NLFP), one observes a very gradual decrease of $t_{p,eff}$ as ε_p increases. At the same time the 'phonon distribution function', $|c^m|^2$, gets wider but the maximum is still located at the zero–phonon state. In the adiabatic regime, one notices a crossover from a quasi–free (large–size) polaron (LP), described by a $t_{p,eff}$ that is only weakly reduced from its noninteracting value, to a less mobile (small–size) adiabatic Holstein polaron (AHP) for large ε_p. As expected this transition occurs if the EP coupling approximately exceeds half the bare electronic bandwidth and, in accordance with Monte Carlo results [428, 409], is much sharper in two dimensions [450, 414] (cf. Sec. 9.4). Nonetheless, all physical quantities are smooth functions of ε_p, in particular there are no ground–state level crossings, i.e., the transition from LP to AHP is *continuous* and not accompanied by any

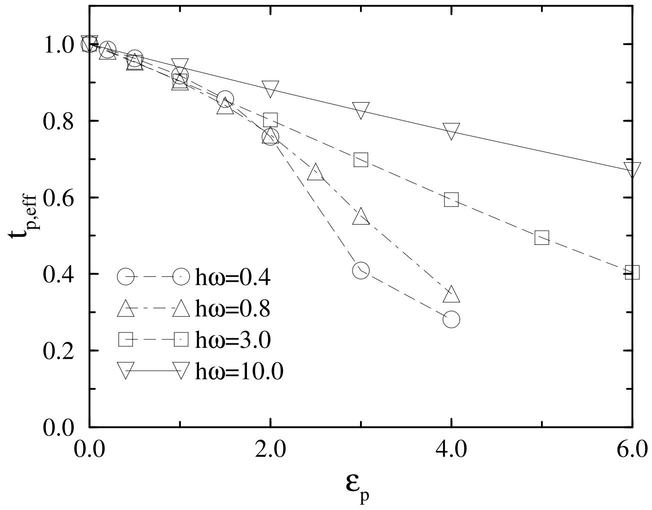

Figure 9.2: Effective hopping amplitude, $t_{p,eff}$ *vs* ε_p, for a single electron on a ten–site chain described by the 1D Holstein model.

non–analyticities. While in the weak–coupling case we have $m_{max} = 0$ and the inclusion of higher phonon states ($m \gtrsim 5$) do not improve the ground–state energy at all, in the adiabatic strong–coupling case ($\varepsilon_p = 4$, $\hbar\omega = 0.4$), the maximum in $|c^m|^2$ is shifted to multi–phonon states ($m_{max} \simeq 8$) and we need about 16 phonons to reach a sufficient accuracy within our truncation procedure. Note that a similar behaviour can be observed in the *non–adiabatic* regime ($\hbar\omega > t$) provided that $\varepsilon_p \gg \hbar\omega$, e.g., for $\hbar\omega = 3$ and $\varepsilon_p = 8$ we find $m_{max} \simeq 2$.

To elucidate the difference between the ‘extended’ LP and ‘quasi–localized’ AHP states in more detail, we have calculated the electron–phonon density correlation function

$$C_{el-ph}(|i-j|) = \langle \Psi_0 | n_i b_j^\dagger b_j | \Psi_0 \rangle \,, \tag{9.6}$$

which measures the correlation between the electron occupying site i and the density of phonons on site j. Results for $C_{el-ph}(|i-j|)$, plotted in Fig. 9.3 at $\hbar\omega = 0.4$ for all distances $i - j := \vec{R}_i - \vec{R}_j$, show that for small ε_p the correlation between the electron and the phonons is pretty weak and exhibits little structure, i.e., the few phonons contained in the ground state are nearly uniformly distributed over the whole lattice. In contrast, in the case of large EP coupling ($\varepsilon_p = 3$), the phonons are strongly correlated with the position of the electron, thus implying a very small radius of the polaron.[1] Since a polaron’s mass is inversely proportional to its size, the AHP formed at large ε_p is an extremely heavy quasiparticle. As can be seen from the inset of Fig. 9.3, the on–site electron–phonon correlation increases dramatically around the same value of ε_p at which $t_{p,eff}$ becomes depressed (cf. Fig. 9.2). This means, in the adiabatic regime a strong short–range EP interaction can lower the energy of the system due to a deformation–potential–like contribution sufficiently to overcompensate the loss of kinetic energy. Nonetheless, the ‘quasi–localized’ (self–trapped) polaronic state has band–like character, i.e., the AHP can move itinerantly.

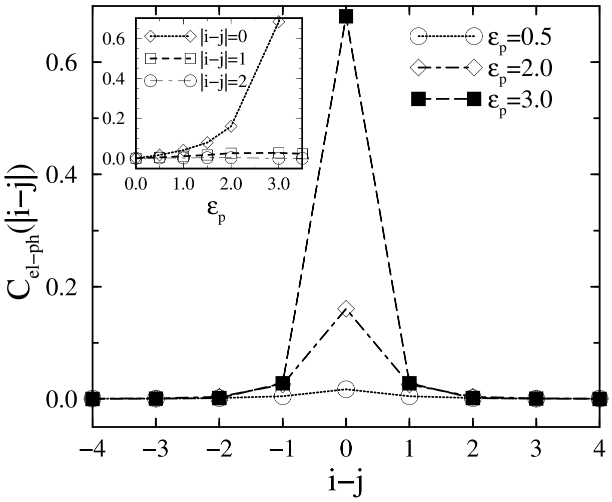

Figure 9.3: Electron–phonon density correlation function $C_{el-ph}(|i-j|)$ as a function of the distance $i - j$ and EP coupling ε_p (inset) at $\hbar\omega = 0.4$. The results are given for the single–electron Holstein model on a eight–site chain.

In order to discuss the formation of a small–polaron band one has to calculate the low–lying excited states. As a first step, in Fig. 9.4 we classify the lowest eigenvalues of the Holstein model according to the allowed wave–vectors of the eight–site lattice for various phonon frequencies at $\varepsilon_p = 3$. Here the ‘band dispersion’ $E_K - E_0$ is scaled with respect to the so–called coherent bandwidth $\Delta E = \sup_K E_K - \inf_K E_K$ (cf. Sec. 3.1.2). ΔE strongly depends on both ratios

---

[1] Note, however, that the translational invariance of the ground state is not broken.

$\varepsilon_p/\hbar\omega$ and ε_p/t, for example, we found $\Delta E(\varepsilon_p = 3, \hbar\omega) = 0.0157$, 0.1957, 2.9165, and 4.0 for $\hbar\omega = 0.4$, 0.8, 10.0 and ∞, respectively. Of course, the simple Lang–Firsov formula, $\Delta E_{LF} = 4D \exp[-\varepsilon_p/\hbar\omega]$, gives a good estimate of the polaronic bandwidth only in the non–adiabatic regime: $\Delta E_{LF}(\varepsilon_p = 3, \hbar\omega) = 0.0022$ ($\hbar\omega = 0.4$), 0.0941 (0.8), 2.9633 (10.0), 4 (∞). Besides the strong renormalization of the bandwidth in the low–frequency strong–coupling regime it is interesting to note that the deviation of the polaron band dispersion from a (rescaled) 'cosine–dispersion' of noninteracting electrons is most pronounced at *intermediate* phonon frequencies $\hbar\omega \sim t$, i.e., in between the extreme adiabatic (AHP) and antiadiabatic (NLFP) limits. This deviation may be due to a residual polaron–phonon interaction, with the phonons sitting on sites other than the polaron. To demonstrate that the low–lying eigenvalues do indeed form a well–separated quasiparticle band in the adiabatic strong–coupling regime ($\varepsilon_p = 3$, $\hbar\omega = 0.4$), in the inset of Fig. 9.4 we have displayed the lowest few eigenvalues in dependence on ε_p. In the very weak–coupling regime ($\varepsilon_p = 0.5$) the eigenvalues are barely changed from their $\varepsilon_p = 0$ values, where additional eigenvalues, separated from the ground–state energy E_0 by multiples of $\hbar\omega$ (e.g., E_2, E_3, and E_4), enter the spectrum. As ε_p increases a band of states separates from the rest of the spectrum. These states become very close in energy and a narrow well–separated energy band evolves in the strong–coupling case ($\varepsilon_p = 3$). Obviously, the gap to the next higher band of eigenvalues is of the order of the bare phonon frequency $\hbar\omega$. Neglecting degeneracies one may tentatively identify those five states as the states of the small–polaron band on the eight–site lattice.

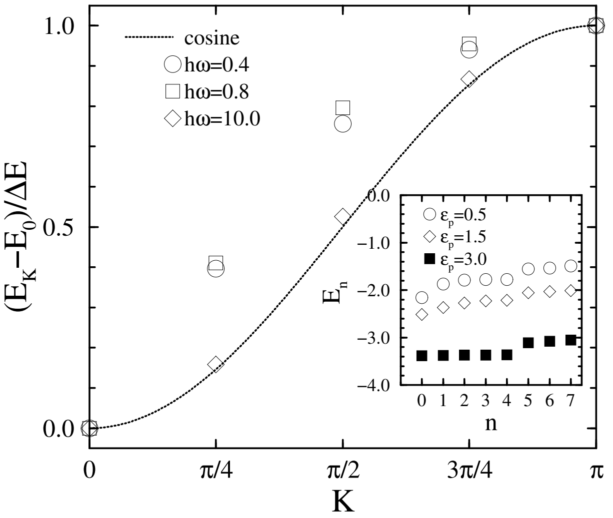

Figure 9.4: Single–electron band dispersion $E_K - E_0$ at $\varepsilon_p = 3$ in units of the coherent bandwidth ΔE. The inset shows the distribution of the eigenvalues at $\hbar\omega = 0.4$, where the horizontal axis counts the eigenvalues sorted by magnitude and the vertical axis gives their absolute values $E_n := E_n^{(tot)} - N\hbar\omega/2$. All results are given for the eight–site chain with $M = 18$ phonons.

Keeping this identification in mind, in Fig. 9.5 we have plotted the lowest eigenvalues as a function of the (1D) K–vectors belonging to various system sizes ($N = 6$, 8, 10). One notices that the dispersion E_K is rather size–independent, i.e., the E_K–values obtained for larger systems just fill the gaps. Undoubtedly, the smooth shape of E_K already provides good reasons for a quasiparticle band description of the AHP in the strong–coupling regime. To further substantiate this quasiparticle interpretation, we also have calculated the one–particle spectral functions

$$A_K(E) = \sum_n |\langle \Psi_n^{(N_{el})} | c_K^\dagger | \Psi_0^{(N_{el}-1)} \rangle|^2 \, \delta(E - E_n^{(N_{el})} + E_0^{(N_{el}-1)}) \tag{9.7}$$

with $N_{el} = 1$ for the non–equivalent K–values of the six–site system using a polynomial moment method [467] (cf. Sec. 10.1). The idea is to see a direct verification of the coherent band dispersion E_K in terms of $A_K(E)$. The electronic spectral functions $A_K(E)$ are shown in the four insets of Fig. 9.5. The important point, we would like to emphasize, is that the position of the first peak in each spectral function $A_K(E)$ exactly coincides with the corresponding $E_0(K)$–value and the other peaks are at higher energies than any of the coherent band–energy values. This means, our exact results for the low–energy excitation spectrum of a single electron corroborate the existence of heavily dressed polaronic quasiparticles, where the electronic and phononic degrees of freedom are strongly mixed.[2]

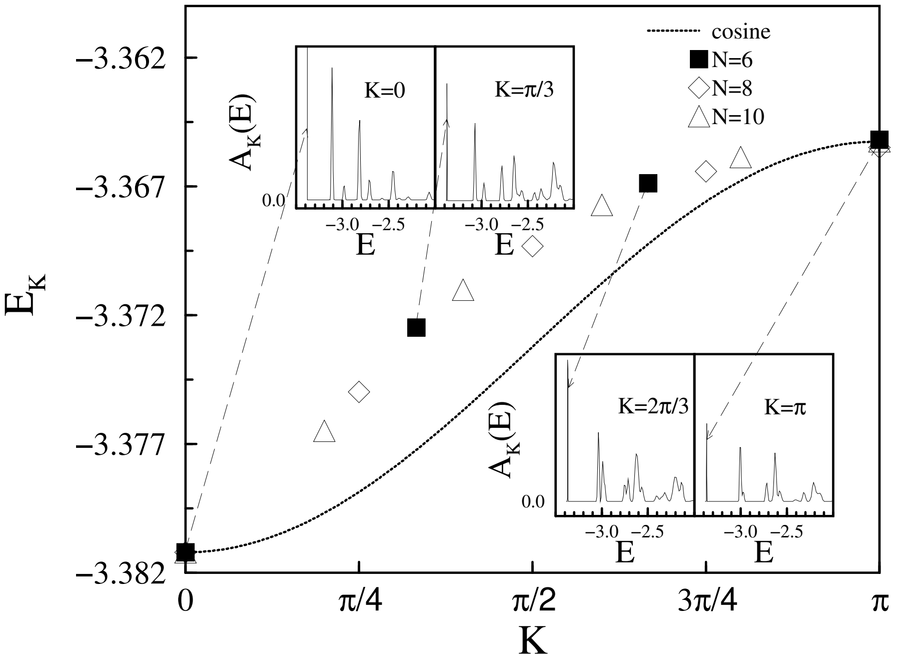

Figure 9.5: Band dispersion E_K of a single electron described by the Holstein model on 1D rings with N sites, where $\varepsilon_p = 3.0$ and $\hbar\omega = 0.4$. The insets show the low–energy part of the one–particle spectral function A_K(E) taken at the K–values indicated by arrows. The dotted line corresponds to the dispersion of a free particle with a renormalized bandwidth.

9.3 Two–electron case [414]

Next, we wish to discuss the two–electron problem in 1D. Here it is of special interest to understand in detail the conditions under which the two electrons form a bipolaron. Whether or not a transition to a bipolaronic state will occur depends sensitively on the competition between the short–ranged phonon–mediated, i.e., retarded ($\hbar\omega < \infty$), attraction ($\propto \varepsilon_p$) and the instantaneous on–site Hubbard repulsion ($\propto U$).

We start again with a discussion of the mobility of the particles. Fig. 9.6 (a) shows the strong (gradual) reduction of the effective *polaronic* transfer amplitude $t_{p,eff}$ as ε_p increases

---

[2] Of course, in the very high–energy regime the results for $A_K(E)$ can not be trusted just due to the errors induced by the necessary truncation of the phononic Hilbert space.

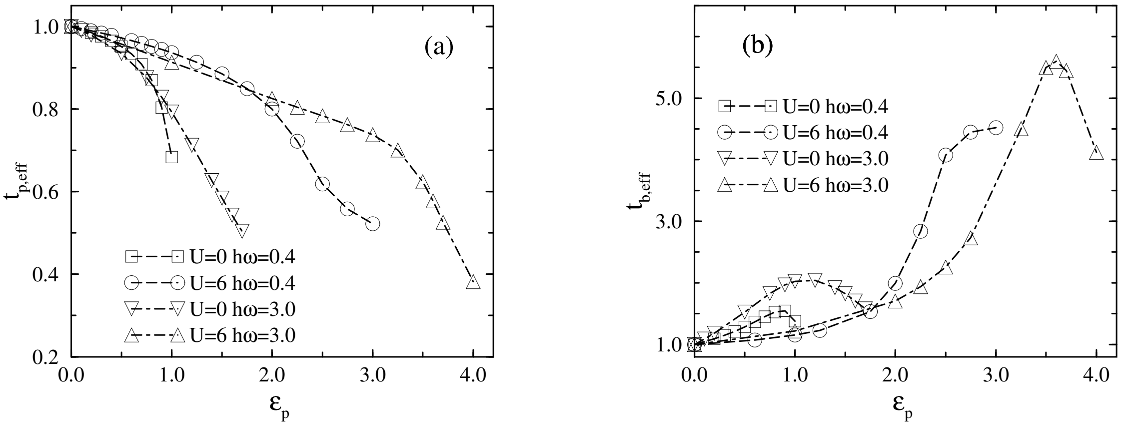

Figure 9.6: The effective polaron and bipolaron transfer amplitudes, $t_{p,eff}$ and $t_{b,eff}$, are shown as a function of the EP coupling strength ε_p in (a) and (b), respectively. The results are given for two electrons on the eight–site chain with $M = 21$ phonons using periodic boundary conditions.

in the adiabatic (non–adiabatic) regime. Now let us mainly focus on the physically more interesting regime of 'small' phonon frequencies, $\hbar\omega = 0.4$. In the case of vanishing Coulomb interaction $U = 0$ any finite EP interaction causes an effective on–site attraction between the electrons forming a bipolaronic bound state (remember, e.g., that $U_{eff} = \tilde{U} = U - 2\varepsilon_p$ follows from the simple Lang–Firsov approach). This means, in the pure Holstein model the state with two nearly free (large) polarons does not exist at least in one spatial dimension [431]. In the weak–coupling limit, the two–polaron state can, however, be stabilized by taking into account the on–site Coulomb repulsion. In this case, a crossover from a state of two mobile large polarons to an extended bipolaronic state occurs. The 'transition' will be shifted to larger EP couplings as U increases (see Fig. 9.6 (a)). For example, at $U = 6$ and $\hbar\omega = 0.4$ (3.0), we find that the binding energy of two electrons, $E_B^2 = E_0(2) - 2E_0(1)$, becomes negative at about $\varepsilon_p = 1.7$ (2.8). Further justification for this interpretation can be found from the behaviour of the effective bipolaronic transfer amplitude [451],

$$t_{b,eff} = E_{b,kin}(\varepsilon_p, U)/E_{b,kin}(0, U) \tag{9.8}$$

with

$$E_{b,kin}(\varepsilon_p, U)/t = -\sum_{<ij>} \langle \Psi_0(\varepsilon_p, U)|(c_{i\uparrow}^\dagger c_{i\downarrow}^\dagger c_{j\uparrow} c_{j\downarrow} + \text{H.c.})|\Psi_0(\varepsilon_p, U\rangle\,, \tag{9.9}$$

shown in Fig. 9.6 (b). $t_{b,eff}$ describes the coherent hopping of a on–site bipolaron from site i to site j. Contrary to $t_{p,eff}$, at low EP coupling strengths, the bipolaronic hopping amplitude $t_{b,eff}$ *grows* with increasing ε_p showing the increasing importance of the correlated motion of two electrons (but, quite clearly, we have $|E_{b,kin}| < |E_{p,kin}|$). At large EP couplings (e.g., for $\varepsilon_p \gtrsim 1$ at $U = 0$ and $\hbar\omega = 0.4$), the on–site bipolaron becomes more and more localized and accordingly we observe a drop in $t_{b,eff}$ which corresponds to the drop in $t_{p,eff}$ in the case of one electron at the parameter values where the AHP becomes stable. Hence we will call this quasiparticle an adiabatic Holstein bipolaron (AHBP).

To better illustrate the effect of pair formation in the 1D Holstein (Hubbard) model, we present in Fig. 9.7 the electron–electron density correlation function

$$C_{el-el}(|i-j|) = \langle \Psi_0(\varepsilon_p, U)|n_i n_j|\Psi_0(\varepsilon_p, U)\rangle - \langle \Psi_0(0, U)|n_i n_j|\Psi_0(0, U)\rangle \tag{9.10}$$

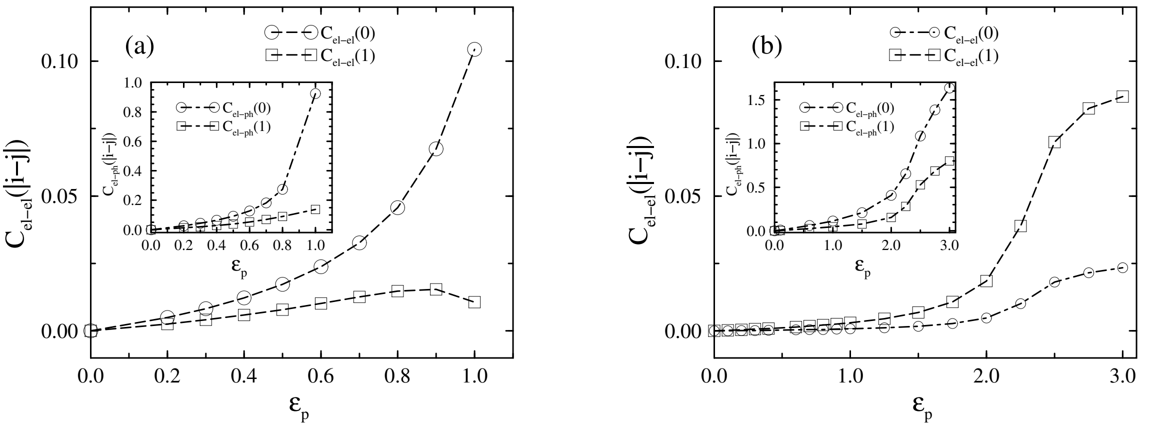

Figure 9.7: Electron–electron [electron–phonon] correlation function C_{el-el} [C_{el-ph} (inset)] *vs* ε_p at $\hbar\omega = 0.4$ for $U = 0$ (a) and $U = 6$ (b).

in the adiabatic regime with and without Hubbard repulsion. In each case we have displayed the results for $C_{el-el}(|i-j|)$ as a function of ε_p in comparison to the electron–phonon correlation function $C_{el-ph}(|i-j|)$ given by (9.6). As Fig. 9.7 (a) shows, in the limit of vanishing Coulomb interaction the on–site electron–electron correlation $C_{el-el}(0)$ dominates the inter–site correlations $C_{el-el}(|i-j|)$ with $|i-j| \geq 1$, in particular for $\varepsilon_p \gtrsim 0.9$, i.e., in the AHBP regime where both electrons are mainly confined to the same site sharing a common lattice distortion. Therefore the transition from a mobile large bipolaron to a 'quasi–self–trapped' on–site AHBP is manifest in a strongly enhanced $C_{el-ph}(0)$ as well (see inset). Moreover, the transition should be associated with a significant reduction of the local magnetic moment, $m_{loc}(\varepsilon_p, U) \propto \langle \Psi_0 | (n_{i\uparrow} - n_{i\downarrow})^2 | \Psi_0 \rangle$, indicating the local pairing of spin up and down electrons. Indeed we found $m_{loc}(\varepsilon_p = 1)/m_{loc}(\varepsilon_p = 0.9)|_{U=0,\hbar\omega=0.4} = 0.66$. As can be seen from Fig. 9.7 (b), a somewhat different scenario emerges in the presence of a finite Coulomb interaction. Here, the Hubbard repulsion prevents the formation of an on–site bipolaronic bound state in the weak EP coupling regime. On the other hand, as recently pointed out by Marsiglio [464], the retardation effect of the EP interaction may favour the formation of more extended pairs. That is, due to the time–delay the second electron can take the advantage of the lattice distortion left by the first one still avoiding the direct Coulomb repulsion. In fact, increasing the EP interaction, we find that both the nearest–neighbour electron–electron and electron–phonon density correlations starts to rise, while the on–site correlations remain small (cf. Fig. 9.7 (b)). Consequently, we may label this state an adiabatic inter–site bipolaron. We expect that at larger values of ε_p the short–range EP interaction overcomes the Hubbard repulsion and as a result the two electrons coalesce on a single site forming an 'self–trapped' bipolaron. Unfortunately we are unable to increase the dimension of the Hilbert space to contain a large enough number of phonons in the adiabatic very strong–coupling regime.

As already mentioned for the one–electron case, the description of the self–trapping phenomenon requires the inclusion of multi–phonon states. This is clearly displayed in Fig. 9.8, where we have shown the weight of the m–phonon state in the ground state for various EP coupling strengths. One sees immediately that the maximum of $|c^m|^2$ is rapidly shifted to larger values of m as ε_p increases. Increasing the phonon frequency at fixed ε_p, this tendency is reversed (see inset). In the extreme antiadiabatic limit we have $m_{max} = 0$ and the binding disappears for $U > 2\varepsilon_p$.

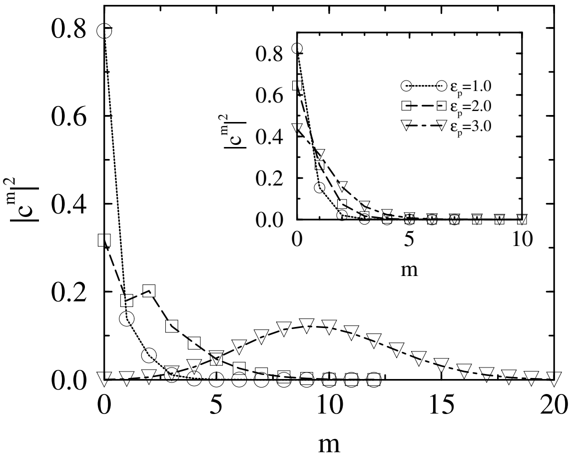

Figure 9.8: Weight of the m–phonon state in the two–electron ground state of the Holstein Hubbard model, where $U = 6$ and $\hbar\omega = 0.4$ [$\hbar\omega = 3$ (inset)].

As in the case of one electron it is interesting to look at the low–lying excitations of the inter–site bipolaron. Although we do not have a clear definition as to the momentum of this compound particle, it turns out that we indeed find a well–separated energy band if we again classify the lowest energy eigenvalues with respect to the allowed K–states of our finite system (see Fig. 9.9). Surprisingly the dispersion of this 'quasiparticle' band becomes exactly like that

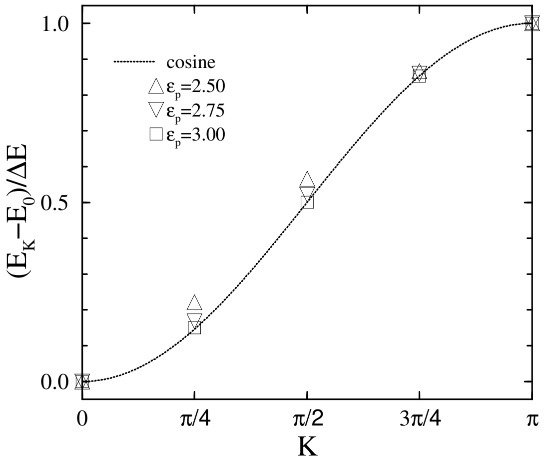

Figure 9.9: The lowest eigenvalues E_K for the two–electron case on the eight–site chain, where $\hbar\omega = 0.4$ and $U = 6$. The energy band is given in units of the coherent bandwidth $\Delta E = 0.0481$, 0.0217, and 0.0190 for $\varepsilon_p = 2.5$, 2.75, and 3.0, respectively.

of a free particle (with a renormalized bandwidth) at $\varepsilon_p = U/2$.

Of course, the exact results presented in this chapter hold for the Holstein Hubbard model with one and two electrons on *finite* one–dimensional systems, i.e., we are not prepared to prove any *rigorous* statements about the thermodynamic limit here. However, we believe that our main conclusions, concerning (i) the continuous nature of the transition from large–size nearly free polarons to 'quasi–localized' adiabatic Holstein polarons and (ii) the existence of well–separated polaronic and bipolaronic quasiparticle bands even in the adiabatic strong–coupling regime, will survive in the infinite system and $D > 1$.

9.4 Comparison with variational Lanczos results [359]

In this section the applicability of the various variational treatments of the phonon subsystem described in Sec. 8.1 to the Holstein Hubbard Hamiltonian is discussed. In particular, we demonstrate that the IMVLF approach combined with Lanczos diagonalization of the resulting effective Hamiltonian is in good agreement with the exact solution in adiabatic and non–adiabatic regimes, for a wide range of EP coupling strength.

Applying the IMVLF scheme (8.1)–(8.4) to the Holstein Hubbard model and performing the average (8.11) over the phonon vacuum, we are left with the effective electronic Hamiltonian $\overline{\mathcal{H}}_{H-H}(\bar{\gamma},\gamma,\tau^2,\{\Delta_i\})$ (cf. Eq. (8.12)). In order to investigate the ground–state properties of $\overline{\mathcal{H}}_{H-H}$ we use a Lanczos diagonalization technique, where according to Hellmann–Feynman's theorem the ground–state energy $\overline{E}_0(\bar{\gamma},\gamma,\tau^2,\{\Delta_i\})$ and wave–function $|\Psi_{el}(\bar{\gamma},\gamma,\tau^2,\{\Delta_i\})\rangle$ can be obtained by iteratively solving the following set of self–consistency equations:

$$\bar{\gamma} = (1-\gamma)\,n\,, \quad \tilde{\lambda} = -\bar{\gamma}\,, \tag{9.11}$$

$$\gamma = \frac{\hbar\omega\,[n(1-n)+2E_U - E_{\Delta n}/2\varepsilon_p]}{\hbar\omega\,[n(1-n)+2E_U] - \tau^2 E_t}\,, \tag{9.12}$$

$$\tau^2 = \frac{\hbar\omega}{\sqrt{\hbar^2\omega^2 - 4\varepsilon_p\gamma^2 E_t}}\,, \tag{9.13}$$

$$\Delta_i = 2\varepsilon_p(1-\gamma)(\langle n_i\rangle - n)\,. \tag{9.14}$$

Note that each iteration step involves the exact diagonalization of $\overline{\mathcal{H}}_{H-H}(\bar{\gamma},\gamma,\tau^2,\{\Delta_i\})$. Since the free spatial variation of the displacement fields Δ_i in general breaks the translation invariance, we have to work with an unsymmetrized basis set of many–particle states. In (9.11) to (9.14),

$$E_t = -\frac{\rho t}{N}\sum_{\langle ij\rangle\sigma}\langle(c_{i\sigma}^{\dagger}c_{j\sigma} + \mathrm{H.c.})\rangle\,, \tag{9.15}$$

$$E_U = \frac{1}{N}\sum_i\langle n_{i\uparrow}n_{i\downarrow}\rangle\,, \tag{9.16}$$

$$E_{\Delta n} = \frac{1}{N}\sum_{i\sigma}\langle\Delta_i n_i\rangle\,, \tag{9.17}$$

and n ($\langle n_i\rangle$) denote the kinetic, electron–electron, (static) electron–phonon contribution to the ground–state energy, and the mean (local) electron density ($\langle n_i\rangle$), respectively, where

$$\langle\ldots\rangle = \langle\Psi_{el}(\bar{\gamma},\gamma,\tau^2,\{\Delta_i\})|\ldots|\Psi_{el}(\bar{\gamma},\gamma,\tau^2,\{\Delta_i\})\rangle\,. \tag{9.18}$$

Figure 9.10 displays the band renormalization, $t_{p,eff} = E_t(\varepsilon_p,U)/E_t(0,U)$, and the ground–state energy E_0 of the one–electron Holstein model in *two dimensions*. Exact results are compared with the approximative ones as a function of EP coupling strength at two characteristic phonon frequencies, corresponding to the adiabatic ($\hbar\omega = 0.4$) and non–adiabatic regimes ($\hbar\omega = 3.0$). Besides the IMVLF–Lanczos method we have used the uniform variational Lang–Firsov transformation (UMVLF; $\Delta_i = 0$) and the usual Lang–Firsov transformation (LF; $\Delta_i = 0$, $\tau^2 = 1$, $\gamma = 1$, $\bar{\gamma} = 0$) to calculate $t_{p,eff}$ and E_0 on a ten–site cluster.

As follows from the comparison there is an overall qualitative agreement of the IMVLF–Lanczos approach with exact results in the weak– and strong–coupling cases. In particular,

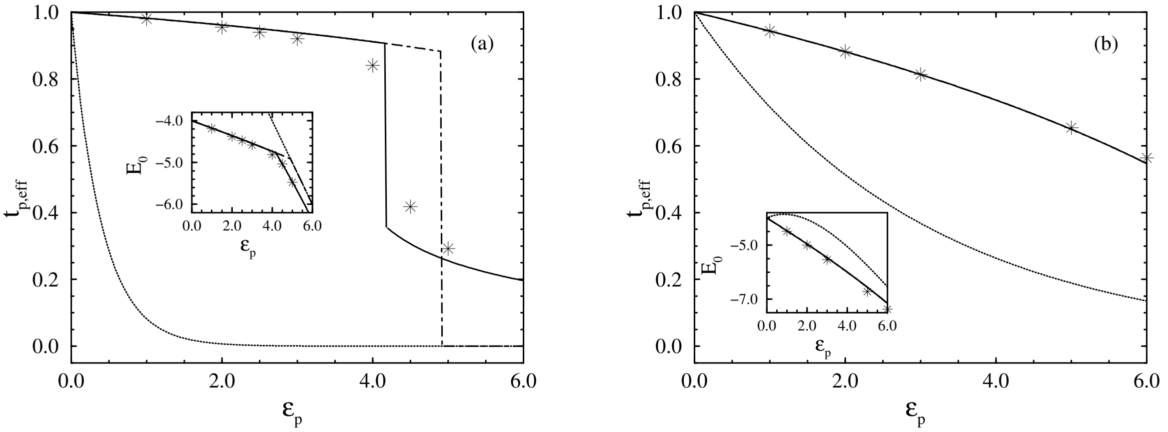

Figure 9.10: Effective hopping amplitude $t_{p,eff}$ and shifted ground–state energy $E_0 = E_{tot} - N\hbar\omega/2$ (inset) as a function of EP coupling ε_p for the 2D single–electron Holstein model at $\hbar\omega = 0.4$ (a) and $\hbar\omega = 3.0$ (b). Exact results for the ten–site square lattice (stars) are compared with approximative solutions based on the IMVLF (solid curve), UMVLF (chain dashed curve) and LF (dotted curve) transformations, respectively.

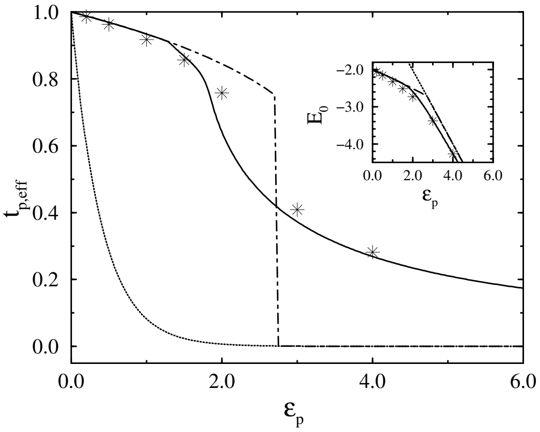

Figure 9.11: $t_{p,eff}$ and E_0 *vs* ε_p for the 1D single–electron Holstein model on a ten–site ring at $\hbar\omega = 0.4$ (a). The notations are the same as in Fig. 9.10.

the IMVLF theory is able to describe the formation of the self–trapped AHP state in the adiabatic strong–coupling regime, where both LF and UMVLF canonical transformations are bad approximations to the true ground state. It is worthwhile to point out that the simple LF/UMVLF approximations in that case give a polaronic band narrowing which is three orders of magnitude too large $t_{p,eff} = \rho \sim 10^{-4}$ (cf. Sec. 8.4). In fact, the structure of the exact ground state deviates considerably from that of a band of extremely heavy Lang–Firsov–type polarons.

It is also interesting to note that the IMVLF–Lanczos approach reproduces to some extent the well–known differences between polaron formation in one and two dimensions. In 1D, we found a rather smooth transition from a large–size polaron (LP) to the AHP (cf. Fig. 9.11, and the the discussion of Fig. 9.12 below). Contrary, in the 2D case the transition becomes sharp, where, of course, the non–analytic jump–like behaviour is an apparent shortcoming of the variational approach. In the non–adiabatic regime, we obtain $\Delta_i = 0$, i.e., the IMVLF and UMVLF approaches coincide. At larger EP couplings, our variational Lanczos method, based on only two–phonon coherent states, yields too narrow a polaronic band, especially for the 1D case (see Ref. [359]). Although the squeezing phenomena weakens the mass renormalization inherent to the polaron effect to some extent (cf. the LF results), the inclusion of higher–order phonon processes is necessary to offset the strong polaronic band narrowing more completely.

Having established the power of the IMVLF–Lanczos method, we calculate, in a next step, the phase diagram of the one–electron Holstein model in 1D and 2D. Note that the size of the clusters that this technique can reach is large enough to exclude finite–size effects. For the 2D case the transition line, presented in Fig. 9.12, separates two main regimes, which correspond to 'delocalized' nearly free polarons (FP)[3] and 'quasi–localized' (AHP) states, respectively. Within our variational treatment, the transition is of first order. In accordance with recent results [415], we find a small metastability region just above the transition point, where the (metastable) FP state is separated by an energy barrier from the AHP state. In the 1D case the results differ from the 2D case essentially. Performing a finite–size analysis, it can be shown [450] that the FP state becomes unstable at any finite EP coupling. Instead we observe a large–size polaron (LP) in the weak–coupling regime, which continuously turns into a small–size polaron with increasing EP coupling. In this case, we identified the critical value of EP coupling with the minimum in the second derivative of the total energy with respect to ε_p. For $\varepsilon_p < \varepsilon_p^c$, the polaron density grows with increasing ε_p for several sites around the center of the polaron, whereas for $\varepsilon_p > \varepsilon_p^c$, the polaron density becomes enhanced at the central site $i = 0$ only as ε_p increases. To elucidate in 1D the different nature of polaronic states occurring in the adiabatic strong and weak EP coupling regimes, we present in the insets of Fig. 9.12 the variation of the displacement fields away from the central site $i = 0$ (where, the polaron

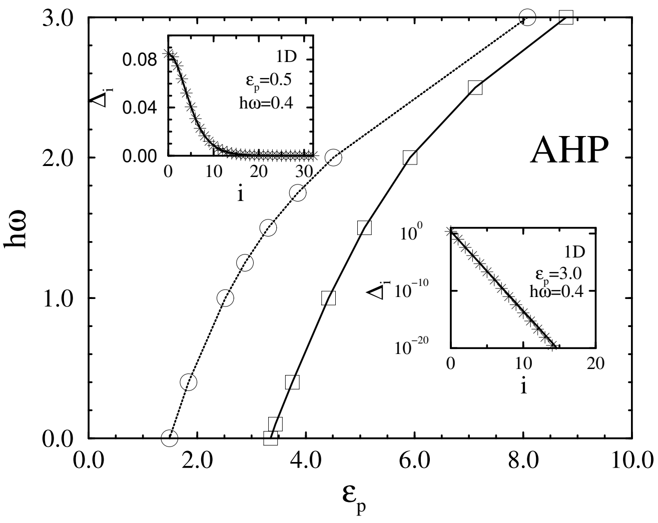

Figure 9.12: 'Phase diagram' of the 1D (2D) Holstein model with one electron, where the dotted (solid) line 'separates' the LP (FP) state at small ε_p from the self–tapped AHP at strong EP coupling. Results are obtained for finite lattices with $N = 64$ (1D, open circles) and $N = 256$ (2D, open squares) sites using the IMVLF–Lanczos method. The insets show the variation of the displacement fields Δ_i away from the central site $i = 0$ for two characteristic parameter values (ε_p, $\hbar\omega$) corresponding to different types of polaronic states in the 1D case.

---

[3] We use the abbreviation FP to distinguish the quasi–free polaron state in 2D from the corresponding large–polaron state in 1D.

is assumed to be located). For the large–size polaron, the lattice displacements fits extremely well to the functional form

$$\Delta_i = a_0 \, \mathrm{sech}^2(a_1 \cdot i) \tag{9.19}$$

(cf. the solid curve in Fig. 9.12 (upper inset)), where $(2a_1)^{-1}$ defines the polaron radius and the distances i are measured in units of the lattice constant a. It should be emphasized that the result (9.19) was derived more recently within an alternative approach to polaron formation in 1D based on the solution of an nonlinear Schrödinger equation [468]. In contrast, we obtain for the AHP an exponential decay of the lattice distortions,

$$\Delta_i = \Delta_o \, \mathrm{e}^{-i/\xi} \,, \tag{9.20}$$

away from the polaron site (see Fig. 9.12 (lower inset)). Here, ξ denotes the radius of the small–size polaron. We found $\xi \sim 0.3$, i.e., for large ε_p the self–trapped AHP is confined to a single lattice site.

Finally, we consider the 1D Holstein Hubbard model with two electrons. First, we would like to point out that the main features of the two–electron problem (e.g., the tendency to bipolaron formation) can be described adequately within our IMVLF scheme. In particular, as can be seen from the comparison of the IMVLF results with the exact data for ground–state energy and polaronic band renormalization presented in Fig. 9.13, the IMVLF–Lanczos method provides a satisfactory estimate for both E_0 and $t_{p,eff}$ in a wide coupling region including the adiabatic strong–coupling case. Obviously, we can distinguish three different regimes. For small ε_p, the ground state resembles that of two nearly free polarons. The nearly–free polaron state is stabilized by the on–site Coulomb repulsion and, in 1D, does not exist for $U = 0$ [431]. As ε_p exceeds a critical value, the binding energy of two electrons becomes negative and at $\varepsilon_p \sim 2.5$ a transition to an extended bipolaronic state takes place. Here, the nearest–neighbour density–density correlation function $C_{el-el}(1)$ exhibits a pronounced maximum. When $\tilde{U}$ becomes negative, the electron pair is tightly bound on the same site forming an on–site adiabatic Holstein bipolaron (AHBP). In fact, we find for $\varepsilon_p = 3.5$ a large negative binding energy $E_B^2 = -0.903$ (-0.911; IMVLF). Increasing the phonon frequency, the intermediate inter–site bipolaronic state is smeared out and the crossover to the on–site AHBP is shifted to larger values of the EP coupling [359].

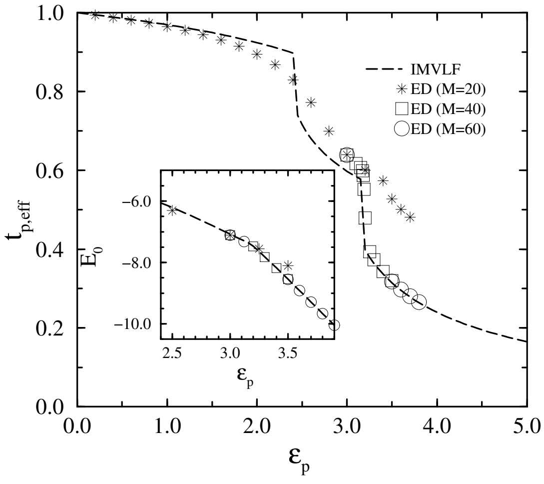

Figure 9.13: Effective hopping amplitude $t_{p,eff}$ and ground–state energy E_0 (inset) *vs* ε_p for the 1D Holstein Hubbard model with two electrons on a four–site ring. Exact results with M phonons are compared with the IMVLF–Lanczos approach for $U = 6$ and $\hbar\omega = 0.4$. Note that the IMVLF results do not change qualitatively if we increase the size of the system (using direct ED we are unable to reach the AHBP regime even for the $N = 8$ (see 9.6 (a)).

Chapter 10

Variational Lanczos study of the 2D Holstein t–J model

Whereas the electronic properties of the pure t-J model have been extensively studied in the context of high–T_c superconductivity, very little is known theoretically about the interplay between electron–phonon coupling and antiferromagnetic exchange interactions in the framework of the 2D Holstein t–J model. For example, in view of the strong correlations in the AFM spin background, the dynamics even of a single dopant–induced hole coupled to lattice phonons becomes much more complex than the corresponding uncorrelated (spinless–fermion) problem. As yet, there exist no well–controlled analytical techniques to analyze hole–polaron formation or possible (local) phonon–driven charge instabilities in such systems exhibiting both strong Coulomb and EP interactions. In principle, the direct exact diagonalization method, as applied to discuss (bi)polaronic features of a few charge carriers in terms of the Holstein Hubbard model in the preceding chapter, can close this gap for the Holstein t–J model as well. Here, however, one usually works near half–filling, i.e., the electronic basic is very large from the outset, and hence memory limitations impose severe restrictions on the phononic Hilbert space truncation method, in particular in the low–frequency strong–coupling regime, where a large number of phonon states is required.

In order to obtain results at higher electron densities and to access the complete range of phonon frequencies and EP couplings, in this chapter we will employ a numerical technique which combines exact Lanczos diagonalization with a variational treatment of the phonon system. First, we explore the ground–state properties of the 2D Holstein t–J model in the adiabatic limit using the frozen–phonon approximation. In a next step, the phonon dynamics is incorporated by an inhomogeneous modified variational Lang–Firsov transformation.

10.1 Adiabatic limit: Frozen–phonon approach [443, 469]

10.1.1 Model and methodology

The electron–phonon Hamiltonian considered in this section is

$$\mathcal{H} = \frac{K}{2} \sum_i \Big((\bar{\Delta}_i^x)^2 + (\bar{\Delta}_i^y)^2 \Big) - \bar{\lambda} \sum_i \bar{\Delta}_i \, \tilde{n}_i + \mathcal{H}_{t-J} \, , \tag{10.1}$$

where $\mathcal{H}_{t-J}$ denotes the standard t–J model (2.7) with nearest–neighbour transfer t and antiferromagnetic exchange J on a square lattice. The first and second terms of $\mathcal{H}$ represent the elastic energy of a harmonic lattice and the electron–phonon coupling, respectively. Those

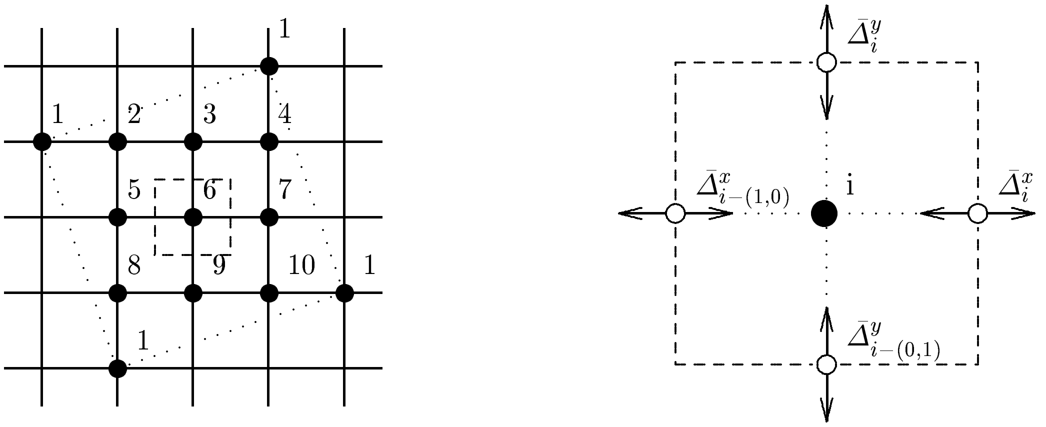

Figure 10.1: Left panel: Tilted effective ten–site cluster used in this work, where periodic boundary conditions are applied at the dotted lines. Right panel: Definition of the harmonic lattice distortions $\bar{\Delta}_i^{x,y}$ for a single CuO$_4$ unit (broken square). The solid and open circles represent copper and oxygen respectively.

terms are treated classically within the adiabatic limit, i.e., the electronic system is coupled locally to *static* lattice distortions. Modelling the in–plane lattice vibrations of the nickel/copper oxides, the collective Holstein coordinates $\{\bar{\Delta}_i\}$ describe the bond–parallel oxygen lattice displacements shown Fig. 10.1. In this case, we have

$$\bar{\Delta}_i = \bar{\Delta}_i^x - \bar{\Delta}^x_{i-(1,0)} + \bar{\Delta}_i^y - \bar{\Delta}^y_{i-(0,1)}\,, \tag{10.2}$$

and the effect of the EP coupling ($\bar{\lambda}$) is that holes tend to move to sites where the oxygen atoms are displaced towards the nickel/copper site (cf. the discussion in Sec. 7.2). Rescaling $\bar{\lambda}\bar{\Delta}_i^{x,y} \to \Delta_i^{x,y}$ we introduce the dimensionless coupling constant $\lambda = \bar{\lambda}^2/K$ (in units of t).[1] Whereas the physics of the Holstein Hubbard model is dominated by a (π,π) CDW instability (near half–filling and at not too large Hubbard interaction; see Sec. 8.3) [403, 179, 177], the CDW state becomes suppressed in the Holstein t–J model at least at low doping level. Therefore in our model the phonon system is mainly coupled to the doped charge carriers (holes) and as a result we expect the formation of local lattice distortions, such as hole–(bi)polarons.

To investigate the ground–state properties of the adiabatic Holstein t–J model one needs to find those lattice distortions $\{\Delta_i^{x,y}\}$ that minimize the variational energy. Using the Hellmann–Feynman theorem, $\partial_{\Delta_i^{x,y}} \langle \Psi\left(\{\Delta_i^{x,y}\}\right) | \mathcal{H} | \Psi\left(\{\Delta_i^{x,y}\}\right)\rangle = 0$, we obtain

$$\Delta_i^{x,y} = \lambda\left(\langle \tilde{n}_i\rangle - \langle \tilde{n}_{i+(x,y)}\rangle\right) \tag{10.3}$$

with $\langle \tilde{n}_i\rangle = \langle \Psi\left(\{\Delta_i^{x,y}\}\right) | \tilde{n}_i | \Psi\left(\{\Delta_i^{x,y}\}\right)\rangle$. We solve this set of $2N$ equations iteratively, where each iteration step involves the diagonalization of the sparse Hamiltonian matrix by means of a Lanczos algorithm which only needs matrix vector multiplications as the basic ingredient.

---

[1] Since the elastic energy in (10.1) is defined in a somewhat different way (compared to Sec. 7.2, Chap. 8, and Sec. 10.2 below), in this section we will use λ, instead of ε_p, to denote the rescaled dimensionless EP coupling constant. No confusion should arise over these different notations.

Since the possible spatial variation of the $\{\Delta_i^{x,y}\}$ breaks translational invariance, we can not use momentum as a good quantum number to reduce the size of the Hamiltonian matrix. For the largest system sizes considered, $N = 16$, and for six holes, we are left with a matrix of dimension 2 018 016 in the total $S^z = 0$ subspace. The state vectors are stored through a variant of a multi–spin coding technique [470].

Having obtained the ground state and the corresponding lattice distortions $\{\Delta_i\}$, in some cases one may be interested in calculating the whole spectrum of the Hamiltonian for this *fixed* set of $\{\Delta_i\}$. Since it is impossible to find all the eigenvalues of a mega–dimensional matrix exactly, we use a method, proposed by Silver and Röder [467], that gives a polynomial approximation to the *many–particle* density of states $N(E)$. Doing this, one expands $N(E) = \sum_n \delta(E - E_n) = \lim_{M\to\infty} \sum_s^M \mu_s^P P_s(E) w_s^P$, where $P_s(x)$ are orthogonal polynomials with $\int dx P_s(x) P_{s'}(x) = w_s^P \delta_{s,s'}$. The polynomial moments μ_s^P are given by $\mu_s^P = \int dE N(E) P_s(E) = \sum_n P_s(E_n) = \mathrm{Tr}\{P_s(\mathcal{H})\}$. The trace can approximately be obtained as follows: One chooses a random vector of unit norm $|\varPsi^R\rangle$ such that $|\varPsi^R\rangle = \sum a_n |n\rangle$ with the a_n drawn from a normal distribution. Averaging over independent sets of those vectors gives $[\langle\varPsi^R|P_s(\mathcal{H})|\varPsi^R\rangle] = \sum_n [a_n^2] P_s(E_n) = \mathrm{Tr}\{P_s(\mathcal{H})\}$, where $[\ldots]$ stands for an average over realizations. Of course, one can only compute a finite number of moments, therefore the sum over polynomials must be truncated at a finite value of M. This leads to the well–known Gibbs phenomenon and causes ringing in the density of states. To reduce this effect we use Gibbs damping factors [467]. The resolution along the energy axis depends on the number of moments. We found that 600 moments are plenty to describe the gross features of our spectra. The error caused by the randomness of $|\varPsi^R\rangle$ goes as $\bar{D}^{-1}$ [467], where $\bar{D}$ is the dimension of the matrix. So for the large matrices we have, it is sufficient to consider only one random vector.

The quantities of interest are the ground–state energy (E), the local expectation values of spin $(\langle S_i^z\rangle)$ and charge $(\langle\tilde{n}_i\rangle)$ density, the local lattice distortions $(\varDelta_i)$, and the 'averaged' displacement

$$\varDelta = \frac{1}{N}\sum_{i=1}^{N} |\varDelta_i| \ , \tag{10.4}$$

which plays the role of an 'order' parameter separating ground states with finite lattice distortion $(\varDelta \neq 0)$ from uniform states $(\varDelta = 0)$. Moreover, we calculate the (equal–time) spin and charge correlation functions, $\langle S_i^z S_j^z\rangle$ and $\langle\tilde{n}_i\tilde{n}_j\rangle$, as well as the related (Fourier–transformed) density and magnetic structure factors,[2] $S_{c,s}(\vec{q}) = S_{c,s}(\vec{q}, -\vec{q})$, where

$$\begin{aligned} S_c(\vec{q},\vec{q}\,') &= \frac{1}{N}\sum_{i,j} \langle\tilde{n}_i\tilde{n}_j\rangle \, \mathrm{e}^{i\vec{q}(\vec{R}_i-\vec{R}_j)} \mathrm{e}^{i(\vec{q}+\vec{q}\,')\vec{R}_j} \ , & (10.5)\\ S_s(\vec{q},\vec{q}\,') &= \frac{1}{N}\sum_{i,j} \langle S_i^z S_j^z\rangle \, \mathrm{e}^{i\vec{q}(\vec{R}_i-\vec{R}_j)} \mathrm{e}^{i(\vec{q}+\vec{q}\,')\vec{R}_j} \ . & (10.6) \end{aligned}$$

10.1.2 Numerical results

Let us now present our numerical results for the ground–state phase diagram of the 2D Holstein t–J model in the adiabatic limit. We start with the case of one hole, for which the phase diagram is shown in Fig. 10.2. We can distinguish two main regimes, referred to below as the FP [nearly free (hole) polaron] and AHP [adiabatic Holstein (hole) polaron] state, respectively. In the first state, which may be also called the 'delocalized' phase [463, 471], the ground state

---

[2] Note that the lack of full translational invariance means that $S_{c,s}(\vec{q},\vec{q}\,')$ will in general depend on two discrete momenta in our finite–cluster calculation. Thus, we are restricted to the N allowed $\vec{q}$–vectors of the $\sqrt{N}\times\sqrt{N}$ lattice (see Fig.3.1), and $\vec{q}\,' = -\vec{q}$.

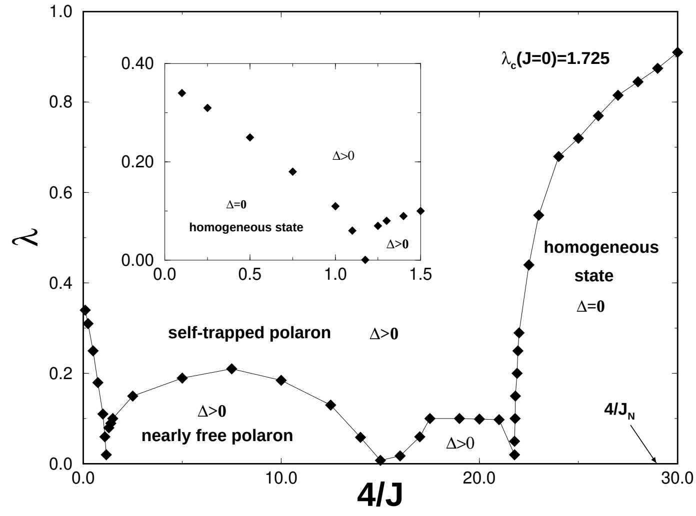

Figure 10.2: Phase diagram of the 2D Holstein t–J model with one hole on a $N = \sqrt{10} \times \sqrt{10}$ lattice. The inset shows an enlargement of the region with strong antiferromagnetic exchange coupling J.

of the Holstein t–J model is essentially the same as in the pure t–J model ($\lambda = 0$). Here, i.e. for small λ, the occurrence of a finite averaged lattice distortion Δ depends on the symmetries of the electronic part of the ground–state wave–function which in turn depends strongly on the interaction strength (J) as well as on the system size (N) (cf., e.g., Table 3.1 in Sec. 3.1.2). If this ground state carries a finite momentum, the lattice is forced into a structure which is compatible with the non–trivial symmetry of the electronic wave–function.[3] Obviously, the FP state reflects the transitions between states with non–trivial $\vec{K}$–values (here the local electron densities $\langle \tilde{n}_i \rangle$ are inhomogeneous even for $\lambda = 0$ and $\Delta \neq 0$ is possible) and an uniform phase with $\vec{K} = (0,0)$ or (π,π) ($\langle \tilde{n}_i \rangle = n$) and $\Delta = 0$. The same qualitative behaviour was found for the 16– and 18–site lattice [463], but of course, the location of the transition to the homogeneous undistorted phase is strongly finite–size dependent. In the 'delocalized' state with finite Δ we observe at the largest possible distance *two* 'hole–sites' which corresponds to the translational symmetry of the ground state. For example, at $J = 0.8$ and $\lambda = 0.1$, we have $\langle \tilde{n}_i \rangle = 0.727$ ($i = 1, 6$) and $\langle \tilde{n}_i \rangle = 0.943$ ($i \neq 1, 6$) for the ten–site lattice [443] (see also Table 10.1 in Sec. 10.2.1). In fact, however, the charge–density fluctuations are rather small. On the other hand, the spin density is mainly concentrated at the 'hole–sites'; here we find $\langle S_i^z \rangle = 0.408$ ($i = 1, 6$), whereas $\langle S_i^z \rangle = 0.023$ at the 'electron–sites' ($i \neq 1, 6$). The nearest–neighbour spin correlations $\langle S_i^z S_j^z \rangle < 0$ indicate antiferromagnetic short–range order $\forall \langle ij \rangle$.

Increasing the EP coupling λ at fixed J a 'self–trapping' transition of the hole takes place. At λ_c, $E(\lambda)$ shows a discontinuity in slope and the order parameter Δ jumps by a finite amount reflecting the fact that the distributions of $\langle \tilde{n}_i \rangle$, $\langle S_i^z \rangle$, and $\langle S_i^z S_j^z \rangle$ are different in both phases (see Fig. 10.3). As a result we found a numerical hysteresis, so one must carefully scan the J–λ plane to find out the true ground state. For large λ a strong local lattice distortion can trap the hole at a *single* site (AHP): $\langle \tilde{n}_1 \rangle = 0.142$ and $\langle \tilde{n}_i \rangle \simeq 0.97$-$0.99$ ($i \neq 1$) [$J = 0.8$, $\lambda = 0.8$, $N = 10$]. This leads to a substantial energy gain in E_{el-ph} (see Table 1 in Ref. [443]), therefore E is lowered despite the cost of elastic and kinetic energy. The variation of the $\langle \tilde{n}_i \rangle$ shows that the hole–trapping is accompanied by the occurrence of weak charge–density oscillations on the other sites which are reminiscent of a (π,π) CDW [443]. At the same time we observe a significant change in the spin correlations $\langle S_i^z S_j^z \rangle$. Whereas the local magnetic moment

---

[3] Since in the physically most interesting parameter regime of J the existence of a pocket–like hole Fermi surface for the infinite system is still a matter of debate, this point is not an academic one.

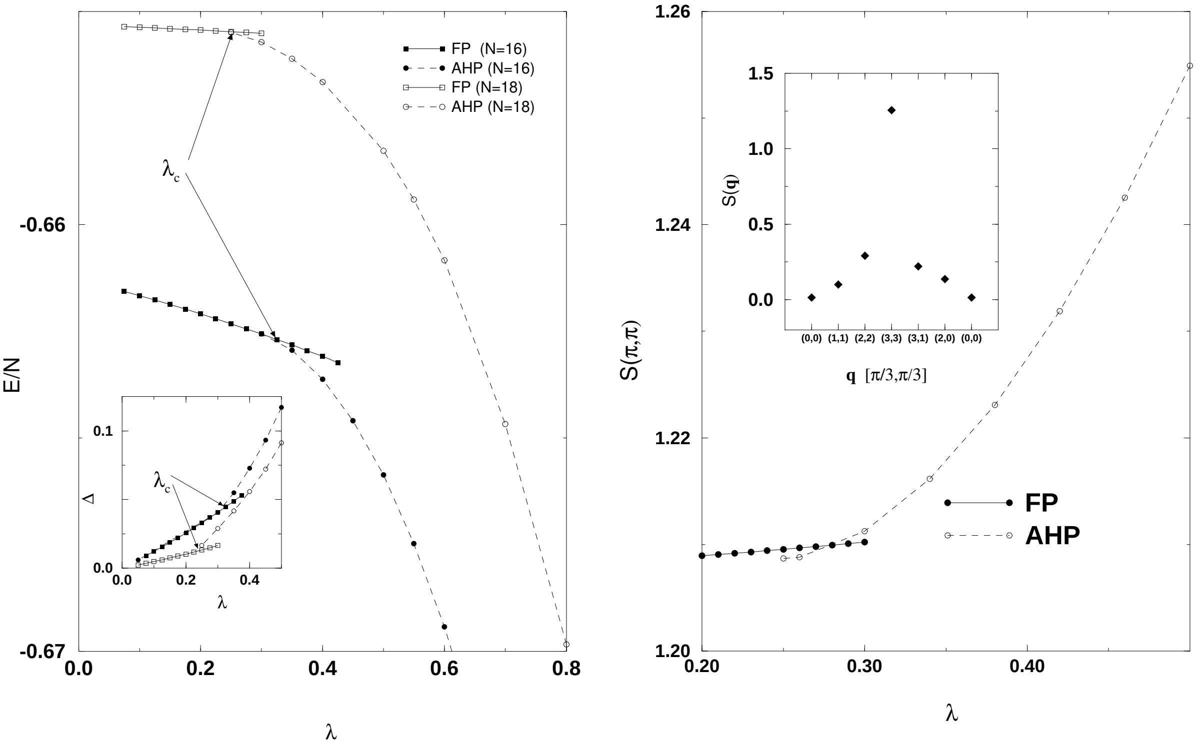

Figure 10.3: Left panel: Ground–state energy E of the single–hole Holstein t–J model and 'order parameter' Δ (inset) as a function of EP coupling strength λ at $J = 0.5$ for finite square lattices with 16 and 18 sites. The self–trapping transition takes place at λ_c. Right panel: Magnetic structure factor $S_s[(\pi,\pi)]$ *vs* λ at $J = 0.5$. The inset shows $S_s(\vec{q})$ for $\lambda = 0.5$ at the allowed inequivalent momenta of the 18–site lattice. All energies are measured in units of t.

on the 'hole–site' is coupled ferromagnetically to NN moments indicating the formation of a small ferromagnetic spin–polaron, the AFM correlations in the spin background become strongly enhanced. Note that now $\left|\langle S^z_{el-sites}\rangle\right| \gg \left|\langle S^z_{ho-site}\rangle\right|$. As can be seen from the inset of Fig. 10.3 (b), the magnetic structure factor $S_s(\vec{q})$ exhibits a pronounced peak at the AFM wave–vector (π,π). The curves obtained for $S_s[(\pi,\pi)]$ clearly indicate the transition to the AHP state: Increasing λ, the smooth variation of $S_s[(\pi,\pi)]$ in the FP state is followed by a strong enhancement in the quasi–localized hole state. Evidently, the hole–pinning favours the AFM structure of the bulk spin background and vice versa.

To demonstrate the effect of the electronic correlations on the 'self–trapping' transition, we have considered the case of spinless fermions ($S^z = S^z_{max}$) as well. For the one–hole case this can be mimicked by setting $J = 0$ (Nagaoka limit). Here we obtain a much larger critical λ, where the transition values $\lambda_c = 1.725$ ($N = 10$), 1.750 ($N = 18$), and 1.751 ($N = 20$) indicate a rather small finite–size dependence [463]. In addition, it is worthwhile to emphasize that the single hole (or equivalently a single electron) is not perfectly localized even at very large λ. Away from the 'hole–site', a small 'rest' of the hole density oscillates even in this limit in a way which corresponds to a (π,π) CDW [463].

The phase diagram for the two–hole case is displayed in Fig. 10.4. First let us briefly recapitulate the results at $\lambda = 0$. Here, for $4/J \leq 19.88$, the lowest energy state ($S = 0$) is five–fold degenerate, the momentum being one out of the star of $\vec{K} = (0,0), (2\pi/5, 4\pi/5)$. In

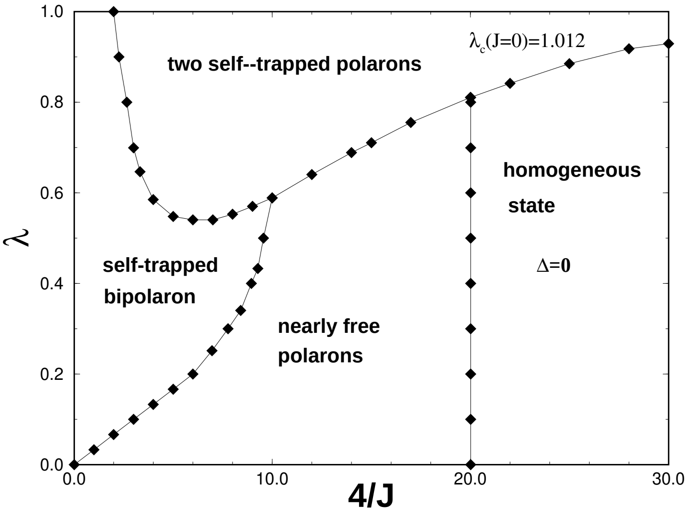

Figure 10.4: Ground–state phase diagram of the Holstein t–J model with two doped holes.

the region $4/J \geq 19.88$, the ground state is taken over by a state with $S = 0$ and $\vec{K} = (0,0)$. At finite EP coupling, we can distinguish again between a phase, where the holes are 'delocalized', and a 'self–trapped' state. Depending on the relative strengths of exchange interaction and EP coupling, the holes will be trapped, for large enough λ, as two single polarons (AHP) or as one adiabatic Holstein bipolaron (AHBP). In the context of the Holstein t–J model (remember that double occupancy is strictly forbidden), we use the term 'bipolaron' for the state, where the two holes are 'located' at adjacent sites sharing the same lattice distortion. There is a naive argument suggesting that different types of self–trapped states will exist: Two separate immobile polarons lose the antiferromagnetic exchange energy $2J$ on four bonds each, but can gain maximal trapping energy ($\sim E_{el-ph}$). On the other hand, two holes on neighbouring sites lose the exchange energy on only 7 bonds together, however, one displacement (e.g. $\Delta^x_{i-(1,0)}$) does not contribute to E_{el-ph} now. The net result, including the effect of delocalization energy, gives the phase boundary shown in Fig. 10.4. In the 'delocalized' regime, we obtain at intermediate values of J a FP state with finite Δ. Here the hole density is mainly concentrated at four sites, where always two sites are nearest neighbours. The particle densities are given for the different regimes in Table 1 of Ref. [443]. The transitions between 'delocalized' and 'localized' states are of first order. At $J = 0$, the self–trapping transition occurs at $\lambda_c = 1.01$, where the AHP state carries maximal total spin $S = S_{max}$. For any finite value of J, however, the ground state has $S = 0$.

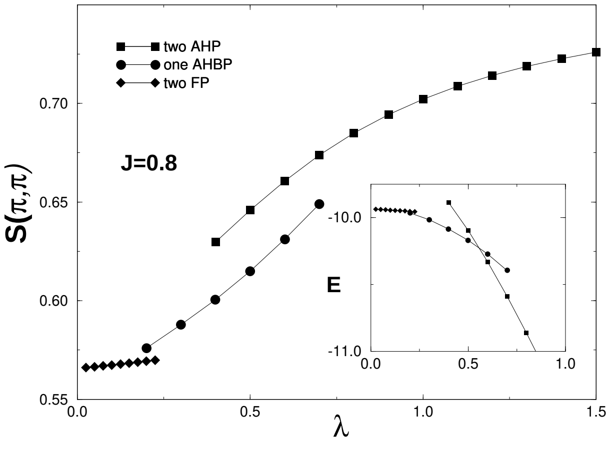

Figure 10.5: Magnetic structure factor $S_s[(\pi,\pi)]$ and ground–state energy E (inset) as a function of EP coupling strength λ at $J = 0.8$. For further explanation see text.

It is very instructive to investigate the behaviour of the magnetic structure factor $S_s(\vec{q})$, which for the pure t–J model exhibits a peak structure in the vicinity of the AFM wave–vector [472]. Our results, presented in Fig. 10.5 for $S_s[(\pi,\pi)]$ and $E(\lambda)$, clearly indicate a different nature of the hole states in the various phases. Increasing λ at fixed $4/J = 5$ we observe a jump–like enhancement at the self–trapping transition and a much stronger variation in the AHBP state. At still larger EP coupling strength a further first–order transition to the AHP state takes place. As mentioned Chap. 3 and 4, depending on the ratio of J/λ a ground state with two well–separated small polarons or with a self–trapped bipolaron (i.e., a 'hole–cluster') gives the lowest energy [443]. This result should be contrasted with the situation for the Holstein Hubbard model [358], where strong EP coupling always favours an *on–site* AHBP state (cf. Chap. 9).

Next, in order to look for the formation of a polaronic superlattice in the Holstein t–J model, we present results around quarter–filling. Due to limited computer resources it was not possible to map out a complete phase diagram for the 4×4 site lattice. Instead the parameter dependence of the Holstein t–J model at exactly quarter–filling is demonstrated for the ten–site lattice (see Fig. 10.6). Apart from two types of phase separated ground states (labelled PS1 and PS2) for unphysically large J, the phase diagram consists mainly of two phases separated by the line $\lambda_c(J)$. For small values of λ we find a FP ground state as observed in the one– and two–hole cases. For large values of λ we obtain a (π,π) CDW structure with a frozen–in lattice distortion (superlattice of self–trapped polarons).

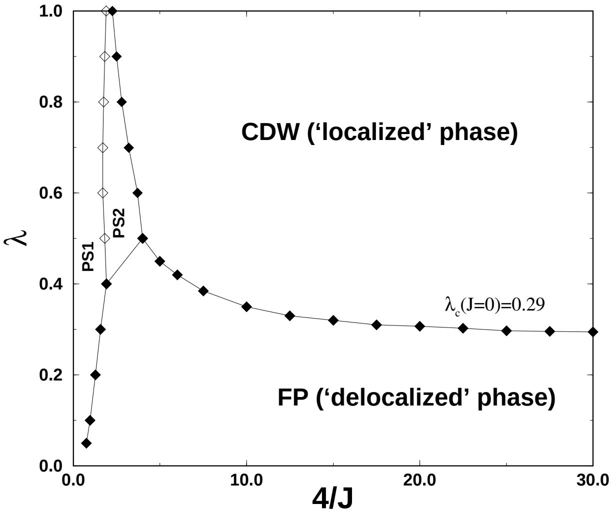

Figure 10.6: Phase diagram of the ten–site adiabatic Holstein t–J model at quarter–filling. CDW labels the phase with a polaronic superlattice, FP labels the phase that resembles the symmetries of the pure electronic system and PS1 and PS2 label two phase separated states.

Having established the existence of a polaronic superlattice in the ten–site Holstein t–J model for strong enough EP coupling, we shall now investigate this phase for the quarter–filled 4×4 site square lattice at $J = 0.4$ and $\lambda = 1$. At this filling fraction one obtains only two different values for the local electron densities: $\langle \tilde{n}_{2k+1} \rangle = 0.9366$ at the 'electron–sites' and $\langle \tilde{n}_{2k} \rangle = 0.0634$ at the 'hole–sites'. Note the small electron density at the 'hole–sites', which only goes to zero as λ goes to infinity. Using the polynomial moment approach [467] described briefly in Sec. 10.1.1 we study the basic excitations for this polaronic superlattice within the adiabatic approximation. In Fig. 10.7 (a) we show the many–body density of states in the CDW phase for the possible values of total S^z . The overall structure of $N(E)$ consists of a set of 'bands' above the ground state (labelled GS in Fig. 10.7 (a)) separated by gaps. Our interpretation is that the first band above the ground state contains states, where one electron is moved from an 'electron–site' to a 'hole–site', that the second band contains states, where

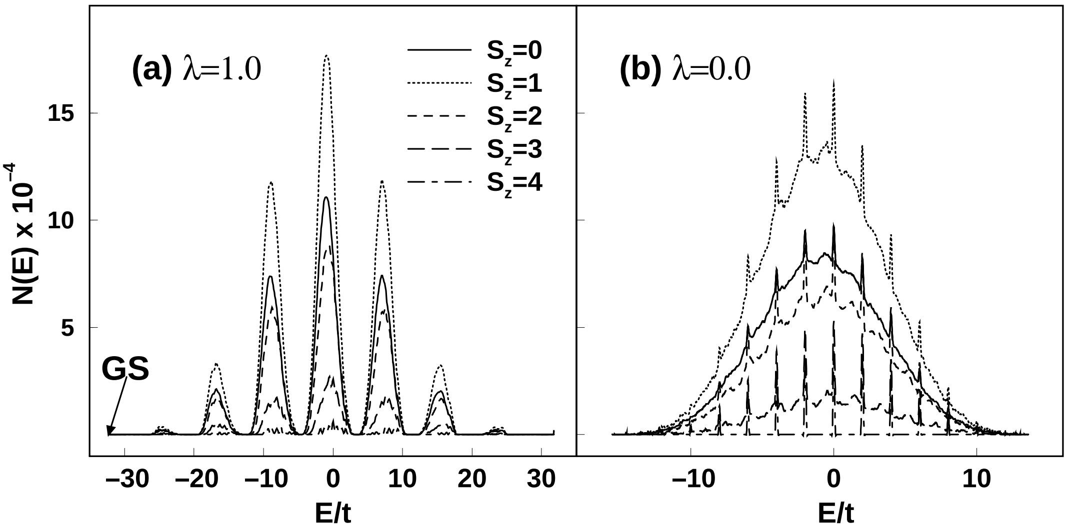

Figure 10.7: The many–body density of states $N(E)$ for the 16–site adiabatic Holstein t–J model at $J = 0.4$ and $\lambda = 1.0$ (a) and $\lambda = 0.0$ (b).

two electrons are moved from 'electron–sites' to 'hole–sites', and so on until all electrons are moved from 'electron–sites' to 'hole–sites' (of course the lattice distortion for highly excited states is extremely unstable, and the frozen–phonon approximation breaks down). When four electrons are moved to 'hole–sites', the bandwidth and the density of states are largest, because the maximum number of electrons can interact via the AFM exchange J, and the number of positions for the electrons to move to is maximum. When all electrons are on the 'wrong' sites, we get only one state again. We checked this interpretation by selectively calculating states at the edges of the various bands. This $N(E)$ should to be contrasted to the case of the purely electronic model, i.e. $\lambda = 0$, depicted in Fig. 10.7 (b), where $N(E)$ has no gaps. It is interesting that for the CDW phase the ground state is nearly degenerate with respect to S^z, i.e., the lowest eigenvalues for all of the different S^z subsectors are approximately at the value depicted by GS in Fig. 10.7 (a). As λ goes to infinity this degeneracy becomes exact. In contrast, in the purely electronic model the ground states for the different S^z sectors are well separated.

To study the stability of the polaronic superlattice *away* from quarter–filling we have calculated the ground state of the 4×4 site lattice at $J = 0.4$ and $\lambda = 1.0$ for all possible numbers of holes N_h (for $N_h = 5$ to $N_h = 11$ the on–site electron densities are given in Table 1 of Ref. [469]). At quarter–filling plus one hole ($N_h = 9$), one observes that one electron gets removed mainly from site 10 (for this configuration) and that the other sites remain to a large extent in the CDW state.[4] Adding one further hole ($N_h = 10$) has a similar effect. Now sites 7 and 10 become additional 'hole–sites'. For $N_h > 10$ the polaronic superlattice breaks down. Adding electrons to the quarter–filled system causes the opposite effect. For $N_h = 7$ site 11 is occupied by the additional electron, for $N_h = 6$ sites 11 and 6. The CDW–like polaronic superlattice disappears for $N_h < 6$. To illustrate the density and spin correlations in more detail we present in Fig. 10.8 the charge and magnetic structure factors, defined in Eqs. (10.5) and (10.6), as a function of the number of holes N_h at the allowed, non–trivial wave–vectors

---

[4] The sites of the 4×4 lattice are counted in such way that the top row contains sites $1 \ldots 4$ from left to right, the row one further down sites $5 \ldots 8$ and so on.

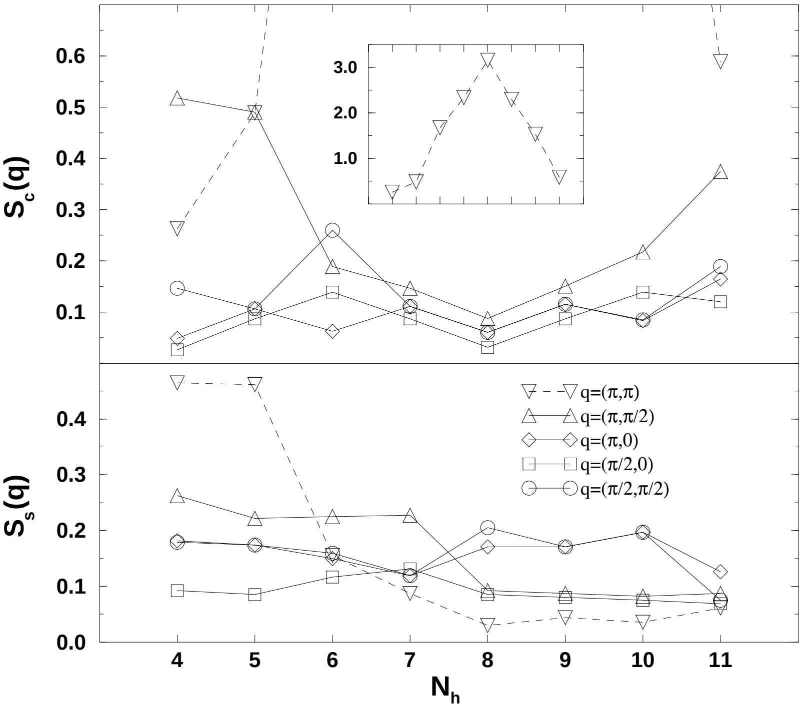

Figure 10.8: Dependence of the charge and magnetic structure factors $S_c(\vec{q})$ and $S_s(\vec{q})$ on the number of holes N_h at $\lambda = 1.0$ and $J = 0.4$.

of the 4×4 lattice. The pronounced peak in $S_c[(\pi,\pi)]$ at quarter–filling reflects the commensurate ordering of 'localized' hole–polarons. The (π,π)–component of $S_c(\vec{q})$ is the dominant contribution in the relatively large regime from six to ten holes. For smaller hole densities a crossover to a density modulation with wave–vector $(\pi,\pi/2)$ takes place around $N_h = 5$. For larger hole concentrations ($N_h > 11$) the structure in $S_c(\vec{q})$ disappears and we can no longer specify a definite wave–vector. The maximum in the magnetic structure factor $S_s(\vec{q})$ at the value (π,π) increases with the electron concentration indicating increasing AFM correlations. Since the mobility of the electrons (holes) is dramatically reduced by the frozen–in lattice distortions, at very large λ the system might well be described by a Heisenberg model with immobile vacancies for $x < 0.5$. Of course, these vacancies are not at random positions, but are located in such a way that the total energy is minimized.

10.2 Formation of hole–polarons in the Holstein t–J model [359]

The purpose of this section is to extend the variational diagonalization techniques used in Sec. 9.4 for the Holstein Hubbard model, in particular the IMVLF–Lanczos method, to the Holstein t–J model, preserving partly the dynamics of phonons. The Hamiltonian of the Holstein t–J model is given by

$$\mathcal{H}_{H-t-J} = \hbar\omega \sum_i \left(b_i^\dagger b_i + \frac{1}{2}\right) - \sqrt{\varepsilon_p \hbar\omega} \sum_i \left(b_i^\dagger + b_i\right) \tilde{h}_i - t \sum_{\langle ij\rangle\sigma} \left(\tilde{c}_{i\sigma}^\dagger \tilde{c}_{j\sigma} + \text{H.c.}\right) + J \sum_{\langle ij\rangle} \left(\vec{S}_i \vec{S}_j - \frac{1}{4} \tilde{n}_i \tilde{n}_j\right). \tag{10.7}$$

Here, $\tilde{h}_i = 1 - \tilde{n}_i$ denotes the hole number operator, i.e., the dominant source of EP coupling is assumed to come from the interaction of doped *holes* with a single dispersionsless phonon mode [455]. Treating the hole–polaron formation by a variational approach, we perform the IMVLF transformation in the form

$$\tilde{\mathcal{H}}_{H-t-J} = \mathcal{U}^{\dagger}\,\mathcal{H}_{H-t-J}\,\mathcal{U}\,, \qquad \mathcal{U} = \mathrm{e}^{-\mathcal{S}_1(\Delta_i)}\,\mathrm{e}^{-\mathcal{S}_2(\bar{\gamma},\gamma)} \tag{10.8}$$

with

$$\begin{aligned} \mathcal{S}_1(\Delta_i) &= \frac{1}{2\sqrt{\hbar\omega\varepsilon_p}}\sum_i \Delta_i(b_i^{\dagger} - b_i)\,, & (10.9)\\ \mathcal{S}_2(\bar{\gamma},\gamma) &= -\sqrt{\varepsilon_p/\hbar\omega}\sum_i(\bar{\gamma} + \gamma\tilde{h}_i)(b_i^{\dagger} - b_i)\,. & (10.10) \end{aligned}$$

Taking the average of $\tilde{\mathcal{H}}_{H-t-J}$ over the squeezed phonon state (8.62), we are left with an effective t–J model

$$\begin{aligned} \overline{\mathcal{H}}_{H-t-J} &= \frac{\hbar\omega}{4}N(\tau^2 + \tau^{-2}) + \bar{\gamma}^2\varepsilon_p N + \frac{1}{4\varepsilon_p}\sum_i \Delta_i^2 + \tilde{\lambda}\sum_i \Delta_i \qquad (10.11)\\ &\quad + (1-\gamma)\sum_i \Delta_i\,\tilde{h}_i - \tilde{\varepsilon}_p\sum_i \tilde{h}_i - \rho t \sum_{\langle ij\rangle\sigma}\left(\tilde{c}_{i\sigma}^{\dagger}\tilde{c}_{j\sigma} + \mathrm{H.c.}\right) + J\sum_{\langle ij\rangle}\left(\vec{S}_i\vec{S}_j - \frac{1}{4}\tilde{n}_i\tilde{n}_j\right). \end{aligned}$$

The definitions of $\tilde{\varepsilon}_p$, ρ and τ^2 are given in Sec. 8.1. We are now in a position to examine the ground–state properties of the purely electronic Hamiltonian $\overline{\mathcal{H}}_{H-t-J}(\bar{\gamma},\gamma,\tau^2,\{\Delta_i\})$ by means of exact diagonalization in the subspace of fixed hole numbers N_h and minimal total S^z. By analogy to (9.11)–(9.14), the variational parameters are determined by the self–consistent equations:

$$\begin{aligned} \bar{\gamma} &= (1-\gamma)\,\delta\,, \quad \tilde{\lambda} = -\bar{\gamma}\,, & (10.12)\\ \gamma &= \frac{\hbar\omega\left[\delta(1-\delta) + E_{\Delta h}/2\varepsilon_p\right]}{\hbar\omega\delta(1-\delta) - \tau^2 E_t}\,, & (10.13)\\ \tau^2 &= \frac{\hbar\omega}{\sqrt{\hbar^2\omega^2 - 4\varepsilon_p\gamma^2 E_t}}\,, & (10.14)\\ \Delta_i &= 2\varepsilon_p(1-\gamma)(\delta - \delta_i)\,. & (10.15) \end{aligned}$$

where

$$\begin{aligned} E_t &= -\frac{\rho t}{N}\sum_{\langle ij\rangle\sigma}\langle(\tilde{c}_{i\sigma}^{\dagger}\tilde{c}_{j\sigma} + \mathrm{H.c.})\rangle\,, & (10.16)\\ E_{\Delta h} &= \frac{1}{N}\sum_i\langle\Delta_i\tilde{h}_i\rangle\,, & (10.17) \end{aligned}$$

and $\delta_i = \langle\tilde{h}_i\rangle$ with $\delta = \frac{1}{N}\sum_i \delta_i$. Accordingly, we define the effective transfer amplitude

$$t_{p,eff} = E_t(\varepsilon_p, J)/E_t(0, J) \tag{10.18}$$

as a measure of the phonon–induced band renormalization.

10.2.1 One– and two–hole cases

In the numerical analysis of the polaronic t–J model, we shall start with the study of just a single dynamic hole. Due to the competition between the antiferromagnetic exchange energy loss and the delocalization energy gain this problem is highly nontrivial even for the pure t–J model, and considerable effort has been devoted to this subject [7]. Including the EP coupling, both static lattice deformations ($\hbar\omega \ll \varepsilon_p, t$) and dynamic polaron formation ($\hbar\omega, \varepsilon_p \gg t$) can introduce anharmonic effects, further enhancing the effective mass of the charge carriers. For a more quantitative discussion we show in Fig. 10.9 the effective transfer amplitude $t_{p,eff}$, the polaronic band narrowing factor ρ and the 'averaged' static displacement $\Delta = \frac{1}{N}\sum_i |\Delta_i|$ as a function of ε_p for the ten–site square lattice. In the following, except where otherwise stated, the exchange interaction strength is fixed to $J/t = 0.4$. For low frequencies ($\hbar\omega < t$), we can

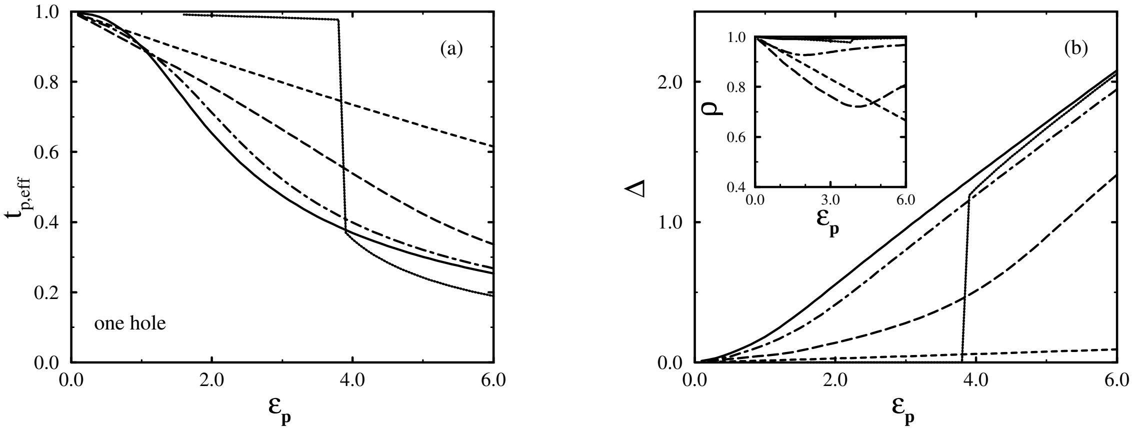

Figure 10.9: Dependence of the effective transfer amplitude $t_{p,eff}$ (a), averaged 'static' displacement Δ (b), and the polaronic band narrowing factor ρ (inset) on the EP coupling ε_p for the one–hole case ($N = 10$). The solid, chain dashed, long dashed, and dashed curves refer to $\hbar\omega = 0.1$, 0.8, 3.0, 10.0, respectively. At $\hbar\omega = 0.1$, the corresponding dependencies are given for the case of spinless fermions (dotted curves).

again distinguish between the FP and AHP regimes. In the FP state for small $\varepsilon_p \leq 0.4$, the hole is mainly 'delocalized' and we observe two 'hole–sites', where the spin density is concentrated (cf. the on–site electron/spin densities tabulated in Table 10.1). In addition, the polaron effect is very weak (see the γ value at $\varepsilon_p = 0.2$ given in Table 10.1 and ρ *vs* ε_p shown in the inset of Fig. 10.9 (b)). As mentioned in the preceding section, the finite (but very small) value of Δ (Fig. 10.9 (b)) is due to the non–trivial wave–vector of the ground–state. If we take for example $J = 0.1$, where the momentum of the ground state is zero, we found $\langle\tilde{n}_i\rangle = 0.9\ \forall i$ and $\Delta \equiv 0$ in the FP regime. Increasing the EP coupling the mobility of the hole ($\propto t_{p,eff}$) is strongly reduced and an AHP is formed. As can be seen from Fig. 10.9 (b) and Table 10.1, a strong local static lattice distortion traps the hole mainly on a single site for $\varepsilon_p > \varepsilon_{p,1}^c \sim 0.4$. Note that the hole–trapping is accompanied by an enhancement of the AFM correlations $\langle S_i^z S_j^z\rangle$ between nearest–neighbour sites in the spin background which was discussed in Sec. 10.1. Thus the substantial gain in exchange and EP interaction energy overcompensates the cost of elastic and kinetic energy. On the other hand, the polaronic variational parameter γ becomes even smaller which means that ρ is not influenced by this 'self–trapping' transition. This is worth emphasizing because it shows that our IMVLF approach correctly incorporates the two different types of polaronic states, the adiabatic Holstein polarons (AHP) and the non-adiabatic Lang–Firsov polarons (NLFP). In the case of (noninteracting) spinless fermions, we find the self–trapping transition at a much larger critical EP interaction $\varepsilon_{p,1}^{c,SF} \sim 4.0$ (see Fig. 10.9), which is in the order of half the bare bandwidth. As mentioned above, due to the strong coupling of spin and hole dynamics in the t–J model, the characteristic energy scale for the single–hole motion is J and not t; therefore we get $\varepsilon_{p,1}^{c} \sim J = 0.4$. Increasing $\hbar\omega$ in the adiabatic regime the transition from FP to AHP is shifted to somewhat larger values of ε_p. For high phonon frequencies ($\hbar\omega \gg t$), we found a smooth crossover from light FP to NLFP, whereby the effective mass ($\propto 1/t_{p,eff}$) becomes weakly enhanced. In contrast to the adiabatic regime, the mass enhancement now results from the dynamical polaronic band renormalization $\propto \rho$, i.e., $\gamma \to 1$ (see Fig. 10.9 (b) and Table 10.1). On the other hand, the static lattice distortions almost disappear and the $\langle \tilde{n}_i \rangle$ exhibit the same spatial variation as for the pure t–J model (cf. Table 10.1). Let us emphasize that the polaronic mass renormalization is rather moderate and vanishes in the antiadiabatic limit $\hbar\omega > \varepsilon_p \gg t$, where the *Lang–*

	$N_h = 1$			$N_h = 2$		
ε_p	0.2	4.0	4.0	0.2	4.0	4.0
$\hbar\omega$	0.8	0.8	10.0	0.8	0.8	10.0
E	–6.07011	–8.44394	–9.32013	–7.5940	–12.1313	–14.0264
γ	0.22112	0.10005	0.82442	0.19574	0.10787	0.80498
τ^2	0.99260	0.98781	0.99020	0.98754	0.97654	0.98029
i		$\langle \tilde{n}_i \rangle$ / $\langle S_i^z \rangle$			$\langle \tilde{n}_i \rangle$	
1	$\boxed{0.7782/+.2386}$	$\boxed{0.0712/+.0169}$	$\boxed{0.7593/+.2257}$	$\boxed{0.7679}$	$\boxed{0.0644}$	$\boxed{0.7554}$
2	0.9304/+.0028	0.9826/+.2300	0.9352/+.0061	$\boxed{0.7679}$	$\boxed{0.0644}$	$\boxed{0.7554}$
3	0.9304/+.0028	0.9996/–.1608	0.9352/+.0061	0.8214	0.9787	0.8300
4	0.9304/+.0028	0.9826/+.2300	0.9352/+.0061	0.8214	0.9787	0.8300
5	0.9304/+.0028	0.9996/–.1608	0.9352/+.0061	0.8214	0.9787	0.8300
6	$\boxed{0.7782/+.2386}$	0.9999/+.2065	$\boxed{0.7593/+.2257}$	$\boxed{0.7679}$	0.9995	$\boxed{0.7554}$
7	0.9304/+.0028	0.9996/–.1608	0.9352/+.0061	$\boxed{0.7679}$	0.9995	$\boxed{0.7554}$
8	0.9304/+.0028	0.9826/+.2300	0.9352/+.0061	0.8214	0.9787	0.8300
9	0.9304/+.0028	0.9996/–.1608	0.9352/+.0061	0.8214	0.9787	0.8300
10	0.9304/+.0028	0.9828/+.2300	0.9352/+.0061	0.8214	0.9787	0.8300

Table 10.1: Shifted ground–state energy ($E = E_{tot} - N\hbar\omega/2$), polaron ($\gamma$) and squeezing ($\tau^2$) variational parameter, as well as the on–site electron ($\langle \tilde{n}_i \rangle$) and spin ($\langle S_i^z \rangle$) densities in the ground state of the effective 2D Holstein t–J Hamiltonian (10.11) at $J = 0.4$. The results are given for one and two holes on a ten–site lattice with periodic boundary conditions at characteristic EP coupling strengths (ε_p) and phonon frequencies ($\hbar\omega$). The sites are counted according to Fig. 10.1, where values within boxes indicate 'hole–sites' with less than average electron density (see text). For $N_h = 2$ we have $\langle S_i^z \rangle \equiv 0$.

Firsov–type polaron effect becomes strongest ($\gamma = 1$). Increasing ε_p further at large but *fixed* $\hbar\omega$ we always find a transition to a 'self–trapped' heavy–polaron state. In spite of the fact that $\hbar\omega$ is much larger than t, this state bears a strong resemblance to the *adiabatic* Holstein polaron. That means, within our IMVLF–Lanczos treatment, we found no parameter region where an extremely heavy NLFP ($\rho \to 0$) does exist. This fact seems to be in agreement with the exact results presented in Chap. 9 for the single–electron Holstein model.

To check for finite–size effects in the results presented so far, $t_{p,eff}$ is calculated on square lattices with 16 and 18 sites. For the particular case of a single hole, results are shown in Fig. 10.2.1 at $\hbar\omega = 0.1$ and $\hbar\omega = 10.0$, corresponding to adiabatic and antiadiabatic regimes. As is intuitively clear, at large frequencies we find the finite–size dependence to be weaker than that in the adiabatic limit. But also in the adiabatic region, no major differences between the currently available cluster sizes are observed. Especially, the qualitative features of the weak–coupling FP and strong–coupling AHP states remains unchanged. Note that with increasing lattice size the AHP becomes even more localized for $\varepsilon_p \gg t \gg \hbar\omega$.

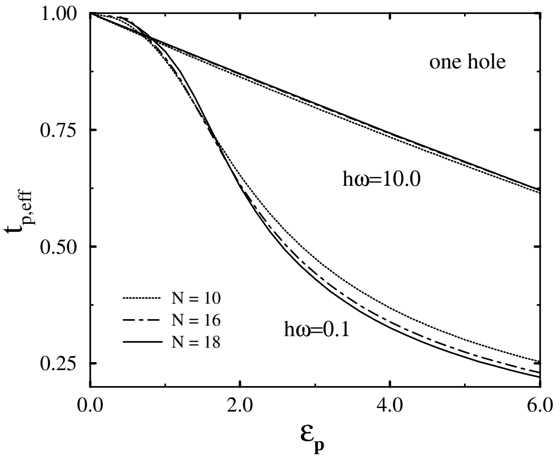

Figure 10.10: Effective hopping amplitude $t_{p,eff}$ *vs* ε_p for the 2D Holstein t–J model with a single hole. Results are given for lattices with $N = 10$, 16, and 18 sites in the adiabatic ($\hbar\omega = 0.1$; lower curves) and antiadiabatic ($\hbar\omega = 10.0$; upper curves) regimes.

In a next step we consider the two–hole case. Here, $t_{p,eff}$, ρ and Δ, depicted in Fig. 10.11 as a function of ε_p, show qualitatively the same behaviour as for the one–hole case. Depending on the EP coupling strength, the holes will be trapped in the adiabatic regime, for large enough ε_p, on two adjacent sites sharing a common lattice distortion (cf. Table 10.1). Compared to the one–hole case the transition from FP to the self–trapped state takes place at larger critical coupling ($\varepsilon^c_{p,2} \sim 2\varepsilon^c_{p,1}$), which can be traced back to a larger effective transfer amplitude of the pure t–J model with two holes [$E_{t,2}(J, \varepsilon_p = 0) = -0.536 \sim 2E_{t,1}(J, \varepsilon_p = 0) = -0.249$] at $J = 0.4$.

Of special interest is the question whether the EP interaction enhances the two–hole binding, i.e., whether $E^2_B(J, \varepsilon_p, \hbar\omega)$ defined as usual by Eq. (3.9) becomes more negative. In Table 10.2 the binding energies of two holes are given with respect to the Heisenberg AFM state at half–filling. At $\varepsilon_p = 0$, it is clear that a bound state of holes will be formed at large values of J since two holes on neighbouring sites lose the exchange energy on only seven bonds together instead of on eight bonds. On the other hand, at very small J, one would expect two independent holes. To exclude finite–size effects in calculating E^2_B at finite ε_p, one has to take care that one compares with respect to the polaronic features the same type of ground state for the one– and two–hole systems, respectively. In the FP regime (see Table 10.2, $\varepsilon_p = 0.1$, 0.2 at $J = 0.4$), hole binding is enhanced as ε_p increases, whereas at fixed ε_p, it slightly decreases with increasing phonon frequency. This behaviour is a net result, including both the static

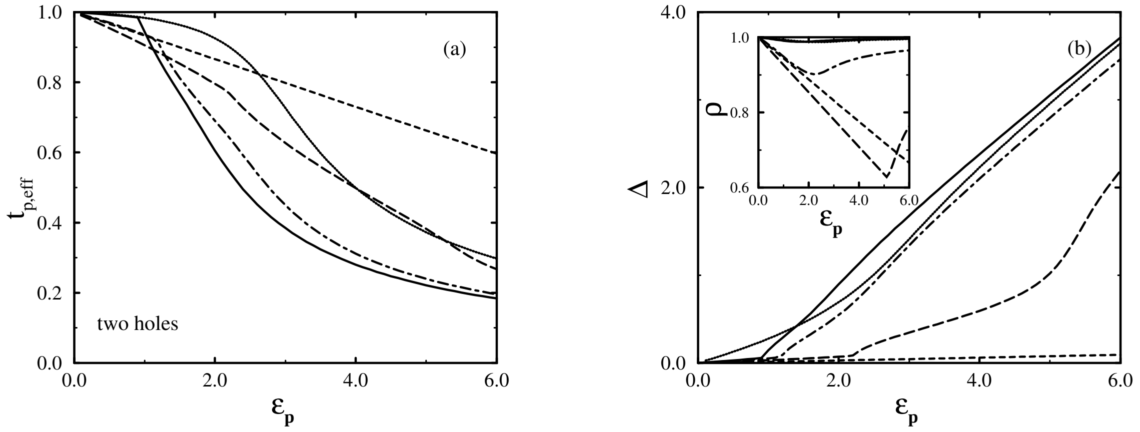

Figure 10.11: $t_{p,eff}$ (a), Δ (b), and ρ (inset) *vs* ε_p for the two–hole case. The notations are the same as in Fig. 10.9.

and the dynamic effect of the EP coupling. As stated above, due to the non–trivial symmetry of the electronic wave–function, the ground state carries a small but finite static distortion even in the FP state, which becomes enhanced $\propto \varepsilon_p$. Then the effect of a finite phonon frequency is twofold. First it counteracts such an enhancement of the static displacement fields and therefore weakens the 'static part' of the hole binding. On the other hand, we have found convincing numerical evidence that in the FP state hole attraction may result as a purely dynamic effect of the EP coupling. To show this, it is instructive to calculate E_B^2 at $J = 0.1$, where the one– and two–hole FP ground state is uniform $[\vec{K} = (0,0),\ \Delta \equiv 0]$ up to $\varepsilon_p \lesssim 3.0$. In this case $E_B^2 (> 0)$ is strongly reduced with increasing ε_p (see Table 10.2). In addition, we observe that now the strongest attraction of hole–polarons results for an *intermediate* phonon frequency, where $\hbar\omega$ and the renormalized transfer amplitude are about equal in value. For example, at $\varepsilon_p = 2.5$ and $\hbar\omega = 0.8$ we have $t_{p,eff,1} = \rho_1 \sim t_{p,eff,2} = \rho_2 \sim 0.9$ (remember that $\rho \to 1$ if $\hbar\omega \to 0, \infty$).

$\hbar\omega$	E_B^2							
	$J = 0.4$				$J = 0.1$		$J = 0.0$	
	$\varepsilon_p = 0.0$	0.1	0.2	10.0	$\varepsilon_p = 0.0$	2.5	$\varepsilon_p = 0.0$	2.5
0.0	$\underline{-0.3609}$	−0.3744	−0.3877	−0.2755	$\underline{+0.5198}$	+0.0198	$\underline{+2.0000}$	+1.5000
0.1		−0.3732	−0.3853	−0.2751		+0.0065		+1.4868
0.4		−0.3703	−0.3794	−0.2738		−0.0208		+1.4597
0.8		−0.3680	−0.3738	−0.2720		−0.0354		+1.4453
1.2		−0.3654	−0.3694	−0.2701		−0.0345		+1.4463
3.0		−0.3616	−0.3613	−0.2601		+0.0315		+1.5125

Table 10.2: Binding energy E_B^2 of two holes in the ground state of the Hamiltonian (10.11) at different exchange interactions J, EP couplings ε_p, and phonon frequencies $\hbar\omega$.

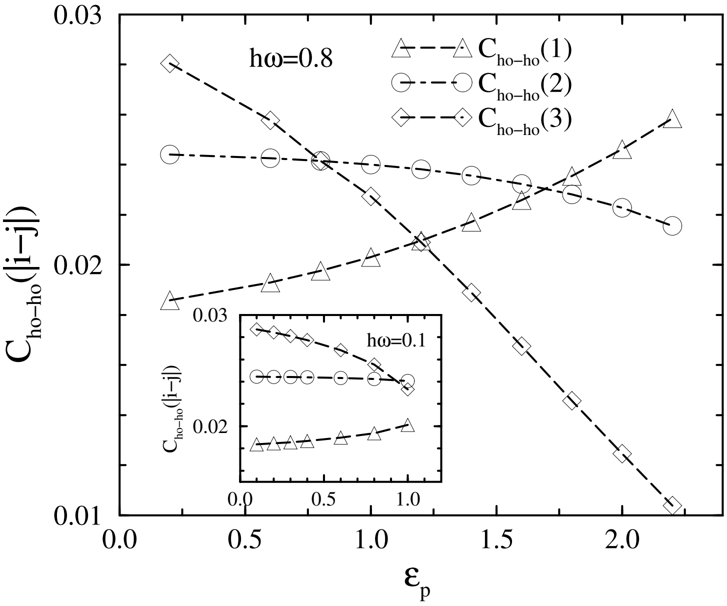

Figure 10.12: The hole–hole density correlation function $C_{ho-ho}(|i-j|)$ of the 2D Holstein t–J model, Eq. (10.7), shown as a function of the EP coupling ε_p for $\hbar\omega = 0.8$ and $\hbar\omega = 0.1$ (inset), where the numbers 1-3 label the non–equivalent distances $|\vec{R}_i - \vec{R}_j|/a = 1$, $\sqrt{2}$, and $\sqrt{5}$ between NN, NNN, and third nearest–neighbour sites on a ten–site lattice, respectively. The results are obtained by *direct* Lanczos diagonalization of the model (10.7) with $M = 12$ phonons.

These variational results are corroborated by very recent *direct* ED data obtained for the hole–hole density correlation function

$$C_{ho-ho}(|i-j|) = \langle \Psi_0(\varepsilon_p, J)|\tilde{h}_i\tilde{h}_j|\Psi_0(\varepsilon_p, J)\rangle \tag{10.19}$$

in the 2D Holstein t–J model [414]. Note that $C_{ho-ho}(|i-j|)$ provides an even more reliable test for the occurrence of hole binding than the effective binding energy E_B^2 [213].[5] In Fig. 10.2.1 we present results for the non–equivalent hole–hole pair correlation functions in the ground state of the Holstein t–J model with two holes. In the weak–coupling region the hole–density correlation function becomes maximum at the largest distance of the ten–site lattice, while in the intermediate EP coupling regime the preference is on NNN pairs. As expected, increasing further the EP interaction strength, the maximum in $C_{ho-ho}(|i-j|)$ is shifted to the shortest possible distance indicating the formation of hole–bipolarons.

To complete the analysis of hole binding, let us turn to the adiabatic strong–coupling regime. In the limit $\varepsilon_p \gg (\hbar\omega, t)$, the two AHP becomes self–trapped on nearest–neighbour sites forming a nearly immobile AHBP (cf. Table 10.1). As one increases the phonon frequency, one observes a weaker localization effect. As Table 10.2 shows, our expectation of finding a negative binding energy at extremely large EP coupling, like $\varepsilon_p = 10.0$, is correct. However, it is important to note that this static type of hole binding, forced by both ε_p and J, is much less effective than the dynamic one in the weak–coupling (FP) regime.

10.2.2 Quarter–filled band case: Application to $\mathrm{La_{1.5}Sr_{0.5}NiO_4}$

Now let us consider the 2D Holstein t–J model at quarter–filling in order to show that the interplay of charge, lattice and spin degrees of freedom can lead to the formation of a polaronic superlattice as observed in $\mathrm{La_{1.5}Sr_{0.5}NiO_4}$. Fig. 10.13 displays the behaviour of $t_{p,eff}$ (a), Δ (b) and ρ (inset(b)) as function of EP coupling for different phonon frequencies. In the adiabatic regime, we found a sequence of transitions as ε_p increases from nearly free polarons to several

---

[5] Indeed, when calculating E_B^2, we are comparing states with different quantum numbers, specifically with different S and S^z.

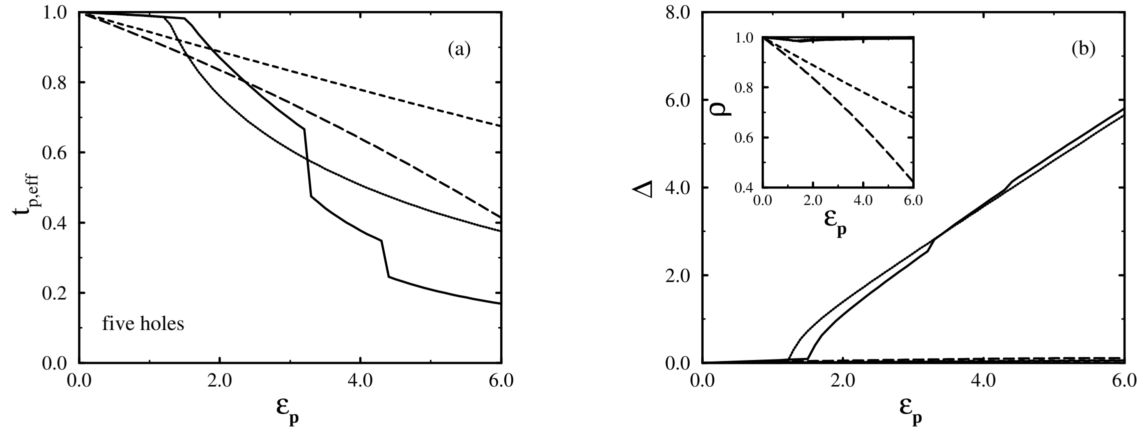

Figure 10.13: $t_{p,eff}$ (a), Δ (b), and ρ are shown as function of ε_p at quarter–filling ($N_h = 5$), where the solid, dotted, long dashed, and dashed curves correspond to $\hbar\omega = 0.1$, 0.1 (spinless fermions), 3.0, 10.0, respectively.

charge–ordered states with (frozen–in) static lattice distortions. To characterize the various states in more detail, in Table 10.3 the on–site charge and spin densities on the ten–site lattice are given at $\hbar\omega = 0.1$. For small values of ε_p, the holes are completely delocalized (FP) destroying the antiferromagnetic order of the spin background. Note that compared to the low–doping region the squeezing phenomenon is more pronounced. For larger values of ε_p, the holes self–trap on every other site as a consequence of the static displacements fields, forming a polaronic superlattice of adiabatic Holstein polarons. This crossover is signaled by a pronounced peak in the charge structure factor $S_c(\vec{q})$ at (π, π).

To make contact with the experimental situation in the cuprates and nickelates, we note that we obtain a critical EP coupling strength $\varepsilon^c_{p,5} \sim 1.5$ at $\hbar\omega = 0.1$ for the transition from the FP metallic phase to the (π, π) ordering of self–localized hole–polarons. From an analysis of the optical conductivity data for $La_{2-x}Sr_xNiO_{4+\delta}$ and $La_{2-x}Sr_xCuO_{4+\delta}$, Bi and Eklund [384] have estimated values for the (dimensionless) polaron parameters $\zeta = 1/2\varepsilon_p$ and $\eta = 2\varepsilon_p/\hbar\omega$ at low doping levels ($x \leq 0.2$). In the cuprates, ζ increases from 0.33 ($x = 0.02$) to 1.7 ($x = 0.2$), i.e., $\varepsilon_p \ll \varepsilon^c_p$, and the small–polaron contribution to the optical response (conductivity) is overwhelmed by the contribution from band–like carriers (FP) [384]. Contrary for the nickelates, which become metallic only near $x \approx 1$, they found a nearly doping independent ratio $\zeta \sim 0.15$ ($\eta \sim 10$, i.e., $\hbar\omega = 0.625$ [473]), which corresponds to $\varepsilon_p \sim 3$, indicating that the polarons are small [474]. For comparison, the classical small polaron material $TiO_{2-\delta}$ has $\zeta \sim 0.12$. As can be seen from Fig. 10.13 (a) and Table 10.3, at $\varepsilon_p = 3$, the ground state of the quarter–filled polaronic t–J model exhibits a commensurate ordering of polarons which qualitatively agrees with the experimental findings for the nickelates.

If in our model calculation the EP coupling is further enhanced, a second transition occurs to a ‘stripe-like’ phase and finally, at $\varepsilon_p > 4$, to a charge separated state (cf. Table 10.3). Both transitions are accompanied by changes in the spin arrangements. In the fully phase separated state the segregation of holes becomes complete at large ε_p, where $\{\sum_i(\Delta_i^2/4\varepsilon_p) + \bar{\gamma}^2\varepsilon_p N - E_{\Delta h}\} \to 0$. At the same time, the importance of the kinetic energy part ($\propto t_{p,eff}$) is reduced, due to the formation of self–trapped Holstein polarons. Then the physical reason for the occurrence of phase separation at *moderate* exchange interactions ($J = 0.4$) is that the gain in exchange energy by maximizing the number of antiferromagnetic bonds in the electron–rich part of the system may outweigh the relatively low cost in kinetic energy.

	$N_h = 5$			
ε_p	1.0	3.0	4.0	5.0
E	–11.7159	–18.2625	–22.6763	–27.4133
γ	0.034501	0.018051	0.013101	0.010331
τ^2	0.847707	0.903121	0.959526	0.981952
i	$\langle \tilde{n}_i \rangle$ / $\langle S_i^z \rangle$			
1	0.5241/+0.1213	$\boxed{0.0996/+0.0081}$	0.9711/+0.3190	0.9778/+0.2717
2	0.5241/+0.1213	0.9001/+0.2528	0.9612/–0.1322	0.9879/–0.1645
3	0.5241/+0.1213	$\boxed{0.1130/+0.0058}$	0.9489/+0.2137	0.9778/+0.2717
4	$\boxed{0.4638/-0.0569}$	0.8809/–0.1461	$\boxed{0.0451/+0.0097}$	0.9879/–0.1645
5	$\boxed{0.4638/-0.0569}$	$\boxed{0.1130/+0.0058}$	$\boxed{0.0392/-0.0042}$	0.9778/+0.2717
6	0.5241/+0.1213	0.8809/–0.1461	$\boxed{0.0401/+0.0072}$	$\boxed{0.0218/+0.0057}$
7	0.5241/+0.1213	$\boxed{0.1130/+0.0058}$	0.9489/+0.2136	$\boxed{0.0128/-0.0016}$
8	0.5241/+0.1213	0.9001/+0.2528	0.9612/–0.1322	$\boxed{0.0218/+0.0057}$
9	$\boxed{0.4638/-0.0569}$	$\boxed{0.0996/+0.0081}$	$\boxed{0.0392/-0.0042}$	$\boxed{0.0128/-0.0016}$
10	$\boxed{0.4638/-0.0569}$	0.9001/+0.2528	$\boxed{0.0451/+0.0097}$	$\boxed{0.0218/+0.0057}$

Table 10.3: Ground–state energies (E), polaron/squeezing parameters (γ/τ^2), and on–site charge/spin densities ($\langle \tilde{n}_i \rangle / \langle S_i^z \rangle$) of the quarter–filled Holstein t–J model (10.11) on a ten–site square lattice. The results are given for different EP interactions (ε_p) at $\hbar\omega = 0.1$ and $J = 0.4$.

Summary

In this chapter we have performed an extensive numerical study of the 2D Holstein t–J model on finite square lattices in order to investigate the problem of hole–polaron formation in strongly correlated electron–phonon systems. We present an IMVLF–Lanczos scheme that allows for the description of static displacement field, polaron and squeezing effects and contains the strong Coulomb correlations in an exact way. The method is designed to investigate the interplay between electron–electron and electron–phonon interactions at arbitrary band–fillings for a wide range of phonon frequencies, where both adiabatic and anti–adiabatic limiting cases are well–reproduced. The quality of this IMVLF–Lanczos approach [359] was impressively demonstrated by comparison with direct ED results available for the Holstein Hubbard model (cf. Sec. 9.4). The finite–size effects in the IMVLF–Lanczos data were checked to be small.

Concerning the ground–state properties of the effective polaronic t–J model, our main results are the following.

(i) In the adiabatic regime, we find a *narrow* crossover region from nearly free polarons (FP) to adiabatic Holstein polarons (AHP) as the EP coupling increases. This transition is accompanied by a strong renormalization of the polaronic bandwidth ($\propto t_{p,eff} \neq \rho$) and the occurrence of an *inhomogeneous* displacement field. Whereas the 'delocalized' FP state reflects the ground–state symmetry of the pure t–J model, the AHP becomes 'quasi–localized' (self–trapped) due to a strong *local* lattice distortion. In the non–adiabatic regime, we found a *smooth* evolution from FP to Lang–Firsov type polarons (NLFP). The NLFP state is characterized by a rather *moderate* polaronic mass enhancement and a *uniform* distribution of the static displacement fields. Note that an extremely heavy NLFP ($t_{p,eff} = \rho \to 0$) does *not* exist.

(ii) The critical EP coupling strength for the 'self–trapping' transition of the doped charge carriers is considerably reduced by the antiferromagnetic exchange interaction compared to that in the uncorrelated model (spinless fermions). This means that a rather weak EP interaction can cause polaronic effects in strongly correlated electron systems supporting a prominent role of the lattice degrees of freedom in the cuprates and even more in the isostructural nickelates.

(iii) The finite density (many–polaron) effects on the hole–polaron formation, treated by the IMVLF–Lanczos approach, are mainly realized via correlation and squeezing effects, which counteract each other and become most pronounced in the low– and high–doping regime, respectively. Therefore, with increasing hole density, the transition to the AHP state is shifted to higher EP couplings.

(iv) Analyzing the two–hole binding energy in the 2D polaronic t–J model, we have found that hole binding is enhanced in the weak–coupling (FP) regime as a dynamical effect of the EP interaction. In this case, the strongest attraction of hole–polarons results for intermediate phonon frequencies, being comparable in magnitude to the renormalized transfer amplitude. On the other hand, in the adiabatic strong EP coupling case a rather static type of hole binding is realized, where the two holes becomes 'self–trapped' on nearest–neighbour sites forming a nearly immobile bipolaron.

(v) For the quarter–filled band case, the ground–state of the polaronic t–J model exhibits a sequence of transitions as the EP coupling increases from a FP state to a polaronic superlattice related to a frozen–in (π, π) lattice distortion and finally to a phase (charge) separated state. Let us emphasize that the experimental estimates of the polaron parameters (ζ, η) for the cuprates and nickelates coincide with the values where we find the FP and the commensurate polaronic superlattice in the Holstein t–J model.

Bibliography

[1] I. G. Bednorz and K. A. Müller, Z. Phys. B **64**, 189 (1986).

[2] A. Schilling, M. Cantoni, J. D. Guo, and H. R. Ott, Nature **363**, 56 (1993).

[3] Y. Tokura, in S. Maekawa and M. Sato, editors, *Physics of High–Temperature Superconductors*, Springer–Verlag, (Berlin 1991).

[4] J. B. Torrance et al., Phys. Rev. Lett. **61**, 1127 (1988).

[5] H. Takagi, S. Uchida, and Y. Tokura, Phys. Rev. Lett. **62**, 1197 (1989).

[6] C. Almasan and M. B. Maple, in C. N. R. Rao, editor, *Chemistry of High–Temperature Superconductors*, World Scientific, (Singapore 1991).

[7] E. Dagotto, Rev. Mod. Phys. **66**, 763 (1994).

[8] W. E. Pickett, H. Krakauer, R. E. Cohen, and D. J. Singh, Science **255**, 46 (1992).

[9] J. Fink, N. Nucker, H. A. Romberg, and J. C. Fuggle, IBM J. Res. Develop. **33**, 372 (1989).

[10] P. Fulde, *Electron Correlation in Molecules and Solids*, Springer–Verlag, (Berlin 1991).

[11] W. E. Pickett, Rev. Mod. Phys. **61**, 433 (1989).

[12] L. F. Mattheiss, Phys. Rev. Lett. **58**, 1028 (1987).

[13] S. Massida, N. Hamada, J. Yu, and A. J. Freeman, Physica C **157**, 571 (1989).

[14] W. A. Harrison, in S. A. Wolf and V. Z. Kresin, editors, *Novel Mechanisms of Superconductivity*, Plenum, (New York 1987).

[15] P. H. Dickinson and S. Doinach, Phys. Rev. B **47**, 1147 (1993).

[16] Z.-X. Shen and D. S. Dessau, Physics Reports **253**, 1 (1995).

[17] J. M. Luttinger, Phys. Rev. B **119**, 1153 (1960).

[18] W. E. Pickett, R. E. Cohen, and H. Krakauer, Phys. Rev. B **42**, 8764 (1990).

[19] R. Liu et al., Phys. Rev. B **46**, 11056 (1992).

[20] A. A. Abrikossov, J. C. Campuzano, and K. Gofran, Physica C **214**, 73 (1993).

[21] C. C. Tsuei et al., Phys. Rev. Lett. **69**, 2134 (1992).

[22] E. Dagotto, A. Nazarenko, and M. Bonsinsegni, Phys. Rev. Lett. **73**, 728 (1994).

[23] N. Bulut, D. J. Scalapino, and S. R. White, Technical report, University of Illinois, (1994).

[24] D. M. King et al., Phys. Rev. Lett. **70**, 3159 (1993).

[25] K. Gofron et al., J. Phys. Chem. Solids **54**, 1185 (1993).

[26] D. S. Dessau et al., Phys. Rev. Lett. **71**, 2781 (1993).

[27] M. Eschrig, J. Heym, and D. Rainer, J. Low Temp. Phys. **95**, 323 (1994).

[28] K. Levin, J. H. Kim, J. P. Lu, and Q. Si, Physica C **175**, 449 (1991).

[29] B. Batlogg et al., J. Low Temp. Phys. **95**, 23 (1994).

[30] A. Freimuth, in L. C. Gupta and M. S. Multani, editors, *Selected Topics in Superconductivity*, Frontiers in Solid State Sciences, page 393, World Scientific, (1993).

[31] P. Wyder, editor, *Proc. Int. Conf.* M^2S *HTSC IV*, volume 235–240 of *Physica C*, (Grenoble 1994).

[32] T. Thio et al., Phys. Rev. B **38**, 905 (1988).

[33] Y. Endoh et al., Phys. Rev. B **37**, 7443 (1988).

[34] M. A. Kastner et al., Phys. Rev. B **38**, 6636 (1988).

[35] A. P. Kampf, Physics Reports **249**, 219 (1994).

[36] F. Mila, Phys. Rev. B **42**, 2677 (1990).

[37] T. Kopp and F. Mila, Phys. Rev. B **43**, 12980 (1991).

[38] G. Baumgärtel, J. Schmalian, and K. H. Bennemann, Europhys. Lett. **24**, 601 (1993).

[39] U. Trapper, D. Ihle, and H. Fehske, Phys. Rev. B **52**, R 11553 (1995).

[40] D. C. Johnston, Phys. Rev. Lett. **62**, 957 (1989).

[41] J. B. Torrance et al., Phys. Rev. B **40**, 8872 (1989).

[42] D. C. Johnston, S. K. Sinha, A. J. Jacobson, and J. M. Newson, Physica C **153-155**, 572 (1988).

[43] T. E. Mason, G. Aeppli, and H. A. Mook, Phys. Rev. Lett. **68**, 1414 (1992).

[44] S.-W. Cheong et al., Phys. Rev. Lett. **67**, 1791 (1991).

[45] Q. Si, Int. J. Mod. Phys. B **1 & 2**, 47 (1994).

[46] B. J. Sternlieb et al., Phys. Rev. B **47**, 5320 (1993).

[47] J. M. Tranquada et al., Phys. Rev. B **46**, 5561 (1992).

[48] T. R. Thurston et al., Phys. Rev. Lett. **65**, 263 (1990).

[49] Q. Si, Y. Zha, K. Levin, and J. P. Lu, Phys. Rev. B **47**, 9055 (1993).

[50] T. Tanamoto, H. Kohno, and H. Fukuyama, J. Phys. Soc. Jpn. **62**, 717 (1993).

[51] M. Deeg, H. Fehske, and H. Büttner, J. Phys. Condens. Matter **7**, L 245 (1995).

[52] B. Keimer et al., Phys. Rev. Lett. **67**, 1930 (1991).

[53] C. M. Varma et al., Phys. Rev. Lett. **63**, 1996 (1989).

[54] J. Rossat-Mignod et al., Physica B **180 & 181**, 383 (1992).

[55] C. Berthier et al., Physica C **235–240**, 67 (1994).

[56] C. Berthier et al., Physica Scripta **T 49 a**, 131 (1993).

[57] J. Rossat-Mignod et al., in L. C. Gupta and M. S. Multani, editors, *Selected Topics in Superconductivity*, Frontiers in Solid State Sciences, page 265, World Scientific, (1993).

[58] S. Uchida et al., Phys. Rev. B **43**, 7942 (1991).

[59] S. Uchida, H. Tagaki, and Y. Tokura, J. Less-Common Met. **164 & 165**, 741 (1990).

[60] H. Romberg et al., Phys. Rev. B **42**, 8768 (1990).

[61] T. Timusk and D. Tanner, in D. M. Ginsberg, editor, *Physical Properties of High–Temperature Superconductors III*, World Scientific, (Singapore 1989).

[62] W. Brenig, Physics Reports **251**, 153 (1995).

[63] S. Uchida, K. Tamasaku, K. Takenaka, and H. Tagaki, J. Low Temp. Phys. **95**, 109 (1994).

[64] B. Batlogg et al., Physica C **235–240**, 130 (1994).

[65] T. Ito, K. Takenaka, and S. Uchida, Phys. Rev. Lett. **70**, 3995 (1993).

[66] Y. Hidaka and M. Suzuki, Nature **338**, 635 (1989).

[67] H. Takagi et al., Phys. Rev. Lett. **69**, 2975 (1992).

[68] S. Uchida, H. Tagaki, and Y. Tokura, Physica C **162–164**, 1677 (1989).

[69] N. P. Ong, in D. M. Ginsberg, editor, *Physical Properties of High Temperature Superconductors*, volume II, World Scientific, (New Jersey 1990).

[70] H. Y. Hwang et al., Phys. Rev. B **72**, 2636 (1994).

[71] E. Sigmund and K. A. Müller, editors, *Phase Separation in Cuprate Superconductors*, Springer–Verlag, (Berlin 1994).

[72] V. J. Emery and S. A. Kivelson, Physica C **209**, 597 (1993).

[73] G. Yu et al., Phys. Rev. B **45**, 4964 (1992).

[74] J. D. Jorgensen et al., Phys. Rev. B **38**, 11337 (1988).

[75] P. C. Hammel et al., Phys. Rev. B **42**, 1992 (6781).

[76] J. H. Chou, F. C. Chou, and D. C. Johnston, Phys. Rev. Lett. **70**, 222 (1993).

[77] A. P. Reyes et al., in *Proc. Conf. on Spectroscopies in Novel Superconductors*, (Santa Fe 1993).

[78] V. J. Emery, S. A. Kivelson, and H. Q. Lin, Phys. Rev. Lett. **64**, 475 (1990).

[79] D. C. Johnston et al., in E. Sigmund and K. A. Müller, editors, *Phase Separation in Cuprate Superconductors*, page 82, Springer–Verlag, (Berlin 1994).

[80] C. Di Castro and M. Grilli, in E. Sigmund and K. A. Müller, editors, *Phase Separation in Cuprate Superconductors*, page 12, Springer–Verlag, (Berlin 1994).

[81] M. Grilli et al., Phys. Rev. Lett. **67**, 259 (1991).

[82] E. Dagotto and J. Riera, Phys. Rev. Lett. **70**, 682 (1993).

[83] S. Haas, E. Dagotto, A. Nazarenko, and J. Riera, Phys. Rev. B **51**, 5989 (1995).

[84] P. W. Anderson and J. R. Schrieffer, Physics Today **44**, 55 (1991).

[85] J. W. Serene and D. Rainer, Physics Reports **101**, 223 (1983).

[86] P. B. Allen and D. Rainer, Nature **439**, 396 (1991).

[87] D. M. News, M. Rasolt, and P. Pattnik, Phys. Rev. B **38**, 6513 (1988).

[88] G. Kotliar, P. Lee, and N. Read, Physica C **153–155**, 538 (1988).

[89] J. H. Kim, K. Levin, and A. Auerbach, Phys. Rev. B **39**, 11633 (1989).

[90] F. Steglich et al., Phys. Rev. Lett. **43**, 3054 (1979).

[91] J. R. Schrieffer, X.-G. Wen, and S.-C. Zhang, Phys. Rev. Lett. **60**, 944 (1988).

[92] A. P. Kampf and J. R. Schrieffer, Phys. Rev. B **42**, 7967 (1990).

[93] H. Monien, P. Monthoux, and D. Pines, Phys. Rev. B **42**, 167 (1990).

[94] N. E. Bickers, D. J. Scalapino, and S. R. White, Phys. Rev. Lett. **62**, 961 (1989).

[95] A. Virosztek and J. Ruvalds, Phys. Rev. B **42**, 4064 (1990).

[96] E. Dagotto, A. Nazarenko, and A. Moreo, Phys. Rev. Lett. **74**, 310 (1995).

[97] D. M. News, P. C. Pattnik, and C. C. Tsuei, Phys. Rev. B **43**, 3075 (1991).

[98] E. Dagotto and R. Schrieffer, Phys. Rev. B **43**, 8705 (1991).

[99] N. Nagaosa and P. A. Lee, Phys. Rev. Lett. **64**, 2450 (1990).

[100] R. B. Laughlin, Science **242**, 525 (1988).

[101] X.-G. Wen, F. Wilczek, and A. Zee, Phys. Rev. B **39**, 11413 (1989).

[102] P. W. Anderson and Y. R. Ren, in *Proc. Los Alamos Conf. on High–T_c Superconductivity*, page 3, Addison–Wesley Publishing Company, (1990).

[103] T. M. Rice, J. Less-Common Met. **164–165**, 1439 (1990).

[104] P. W. Anderson, Science **235**, 1196 (1987).

[105] V. J. Emery, Phys. Rev. Lett. **58**, 2794 (1987).

[106] N. Kothekar, K. F. Quader, and D. W. Allender, Phys. Rev. B **51**, 5899 (1995).

[107] J. Zaanen, G. A. Sawatzky, and J. W. Allen, Phys. Rev. Lett. **55**, 418 (1985).

[108] M. S. Hybertsen, M. Schlüter, and N. E. Christensen, Phys. Rev. B **39**, 9028 (1989).

[109] H. Romberg et al., Z. Phys. **78**, 367 (1990).

[110] P. W. Anderson, Phys. Rev. **115**, 2 (1959).

[111] H. Eskes and J. H. Jefferson, Phys. Rev. B **48**, 9788 (1993).

[112] M. S. Hybertsen, E. B. Stechel, M. Schlüter, and D. R. Jennison, Phys. Rev. B **41**, 11068 (1990).

[113] N. Nücker et al., Z. Phys. **67**, 9 (1987).

[114] F. C. Zhang and T. M. Rice, Phys. Rev. B **37**, 3759 (1988).

[115] M. C. Gutzwiller, Phys. Rev. Lett. **10**, 159 (1963).

[116] J. Hubbard, Proc. Roy. Soc. London **A 276**, 238 (1963).

[117] J. Kanamori, Prog. Theor. Phys. **30**, 275 (1963).

[118] A. Montorsi, editor, *The Hubbard Modell - A Reprint Volume*, World Scientific, (1992).

[119] M. Rasetti, editor, *The Hubbard Modell - Recent Results*, World Scientific, (Singapore 1991).

[120] P. A. Bares and G. Blatter, Phys. Rev. Lett. **64**, 2567 (1990).

[121] E. H. Lieb and F. Y. Wu, Phys. Rev. Lett. **20**, 1445 (1968).

[122] T. M. Rice, in S. Maekawa and M. Sato, editors, *Physics of High–Temperature Superconductors*, Springer–Verlag, (Berlin 1991).

[123] T. Tanamoto, H. Kohno, and H. Fukuyama, J. Phys. Soc. Jpn. **62**, 1455 (1993).

[124] P. Bénard, L. Chen, and A.-M. S. Tremblay, Phys. Rev. B **47**, 15217 (1993).

[125] M. Lavagna and G. Stemmann, Phys. Rev. B **49**, 4235 (1994).

[126] M. Deeg and H. Fehske, Phys. Rev. B **50**, 17874 (1994).

[127] P. A. Lee, Phys. Rev. Lett. **63**, 680 (1989).

[128] A. H. MacDonald, S. M. Girvin, and D. Yoshioka, Phys. Rev. B **37**, 9753 (1988).

[129] P. Horsch, Helv. Phys. Acta **63**, 345 (1990).

[130] V. J. Emery and G. Reiter, Phys. Rev. B **38**, 11938 (1988).

[131] V. J. Emery and G. Reiter, Phys. Rev. B **41**, 7247 (1990).

[132] F. C. Zhang and T. M. Rice, Phys. Rev. B **41**, 7243 (1990).

[133] M. S. Hybertsen, E. B. Stechel, W. M. C. Foulkes, and M. Schlüter, Phys. Rev. B **45**, 10032 (1992).

[134] H. Schüttler and A. J. Fedro, Phys. Rev. B **45**, 7588 (1992).

[135] K. Binder and D. W. Heermann, *Monte Carlo Simulation in Statistical Physics*, Springer–Verlag, (Berlin 1992).

[136] W. v. d. Linden, Physics Reports **220**, 53 (1992).

[137] E. Gagliano and C. Balseiro, Phys. Rev. Lett. **59**, 2999 (1987).

[138] E. Dagotto, Int. J. Mod. Phys. B **5**, 77 (1991).

[139] E. B. Stechel and D. R. Jennison, Phys. Rev. B **38**, 4632 (1988).

[140] S. Bacci, E. Gagliano, R. Martin, and J. Annett, Phys. Rev. B **44**, 7504 (1991).

[141] Z. Fisk et al., Science **239**, 33 (1988).

[142] P. Fulde, J. Keller, and G. Zwicknagel, volume 41 of *Solid State Physics*, Academic Press, (New York 1988).

[143] R. L. Stratonovich, Dokl. Akad. Nauk SSSR **115**, 1097 (1957).

[144] S. Sorella, in M. Rasetti, editor, *The Hubbard Modell - Recent Results*, World Scientific, (Singapore 1991).

[145] S. E. Barnes, J. Phys. F **6**, 1375 (1976).

[146] P. Wölfle, J. Low Temp. Phys. **3/4**, 625 (1995).

[147] P. Coleman, Phys. Rev. B **29**, 3935 (1984).

[148] N. Read and D. Newns, J. Phys. C **16**, 3273 (1983).

[149] A. Auerbach and K. Levin, Phys. Rev. Lett. **57**, 877 (1986).

[150] A. J. Millis and P. A. Lee, Phys. Rev. B **35**, 3394 (1987).

[151] Z. Zou and P. W. Anderson, Phys. Rev. B **37**, 627 (1988).

[152] T. Tanamoto, K. Kuboki, and H. Fukuyama, J. Phys. Soc. Jpn. **60**, 3072 (1991).

[153] A. Auerbach and D. P. Arovas, Phys. Rev. Lett. **61**, 617 (1988).

[154] D. Yoshioka, J. Phys. Soc. Jpn. **58**, 1516 (1989).

[155] C. Jayaprakash, H. R. Krishnamurty, and S. Sarker, Phys. Rev. B **40**, 2610 (1989).

[156] G. Kotliar and A. E. Ruckenstein, Phys. Rev. Lett. **57**, 1362 (1986).

[157] A. Sudbø and A. Houghton, Phys. Rev. B **42**, 4105 (1990).

[158] R. Frésard and P. Wölfle, Int. J. Mod. Phys. B **5&6**, 685 (1992).

[159] D. Vollhardt, Physics Reports **56**, 99 (1984).

[160] D. P. Arovas and A. Auerbach, Phys. Rev. B **38**, 316 (1988).

[161] S. Sarker, C. Jayaprakash, H. R. Krishnamurthy, and M. Ma, Phys. Rev. B **40**, 5028 (1989).

[162] K. Flensberg, P. Hedegård, and M. B. Pedersen, Phys. Rev. B **40**, 850 (1989).

[163] Y. M. Li, D. N. Sheng, Z. B. Su, and L. Yu, Phys. Rev. B **45**, 5428 (1992).

[164] E. Arrigoni and G. C. Strinati, J. Low Temp. Phys. **3/4**, 599 (1995).

[165] H. Kaga, Phys. Rev. B **46**, 1979 (1992).

[166] T. Li, P. Wölfle, and P. J. Hirschfeld, Phys. Rev. B **40**, 6817 (1989).

[167] R. Frésard, M. Dzierzawa, and P. Wölfle, Europhys. Lett. **15**, 325 (1991).

[168] R. Frésard and P. Wölfle, J. Phys. Condens. Matter **4**, 3625 (1992).

[169] P. Wölfle and T. Li, Z. Phys. B **78**, 45 (1990).

[170] E. Arrigoni and G. C. Strinati, Phys. Rev. Lett. **71**, 3178 (1993).

[171] J. W. Negele and H. Orland, *Quantum Many-Particle Systems*, Addison–Wesley, (Reading, MA 1988).

[172] G. Hooijer and Van Himbergen, Phys. Rev. B **36**, 7678 (1987).

[173] N. E. Bickers, Rev. Mod. Phys. **59**, 845 (1987).

[174] J. W. Rasul and T. Li, J. Phys. C **21**, 5119 (1988).

[175] M. Lavagna, Phys. Rev. B **41**, 142 (1990).

[176] T. Jolicoeur and J. C. L. Guillou, Phys. Rev. B **44**, 2403 (1991).

[177] M. Deeg, H. Fehske, and H. Büttner, Z. Phys. B **88**, 283 (1992).

[178] M. Deeg, Master's thesis, University of Bayreuth, (1991).

[179] H. Fehske, M. Deeg, and H. Büttner, Phys. Rev. B **46**, 3713 (1992).

[180] L. Lilly, A. Muramatsu, and W. Hanke, Phys. Rev. Lett. **65**, 1379 (1990).

[181] E. Arrigoni, C. C. R. Raimondi, and G. C. Strinati, Phys. Rev. Lett. **50**, 2700 (1994).

[182] E. Arrigoni et al., Physics Reports **241**, 291 (1994).

[183] Y. Nagaoka, Phys. Rev. **147**, 392 (1966).

[184] E. Dagotto, A. Moreo, and T. Barnes, Phys. Rev. B **40**, 6721 (1989).

[185] P. W. Anderson, Phys. Rev. Lett. **64**, 1839 (1990).

[186] T. Tohyama, P. Horsch, and S. Maekawa, Phys. Rev. Lett. **74**, 980 (1995).

[187] W. Stephan and P. Horsch, Phys. Rev. Lett. **66**, 2258 (1991).

[188] R. J. Gooding, K. J. E. Vos, and P. W. Leung, Phys. Rev. B **49**, 4119 (1994).

[189] R. Eder and Y. Ohta, Phys. Rev. B **51**, 6041 (1995).

[190] P. Prelovšek and X. Zotos, Phys. Rev. B **47**, 5984 (1993).

[191] D. Poilblanc, Phys. Rev. B **48**, 3368 (1993).

[192] P. W. Leung, Phys. Rev. B **46**, 11779 (1992).

[193] W. Stephan and P. Horsch, Phys. Rev. B **42**, 8736 (1990).

[194] A. Moreo and E. Dagotto, Phys. Rev. B **42**, 8736 (1990).

[195] J. A. Riera and A. P. Young, Phys. Rev. B **40**, 5285 (1989).

[196] D. Poilblanc, Phys. Rev. B **45**, 10775 (1992).

[197] R. Hirsch, PhD thesis, University of Cologne, (1994).

[198] H. Fehske, V. Waas, H. Röder, and H. Büttner, Solid State Commun. **76**, 1333 (1990).

[199] H. Röder, V. Waas, H. Fehske, and H. Büttner, Phys. Rev. B **43**, 6284 (1991).

[200] H. Fehske, V. Waas, H. Röder, and H. Büttner, Phys. Rev. B **44**, 8473 (1991).

[201] H. Röder, H. Fehske, V. Waas, and H. Büttner, Phys. Rev. B **45**, 13092 (1992).

[202] V. Waas, H. Fehske, and H. Büttner, Phys. Rev. B **48**, 9106 (1993).

[203] J. A. Riera, Phys. Rev. B **43**, 3681 (1991).

[204] J. Oitmaa and D. Betts, Can. J. Phys. **56**, 897 (1978).

[205] V. Waas, PhD thesis, University of Bayreuth, (1992).

[206] E. Dagotto and A. Moreo, Phys. Rev. D **31**, 865 (1985).

[207] J. K. Cullum and R. A. Willoughby, *Lanczos Algorithms for Large Symmetric Eigenvalue Computations*, volume I & II, Birkhäuser, (Boston 1985).

[208] Y. Hasegawa and D. Poilblanc, Phys. Rev. B **40**, 9035 (1989).

[209] T. Itoh, M. Arai, and T. Fujiwara, Phys. Rev. B **42**, 4834 (1990).

[210] V. Elser, D. A. Huse, B. I. Shraiman, and E. D. Siggia, Phys. Rev. B **41**, 6715 (1990).

[211] M. Uchinami, Phys. Rev. B **42**, 10178 (1990).

[212] E. Dagotto et al., Phys. Rev. B **41**, 9049 (1990).

[213] J. Bonča, P. Prelovšek, and I. Sega, Phys. Rev. B **39**, 7074 (1989).

[214] M. Ogata and H. Shiba, J. Phys. Soc. Jpn. **58**, 2836 (1989).

[215] J. R. Schrieffer, X.-G. Wen, and S.-C. Zhang, Phys. Rev. B **39**, 11663 (1989).

[216] D. Poilblanc and E. Dagotto, Phys. Rev. B **42**, 4861 (1990).

[217] R. Eder and K. W. Becker, Z. Phys. B **78**, 219 (1990).

[218] S. Tang and J. E. Hirsch, Phys. Rev. B **39**, 4548 (1989).

[219] V. A. Sherman, Solid State Commun. **76**, 321 (1990).

[220] S. A. Trugman, Phys. Rev. B **41**, 892 (1990).

[221] K. v. Szczepanski, P. Horsch, W. Stephan, and M. Ziegler, Phys. Rev. B **41**, 2017 (1990).

[222] S. A. Trugman, Phys. Rev. B **37**, 1597 (1988).

[223] P. A. Lee, in K. S. Bedell, editor, *High–Temperature Superconductivity*, Addison–Wesley, (Redwood, CA 1990).

[224] A. Moreo et al., Phys. Rev. B **41**, 2313 (1990).

[225] D. C. Mattis, M. Dzierzawa, and X. Zotos, Phys. Rev. B **42**, 6787 (1990).

[226] X. Zotos, P. Prelovšek, and I. Sega, Phys. Rev. B **42**, 8445 (1992).

[227] T. Xiang, Phys. Rev. B **44**, 2276 (1991).

[228] J. Bonča, P. Prelovšek, and I. Sega, EuroPhys. Lett. **10**, 87 (1989).

[229] E. Dagotto et al., Phys. Rev. B **45**, 10741 (1992).

[230] M. Fabrizio, A. Parola, and E. Tosatti, Phys. Rev. B **44**, 1033 (1991).

[231] H. Q. Lin, Phys. Rev. B **44**, 4674 (1991).

[232] D. Poilblanc, H. J. Schulz, and T. Ziman, Phys. Rev. B **46**, 6435 (1992).

[233] S. A. Trugman, Phys. Rev. B **42**, 6612 (1990).

[234] G. S. Tian, J. Phys. A **24**, 513 (1991).

[235] H. Tasaki, Phys. Rev. Lett. **69**, 1608 (1992).

[236] A. Mielke and H. Tasaki, Comm. Math. Phys. **158**, 341 (1993).

[237] E. Müller-Hartmann, T. Hanisch, and R. Hirsch, Physica B **186–188**, 834 (1993).

[238] P. Wurth and E. Müller-Hartmann, Ann. Phys. **4**, 144 (1995).

[239] B. S. Shastry, H. R. Krishnamurty, and P. W. Anderson, Phys. Rev. B **41**, 2375 (1990).

[240] W. v. d. Linden and D. M. Edwards, J. Phys. C **3**, 4917 (1991).

[241] J. A. Riera and A. P. Young, Phys. Rev. B **39**, 9697 (1990).

[242] A. Barbieri, J. A. Riera, and A. P. Young, Phys. Rev. B **41**, 11675 (1990).

[243] C. Zhou and C. D. Gong, Physica C **169**, 245 (1990).

[244] K. W. Becker and U. Muschelknautz, Phys. Rev. B **48**, 13826 (1993).

[245] M. Marder, N. Papanicolaou, and G. C. Psaltakis, Phys. Rev. B **41**, 6920 (1990).

[246] W. O. Puttika, M. Luchini, and T. M. Rice, Phys. Rev. Lett. **68**, 538 (1992).

[247] P. B. Visscher, Phys. Rev. B **10**, 943 (1974).

[248] F. F. Assaad and D. Würtz, Phys. Rev. B **44**, 2681 (1991).

[249] M. Ogata, M. U. Luchini, S. Sorella, and F. F. Assaad, Phys. Rev. Lett. **66**, 2388 (1991).

[250] H. Yokoyama and M. Ogata, Phys. Rev. Lett. **67**, 3610 (1991).

[251] L. B. Ioffe and A. I. Larkin, Phys. Rev. B **37**, 5730 (1988).

[252] J. E. Hirsch, Phys. Rev. B **31**, 4403 (1985).

[253] J. E. Hirsch, Phys. Rev. B **35**, 1851 (1987).

[254] J. Callaway, D. P. Chen, and Y. Zhang, Phys. Rev. B **36**, 2084 (1987).

[255] H. Shiba, Prog. Theor. Phys. **48**, 2171 (1972).

[256] H. Shi and E. H. Rezayi, Phys. Rev. B **43**, 13618 (1991).

[257] D. Bormann, T. Schneider, and M. Frick, EuroPhys. Lett. **14**, 101 (1991).

[258] A. Moreo, D. J. Scalapino, and E. Dagotto, Phys. Rev. B **43**, 11442 (1991).

[259] M. Takahashi, J. Phys. Soc. Jpn. **47**, 47 (1979).

[260] M. Grilli and G. Kotliar, Phys. Rev. Lett. **64**, 1170 (1990).

[261] T. I. Ivanov, Phys. Rev. B **44**, 12077 (1991).

[262] S. K. Sarker, Phys. Rev. B **47**, 2940 (1993).

[263] J. Fröhlich and P. A. Marchetti, Phys. Rev. B **46**, 6535 (1992).

[264] J. Igarashi and P. Fulde, Phys. Rev. B **48**, 998 (1993).

[265] Y. M. Li, D. N. Sheng, Z. B. Su, and L. Yu, Int. J. Mod. Phys. B **5**, 1467 (1991).

[266] S. D. Liang, B. Doucot, and P. W. Anderson, Phys. Rev. Lett. **61**, 365 (1988).

[267] J. D. Reger and A. P. Young, Phys. Rev. B **37**, 5978 (1988).

[268] M. Deeg, H. Fehske, and H. Büttner, Europhys. Lett. **26**, 109 (1994).

[269] R. Frésard and P. Wölfle, Erratum, Int. J. Mod. Phys. B **5&6**, 3087 (1992).

[270] E. Arrigoni and G. C. Strinati, Phys. Rev. B **44**, 7455 (1991).

[271] B. Möller, K. Doll, and R. Frésard, J. Phys. Condens. Matter **5**, 4847 (1993).

[272] M. Deeg, H. Fehske, and H. Büttner, Z. Phys. B **91**, 31 (1993).

[273] A. P. Kampf and W. Brenig, J. Low Temp. Phys. **95**, 335 (1994).

[274] H. Eskes, S. A. Sawatzky, and L. F. Feiner, Physica C **160**, 424 (1989).

[275] T. Tohyama and S. Maekawa, Phys. Rev. B **49**, 3596 (1994).

[276] J. C. Campuzano et al., Phys. Rev. Lett. **64**, 2308 (1990).

[277] D. Boies, F. A. Jackson, and A.-M. S. Tremblay, Int. J. Mod. Phys. B **9**, 1001 (1995).

[278] G. C. Psaltakis and N. Papanicolaou, Phys. Rev. B **48**, 456 (1993).

[279] H. Mori and M. Hamada, Phys. Rev. B **48**, 6242 (1993).

[280] V. Chechersky et al., Phys. Rev. Lett. **70**, 3355 (1993).

[281] M. Matsuda et al., Phys. Rev. B **45**, 12548 (1992).

[282] G. M. Luke et al., Phys. Rev. B **42**, 7981 (1990).

[283] T. R. Thurston et al., Phys. Rev. B **40**, 4585 (1990).

[284] E. V. L. de Mello, J. Phys. Condens. Matter **6**, 117 (1994).

[285] H. Fehske and M. Deeg, Solid State Commun. **93**, 41 (1995).

[286] H. Takagi et al., Phys. Rev. B **40**, 2254 (1989).

[287] E. C. Jones et al., Phys. Rev. B **47**, 8986 (1993).

[288] S. J. Hagen, J. L. Peng, Z. Y. Li, and R. L. Greene, Phys. Rev. B **43**, 13606 (1991).

[289] S. A. Trugman, Phys. Rev. Lett. **65**, 500 (1990).

[290] H. Kaga and T. Saikawa, Solid State Commun. **82**, 189 (1992).

[291] H. Chi and A. D. S. Nagi, Phys. Rev. B **46**, 421 (1992).

[292] C. A. R. Sá de Melo, Z. Wang, and S. Doniach, Phys. Rev. Lett. **68**, 2078 (1992).

[293] J. R. Cooper et al., Phys. Rev. B **35**, 8794 (1987).

[294] S. Sarker, C. Jayaprakash, H. R. Krishnamurthy, and W. Wenzel, Phys. Rev. B **43**, 8775 (1991).

[295] H. Fehske and M. Deeg, J. Low Temp. Phys. **3/4**, 425 (1995).

[296] A. J. Millis and H. Monien, Phys. Rev. Lett. **70**, 2810 (1993).

[297] P. Monthoux and D. Pines, Phys. Rev. B **49**, 4261 (1941).

[298] P. Littlewood, J. Zaanen, G. Aeppli, and H. Monien, Phys. Rev. B **48**, 487 (1993).

[299] T. Tanamoto, H. Kohno, and H. Fukuyama, J. Phys. Soc. Jpn. **63**, 2739 (1994).

[300] R. Grempel and M. Lavagna, Solid State Commun. **83**, 595 (1992).

[301] M. Takigawa, Phys. Rev. B **49**, 4158 (1994).

[302] V. Barzykin, D. Pines, and D. Thelen, Phys. Rev. B **50**, 16052 (1994).

[303] F. Mila and T. M. Rice, Physica C **157**, 561 (1989).

[304] J. Rossat-Mignod et al., Physica C **185–189**, 86 (1991).

[305] M. Takigawa et al., Physica C **162**, 853 (1989).

[306] P. C. Hammel et al., Phys. Rev. Lett. **63**, 1992 (1989).

[307] M. Deeg, PhD thesis, University of Bayreuth, (1995).

[308] M. Takigawa et al., Phys. Rev. B **43**, 247 (1991).

[309] Y. Itoh et al., J. Phys. Soc. Jpn. **61**, 1287 (1992).

[310] M. Deeg et al., Z. Phys. B **95**, 87 (1994).

[311] T. Li, Y. S. Sun, and P. Wölfle, Z. Phys. B **82**, 369 (1991).

[312] T. Li, Phys. Rev. B **46**, 9301 (1992).

[313] M. Gabay and M. T. Béal-Monod, Phys. Rev. B **18**, 5033 (1978).

[314] S. Wermbter and L. Tewordt, Phys. Rev. B **43**, 10530 (1991).

[315] J. Rossat-Mignod et al., Physica B **186–188**, 1 (1993).

[316] M. Horvatic et al., Physica C **166**, 151 (1990).

[317] A. J. Millis and H. Monien, Phys. Rev. B **45**, 3059 (1992).

[318] Y.-Q. Song, M. A. Kennard, K. R. Poeppelmeier, and W. P. Halperin, Phys. Rev. Lett. **70**, 3131 (1993).

[319] Z. P. Han and R. Dupree, Physica C **208**, 328 (1993).

[320] R. E. Walstedt et al., Phys. Rev. B **45**, 8047 (1992).

[321] T. Kopp and F. Mila, Phys. Rev. B **50**, 13017 (1994).

[322] U. Trapper, D. Ihle, and H. Fehske, NTZ Universität Leipzig, preprint 13/1995; Phys. Rev. B **54**, 7614 (1996).

[323] Y. Kakehashi, J. Phys. Soc. Jpn. **50**, 1505 (1981).

[324] H. Fehske, E. Kolley, and W. Kolley, Phys. Status Solidi B **123**, 553 (1984).

[325] H. Hasegawa, J. Phys. Condens. Matter **1**, 9325 (1989).

[326] P. Fazekas, B. Menge, and E. Müller-Hartmann, Z. Phys. B **78**, 69 (1990).

[327] H. J. Schulz, Phys. Rev. Lett. **65**, 2462 (1990).

[328] W. Zhang, M. Avignon, and K. H. Bennemann, Phys. Rev. B **45**, 12478 (1992).

[329] H. Shiba, Prog. Theor. Phys. **46**, 77 (1971).

[330] B. M. McCoy and T. T. Wu, *The Two-Dimensional Ising Model*, Havard University Press, (Cambridge, Massachusetts 1973).

[331] A. Auerbach and B. E. Larson, Phys. Rev. B **43**, 7800 (1991).

[332] A. N. Andriotis, E. N. Economou, Q. Lin, and C. M. Soukoulis, Phys. Rev. B **47**, 9208 (1993).

[333] L. Chen and A.-M. S. Tremblay, Phys. Rev. B **49**, 4338 (1994).

[334] D. K. Campell, T. A. DeGrand, and S. Mazumdar, Phys. Rev. Lett. **52**, 1717 (1984).

[335] H. J. Schulz, Phys. Rev. Lett. **64**, 2831 (1990).

[336] B. Fourcade and G. Spronken, Phys. Rev. B **29**, 5089 (1984).

[337] B. Fourcade and G. Spronken, Phys. Rev. B **29**, 5096 (1984).

[338] J. Voit, Phys. Rev. B **45**, 4027 (1992).

[339] L. M. del Bosch and L. M. Falicov, Phys. Rev. B **37**, 6073 (1988).

[340] V. Waas, H. Büttner, and J. Voit, Phys. Rev. B **41**, 9366 (1990).

[341] J. W. Cannon, R. T. Scalettar, and E. Fradkin, Phys. Rev. B **44**, 5995 (1991).

[342] J. E. Hirsch, Phys. Rev. Lett. **53**, 2327 (1984).

[343] H. Q. Lin and J. E. Hirsch, Phys. Rev. B **33**, 8155 (1986).

[344] J. W. Cannon and E. Fradkin, Phys. Rev. B **41**, 9435 (1990).

[345] V. J. Emery, in J. T. Devreese, R. P. Evrard, and V. E. van Doren, editors, *Highly Conducting One–Dimensional Solids*, Plenum Press, (New York 1979).

[346] D. Cabib and E. Callen, Phys. Rev. B **12**, 5249 (1975).

[347] Y. Zhang and J. Callaway, Phys. Rev. B **39**, 9397 (1989).

[348] R. Micnas, J. Ranninger, and S. Robaszkiewicz, Rev. Mod. Phys. **62**, 113 (1990).

[349] A. S. Alexandrov and J. Ranninger, Phys. Rev. B **23**, 1796 (1981).

[350] N. Tsuda, K. Nasu, A. Yanese, and K. Siratori, *Electronic Conduction in Oxides*, Springer–Verlag, (Berlin 1990).

[351] G. Stollhoff and P. Fulde, Z. Phys. B **26**, 257 (1977).

[352] A. M. Oleś, R. Micnas, S. Robaszkiewicz, and K. A. Chao, Phys. Lett. A **102**, 323 (1984).

[353] C. M. Varma, Phys. Rev. Lett. **61**, 2713 (1988).

[354] M. S. Laad and D. K. Gosh, J. Phys. C **3**, 9723 (1991).

[355] P. G. J. van Dongen, Phys. Rev. Lett. **74**, 182 (1995).

[356] Y. Bar-Yam, T. Egami, J. M. de Leon, and A. R. Bishop, *Lattice Effects in High–T_c Superconductors*, World Scientific, (Singapore 1992).

[357] M. Grilli and C. Castellani, Phys. Rev. B **50**, 16880 (1994).

[358] J. Zhong and H.-B. Schüttler, Phys. Rev. Lett. **69**, 1600 (1992).

[359] H. Fehske, H. Röder, G. Wellein, and A. Mistriotis, Phys. Rev. B **51**, 16582 (1995).

[360] J. Loos, Z. Phys. B **71**, 161 (1988).

[361] B. Gerlach and H. Löwen, Rev. Mod. Phys. **63**, 63 (1991).

[362] S. Ciuchi, F. de Pasquale, and D. Feinberg, EuroPhys. Lett. **30**, 151 (1995).

[363] J. K. Freericks and E. H. Lieb, Phys. Rev. B **51**, 2812 (1995).

[364] A. B. Migdal, Sov. Phys. JETP **7**, 996 (1958).

[365] G. M. Eliashberg, Sov. Phys. JETP **11**, 696 (1960).

[366] A. S. Alexandrov and A. B. Krebs, Usp. Fiz. Nauk **162**, 1 (1992).

[367] L. D. Landau, Z. Phys. **3**, 664 (1933).

[368] A. L. Shluger and A. M. Stoneham, J. Phys. Condens. Matter **5**, 1993 (1993).

[369] A. S. Alexandrov and N. F. Mott, Int. J. Mod. Phys. B **8**, 2075 (1994).

[370] D. Manh, D. Mayou, and F. Cyrot-Lackmann, Europhys. Lett. **13**, 167 (1990).

[371] B. Friedl, C. Thomsen, and M. Cordona, Phys. Rev. Lett. **65**, 1990 (1990).

[372] B. Güttler et al., J. Phys. Condens. Matter **2**, 8977 (1990).

[373] A. P. Litvinchuk et al., Phys. Rev. B **44**, 9723 (1991).

[374] R. E. Cohen, W. E. Pickett, and H. Krakauer, Phys. Rev. Lett. **64**, 2575 (1990).

[375] V. I. Anisimov, M. A. Korotin, J. Zaanen, and O. K. Andersen, Phys. Rev. Lett. **68**, 345 (1992).

[376] H. Rietschel, J. Low Temp. Phys. **95**, 293 (1994).

[377] R. P. Sharma, L. E. Rehn, P. M. Baldo, and J. Z. Lin, Phys. Rev. Lett. **62**, 2869 (1989).

[378] T. Haga et al., Phys. Rev. B **41**, 826 (1990).

[379] T. Egami et al., in J. Ashkenazi and G. Vezzoli, editors, *Electronic Structure and Mechanisms of High Temperature Superconductivity*, Plenum Press, (New York 1991).

[380] Y. H. Kim et al., Phys. Rev. B **38**, 6478 (1988).

[381] J. D. Jorgenson, Physics Today **44**, 34 (1991).

[382] J. Ranninger, Z. Phys. B **84**, 167 (1991).

[383] D. Emin, Phys. Rev. B **45**, 5525 (1992).

[384] X.-X. Bi and P. C. Eklund, Phys. Rev. Lett. **70**, 2625 (1993).

[385] E. K. H. Salje, A. S. Alexandrov, and W. Y. Liang, *Polarons and Bipolarons in High Temperature Superconductors and Related Materials*, Cambridge Univ. Press, (Cambridge 1995).

[386] C. H. Chen, S.-W. Cheong, and A. S. Cooper, Phys. Rev. Lett. **71**, 2461 (1993).

[387] D. Mihailović, C. M. Foster, K. Voss, and A. J. Heeger, Phys. Rev. B **42**, 7989 (1990).

[388] P. Calvani, Solid State Commun. **91**, 113 (1994).

[389] J. P. Falck, A. Levy, M. A. Kastner, and R. J. Birgenau, Phys. Rev. B **48**, 4043 (1993).

[390] Y. Y. Suzuki, P. Pincus, and A. J. Heeger, Phys. Rev. B **44**, 7127 (1991).

[391] G. Verbist, F. M. Peeters, and J. T. Devreese, Physica Scripta **T 39**, 66 (1991).

[392] D. Emin, Phys. Rev. Lett. **72**, 1052 (1994).

[393] A. S. Alexandrov and J. Ranninger, Physica C **198**, 360 (1992).

[394] A. S. Alexandrov, A. M. Bratkovsky, N. F. Mott, and E. K. H. Salje, Physica C **215**, 359 (1993).

[395] J. E. Hirsch, Phys. Rev. B **47**, 5351 (1993).

[396] N. F. Mott, J. Phys. Condens. Matter **5**, 3487 (1993).

[397] J. Ranninger, Acta Phys. Pol. A **85**, 89 (1994).

[398] G. Iadonisi, V. Cataudella, D. Ninno, and M. L. Chiofalo, Phys. Lett. A **196**, 359 (1995).

[399] S.-W. Cheong et al., Phys. Rev. B **49**, 7088 (1994).

[400] S. M. Hayden et al., Phys. Rev. Lett. **68**, 1061 (1992).

[401] E. D. Isaacs et al., Phys. Rev. Lett. **72**, 3421 (1994).

[402] K. Nakajima et al., J. Phys. Soc. Jpn. **64**, 716 (1995).

[403] P. Prelovšek, T. M. Rice, and F. C. Zhang, J. Phys. C **20**, L229 (1987).

[404] J. Kim, K. Levin, R. Wentzcovitch, and A. Auerbach, Phys. Rev. B **44**, 5148 (1991).

[405] S. Barišić, I. Batistić, and J. Friedel, EuroPhys. Lett. **3**, 1231 (1987).

[406] A. Muramatsu and W. Hanke, Physica C **153**, 229 (1988).

[407] D. Feinberg, S. Ciuchi, and F. de Pasquale, Int. J. Mod. Phys. B **4**, 1317 (1990).

[408] A. S. Alexandrov, Phys. Rev. B **38**, 925 (1988).

[409] H. D. Raedt and A. Lagendijk, Phys. Rev. B **27**, 6097 (1983).

[410] I. G. Lang and Y. A. Firsov, Zh. Eksp. Teor. Fiz. **43**, 1843 (1962).

[411] T. Holstein, Ann. Phys. **8**, 325 (1959).

[412] T. Holstein, Ann. Phys. **8**, 343 (1959).

[413] A. S. Alexandrov, V. V. Kabanov, and D. K. Ray, Phys. Rev. B **49**, 9915 (1994).

[414] G. Wellein, H. Röder, and H. Fehske, Phys. Rev. B, **54**, 9666 (1996).

[415] V. V. Kabanov and O. Y. Mashtakov, Phys. Rev. B **47**, 6060 (1993).

[416] J. E. Hirsch, Phys. Rev. B **31**, 6022 (1985).

[417] E. Jurczek and T. M. Rice, Europhys. Lett. **1**, 225 (1986).

[418] H. Zheng, Phys. Rev. B **41**, 4723 (1990).

[419] H. Zheng, D. Feinberg, and M. Avignon, Phys. Rev. B **41**, 11557 (1990).

[420] A. N. Das, J. Konior, D. K. Ray, and A. M. Oleś, Phys. Rev. B **44**, 7680 (1991).

[421] I. Batistić, J. T. Gammel, and A. R. Bishop, Phys. Rev. B **44**, 13228 (1992).

[422] J. E. Hirsch and E. Fradkin, Phys. Rev. B **27**, 4302 (1983).

[423] F. Marsiglio, Phys. Rev. B **42**, 2416 (1990).

[424] R. T. Scalettar, N. E. Bickers, and D. J. Scalapiono, Phys. Rev. B **40**, 197 (1989).

[425] G. Levine and W. P. Su, Phys. Rev. B **42**, 4143 (1990).

[426] S. Aubry, P. Quemerais, and J. Raimbault, in *Proceedings of the third european conference on low dimensional conductors and superconductors*, (Dubrovnik (Yougoslavia) 1989).

[427] S. Suzuki and Y. Toyozawa, J. Phys. Soc. Jpn. **59**, 2841 (1990).

[428] H. D. Raedt and A. Lagendijk, Phys. Rev. Lett. **49**, 1522 (1982).

[429] Y. Toyozawa, Prog. Theor. Phys. **26**, 29 (1961).

[430] D. Emin, Adv. Phys. **12**, 57 (1973).

[431] J. Ranninger and U. Thibblin, Phys. Rev. B **45**, 7730 (1992).

[432] J. Mustre de Leon et al., Phys. Rev. Lett. **68**, 3236 (1992).

[433] H. Zheng, D. Feinberg, and M. Avignon, Phys. Rev. B **39**, 9405 (1989).

[434] H. Fehske et al., Z. Phys. **94**, 91 (1994).

[435] H. Zheng, Solid State Commun. **65**, 731 (1988).

[436] H. P. Yuen, Phys. Rev. A **13**, 2226 (1976).

[437] C. F. Lo and R. Sollie, Phys. Lett. A **169**, 91 (1992).

[438] K. Nasu, Phys. Rev. B **35**, 1748 (1987).

[439] U. Trapper, H. Fehske, M. Deeg, and H. Büttner, Z. Phys. B **93**, 465 (1993).

[440] A. M. Oleś, J. Phys. C **15**, L1065 (1982).

[441] S. Weber and H. Büttner, J. Phys. C **17**, L337 (1984).

[442] D. Ihle, H. Fehske, J. Loos, and U. Trapper, Physica C **235–240**, 2263 (1994).

[443] H. Fehske, H. Röder, A. Mistriotis, and H. Büttner, J. Phys. Condens. Matter **5**, 3635 (1993).

[444] A. Sumi and Y. Toyozawa, J. Phys. Soc. Jpn. **35**, 137 (1973).

[445] A. Klamt, J. Phys. C **21**, 1953 (1988).

[446] Y. Lépine and R. Gutiérrez, Solid State Commun. **85**, 155 (1993).

[447] D. M. Eagles, Phys. Rev. **130**, 1381 (1963).

[448] H. G. Reik and D. Heese, J. Phys. Chem. Solids **28**, 581 (1967).

[449] E. K. Kudinov, D. N. Mirlin, and Y. A. Firsov, Fiz. Tverd. Tela **11**, 2789 (1969).

[450] G. Wellein, Master's thesis, University of Bayreuth, (1994).

[451] D. Ihle and H. Fehske, J. Phys. A **28**, L275 (1995).

[452] J. R. Schrieffer and P. A. Wolff, Phys. Rev. **149**, 491 (1966).

[453] H. Zheng, Phys. Rev. B **37**, 7419 (1988).

[454] A. H. MacDonald, S. M. Girvin, and D. Yoshioka, Phys. Rev. B **41**, 2565 (1990).

[455] A. N. Das, J. Konior, and D. K. Ray, Physica C **170**, 215 (1990).

[456] I. O. Kulik and A. G. Pedan, Zh. Eksp. Teor. Fiz. **79**, 1496 (1980).

[457] A. Teubel, E. Kolley, and W. Kolley, J. Phys. A **23**, L 837 (1990).

[458] R. Oppermann, Z. Phys. **75**, 149 (1989).

[459] J. Stein and R. Oppermann, Phys. Lett. A **184**, 370 (1994).

[460] F. Marsiglio, Phys. Lett. A **180**, 280 (1993).

[461] H. Schüttler, J. Zhong, and A. J. Fedro, preprint.

[462] H. J. Schulz and T. A. Ziman, EuroPhys. Lett. **18**, 355 (1992).

[463] H. Röder, H. Fehske, and H. Büttner, Phys. Rev. B **47**,12420 (1993).

[464] F. Marsiglio, Physica C **244**, 21 (1995).

[465] Y. Inada and C. Ishii, J. Phys. Soc. Jpn. **59**, 612 (1990).

[466] D. Emin and T. Holstein, Phys. Rev. Lett. **36**, 323 (1976).

[467] R. N. Silver and H. Röder, Int. J. Mod. Phys. C **5**, 935 (1994).

[468] A. H. Castro Neto and A. O. Caldeira, Phys. Rev. B **46**, 8858 (1992).

[469] H. Röder, H. Fehske, and R. N. Silver, Europhys. Lett. **28**, 257 (1994).

[470] P. W. Leung and P. E. Oppenheimer, Comput. Phys. **6**, 603 (1992).

[471] A. Dobry, A. Greco, S. Koval, and J. Riera, Phys. Rev. B **52**, 13722 (1995).

[472] G. Dopf, A. Muramatsu, and W. Hanke, Phys. Rev. Lett. **68**, 353 (1992).

[473] L. Pintschovious et al., Phys. Rev. B **40**, 2229 (1989).

[474] H. G. Reik, Z. Phys. **203**, 364 (1967).

Acknowledgements

It is a pleasure to thank H. Büttner for his trust, constant encouragement, and support during the course of this work. I am indebted to D. Ihle for a long–standing invaluable collaboration, for countless discussions and suggestions, and, in particular, for his friendship.

The present Habilitation thesis is basically an outgrowth of a series of accepted or submitted original contributions cited in the headings of each chapter. These publications would not have existed without the fruitful and pleasant cooperation with my colleagues H. Büttner, M. Deeg, D. Ihle, J. Loos, A. Mistriotis, H. Röder, R. N. Silver, U. Trapper, V. Waas, and G. Wellein. All deserve my deepest gratitude. I greatly appreciated the careful and critical reading of parts of the manuscript by L. Buchholtz and J. Stolze. I am grateful for the assistance of F. Schmögner in the preparation of the figures.

I would also like to thank my friends and colleagues in the Physics Department at Bayreuth for their help, advice, and moral support. Especially I am grateful to D. Baranowski, K. Fesser, F. Göhmann, B. Nicklaus, and A. Weber. Moreover, thanks are due A. Muramatsu, W. Pesch, and D. Rainer, who in numerous seminars and conversations have been a constant source of inspiration.

Over the years I have benefited from enlightening and stimulating discussions with more colleagues than I can list here individually. I wish to thank them all.

This work was supported in part by the Bundesministerium für Bildung und Wissenschaft under Contract F0302.00, by the Deutsche Forschungsgemeinschaft through SFB 213 B8 and Project SF–HTSL–SRO, and by the European Economic Community under Contract No. SCI*CT91-0686. Special thanks go to the LRZ München, and also to the HLRZ, c/o KFA Jülich, for the generous granting of their computer facilities. Part of the numerical calculations were performed on a CM5 of the GMD (St. Augustin). Continuing hospitality of the NTZ at the University of Leipzig is greatly acknowledged.